

INFORMATION TO USERS

This manuscript has been reproduced from the microfilm master. UMI films the text directly from the original or copy submitted. Thus, some thesis and dissertation copies are in typewriter face, while others may be from any type of computer printer.

The quality of this reproduction is dependent upon the quality of the copy submitted. Broken or indistinct print, colored or poor quality illustrations and photographs, print bleedthrough, substandard margins, and improper alignment can adversely affect reproduction.

In the unlikely event that the author did not send UMI a complete manuscript and there are missing pages, these will be noted. Also, if unauthorized copyright material had to be removed, a note will indicate the deletion.

Oversize materials (e.g., maps, drawings, charts) are reproduced by sectioning the original, beginning at the upper left-hand corner and continuing from left to right in equal sections with small overlaps.

Photographs included in the original manuscript have been reproduced xerographically in this copy. Higher quality 6" x 9" black and white photographic prints are available for any photographs or illustrations appearing in this copy for an additional charge. Contact UMI directly to order.

ProQuest Information and Learning
300 North Zeeb Road, Ann Arbor, MI 48106-1346 USA
800-521-0600

UMI[®]

NOTE TO USERS

This reproduction is the best copy available.

UMI

**A feasibility study of
adaptive plasma-assisted incineration**

**Julie Fillion
Department of Chemical Engineering
McGill University, Montreal**

**under the supervision of
Richard J. Munz and Eric D. Salin**

**A thesis submitted to the Faculty of Graduate Studies and Research
in partial fulfilment of the requirements of the degree of
Doctor of Philosophy**



**National Library
of Canada**

**Acquisitions and
Bibliographic Services**

**395 Wellington Street
Ottawa ON K1A 0N4
Canada**

**Bibliothèque nationale
du Canada**

**Acquisitions et
services bibliographiques**

**395, rue Wellington
Ottawa ON K1A 0N4
Canada**

Your file Votre référence

Our file Notre référence

The author has granted a non-exclusive licence allowing the National Library of Canada to reproduce, loan, distribute or sell copies of this thesis in microform, paper or electronic formats.

The author retains ownership of the copyright in this thesis. Neither the thesis nor substantial extracts from it may be printed or otherwise reproduced without the author's permission.

L'auteur a accordé une licence non exclusive permettant à la Bibliothèque nationale du Canada de reproduire, prêter, distribuer ou vendre des copies de cette thèse sous la forme de microfiche/film, de reproduction sur papier ou sur format électronique.

L'auteur conserve la propriété du droit d'auteur qui protège cette thèse. Ni la thèse ni des extraits substantiels de celle-ci ne doivent être imprimés ou autrement reproduits sans son autorisation.

0-612-64558-4

Canada

Abstract

Rising awareness in the need for environmental protection has brought into question the adequacy of conventional hazardous waste treatment operations. Regulatory standards are increasingly strict, and there is growing concern over the safety of incineration facilities. This research project examines the techno-economic potential of thermal plasma technology in this context.

Adaptive Plasma-Assisted Incineration (APAI) is a novel concept for secondary gas treatment in hazardous waste incineration. As an energy source for waste destruction, a thermal plasma can provide conditions far higher in temperature and in reactivity than those obtained using a combustion flame. Thus, the plasma is more effective at destroying hazardous materials, albeit at a higher cost.

APAI features a thermal plasma afterburner with continual on-line optical monitoring of the gas product and feedback optimization of the plasma conditions. This approach allows complete destruction of persistent organic compounds and cost-effective response to feed load variations. The process supplements conventional incineration techniques with the effectiveness and flexibility of thermal plasma treatment. The main objectives are to reduce the risk of harmful emissions during hazardous waste incineration and to facilitate compliance with new environmental regulations.

In this project, the technical feasibility of APAI was demonstrated experimentally using a laboratory-scale plasma afterburner model. The work focused on the development of a spectroscopic monitoring procedure and on the application of optimization techniques for cost-effective operation of the model system. The techno-economic potential and limitations of APAI were addressed in a conceptual study. Preliminary designs and cost estimates were developed for

specific applications. The costs of plasma-assisted and conventional methods were compared for contaminated soil remediation (by incineration and desorption) and for organic liquid waste destruction. Economically, APAI appears uncompetitive at the present time. However, it remains a promising alternative in view of ongoing environmental policy changes and developments in plasma technology.

Résumé

Une sensibilisation accrue en matière de protection environnementale remet en question l'efficacité des opérations conventionnelles de traitement des déchets dangereux. Les normes réglementaires sont de plus en plus sévères, et le public est davantage soucieux de la sécurité des installations d'incinération. Ce projet de recherche évalue le potentiel techno-économique des plasmas thermiques dans ce contexte.

L'Incinération Adaptative Assistée par Plasma (IAAP) est un concept novateur pour le traitement secondaire des gaz d'incinération. Comme source d'énergie pour la destruction des déchets, un plasma thermique est en mesure de fournir un environnement plus chaud et plus réactif que celui obtenu à l'aide d'une flamme de combustion. Ainsi, le plasma décompose les substances dangereuses plus efficacement, à un coût cependant plus élevé.

L'IAAP comprend une chambre de post-combustion à plasma avec surveillance continue des gaz produits et optimisation rétroactive des conditions d'opération du plasma. Cette approche permet la destruction complète des composés organiques persistants et le maintien d'un bon rapport rendement-

coût lors de variations de la charge de traitement. Le procédé allie les techniques d'incinération conventionnelles à l'efficacité et à la flexibilité du traitement par plasma. Les objectifs principaux sont de réduire les risques d'émissions nocives durant l'incinération de déchets dangereux et de faciliter l'adaptation aux nouvelles normes environnementales.

Au cours de ce projet, la faisabilité technique de l'IAAP a été démontrée en laboratoire à l'aide d'un modèle de post-combustion par plasma. Ce travail était axé sur le développement d'une procédure d'analyse spectroscopique et sur l'application de techniques d'optimisation pour maximiser le rapport rendement-coût du système-modèle. Les possibilités et limites techno-économiques de l'IAAP ont été abordées par une étude conceptuelle. Des plans préliminaires et estimés des coûts ont été dressés pour des applications spécifiques. Les coûts de l'IAAP et des méthodes conventionnelles ont été comparés pour la rémediation de sols contaminés (par incinération et par désorption) et pour la destruction de déchets liquides organiques. Au plan économique, l'IAAP apparaît peu compétitive dans les circonstances actuelles. Cependant, elle demeure une alternative prometteuse compte tenu de l'évolution des politiques environnementales et du développement technologique des plasmas.

Acknowledgments

I express my gratitude to all those who were helpful to me throughout this work, and in particular:

to my co-supervisors, Professors Richard J. Munz (Department of Chemical Engineering) and Eric D. Salin (Department of Chemistry), for their outstanding guidance and availability;

to the support staff of the Department of Chemical Engineering; special thanks to Walter Greenland, whose creative skills were essential to the construction of my laboratory apparatus;

to my colleagues of the McGill Plasma Technology Research group, including Karen Sum for writing a computer program used in this work and Tony Addona for providing technical information;

to Gisèle Fahmi, for her contribution as a laboratory assistant;

to staff and colleagues from the Department of Chemistry, where the preliminary stage of this work was carried out; special thanks to Cameron Skinner for his patience and skill as a teacher and instrument designer;

to McGill Professors Jean-Luc Meunier (Department of Chemical Engineering) and David Burns (Department of Chemistry), for their teachings on optics and spectroscopy;

to Université de Sherbrooke Professors Pierre Proulx, for providing computer simulation expertise and resources, and Gervais Soucy, for consultations on plasma waste treatment and techno-economics;

to my parents Marcel and Nicole Fillion, for offering unconditional support and encouragement throughout my academic studies;

to my companion Richard Connor, for his professional expertise and editorial skills, for his motivating support and trust, for his comforting perspective in difficult times, and most importantly, for a happiness that gives sense to goals and accomplishments.

This project benefited from the financial support of the Natural Sciences and Engineering Research Council of Canada and of Quebec's Fondation pour la Formation de Chercheurs et l'Aide à la Recherche.

Table of Content

1. INTRODUCTION.....	1
2. LITERATURE REVIEW.....	4
2.1 Fundamental Principles.....	4
2.1.1 Hazardous Waste Treatment.....	4
2.1.1.1 Environmental Organic Pollutants and Toxicology	4
2.1.1.2 Current Technology.....	5
2.1.1.3 Flame Combustion	7
2.1.1.4 Plasma Pyrolysis	14
2.1.2 Optical Emission Spectroscopy.....	16
2.1.2.1 Spectral Line Emission in Thermodynamic Equilibrium.....	17
2.1.2.2 Diatomic Molecular Band Emission.....	19
2.1.2.3 Methods and Instrumentation.....	23
2.1.2.4 The Swan Bands of C ₂	27
2.1.2.5 Composition Diagnostics.....	28
2.1.2.6 Temperature Estimation.....	29
2.1.3 Control and Optimization	34
2.1.3.1 Adaptability and Control	34
2.1.3.2 Gradient-Based Search Methods	36
2.1.3.3 Simplex Method.....	36
2.2 Existing Plasma Processes for Hazardous Waste Treatment	37
2.2.1 Westinghouse Pyroplasma Process	38
2.2.2 INDICIS Process (Electricité de France).....	39
2.2.3 Retech Plasma Arc Centrifugal Treatment (PACT) System.....	40

2.2.4	Moser Glaser & Co. (MGC) Plasma PLASMOX Process.....	41
2.2.5	ScanArc Process	41
2.2.6	CSIRO / SRL Plasma PLASCON Process.....	42
2.2.7	Commissariat de l'Energie Atomique	42
2.3	Existing Hazardous Waste Incineration Processes	43
2.3.1	BOVAR Process	43
2.3.2	Bennett Process.....	44
2.4	Novel Aspects of Adaptive Plasma-Assisted Incineration	44
2.4.1	Advantages over Conventional Incineration.....	45
3.	OBJECTIVES.....	48
3.1	Specific Objectives.....	48
3.1.1	Plasma Afterburner Model	48
3.1.2	Spectroscopic Diagnostics	48
3.1.3	Optimization	48
3.1.4	Techno-Economic Assessment	49
4.	METHODOLOGY	50
4.1	Plasma Afterburner Model	50
4.1.1	Radio Frequency Generator and Induction Plasma Torch.....	50
4.1.2	Manipulated Variables	52
4.1.3	Plasma Operation	53
4.2	Optical Diagnostics	59

4.2.1	Light Collection and Detection	59
4.2.2	Composition Measurement	63
4.2.3	Temperature Measurement	63
4.2.3.1	Temperature Evaluation From High-Resolution Spectra	64
4.2.3.2	Temperature Estimates from Unresolved Spectra	65
4.2.3.3	Heat Balance Calculation Tools	66
4.3	Optimization Techniques and Manual Control.....	67
4.3.1	Scaled Variables	67
4.3.1.1	Manipulated Variables	67
4.3.1.2	Dependent Variables	68
4.3.2	Objective Functions	71
4.3.3	Optimization Programs	73
4.3.3.1	Gradient-Based Program	74
4.3.3.2	Simplex Program	77
4.3.4	Manual Control Loop.....	78
4.3.4.1	Optimization Sequence Procedure.....	78
5.	RESULTS AND DISCUSSION	81
5.1	Optical Diagnostics	81
5.1.1	Spectrum Numerical Simulation.....	81
5.1.2	Composition Assessment	82
5.1.2.1	Selection of Spectral Indicators	84
5.1.2.2	Uncertainty in the Spectral Indicators.....	92
5.1.2.3	Correlation Between C ₂ Concentration and Swan Band Emission	94
5.1.2.4	Choice of an Observation Point.....	95
5.1.3	Temperature Estimation.....	97
5.1.3.1	Boltzmann Plot Method	97

5.1.3.2	Approximate Methods	103
5.1.3.3	Heat Balance Computations.....	105
5.2	Afterburner Model	107
5.2.1	Geometry of the Chemically Reactive Zone.....	107
5.2.2	Concentration, Temperature and Velocity Profiles.....	108
5.2.2.1	Hifi23 Simulations.....	109
5.2.2.2	Experimental Observations	112
5.2.3	Interpretation of Spectral Indicator Values.....	118
5.3	Demonstration of Adaptive Plasma Operation.....	119
5.3.1	Objective Function Development	120
5.3.2	Optimization Strategy Validation	121
5.3.2.1	Optimization on a Conical Hill.....	122
5.3.2.2	Optimization of a Simulated Noiseless System	124
5.3.2.3	Optimization of a Simulated Noisy System.....	125
5.3.3	Error Analysis.....	127
5.3.3.1	Uncertainty in Manipulated and Dependent Variables	128
5.3.3.2	Error Propagation Through the Objective Function	130
5.3.3.3	Run-to-Run Variability in System Response	132
5.3.4	Experimental Optimization Sequences	135
5.3.4.1	Gradient-Based Method	137
5.3.4.2	Simplex Method.....	140
5.3.4.3	Comparative Evaluation of Optimization Methods.....	140
5.3.4.4	Reproducibility	146
5.3.4.5	Role of Economic Factors in the Optimization Strategy	155
5.3.5	Technical Feasibility of the Adaptive Approach	157
6.	TECHNO-ECONOMIC EVALUATION.....	158

6.1	Prototype System Design	159
6.1.1	Configuration.....	159
6.1.2	Equipment Selection.....	160
6.1.3	Optimization Strategy Development.....	161
6.2	Process Flowsheet	162
6.2.1	Waste Treatment Section.....	162
6.2.1.1	Primary Combustion Chamber.....	162
6.2.1.2	Afterburner.....	164
6.2.1.3	Liquid Waste Furnace.....	165
6.2.2	Gas Cleaning Section.....	165
6.2.2.1	Quench Tank.....	166
6.2.2.2	Venturi Scrubber.....	167
6.2.2.3	Absorption Tower.....	167
6.2.2.4	Stack and Additional Units.....	168
6.2.2.5	Nitrogen and Sulfur Oxide Removal.....	169
6.2.3	Computer-Aided Process Simulation Using ASPEN.....	170
6.3	Economic Model	171
6.3.1	Total Capital Investment.....	172
6.3.1.1	Equipment Cost Calculations.....	173
6.3.2	Total Annual Operating Cost.....	174
6.3.2.1	Utility Consumption Calculations.....	176
6.3.3	Cash Flow and Net Present Value Calculations.....	178
6.4	Example Processes	179
6.4.1	Case I: Soil Incineration.....	179
6.4.1.1	Plasma-Assisted System (Case I).....	179
6.4.1.2	Conventional System (Case I).....	180

6.4.2	Case II: Soil Desorption	180
6.4.2.1	Plasma-Assisted System (Case II)	181
6.4.2.2	Conventional System (Case II).....	181
6.4.3	Case III: PCB Liquid Waste Incineration.....	182
6.4.3.1	Plasma Heating System (Case III)	182
6.4.3.2	Gas Combustion System (Case III).....	183
6.5	Comparative Cost Analysis	183
6.5.1	Cost Summaries	184
6.5.1.1	Capital Investment.....	184
6.5.1.2	Operating Costs	186
6.5.1.3	Net Present Value	189
6.5.2	Sensitivity Study.....	191
6.5.2.1	Process Design Variables	191
6.5.2.2	External Economic Factors.....	197
6.6	Incentives and Potential Market for APAI.....	203
6.6.1	Trends in Environmental Policy.....	203
6.6.2	Full Cost Accounting and Total Life Cycle Analysis	205
6.6.3	Techno-Economic Niche for APAI	208
7.	CONCLUSIONS.....	211
8.	BIBLIOGRAPHY	214
9.	APPENDICES.....	224

List of Figures

Figure 2.1.2-1	Morse Potential Curve for a Diatomic Molecule	21
Figure 2.1.2-2	Schematic Diagram of the First Few Vibrational and Rotational Levels of Two Electronic States A and B	21
Figure 4.1.3-1	Schematic Diagram of the Original System with Torch-Reactor Combination	54
Figure 4.1.3-2	Plate Power vs Plate Current at 0.1% Propane	57
Figure 4.1.3-3	Plate Power vs Plate Current at 0.2% Propane	57
Figure 4.1.3-4	Schematic Diagram of the Modified Open System Without Reactor	58
Figure 4.2.1-1	Schematic Diagram of the Optical System	61
Figure 4.2.1-2	Approximation of the Intensity Loss Due to Lack of Focus	62
Figure 4.3.2-1	Three-Dimensional View of the Objective Function	72
Figure 4.3.2-2	Contour Plot of the Objective Function	72
Figure 4.3.4-1	Manual Feedback Control Loop	80
Figure 5.1.2-1	Plasma Emission Spectrum in the Swan Band Region	83
Figure 5.1.2-2	Afterburner Model Plasma Emission Spectra	83
Figure 5.1.2-3	Swan Band Signal and Blank Spectra	83
Figure 5.1.2-4	Effect of Oxygen Content on Swan Band Emission	85
Figure 5.1.2-5	Effect of Power on Swan Band Emission	85
Figure 5.1.2-6	Effect of Oxygen Content on Swan Band Emission	86
Figure 5.1.2-7	Effect of Power on Swan Band Emission	86
Figure 5.1.2-8	OMA Blank Spectra at Low Power	87
Figure 5.1.2-9	OMA Blank Spectra at High Power	87
Figure 5.1.2-10	Swan Band Spectra with Selected Indicator Regions	90

Figure 5.1.2-11	Geometry of the Plasma Jet	96
Figure 5.1.3-1	High-Resolution Band Spectrum for Temperature Estimation	98
Figure 5.1.3-2	Boltzmann Plot for the Range $J'' = 46 - 36$	98
Figure 5.1.3-3	Boltzmann Plot Temperature Estimated Across the Plasma Jet	98
Figure 5.1.3-4	Simulated P-branch Intensity Profiles at Different Temperatures	104
Figure 5.1.3-5	Predicted Plate Power vs Assumed Temperature for an Argon Plasma with 3.5% Oxygen (FACT Equilibrium Calculation)	104
Figure 5.2.2-1	S and B Profile Sets	114
Figure 5.2.2-2	(S/B) Profile Sets	114
Figure 5.2.2-3	(S/B) Ratio Distribution Across the Plasma Jet	115
Figure 5.3.2-1	Optimization Paths on a Circular Hill	123
Figure 5.3.2-2	Three-Dimensional View of a Simulated System Response Over the Operating Space	123
Figure 5.3.2-3	Contour Plot of the Simulated Response with Optimization Paths	126
Figure 5.3.2-4	Effect of Noise on Optimization Paths	126
Figure 5.3.4-1	Optimal Gradient Sequence Paths	138
Figure 5.3.4-2	Optimal Gradient Paths on the Objective Function Contour Plot	138
Figure 5.3.4-3	Optimal Gradient Sequence Paths	139
Figure 5.3.4-4	Simplex Sequence Paths	139
Figure 5.3.4-5	Simplex Paths on the Objective Function Contour Plot	141
Figure 5.3.4-6a	Simplex Sequence Path	141
Figure 5.3.4-6b	Simplex Sequence Path	142

Figure 5.3.4-7	End Point Comparison of Optimization Methods - Under-Treatment Case with 0.2% C ₃ H ₈	142
Figure 5.3.4-8	Performance Comparison of Optimization Methods - Under-Treatment Case with 0.2% C ₃ H ₈	144
Figure 5.3.4-9	End Point Comparison of Optimization Methods - Over-Treatment Case with 0.15% C ₃ H ₈	144
Figure 5.3.4-10	Performance Comparison of Optimization Methods - Over-Treatment Case with 0.15% C ₃ H ₈	145
Figure 5.3.4-11	Variations in the Location of the Optimum Region Over Time	145
Figure 5.3.4-12	Variations in System Response	147
Figure 5.3.4-13	Approaching the Optimum Ridge on the Response Surface	147
Figure 5.3.4-14	Influence of the Starting Point on the Location of the End Point Within the Optimum Region	149
Figure 5.3.4-15	Equivalent Optima Reached From Different Starting Points	149
Figure 5.3.4-16	Predominant Effect of Plate Current on Destruction Efficiency	150
Figure 5.3.4-17	Effect of System Change on Optimization End Points	150
Figure 5.3.4-18	Influence of Response Sensitivity to Manipulated Variables on Optimization Performance	152
Figure 5.3.4-19	Evidence of Change in Thermal Efficiency	152
Figure 5.3.4-20	Finding an Optimum Region from Different Starting Points	153
Figure 5.3.4-21	Repeatability of End Results Within Series of Sequences Starting from Different Points	154
Figure 5.3.4-22a	Influence of the Relative Costs of Manipulated Variables on Optimization Sequence Paths - Under-Treatment Case with 0.26% C ₃ H ₈	154
Figure 5.3.4-22b	Influence of the Relative Costs of Manipulated Variables on Optimization Sequence Paths - Over-Treatment Case with 0.17% C ₃ H ₈	156

Figure 5.3.4-23	Influence of the Relative Costs of Manipulated Variables on Optimization Paths (Limiting Cases)	156
Figure 6.2-1	APAI Process Flowsheet	163
Figure 6.5.1-1	Total Capital Investment (TCI) – Afterburner Options Compared	185
Figure 6.5.1-2	Fixed Capital Investment Breakdown for Soil Incineration with Plasma Afterburner	185
Figure 6.5.1-3	Fixed Capital Investment Breakdown for Soil Incineration with Conventional Afterburner	185
Figure 6.5.1-4	Total Capital Investment (TCI) – Importance of Gas Cleaning Units	187
Figure 6.5.1-5	Total Annual Operating Costs	187
Figure 6.5.1-6	Total Annual Operating Cost Breakdown for Soil Incineration with a Plasma Afterburner	188
Figure 6.5.1-7	Total Annual Operating Cost Breakdown for Soil Incineration with Conventional Afterburner	188
Figure 6.5.1-8	Total Annual Operating Costs – Importance of Gas Cleaning Units	188
Figure 6.5.1-9	Net Present Value (NPV) of Example Processes – Afterburner Options Compared	190
Figure 6.5.1-10	Net Present Value (NPV) Ratio of Competing Options	190
Figure 6.5.2-1	Afterburner Gas Flow Rate per Kilogram of Soil Treated	192
Figure 6.5.2-2	Afterburner Gas Flow Ratio (Plasma-Over-Fuel Oil) Sensitivity to Soil Treatment Capacity via Torch Power Rating	193
Figure 6.5.2-3	Afterburner Gas Flow Ratio (Plasma-Over-Fuel Oil) Sensitivity to Afterburner Temperature	193
Figure 6.5.2-4	Effect of Soil Treatment Capacity on Capital Investment for Soil Incineration	192
Figure 6.5.2-5	Effect of Scale-Up on the Annual Costs of Competing Options	195

Figure 6.5.2-6	Effect of Scale-Up of the Annual Cost Ratio of Competing Options (Plasma-Over-Conventional Heat Source)	195
Figure 6.5.2-7	Total Capital Investment (TCI) - Primary and Secondary Units Compared	196
Figure 6.5.2-8	Total Annual Operating Costs – Primary and Secondary Units Compared	196
Figure 6.5.2-9	Sensitivity to the Price of Fossil Fuel for Soil Incineration	198
Figure 6.5.2-10	Sensitivity to the Price of Fossil Fuel for Liquid Waste Incineration	198
Figure 6.5.2-11	Sensitivity to the Price of Electrical Power for Soil Incineration	191
Figure 6.5.2-12	Sensitivity to the Price of Electrical Power for Liquid Waste Incineration	191
Figure 6.5.2-13	Sensitivity to the Price of Plasma Equipment for Soil Incineration	201
Figure 6.5.2-14	Sensitivity to the Price of Plasma Equipment for Liquid Waste Incineration	201
Figure 6.5.2-15	Plasma Process Operating Costs Sensitivity to Market Prices and Torch Efficiency	202
Figure 6.5.2-16	Conventional Process Operating Costs Sensitivity to Market Prices	202

1. INTRODUCTION

Over the last decades, a sense of environmental awareness has emerged in parallel with technological advances. Among other issues, atmospheric pollution has become a factor of economic, political and social importance. A major point of contention is the toxicological hazard of organic pollutants associated with toxic waste incineration.

Awareness of the harmful effects of organic pollutants has developed over the last 40 years. Polyaromatic hydrocarbons (PAHs) were identified in stack emissions of municipal waste incinerators in the 1960s. Polychlorinated dibenzo dioxins and furans (PCDD/Fs) were recognized as environmental pollutants in the 1970s. Such findings gave rise to an ongoing debate on the adequacy of incineration as a waste management option (Edujee 1995). The 1980s witnessed regulatory updates, commissioned studies and increased research efforts. Yet incineration remains an issue of public concern compounded by controversy and muddled by misinformation. Scientific evidence attests the shortcomings of conventional incineration in the treatment of industrial and domestic waste. Most notably, halogenated organic waste is prone to form toxic products of incomplete combustion, hence its designation as "incineration resistant" (Ramasamy *et al.* 1996). Studies on the combustion of chlorinated plastics revealed that "*[products of environmental concern] are generated at the same relative proportions independent of heating rates and ambiances expected in an incinerator*" (Pasek *et al.* 1996).

The occurrence of hazardous compounds in mixed or dilute form, such as in contaminated soil, is also a problem. When minor contaminants require extreme temperatures for decomposition, an overwhelming proportion of the material is over-treated at considerable expense. Systems designed to treat waste of unknown or varying composition are costly to build and to operate since they are adapted to worst case scenarios.

Growing demands in the field of environmental protection emphasize the need to prevent the formation of toxic products in waste incineration processes. This has spurred interest in alternative treatment methods such as thermal plasma technology. Thanks to their high energy density, high reactivity, extreme temperatures and inherent flexibility, plasmas are well suited to the destruction of persistent compounds. However, due to the associated costs in electrical equipment and power, plasma-based waste treatment processes are economically uncompetitive under current environmental regulations.

The objective of the present work is to examine the potential of Adaptive Plasma-Assisted Incineration (APAI) as a cost-effective approach to waste treatment. In APAI, a controlled plasma afterburner treats the effluent gas of a conventional incinerator to eliminate incomplete combustion products. Novel features include on-line monitoring and optimization capabilities that ensure the safety, flexibility and economy of the operation. The project concentrates on three aspects: spectroscopic monitoring of chemical decomposition in a plasma; application of an optimization strategy; and techno-economic assessment. Laboratory demonstrations show that continual adjustments in plasma conditions allow cost-effective destruction of organic contaminants under variable feed loads.

Given the prevalence of incineration in industry and the need for improved public acceptance, APAI is a practical approach to waste treatment problems. The addition of plasma units to existing facilities is technically and economically achievable. The adaptive strategy fits within the orientation set forth by the United States Environmental Protection Agency on risk assessment and advanced instrumental analysis: *"continuous on-line measurement of the micropollutants of greatest concern (...) is recognized by both regulators and operators of incineration facilities as essential to address public anxiety over adverse health effects, and to reduce the uncertainties in public health risk*

assessments." (Eduljee 1995). The relevance of APAI is supported by Canada's Green Plan for environmental renewal and sustainable development (Government of Canada 1990). The objectives listed in the Green Plan include: "*Virtual elimination of the discharge of toxic substances into the environment*" (under Goal 1: Clean Air, Water and Land); and "*Balanced use of strong and effective environmental laws with market-based approaches for environmental protection*" (under Goal 6: Environmentally Responsible Decision Making). The development of APAI is a step towards pollution control strategies that agree with these long-term policy guidelines.

The next chapter presents a literature review. Chapter 3 details the specific objectives of the present research project. Experimental methodology and results are described in chapters 4 and 5. The techno-economic potential of APAI is assessed in chapter 6. Lastly, chapter 7 summarizes the conclusions and original contributions to knowledge of this research.

2. LITERATURE REVIEW

This section is an overview of the scientific and technological background for the project. It covers fundamental principles, describes existing waste treatment processes, and explains the potential benefits of APAI.

2.1 Fundamental Principles

This project integrates knowledge from three areas: hazardous waste treatment, optical emission spectroscopy, and process optimization. The following section reviews the relevant concepts in each area.

2.1.1 Hazardous Waste Treatment

After a brief introduction to organic pollutants and waste treatment methods, this section examines the mechanisms and properties of waste destruction by flame combustion and plasma pyrolysis.

2.1.1.1 Environmental Organic Pollutants and Toxicology

For ethical reasons, information on the effects of human exposure to specific compounds is mainly derived from circumstantial evidence and animal studies. Conclusions about causal relationships are subject to debate. Yet five classes of organic pollutants are generally recognized as serious health hazards (Harrison 1996). **Polychlorinated dibenzo-p-dioxins** (PCDDs or dioxins) and **polychlorinated dibenzofurans** (PCDFs or furans) arise anthropogenically from the manufacture and use of organochlorine chemicals and from fossil fuel combustion. They cause mortality in animals and chloracne in humans. There is contention over their exact toxicological potency, but evidence points to immunological, reproductive, developmental and carcinogenic effects.

Polychlorinated biphenyls (PCBs) are man-made compounds formerly used as dielectric fluids. They impair the immune response in animals and show carcinogenicity, hepatotoxicity, teratogenicity, neurotoxicity, and reproductive toxicity. **Polyaromatic hydrocarbons (PAHs)** originate from fossil fuel combustion as well as from forest fires and volcanic activity. Upon absorption by aquatic and terrestrial organisms, they are transformed into carcinogenic, teratogenic and mutagenic metabolites. **Organichlorine pesticides (OCPs)** are entirely anthropogenic and subject to bioaccumulation. They show reproductive and direct toxicity in animals. **Volatile organic compounds (VOCs)** are present in many processes and products of the chemical industry. They include an important group of soil contaminants referred to as BTEX (benzene, toluene, ethylbenzene, and three isomeric xylenes). Activities that generate significant amounts of VOCs include: oil and coke refining; manufacturing of solvents, paints and glue; fossil fuel combustion; and transportation. VOC exposure is involved in some domestic activities. Except for benzene (a proven human carcinogen and haemotoxin), compounds of this class have not been linked to long-term health risks. However, their effects on the nervous system cause symptoms such as anesthesia, loss of coordination, dizziness and amnesia.

2.1.1.2 Current Technology

The most common methods for the treatment of toxic waste and contaminated soils use thermal processes (pyrolysis, gasification, combustion), chemical fixation, or biodegradation. **Incineration** refers to waste destruction by volatilization and oxidation of organic materials. It is the most widely applicable method, with few restrictions concerning the composition, phase and feed rate of waste. In contrast, the use of chemical fixation is limited to waste of known composition whose hazardous components can be converted to non-toxic forms - recoverable or immobilized - by chemical reactions or physico-chemical interactions. Bioremediation relies on the ability of adapted microorganisms to

metabolize contaminants under favourable conditions. It is intrinsically slow and limited in its applicability.

Aside from versatility, thermal methods can provide high waste volume reductions (typically $\approx 90\%$), fuel value recovery from the waste, and generation of useful by-products. **Thermal pyrolysis** is a heat-induced (> 1100 K) decomposition of organic waste into low-molecular weight gases (H_2 , CH_4 , CO , CO_2 , H_2O), oily vapours, and char. The final composition is controlled by addition of oxidizing or reducing agents. Low-temperature pyrolysis (725 - 1000 K) produces liquid oils, organic acids, alcohols and ketones; it is of interest in the recycling industry. **Gasification** is a thermochemical conversion of organic materials, including char and oils, into noncondensable combustible gases. It involves heterogenous interactions (adsorption, reaction, desorption) between carbon-based solids and gasifying agents (air, O_2 , CO_2 , H_2O , H_2 or a combination thereof). **Combustion** is the oxidation of organic waste into CO_2 , H_2O and other products (NO_x , SO_x , HCl , ...) by direct heating and ignition in an oxygen-rich environment. Waste incineration generally proceeds through stages of drying, pyrolysis, gasification, and combustion, within a single chamber or in sequential units (Gupta 1996).

The performance of thermal systems depends on a number of factors: operating conditions (temperature, residence time, chemical environment), waste characteristics (composition, degree of homogeneity, feed preparation), and design parameters (configuration, flow dynamics, mixing, heat transfer, quench). Maintaining waste and its gaseous products at a prescribed temperature in an oxidizing atmosphere for an adequate time is a challenge. Incineration systems typically feature a primary chamber where bulk material is pyrolyzed, gasified and/or combusted. The unit is followed by a secondary chamber (afterburner) where addition of supplemental fuel and air furthers the combustion of gaseous products. This results in a large gas throughput to be treated for removal of

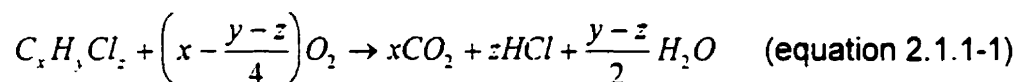
particulate matter, acid gases, nitrogen oxides, and hazardous products of incomplete combustion.

A Typical Afterburner Application: Soil Remediation

Incineration has been used in site decontamination projects involving solid and liquid materials (Brunner 1996). A treatment system typically includes: an incinerator, often a rotary kiln; an afterburner, for secondary combustion of the off-gas and destruction of liquids; if justified, a heat recovery unit (heat exchanger or waste heat boiler); a gas cleaning system with prime mover equipment; control, monitoring and laboratory facilities. The kiln operates at a temperature sufficient for the combustion or volatilization of organic compounds present in soil (e.g., 760°C or 1400°F). The secondary combustion chamber meets residence time and temperature requirements specified by regulations (for halogenated waste, 2 seconds at 1200°C (2200°F) in Canada and the USA). Liquids are introduced in the flame zone of the afterburner, along with supplementary fuel and air. Heat contained in the exhaust gas may be recovered through air preheating or steam generation. However, when the gas stream is rich in chlorine, sulfur, phosphorus or particulate matter, operating and design constraints generally offset the benefits of heat recovery. On-site demand seldom justifies heat recovery from toxic waste incineration processes (Brunner 1997).

2.1.1.3 Flame Combustion

The combustion of a chlorinated hydrocarbon proceeds by the following reaction:



For incineration, oxygen is supplied in excess of stoichiometric requirements. The excess varies from 5-30% to 50-100% with the combustibility of the waste. If $z > y$, additional hydrogen is provided by auxiliary fuel. Solid waste incineration

produces an ash residue largely composed of mineral oxides. Nitrogen- and sulfur-containing waste also releases oxides of these elements (Williams 1995). The residence time in the flame is of the order of microseconds during which, at best, 95% of organic compounds decompose. A residence time of up to 2 seconds in the post-flame zone is required for completion of oxidation reactions (Edujlee 1995).

A simplified model of global decomposition kinetics is:

$$\frac{-d[X]}{dt} = k_1[X]^a + k_2[X]^b[O_2]^c \quad (\text{equation 2.1.1-2})$$

The first and second terms on the right hand side represent pyrolysis and oxidation rates, respectively. The rate constants and reaction order coefficients depend on the nature of the substrate and on breakdown reaction mechanism(s).

A slightly more practical model was proposed to describe the relationship between temperature and degree of oxidation (Edujlee 1995):

$$T = 120E \left[\ln \left(\frac{-At}{\ln(f)} \right) \left(\frac{O_2}{0.21} \right)^c \right]^{-1} \quad (\text{equation 2.1.1-3})$$

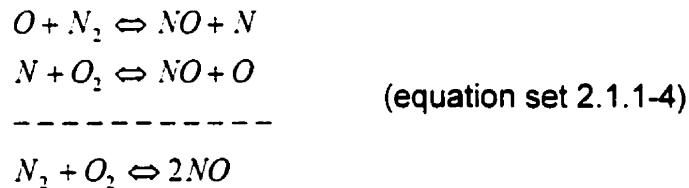
where T = temperature [K]
 f = fraction of species X remaining
 t = residence time
 E = activation energy [kJ/mol]
 A = Arrhenius coefficient [s^{-1}]
 c = reaction order
 O_2 = fraction of oxygen in the reaction atmosphere

A first-order kinetic model was proven adequate by regression of experimental data. Again, the model involves substrate-specific empirical parameters (E , A). Even with ideal mixing, product composition is difficult to predict for waste containing a variety of substances in varying amounts. The complexity of the task is compounded by non-ideal thermal and flow fields.

Generation of Nitrogen and Sulfur Oxides

High-temperature flames in air produce nitric oxide (NO) and nitrogen dioxide (NO₂), collectively termed NO_x. When released into the atmosphere, these photochemically active compounds contribute to ozone depletion, acid rain phenomena, and cause respiratory irritation. In combustion processes, NO is generated by three distinct mechanisms. NO₂ forms by reversible oxidation of NO. This reaction is slow, and the NO₂-to-NO ratio is low at equilibrium. NO₂ is more soluble than NO and easier to remove from a gas stream. Total NO_x emissions are typically 10% NO₂ and 90% NO (de Nevers 1995, Glassman 1996).

Thermal NO forms by oxidation of atmospheric nitrogen in high-temperature post-flame zones, independently of the heat source. The reaction is reversible, with a strong dependence on temperature and oxygen concentration. The Zeldovich kinetics model is based on the following free-radical reactions:



This simplified model is reasonably accurate at high temperatures (de Nevers 1995). Local peak temperatures above 1300°C are required for a significant shift to the right-hand side to occur. Both the formation kinetics of thermal NO and its equilibrium concentration increase dramatically with temperature. Cooling in the post-flame zone freezes the NO_x concentration near its peak temperature value.

Fuel NO results from the oxidation of nitrogen atoms present in fuel (waste or auxiliary). This reaction is characterized by a low activation energy, a weak temperature dependence, and a time scale of the same order as combustion reactions. The extent of fuel NO generation mainly depends on fuel composition,

though fuel-rich conditions minimize the fraction of fuel-bound nitrogen converted to NO.

Prompt NO forms in the flame of carbon-containing fuels through a reaction pathway that involves CN compounds. The rate of prompt NO formation depends on the abundance of carbon and atmospheric nitrogen relative to oxygen. The reaction is faster in fuel-rich conditions, and its temperature dependence is weak.

In high-temperature flames such as incinerator burners, thermal NO is the dominant source of NO_x. Prompt NO is a minor contribution. Fuel NO is not a concern with low-boiling petroleum oils and natural gas, which are practically nitrogen-free. Other fuels (e.g., waste material) offer little control on fuel NO generation. Effective NO_x-control burner designs reduce peak temperatures by promoting flame homogeneity and dilution. In incineration processes, recirculating part of the product gas and using a low excess of air reduce the rate of formation of NO_x by the mass action law (Lambert and McGowan 1996).

Sulfur oxides (SO_x, or SO₂ and SO₃ combined) are environmentally harmful. Their photochemical reaction products are respiratory irritants and acid gas pollutants. SO₂ is a combustion product of all sulfur compounds. SO₃ forms by reversible oxidation of SO₂. Its concentration is generally low and increases with temperature. SO_x generation in combustion systems directly relates to the amount of sulfur present in the fuel. Choosing a clean fuel or heat source is the best method of SO_x emission control. This measure does not apply to waste feed materials. Incineration systems provide for the removal of SO_x and NO_x in standard or pollutant-specific gas cleaning units, as needed (Brunner 1996, de Nevers 1995, Glassman 1996, Rae 1995).

Generation of Incomplete Combustion Products

Ideally, combustion produces water, carbon dioxide, small amounts of nitrogen oxides, with hydrochloric acid and sulfur oxides according to feed composition. This ideal case assumes a stable temperature, perfect mixing, and a residence time sufficient for all reactions to proceed to completion.

Incinerators depart from these ideal conditions. Perturbations may cause local temperature drops. Gas flow patterns such as channeling, layering and recirculation result in a distribution of residence times and temperature histories among flow elements. Incomplete mixing affects reaction kinetics and mechanisms. For example, oxygen-depletion pockets favour pyrolytic decomposition of waste into organic micropollutants.

Feed characteristics are crucial and vary considerably in waste treatment applications. The heating value and reactivity of the waste fluctuate with its composition. Most notably, chlorinated organic molecules are resistant to combustion for several reasons. Halogen substitutions reduce the heat of combustion. The recombination of chlorine into HCl depletes hydrogen radicals, which slows the overall oxidation rate (Ramasamy *et al.* 1996). HCl can affect flame chemistry: for example, it interferes with chain-propagating and branching reactions in the degradation of chlorinated polymers (Pasek *et al.* 1996).

Products of incomplete combustion (PICs) range from soot particles to a variety of organic micropollutants. A primary concern in incineration is the persistence of dioxins and furans (PCDDs and PCDFs). The present discussion focuses on these classes of compounds, but the principles described apply to hazardous PICs in general.

Dioxins and furans found in incineration effluent originate from three main sources: (1) feed component breakthrough; (2) formation from precursors; and

(3) *de novo* synthesis. The next paragraphs summarize the theories pertaining to each source and their implications for emission control.

When present in the feed, dioxins and furans may withstand flame exposure due to their stability. Breakthrough is likely if poor mixing creates channels of low thermal exposure. However, the PCDD/F content of the feed is not a dominant source of emission. In incineration processes, the output of PCDD/Fs generally exceeds the input (Williams 1995).

Formation from precursors occurs in the temperature range 300-800°C through homogenous gas-phase reactions (free-radical condensation, cyclization, dehydrogenation, chlorination/dechlorination, rearrangement, etc.). This mechanism is associated with local oxygen depletion zones. Combustion flames contain an abundance of pyrolytic and partial oxidation products that normally oxidize in the post-flame zone. In oxygen-depleted environments, these precursors persist into lower-temperature regions where recombination is possible. PCDD/F formation from precursors is enhanced by the presence of compounds like chlorophenols and chlorobenzenes, which are reaction pathway intermediates (Harrad 1996, Williams 1995).

De novo synthesis involves heterogenous elementary reactions of carbon, hydrogen, oxygen and chlorine. It is catalyzed by metals, chlorides, oxides or silicates at the surface of fly ash particles in the temperature range 200-450°C. Dioxins and furans form through reactions between gaseous and adsorbed precursors. Synthesis is followed by desorption for mono-, di- and tri-chloro products; more complex products remain adsorbed (Harrad 1996). *De novo* synthesis can proceed in oxygen-rich environments: a metal-catalyzed reaction between O₂ and HCl supplies chlorine, which combines with adsorbed hydrocarbons to form precursors. This mechanism of PIC formation is independent of combustion control, save for the amount of soot particles produced. It occurs in cool post-combustion zones such as in heat exchangers. It

is not a concern above 400°C, where surface-catalyzed dechlorination and decomposition of adsorbed PICs predominate. Thus, rapid quenching at the exit of a high-temperature combustion chamber effectively limits *de novo* synthesis. A quench temperature less than 200°C is recommended prior to particulate collection. Studies reporting similar PIC emissions for different feed and incinerator types suggest that *de novo* synthesis is the dominant source of PCDD/Fs (Eduljee 1995). This conclusion applies in well-controlled combustion equipment. The probabilities of compound breakthrough and PIC formation from precursors are higher in uncontrolled systems such as accidental fires.

When exposed to an oxygen-rich environment, gaseous PICs decompose by equation 2.1.1-1. In contrast, the combustion of PICs adsorbed on or trapped in soot particles obeys surface reaction kinetics. Complex products like PCDD/Fs tend to adsorb on particulates. Consequently, soot production is an important factor in the control of PCDD/F formation.

Soot production pathways involve polyaromatic hydrocarbon and acetylene intermediates. These reaction pathways are favoured by high temperature and local oxygen deficiency. Particle nucleation occurs in successive steps: precursor cyclization, alkylation, oxidation, and conjugation into stable aromatic structures. Incipient formation of single- or two-ring structures is the controlling step. Particle growth proceeds by physico-chemical adsorption of gaseous hydrocarbon species with reformation into carbonaceous structures. Particle size is limited by gradual loss of reactivity. Soot properties vary little with fuel or flame type, but the quantity produced reflects the concentration of precursor pyrolytic products. Soot eventually burns given sufficient residence time and turbulence (Czernichowski *et al.* 1995, Glassman 1996, Williams 1995).

The first step towards reducing PCDD/F emissions is to promote conditions that minimize the amount of precursors: mixing with excess air and rapid quench. When appropriate, waste homogenization by shredding and blending helps

uniform the combustion environment. The use of recirculated exhaust gas as secondary air also limits the formation of by-products (Edujje 1995, Rae 1995). Downstream of the combustion units, PCDD/F emission control is ensured by wet scrubbing, particulate collection, and solids treatment (vitrification or catalytic dechlorination with oxidation). Activated carbon adsorption effectively removes organics and heavy metals from the flue gas and quench/scrubbing water streams.

2.1.1.4 Plasma Pyrolysis

The term *plasma* refers to the state of a gas heated to the point where it ionizes and becomes an electrically conductive medium with distinct physical properties. Plasmas occur naturally in the form of lightning, stars, and (at low pressure) *aurora borealis*. Man-made plasmas are generated by application of intense electromagnetic fields. In waste treatment operations, plasma torches can replace fuel burners as a heat source. The gas stream of a plasma furnace is analogous to that of an incinerator. Applications where solid waste is directly exposed to a plasma also produce an inorganic vitreous slag that meets high standards of inertness, compactness, stability and non-leachability.

The goal of plasma pyrolysis is to decompose toxic materials into their constituent atoms, with subsequent recombination into non-hazardous compounds. This is achieved by exposing the material to the plasma jet before quenching the gas produced in a controlled environment. This type of process differs from other thermal destruction methods by the unique thermochemical properties of plasmas. Atmospheric-pressure plasmas reach temperatures far higher than those obtained in combustion flames. Since plasmas depend on power dissipation (vs combustion reactions) for heat release, their chemical composition can be controlled independently. Oxidizing, reducing or neutral environments can be used. Plasmas are highly reactive due to the abundance of radicals and ionized species (Huhn *et al.* 1997). Experimental evidence has

confirmed the potential of plasma systems for complete destruction of hazardous compounds (Ramasamy *et al.* 1996, Han *et al.* 1995).

Decomposition pathways depend on heat transfer, fluid flow and reaction kinetic phenomena, and are not easily predicted. Experimental and modelling studies on the dissociation of chlorinated hydrocarbons in a plasma reactor suggest multiple reaction mechanisms (unimolecular, radical chain, photochemical), each with its own temperature dependence. These studies emphasize the importance of incomplete mixing, flow inhomogeneities and temperature gradients in real systems (Snyder and Fleddermann 1997).

The quench stage is a key step in plasma waste treatment. It prevents the recombination of atomic species into organic precursors which could form hazardous compounds further downstream. Precursor formation can be controlled by minimizing off-gas exposure to intermediate temperatures (250-450°C to 1200°C, depending on the system). Thermodynamic equilibrium models can predict quench temperatures that preclude the formation of undesirable by-products (Ramasamy *et al.* 1996); however, consideration must be given to the effects of non-equilibrium reaction kinetics on the final composition. As a general rule, incineration flue gas is cooled to 200°C or less prior to particulate collection. This agrees with the previous discussion on PIC formation (section 2.1.1.3) and favours efficient removal of acid gases, oxides and metal vapours (Environment Canada 1985, Williams 1995).

Air plasma torches compare favourably to combustion flames with respect to PICs, NO_x, SO_x and particulates. A plasma heat source facilitates the control of temperature and oxygen content for efficient combustion. Fewer pyrolytic precursors, less particulate catalyst, and a steep quench reduce the formation of PICs. An air plasma introduces no sulfur nor prompt NO_x into the system. Extreme temperatures in the plasma jet imply generation of thermal NO_x. However, the amount of air through a plasma torch is small relative to incinerator

gas throughputs. The importance of NO_x generation is case-specific. In plasma arc furnaces using oxygen-enriched air, NO_x levels are “rarely an issue” (Eddy *et al.* 1996).

2.1.2 Optical Emission Spectroscopy

Emission spectroscopy measures the radiation emitted during the relaxation of atoms and molecules excited by an external source. Electronic transitions from upper to lower energy levels cause emission of light photons whose wavelength reflects the energy jump. Information about the composition and temperature of a system can be inferred from its optical emission spectrum.

Inductively-coupled plasma (ICP) emission spectroscopy uses a small-scale argon plasma (\approx 1-10 kW) as an excitation source. The sample to be analyzed is introduced at the centre of the plasma while spectral readings take place in the tail region. In thermal plasma processes, light emitted by the plasma can be used for diagnostics. Emission spectroscopy offers unique advantages for on-line monitoring: it is an *in situ*, non-invasive method applicable in systems where extreme thermal and electromagnetic conditions preclude the use of measuring instruments and sampling techniques.

The optical spectrum covers the infrared (IR), visible (VIS) and ultraviolet (UV) regions, respectively located at 770 nm-1000 μ m, 350-770 nm, and 180-350 nm. The energy range of infrared radiation matches that required for molecular bending and stretching. IR spectrometry is best suited to qualitative identification of functional groups. The energy range of UV-VIS radiation is of the order of energy differences between the states of valence electrons in atoms and molecules. Due to the variety and specificity of electronic configurations in atomic and molecular structures, UV-VIS spectra are excellent tools for quantitative composition analysis.

2.1.2.1 Spectral Line Emission in Thermodynamic Equilibrium

Excitation mechanisms such as collision and photoabsorption produce a range of excited states among a population of particles. In equilibrium, these excited states follow a Boltzmann distribution. Thermodynamic equilibrium is characterized by microreversibility in all excitation and de-excitation processes.

The emissivity of an electronic transition is proportional to the density of particles in the upper - or initial - state of the transition (Boulos *et al.* 1995):

$$\varepsilon = \frac{1}{4\pi} A n_k h\nu \left[\frac{\text{power}}{\text{volume} \bullet \text{solid angle}} \right] \quad (\text{equation 2.1.2-1})$$

where A is a constant representing the probability of the transition (in reciprocal time units) and n_k is given by the Boltzmann equation:

$$n_k = N \frac{g_k}{Q(T)} e^{\left(\frac{-E_k}{kT}\right)} \left[\frac{\text{particles}}{\text{volume}} \right] \quad (\text{equation 2.1.2-2})$$

where g_k = statistical weight of the upper energy level

N = total population number density

$Q(T)$ = internal partition function of the particles

E_k = energy of the upper level (with respect to the ground state)

This general equation describes an equilibrium distribution of states in terms of a characteristic temperature and energy. The statistical concept of temperature relates to energy level distribution for a specific mode of excitation. The distribution functions of different energy forms (electronic, kinetic, potential, chemical, ionization,...) obey similar equations: energy and its associated temperature appear in the same exponential term, which is multiplied by specific statistical and population parameters.

For example, the Maxwell-Boltzmann particle velocity distribution has kinetic energy on the numerator of the exponential term. The temperature on the denominator is the mean kinetic energy among the particles. In a plasma, the kinetic temperature of the heavy species (atoms, molecules and ions) is denoted T_g . It differs from that of the electrons, T_e , if the frequency of collisions is too low for kinetic energy exchanges to equilibrate between the two species. A plasma where all energy distribution modes - electronic excitation (collisional and radiative), chemical reaction (including ionization), kinetic motion (of electrons and heavy species), and electromagnetic radiation - have identical temperatures is in a state of **Complete Thermodynamic Equilibrium** (CTE). This state is practically impossible to achieve in laboratory systems. Most industrial and laboratory plasmas are optically thin: they do not balance photoemission with photoabsorption. **Local Thermodynamic Equilibrium** (LTE) can be approached if collisions are the dominant mechanism of energy exchange. In LTE, all but radiative processes are microreversible. Excitation, reaction and kinetic distributions equilibrate at the same temperature. In thermal plasmas, particle interactions are largely governed by collisions. Assuming that thermal energy mediates all excitation, reaction and kinetic processes, equilibrium distributions are applicable (Boulos *et al.* 1995).

In atoms, line emission intensity is expressed as:

$$I = \left(\frac{h\nu}{4\pi} \right) \cdot ANg_k \frac{e^{\left(\frac{-E_{exc}}{kT_{exc}} \right)}}{Q(T_{exc})} \quad (\text{equation 2.1.2-3})$$

where T_{exc} is specific to the electronic excitation distribution, and usually not equal to the kinetic temperature of the system. The statistical weight of a state (g_k) is its **degeneracy**, or number of distinct sub-states having the same energy (Thorne 1974).

In molecules, bonds between atoms give rise to rotational and vibrational energy levels in addition to electronic levels. In equilibrium, rotational and vibrational energy states each follow a Boltzmann distribution with a characteristic temperature (T_r and T_v). Combinations of electronic, vibrational and rotational states multiply the number of possible energy levels. Whereas atomic spectra present distinct emission lines, molecular transitions produce complex sets of closely spaced or overlapping lines called *bands*.

A thorough description of molecular electronic structures is far beyond the scope of the present work. A summary of relevant concepts is provided in the next section and in Appendices I to III. The reader is referred to textbooks on the subjects of quantum chemistry and spectrophysics for additional information.

2.1.2.2 Diatomic Molecular Band Emission

The state of an electron within a molecule is described by a set of quantum numbers which designate its angular momentum components. The **axial electronic angular quantum number** Λ represents the component of the electronic angular momentum along the internuclear axis, and depends on the type of molecular orbital. Values $\Lambda = 0, 1, 2, 3, \dots$ are denoted by the Greek letters $\Sigma, \Pi, \Delta, \Phi, \dots$. The **total spin quantum number** S is the resultant of the spin angular momenta of individual electrons. Interaction of S with the magnetic field produced by Λ results in the splitting of the electronic state into **multiplet** levels of slightly different energies. An electron's **axial spin angular quantum number** Σ (not to be confused with $\Lambda = 0$) can take $(2S+1)$ different values. The **total axial angular quantum number** Ω is the resultant of the electronic and spin components, $|\Lambda+\Sigma|$. Thus, for a given value of Λ , there are $(2S+1)$ possible values of Ω . The quantity $(2S+1)$ is called the **multiplicity** of the electronic state. The designation of a molecular state is generally written $(^{2S+1}\Lambda_{\Omega})$. If different

states in a molecule have the same Λ -value, the symbol is preceded by a Roman letter (X, A, B, C, ..., a, b, c, d, ...). Molecules with same-charge nuclei have a center of symmetry relative to which electronic states can be even (*gerade*) or odd (*ungerade*). The symmetry property is indicated by a subscript *g* or *u* to the term symbol (Σ_u , Σ_g , Π_u , Π_g , Δ_u , ...). It is unaffected by spin and is therefore the same for all components of a multiplet.

Electronic motions are altered by the vibration and rotation of atoms within molecules. The effect of vibrational motion on an electronic state is best represented by the potential energy function of an anharmonic oscillator model, or Morse potential curve (Figure 2.1.2-1). This curve describes the energy of an electronic level as a function of internuclear distance. Solution of the Schrödinger wave function equation for this model gives the quantized vibrational levels (designated ν) illustrated in Figure 2.1.2-1. Rotational motion in a linear molecule is approximated by a nonrigid rotor model. Solution of the Schrödinger equation for this model gives quantized levels for the total angular momentum (the resultant of electronic orbital, electron spin and nuclear rotation momenta). These levels are designated by the **rotational angular quantum number J**. A general diagram of the energy levels associated with electronic, vibrational and rotational motions is presented in Figure 2.1.2-2. The quantum numbers of the transition's upper state are single-primed; those of the lower state are double-primed. Rotational states are further characterized by designations such as positive/negative parity (i.e., whether the wave function does or does not change sign upon inversion), symmetric/antisymmetric (in homonuclear molecules), and the even/odd property mentioned above. The degeneracy of rotational states equals $(2J+1)$. States with $\Lambda \neq 0$ show double degeneracy of all rotational levels into two components of equal energy and opposite parity (Herzberg 1950, Ingle and Crouch 1988).

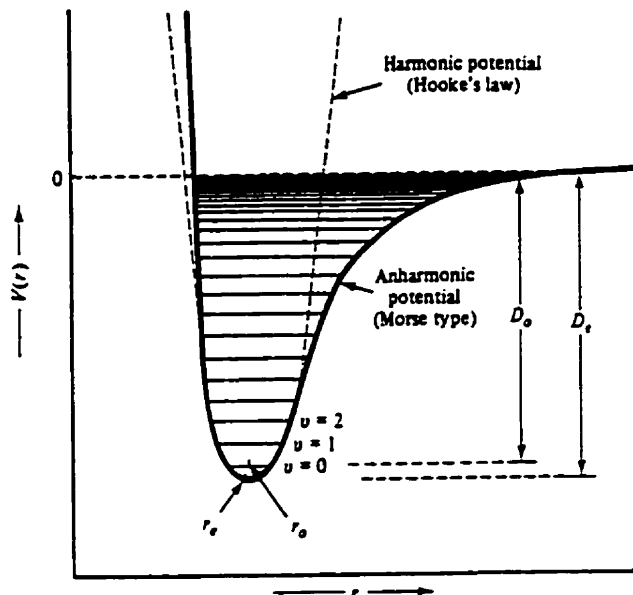


Figure 2.1.2-1: Morse Potential Curve for a Diatomic Molecule
(Ingle and Crouch 1988)

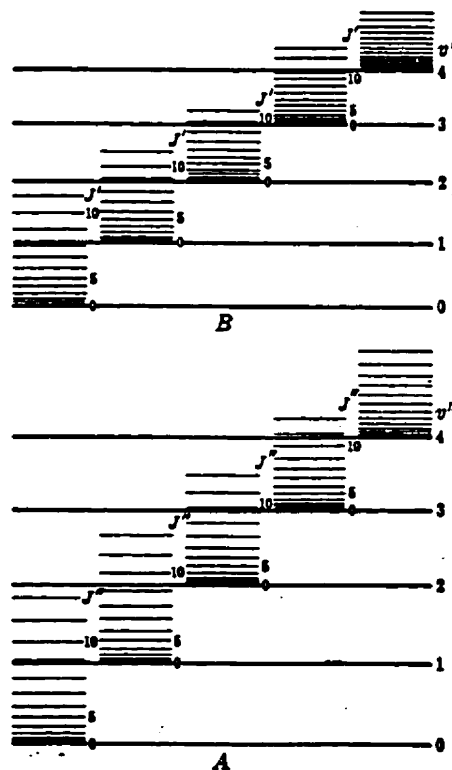


Figure 2.1.2-2: Schematic Diagram of the First Few Vibrational and Rotational
Levels of Two Electronic States A and B (Herzberg 1950)

Molecules produce three types of emission spectra. Electronic (or vibronic) spectra correspond to transitions from between electronic states (Λ). In these transitions, electrons jump from one Morse potential energy curve, or one orbital, to another. Vibrational (or vibrational-rotational) spectra correspond to transitions between two vibrational levels (ν) of the same electronic state. Rotational spectra reflect transitions between two rotational levels (J) of the same vibrational level and electronic state. Purely rotational spectra are normally observed in the microwave region due to the small energy differences between rotational levels. Electronic and vibrational spectra span the UV to IR range (Ingle and Crouch 1988).

A **band** is a set of rotational lines belonging to a specific electronic and vibrational transition. The lines of a vibrational-rotational band fall into three series, or **branches**, according to the change in rotational quantum number from the upper to lower state of the transition ($\Delta J \equiv J' - J''$). Lines where $\Delta J = -1$ form the P branch; lines where $\Delta J = 0$, the Q branch; and lines where $\Delta J = +1$, the R branch. A **sequence** is a series of bands having the same $\Delta \nu = \nu' - \nu''$; a **progression** is a series of bands having the same ν' or ν'' .

On a wavelength scan, a typical band is a group of closely spaced lines marked on one side by a sharp edge (the **band head**) where intensity drops from a maximum to zero, and on the other side by a gradual decrease in line intensities. The origin of this pattern is explained in section 5.1.1, where band spectra simulated from first principles are presented. The distinctive band structures of vibrational-rotational transitions are essential tools in molecular spectroscopy.

Assuming a Boltzmann distribution among rotational levels, the emission intensity of a rotational line ($J' \rightarrow J''$) within a single band ($\nu' \rightarrow \nu''$) is given by:

$$I_{\nu'\nu''J'J''} = A \nu^4 S_{\nu'\nu''J'J''} e^{\left(\frac{-E_{J''}}{kT_e}\right)} \quad (\text{equation 2.1.2-4})$$

where $A =$ a constant

$S_{\nu\nu'JJ'}$ = line oscillator strength

E_r' = rotational energy of the upper level, in Joules

or,

$$I_{\nu\nu'JJ'} = A \nu^4 S_{\nu\nu'JJ'} e^{\left(-\frac{hc}{kT} F(J')\right)} \quad (\text{equation 2.1.2-5})$$

where $F(J')$ = rotational energy of the upper level, in wavenumber

A derivation of this expression and explanation on the physical meaning of its constituent terms are provided in Appendix I.

2.1.2.3 Methods and Instrumentation

A monochromator is an optical instrument that separates light from a polychromatic source according to wavelength. A mirror collimates the incoming light towards a dispersive element - usually a diffraction grating, sometimes a prism. When hit with collimated light, the finely grooved surface of a grating acts as a multislit source. Patterns of constructive and destructive interference from these sources result in different wavelengths being diffracted at different angles. The spectrum of dispersed light is focused onto an exit plane, where a slit allows a thin "slice" of this image, i.e., a narrow waveband, to reach a detector. The orientation of the rotatable grating determines the wavelength at the slit. The focal length, groove density and slit width determine the dispersive power and resolution of the system.

The **reciprocal linear dispersion** (R_d , in nm/mm) relates a wavelength interval to a physical distance on the focal plane. The **baseline resolution** of a scan ($\Delta\lambda$, in nm) is the wavelength interval between adjacent features that are just separated down to the baseline. The **spectral bandpass** (s , in nm) is defined as the half-width of the wavelength distribution passed by the exit slit. There are three contributions to the bandpass: geometric (s_g), aberration-limited (s_a) and

diffraction-limited (s_d). At wide slit widths ($\gg \lambda$), aberrations and diffraction are negligible. The bandpass is controlled by the geometric factor, and resolution is slit width-limited. The geometric bandpass is the product of the slit width (W , in mm) by the reciprocal linear dispersion. The light intensity signal measured during a scan is a convolution of the image of the entrance slit with the exit slit. For identical slits, the resolution is twice the geometric bandpass (Ingle and Crouch 1988). An experimental measure of the spectral bandpass is width of an emission line measured at half-height, or **Full Width at Half-Maximum (FWHM)**.

$$s \approx s_g + s_d + s_d \cong s_g = R_d W \quad (\text{equation 2.1.2-6})$$

$$\Delta\lambda_s = 2s_g = 2R_d W \quad (\text{equation 2.1.2-7})$$

A photomultiplier tube (PMT) detector is made of a photoemissive cathode, focusing electrodes, an electron multiplier, and a collector anode in a vacuum tube. Photoelectrons emitted by the cathode are directed by the electrodes towards the multiplier, which is a series of electrodes called dynodes. Impaction of an electron onto a dynode causes secondary emission of additional electrons towards the next dynode. The signal collected at the anode shows a gain from 10^4 to 10^{10} depending on the number of dynode stages and on the applied voltage. A photomultiplier tube can detect light at extremely low levels (of the order of individual photons).

An alternative mode of detection is a photodiode array (PDA) detector. This device is a linear array of light-sensitive diodes positioned at the image plane of a monochromator, in place of one or more slits. Effectively, dispersed light is projected onto a series of individual detectors (or channels) in parallel. Unlike the PMT, the diodes operate in a charge-storage mode. After an appropriate integration time, the charge accumulated on each diode is read at a rate of 10-25 μ s per diode. The parallel arrangement of diodes allows simultaneous

measurements at multiple wavelengths. The spectrum contains as many points as there are channels, and covers a waveband determined by the width of the array and the linear dispersion. A PDA has no internal gain but can be coupled with a microchannel-plate image intensifier that amplifies signals by 10^3 to 10^4 . The array may be thermo-electrically cooled for noise reduction.

Two main disadvantages of the PDA are (1) a resolution limited by the width of individual diodes, and (2) leakage currents between adjacent diodes, which broaden spectral widths and can impair resolution (Gifford 1990). However, the photodiode array allows rapid and simultaneous measurement of correlated features such as analyte signals and continuum emission in adjacent regions of the spectrum. This, and the absence of moving parts, make PDA detection the preferred choice for industrial process control applications where speed, stability and simplicity of use are important (Malchow 1992).

Emission spectra are composed of atomic and molecular features superimposed on a continuum of emission present at all wavelengths. The continuum is produced by the interaction of atoms and molecules with free electrons, whose energy is not quantized into discrete levels. Spectrometric applications generally involve a background correction procedure. Over wide wavebands, measured spectra are also shaped by wavelength-dependent detector responsivity and transmission efficiency of optical components (windows, lenses, optical fibres).

Optical measurements from a three-dimensional object such as a plasma jet raises questions about where the collected light originates from. An image of the object is usually projected onto an observation plane by refraction through a converging lens, at a set magnification. The plane may contain the entrance slit of a monochromator or an optical fibre termination. The contribution of a point in the emission source to the image depends on its position along the optical axis. The measured signal is a convolution of the axial intensity profile of the plasma with the **axial intensity distribution function** of the lens. A preliminary study on

the subject showed that: (1) axial intensity variations are important near the geometrical focus of the lens only; (2) the depth of focus at a given wavelength is proportional to the square of the imaging F-number (Filion 1995). A depth-of-focus analysis is important in applications where the object subtends a wide solid angle (low F/n) such that light disperses over a broad circle of confusion within a short axial distance from the image plane. This is rarely the case in imaging systems of the type considered here. Hence, light collection is generally assumed uniform across the depth of the object. An optical signal reaching the slit or fibre integrates light from a cylindrical region whose width depends on magnification and on slit or fibre dimensions. The assumption of a long depth of focus is justified when light is collected over a narrow solid angle (high F/n).

For optical diagnostics of spatial distributions in a circular plasma, lateral measurement profiles (along a y-axis from the centre of the jet outwards) must be resolved into radial profiles. For a symmetric jet of radius "a", a geometrical argument shows that the radial emission profile $f(r)$ is related to the measured lateral profile $F(y)$ by the **Abel transform** (Hutchinson 1987).

$$F(y) = 2 \int_y^a \frac{rf(r)}{\sqrt{r^2 - y^2}} dr \quad (\text{equation 2.1.2-8})$$

The inverse of this integral transform is the Abel inversion, a mathematical tool for reconstructing radial signal profiles from lateral measurements.

$$f(r) = \frac{-1}{\pi} \int_r^a \frac{dF}{dy} \frac{1}{\sqrt{y^2 - r^2}} dy \quad (\text{equation 2.1.2-9})$$

$$\text{boundary condition: } f(a) = 0$$

The Abel transform and its inverse assume a radially symmetric plasma. Irregularities in the load coil or injection ports may induce asymmetry in the jet.

Before applying the Abel inversion, symmetry is generally imposed on the data by averaging left- and right-hand side measurements.

The differential term in the Abel integrand is evaluated by curve fitting or interpolation from the discrete lateral readings. The distance between measurement points should be smaller than the distance over which intensity changes appreciably; at least 20 points are recommended across the diameter of an analytical ICP (Omenetto *et al.* 1980). A high F-number imaging configuration facilitates lateral resolution.

By definition, the Abel inversion is subject to computational aberrations caused by measurement uncertainty. The differential term in the integrand is sensitive to random noise, more so near the edge of the jet. Smoothing is usually integrated into the curve-fitting process. Unless the centre of the lateral profile is located exactly, erroneous results are likely near $r = 0$ (Omenetto *et al.* 1980).

2.1.2.4 The Swan Bands of C_2

The Swan rotational-vibrational band system of the C_2 molecular fragment (or *first positive bands of carbon*) is a useful diagnostic tool. This system corresponds to the transition $d^3\Pi_g \rightarrow a^3\Pi_u$ in carbon-carbon bonds. A summary of the Swan band structure and characteristics is presented in Appendix II. The $\nu(0,0)$ band, located in the green region of the visible spectrum (509.8 - 516.5 nm), is well suited for optical diagnostics. Being the first in its sequence, it is free from overlap with other bands over a region extending from the head at 516.5 nm down to the head of the $\nu(1,1)$ band at 512.9 nm.

The calculation of temperature from Swan band emission data is a common procedure (Alder and Mermet 1973, Beulens *et al.* 1994, Bousrih *et al.* 1995, Czernichowski 1987, Pellerin *et al.* 1996, Reeve and Weimer 1995). The

application of Swan bands in composition analysis, as in the present project, is less common.

2.1.2.5 Composition Diagnostics

In ICP atomic emission spectroscopy, Swan bands are undesirable features which may interfere in the measurement of analyte signals. A recommended solution to the presence of Swan bands is to increase plasma power and/or oxygen content (Greenfield *et al.* 1976).

The Swan system is characteristic of organic molecules with two or more carbon atoms. Complete breakdown of these compounds into simple products causes the disappearance of Swan bands from the optical spectrum. In a plasma afterburner, these molecular bands could indicate the presence of incomplete combustion products. Two necessary conditions for the validity this indicator are: (1) that no organic species recombine downstream of the observation point, and (2) that temperature be sufficiently high at the observation point.

With respect to recombination, the high temperature and reactivity of a thermal plasma promote pyrolytic decomposition into atomic elements, thus reducing the number of precursor fragments available. Rapid quench in an oxidizing atmosphere allows carbon to exit the system as CO or CO₂. (This statement applies to the gaseous fraction; in gas-solid systems, possible adsorption of hazardous organics onto soot or ash must be considered in the treatment of these residues).

The temperature requirement is linked to Swan band transition probabilities. At low temperatures, only the low-quantum number energy levels are significantly populated, and excited levels are not in equilibrium (Goyette *et al.* 1998). This has two implications. First, emission lines from high-quantum number transitions may be absent from the spectrum despite the presence of the C₂ dimer. These

lines are used in diagnostic methods because of the clarity of the spectrum in their region. Second, Swan band intensity is proportional to the density of excited species. When energy levels are in equilibrium, this density correlates reliably with total C₂ density. If the system is far from equilibrium, no relationship can be assumed between Swan emission and C₂ concentration. The severity of this limitation is minimized for transitions whose lower level is close to the ground state of the molecule, such as the $d^3\Pi_g \rightarrow a^3\Pi_u$ $v(0,0)$ band of C₂.

The temperature requirement can be verified by estimating the plasma temperature at the point of observation. Alternatively, comparative evidence can be obtained by reference to a characterized plasma with similar parameters (i.e., power, efficiency, gas flow rate, composition) whose temperature is documented.

2.1.2.6 Temperature Estimation

Electronic transitions from upper to lower energy levels are accompanied by light emission. Under a Boltzmann distribution of excited states, light intensity is an exponential function of the temperature associated with the excitation mode of the transition.

In a typical non-isothermal plasma, the temperatures linked to electron kinetic, vibrational, rotational, and gas kinetic movements rank as follows: $T_e > T_v > T_r > T_g$ (Teplý *et al.* 1995). The rate of rotational energy transfer is generally close to the rate of gas kinetic exchange, and about ten times as fast as the rate of vibrational energy transfer (Reeve and Weimer 1995). Therefore, the temperature of a Boltzmann distribution of rotational states is closer to the gas kinetic temperature than the vibrational or electron kinetic temperatures. When rotational states are in equilibrium, T_r approximates T_g (Bousrih *et al.* 1995).

In thermal plasmas at atmospheric pressure, fast rotational relaxation rates justify the assumption of an equilibrium distribution of rotational states

(Czernichowski 1987). The common assumption that thermal excitation dominates over other mechanisms implies $T_v \approx T_r \approx T_g$. If electron impact is the main mechanism, $T_v > T_r \approx T_g$ (Boulos *et al.* 1995, Cavadias *et al.* 1995, Reeve and Weimer 1995). In either case, collisions dominate and the rotational temperature approaches the gas kinetic temperature.

When populations deviate from thermal equilibrium, temperature estimates obtained from a Boltzmann plot are erroneous. One possible source of deviation is the effect on population distributions of non-collisional excitation, dissociation, or recombination. For example, in a C_2 diagnostic study of a non-equilibrium low-pressure plasma, two Boltzmann distributions - hence two rotational temperatures - were reported to correspond to distinct mechanisms of C_2 excitation. One distribution represented C_2 molecules formed in the excited $d^3\Pi_g$ state by chemical reactions. The other distribution characterized C_2 initially present in the ground $a^3\Pi_u$ electronic state and thermally excited to the $d^3\Pi_g$ state (Kini and Savadatti 1977). A similar case was reported by Teplý *et al.* (1995). Another possible source of deviation from equilibrium is fast collisional quenching, where the de-excitation of newly formed species occurs before they thermalize into a Boltzmann distribution. In this project, collisional thermal excitation is a reasonable assumption since argon is both an inefficient quencher and an efficient collision partner for C_2 (Reeve and Weimer 1995).

Important sources of uncertainty in optical temperature measurements from plasmas are light source flicker noise and temperature or concentration gradients along the line of sight. For non-uniform radial profiles without Abel inversion, temperature estimates represent locations along the line of sight where the observed transition is intense, whether at the core of the plasma (high thermal excitation) or at the periphery (high C_2 density due to bypassing or recombination).

The Boltzmann Plot Method

The exponential form of the Boltzmann equation (2.1.2-4) suggests the use of a semi-logarithmic plot of $(I/S\nu^4)$ against E_r for a set of rotational transitions. In principle, the plot is linear with a negative slope inversely proportional to the rotational temperature. This is the Boltzmann plot method of estimating temperature, outlined in Appendix VI. The construction of a Boltzmann plot requires the line strength, wavenumber and activation energy of each transition; these parameters are expressed in terms of fundamental quantities (rotational quantum numbers, electronic coupling constants, etc.) in the equation sets of Appendix III. Choosing transitions that cover a wide range of E_r minimizes error in the slope (Koulidiati *et al* 1990.). Yet, the lines should be close enough in wavelength to justify the assumption of uniform transmission efficiency and detector response over the range (Mermet 1987). A Boltzmann plot should be constructed from lines of the same branch (P, R or Q). It therefore requires a well-resolved spectrum. In the case of the $\nu(0, 0)$ Swan band, a superposition of P and R lines limits the accuracy of the Boltzmann plot method (Beulens *et al.* 1994).

In an argon-hydrocarbon plasma, the $\nu(0, 0)$ C_2 vibrational band at 516.5 nm is relatively free from interference by other rotational or vibrational bands (Beulens *et al.* 1994). Boltzmann plot estimates of T_r are commonly derived from lines of lower quantum numbers $J'' = 47 - 36$ in the P branch of the $\nu(0, 0)$ Swan band (Alder and Mermet 1973, Bleekrode and Nieuwpoort 1965, Czernichowski 1987). At lower J'' -values, interference from argon lines is observed (Alder and Mermet 1973); more generally, spectral complexity and overlap near the band head make measurements in this region unreliable (Gaydon and Wolfhard 1950). At higher J'' , there is overlap with the $\nu(1,1)$ band whose head is located at 512.93 nm.

A cautionary word is in order regarding temperature estimates encountered in the literature. Reported temperatures are sometimes derived from atomic

emission line intensities, using the Boltzmann plot method or the line pair intensity ratio method (equivalent to a two-point Boltzmann plot). The sharp lines of atomic transitions provide excellent estimates of the electronic excitation temperature. However, in plasmas that deviate from local thermodynamic equilibrium, this excitation temperature approaches the electron kinetic temperature and differs significantly from rotational and gas kinetic temperatures.

The Superposition Method

Rotational and vibrational temperatures can be determined by fitting a theoretical spectrum to a measured spectrum (Beulens *et al.* 1994, Pellerin *et al.* 1996, Simek *et al.* 1995). Using equations of the type presented in Appendix III, spectra are generated at different temperatures and convolved with a transfer function representing the optical instrument resolution (the **apparatus function**). The numerical superposition of predicted and measured spectra is programmed into a least squares minimization convergence routine. Agreement between measured and simulated spectra requires the rotational and vibrational populations to be **thermalized** (i.e., obeying Boltzmann distributions) but not necessarily **equilibrated** at the same temperature (Reeve and Weimer 1995). Temperatures are inferred by matching measured spectra with temperature-specific reference spectra. The rotational line profile of a band gives T_r , and the total intensity profile of several bands gives T_v . The procedure is computationally intensive, molecular bands being composed of hundreds of lines. It requires low-noise high-resolution spectra, and accurate knowledge of the optical system's apparatus function.

The application of this rigorous fundamental research tool is beyond the present project, and not a suitable option for on-line analysis in industrial process control systems.

Methods Using Unresolved Spectra

In response to the complexity of acquiring and analyzing fully resolved molecular spectra, researchers have developed alternative procedures for estimating temperature from unresolved spectra. These approximate methods use temperature-sensitive quantities such as a ratio of two peaks. As in the superposition method, simulated spectra provide temperature-specific references to match against measured spectra. Variations on this approach can be developed according to the information available in a given application. The following paragraphs present examples of the use of unresolved Swan band spectra for temperature determination.

The intensity of a band head depends on T_v . The intensity of rotational lines relative to the band head is a function of T_r , and nearly independent of T_v (Beulens *et al.* 1994, Koulidiati *et al.* 1990). Hence, emissivity ratios within a single band and over corresponding regions of different bands contain information on T_r and T_v , respectively. The term "thermometric" applies to lines, heads or ratios that depend on one temperature only and can serve as "spectral thermometers".

In a study of spatial profiles in an argon-hydrogen-methane plasma, Bousrih *et al.* (1995) correlated T_r with an emissivity ratio between two sections of the $\nu(0,0)$ C_2 band (516.0-516.5 nm and 512.9-516.0 nm). T_v was correlated with relative emissivities between vibrational bands: $\nu(0, 0)$ and $\nu(1, 0)$, $\nu(0, 0)$ and $(2, 1)$. Integrated intensities from simulated spectra predicted the temperature dependence of the selected ratios. Approximations of T_r were found accurate within 20% with an uncertainty of 7% in measurements.

As an alternative to band integration, band head intensity can be used to estimate T_v (Simek *et al.* 1995). Band overlap within a sequence is corrected by subtracting the intensity just past the band head from each reading. This method

is approximate, since band head intensity is not exactly proportional to overall band intensity.

Another variation on the method was reported by Czernichowski (1987). Similar in principle to the superposition method, it uses relative intensities between clusters of unresolved triplet lines from the P or R branches. Clusters are assigned emission coefficients whose temperature dependence is modelled as a second-order polynomial. The temperature at which model predictions best approach the measured intensities of two or more clusters approximates T_r . This method recalls one used by Gaydon and Wolfhard in the late 1940's. Faced with Swan band triplets that were just resolvable at low J'' and unresolvable at high J'' , they used a wide slit to measure all three components together. These data points were amenable to a Boltzmann plot at the cost of increased uncertainty.

2.1.3 Control and Optimization

2.1.3.1 Adaptability and Control

This section clarifies the terminology used to describe the adaptive control feature of APAI. In the demonstrations carried out in this work, a cost-efficiency criterion or response value was optimized by manipulating two variables. The purpose the control action was to maintain an optimal response through disturbances. The optimal value of the criterion depended on the feed stream and on conditions in the system. No additional control loop was used to keep the manipulated variables at their set points.

The response criterion was called the **objective function**. It quantified performance with respect to cost-efficiency objectives. The objective function was visualized as a three-dimensional **response surface** whose domain was the two-dimensional space defined by the manipulated variables, or **operating space**.

The response surface was not static; it varied with the feed stream and with conditions in the system. Maintaining an optimal response required continual adjustment of the manipulated variables. Optimization techniques were applied to explore the response surface and move toward an optimum on the operating space.

In APAI, the term *adaptive* has a different sense than in automatic control theory. *Adaptive control* usually refers to the continuing adjustment of automatic controller characteristics to follow variations in the dynamic response of the system under control. The adjustment may be determined from predicted or measured variations, as in *programmed adaptation*, or from on-line process model parameter estimation, as in *self-tuning control* (Seborg *et al.* 1989). Adaptive controllers automatically self-design their control algorithm or mode of action. In the present project, the term *adaptive* refers to the strategy of detecting and responding to performance variations and disturbances. The two situations relate to different levels of control and are not mutually exclusive. Both approaches could be applied in the automatic control of an APAI prototype.

Strategy options for steady-state process optimization by experimentation include: direct search (e.g., Hooke and Jeeves), gradient-based methods (e.g., Box-Wilson), evolutionary operation (EVOP), and Simplex designs. Direct search is reliable but comparatively slow. It works in successive one-variable searches using each manipulated variable in turn (Himmelblau 1990). Gradient-based methods perform local approximations of the response surface around operating points. Surface models can be simple, as in the linear version presented here, or complex, as in the Box-Wilson fitting technique. Simple models requiring few measurements present an advantage for on-line continual optimization. The EVOP procedure developed by Box and Hunter (Himmelblau 1990) is intended for industrial processes. It generates information of immediate applicability in continuous processes (manufacturing, etc.) without upsetting the production.

Gradient-based and EVOP methods use small exploratory changes in manipulated variables to determine the next input settings. The Simplex method evolved from the EVOP strategy. A set of decision rules directs the search on the basis of responses measured at various points. Gradient-based and Simplex programs were developed in this study.

2.1.3.2 Gradient-Based Search Methods

A common strategy for optimizing a response is to develop a surface model based on responses measured at selected points, then use model predictions to identify regions or directions of improved response. The simplest gradient-based method uses a linear model derived from as few as two measurements. The response surface is locally represented by a plane whose orientation depends on response sensitivity to the manipulated variable. The **gradient** is a vector pointing in the direction of steepest ascent on the operating space. It is a tool for choosing the next input settings. After implementation of new settings, the response is measured and, if appropriate, further action is taken (e.g., retraction if the result is unsatisfactory). Through successive gradient evaluation steps, the system reaches its optimal response. A description of gradient optimization principles, rules and strategies is provided in Appendix VIII.

2.1.3.3 Simplex Method

A **Simplex** is a geometric figure in the operating space. Its vertices form a set of experimental conditions where responses are measured. The number of vertices in the figure equals one more than the number of manipulated variables or dimensions in the operating space (Walters *et al.* 1991).

The Simplex algorithm directs the exploration of a surface on the basis of comparative rankings among vertex responses. At each step, the algorithm recommends new settings to replace one of the vertices and form a new

Simplex. On the response surface, successive Simplex figures progress toward the region of optimal response. Details on the Simplex algorithm and its application are provided in Appendix IX.

An advantage of the Simplex method is its simplicity. Each new step requires at most two measurements. Computations are free from differentials, which is beneficial with noisy response signals. No attempt is made to model the surface; the Simplex moves empirically.

Unlike gradient-based methods, where the response surface is continually modelled, the Simplex algorithm assumes a stable surface. Responses are compared with the best of previous points, and these reference points remain until they are displaced by points of higher response. This presents difficulties if process disturbances or variations occur on a similar time scale as the optimization process.

Simplex optimization is effective in finding an optimal region, but model-based techniques are, by definition, more accurate in locating the optimum. Simplex designs are best suited when simplicity and speed of progression take precedence over accuracy, such as in the initial stages of an optimization.

2.2 Existing Plasma Processes for Hazardous Waste Treatment

The majority of plasma-based waste treatment processes use a dc arc plasma to separate solid and liquid waste into a gas fraction (volatilization) and an inert inorganic slag (vitrification). This is usually followed by controlled oxidation of the gas fraction. Other processes focus on the vitrification of solid residues like fly-ash (Inaba *et al.* 1998). Plasma arc melters have been considered for the treatment of municipal solid waste, but no commercial process has been developed (Eddy *et al.* 1996).

A class of processes called "plasma chemical methods" use plasmas as chemical reagents in the recovery of valuable products from gasified waste (Georgiev *et al.* 1995, Czernichowski *et al.* 1990). Other processes apply non-thermal plasmas (such as low-pressure glow discharges) to the decomposition of various products, including hazardous organics, nitrogen oxides, and soot (Czernichowski *et al.* 1995, Itatani 1993). None of these highly specific methods has progressed beyond the stage of laboratory-scale demonstration.

The review presented here is limited to operational thermal plasma waste treatment facilities, with the exception of a patent application for an incineration thermal plasma afterburner.

2.2.1 Westinghouse Pyroplasma Process

This process was specifically developed by Westinghouse Inc. for the destruction of liquid organochlorinated waste. The unit consists of a reaction channel heated by a 1-MW non-transferred torch, followed by a larger pyrolysis reactor. The waste is injected directly into an air plasma jet. A venturi scrubber removes acid gases and particulates from the exhaust stream. The product gas (40% hydrogen, 25% carbon monoxide, 15% nitrogen and 10% water) is normally flared. The operation is computer-controlled.

For a specific feed, the reactor temperature determines the final composition. Temperature is maintained at a set value (typically 1000°C) by adjustments in torch power, waste feed flow or torch gas flow. For any feed composition, the optimal operating parameters and product gas composition are predicted by equilibrium chemistry calculations.

The reactor and gas cleaning units are mounted on a 48 foot-long mobile platform. The effectiveness of the method was demonstrated for methyl ethyl ketone, ethanol, methanol, carbon tetrachloride, and transformer Askarel fluids

(PCBs and trichlorobenzene). Destruction efficiencies in excess of 99.9999% were reported, with emissions of NO_x, HCl and particulate matter well below regulatory standards. Chlorinated dioxins and furans were undetectable in the stack gas and in the scrubber effluent (Heberlein 1993, Joseph *et al.* 1986, UIE 1988).

2.2.2 INDICIS Process (Electricité de France)

This process is designed for the destruction of toxic waste in concentrated forms, such as drums of liquid organic waste. It operates continuously and involves no direct manipulation of the waste material. The pilot plant processes one 220-litre metal or plastic drum per hour.

The first step consists in milling the drums and pulping the resulting mixture with optional addition of liquid or sludge. The destruction step proceeds in two stages: pyrolysis followed by combustion. The feed is continuously poured into a crucible where it is pyrolyzed by a non-transferred air plasma jet (200 - 800 kW) in an oxygen-deficient atmosphere. The content of the crucible is transferred to a rotary furnace for oxidation. Gases from the furnace proceed to a post-combustion chamber. Excess air is provided, along with steam for the control of chemistry and auxiliary propane if treating waste of low fuel value. A holding time of 20 to 90 minutes in the furnace ensures volatilization of organic compounds from the molten solids. The gas spends at least 2 seconds at 1200°C in the afterburner chamber. The remaining metals and salts are extracted in water to form ash. Gas quenching, gas cleaning and ash treatment steps complete the process (Electricité de France 1991, Guillet and Causse 1994, Valy and Guillet 1995).

2.2.3 Retech Plasma Arc Centrifugal Treatment (PACT) System

Retech Inc. developed a process for the pyrolysis and vitrification of mixed solid/liquid hazardous waste. The central unit is a chamber equipped with a rotary hearth and a moveable transferred arc torch (150 kW). Organic materials are vapourized and oxidized by an air plasma. Residual solids are vitrified into a non-leaching slag. Centrifugal action spreads the feed material over a large area, homogenizes the slag, and keeps solids away from a tapping hole at the bottom of the hearth. The slag is collected periodically by reducing the rotational speed of the hearth while interrupting the feed.

The system is built into a portable pilot scale facility including a plasma centrifugal furnace, a secondary combustion chamber with natural gas afterburners, and a gas cleaning module. The feeder type (screw, belt, drum, liquid lance, etc.) is selected according to the waste treated. Gases exit the furnace through the tapping hole into a secondary combustion chamber. Tangential gas entry promotes mixing by inducing a turbulent vortex flow through the chamber. Combustion is ensured by a minimum residence time of 2 seconds at 1090°C in an oxidizing atmosphere. Quench and wet scrubbing units remove particulate matter, metals and acid gases. Given the relatively small gas throughput, gas recycling is an option for applications such as the treatment of radioactive waste where gas release is a concern. Closed loop operation was demonstrated experimentally.

Test results for synthetic soil matrices contaminated with hexachlorobenzene indicated destruction efficiencies in excess of 99.99%. Heavy metals were immobilized in the slag but, as in other vitrification processes, volatilization of mercury, cesium and cadmium occurred (Eschenbach *et al.* 1994, Filius and Whitworth 1996, Hill and Olexsey 1989, Schlienger 1993).

2.2.4 Moser Glaser & Co. (MGC) Plasma PLASMOX Process

Based on the rotating plasma furnace developed by Retech, the Plasmax process is designed for the destruction of liquid waste drums. Like the PACT system, it oxidizes organic materials and vitrifies inorganic residues. The furnace is equipped with a mechanical drum handler, liquid injection by lance, and three Retech transferred arc torches: a 0.1-MW rotodode for drum-cutting, a 1.2-MW main torch, and a 0.3-MW casting torch. The main torch operates with oxygen-enriched air. Combustion is furthered by injection of air or oxygen at the entrance of an oxidation chamber maintained at 1400°C. The gas treatment train includes wet scrubbers and NO_x-reducing absorbers. The Plasmax process is highly integrated: it features closed-loop cooling, recycling of filtered dust, and energy recovery. Continuous monitoring indicated destruction efficiencies of at least 99.9968% (Electricité de France 1991, Heberlein 1993, UIE 1988).

2.2.5 ScanArc Process

ScanArc Plasma Technologies Inc. completed a development program on hazardous product decomposition under a controlled atmosphere. The program focused on the applicability of plasma heat sources in different chemical environments. Pilot plant studies demonstrated the potential of plasma chemistry in the decomposition of chlorinated hydrocarbons (including PCBs) and of nitrogen-containing by-products of explosive manufacturing.

The generic process comprises three stages: heating, reaction, and gas cleaning. In the first stage, an air-hydrocarbon mixture is heated by a non-transferred plasma torch (300 kW). The air-to-fuel ratio is controlled to keep the CO₂-to-CO ratio below 0.25. Under these conditions, thermodynamics limit the production of NO_x to less than 50 ppm. In the second stage, the hot gas enters a reaction chamber along with the material to be decomposed. The CO₂-to-CO

ratio is maintained by addition of secondary air or hydrocarbon. The third stage is a venturi scrubber (Thörnblom and Røihjert 1992).

2.2.6 CSIRO / SRL Plasma PLASCON Process

The Commonwealth Scientific and Industrial Research Organization, in collaboration with SRL Plasma Ltd., developed a process for on-site treatment of waste in liquid and gaseous forms. Waste and oxygen are injected into the jet of a 150 kW argon plasma torch. The mixture flows through a reaction tube, water spray quench, and wet scrubber. Destruction efficiencies in excess of 99.9999% were obtained with chlorophenols and PCB transformer oil. Commercial PLASCON units were integrated to herbicide manufacturing facilities. Further projects include the application of the PLASCON process to the destruction of CFCs and Halon gases (Farmer 1999, McAllister 1995, SRL Plasma Ltd. 1995).

2.2.7 Commissariat de l'Energie Atomique

A French patent application for a plasma post-combustion process was made available to the public on March 25, 1994. This afterburner uses an oxygen plasma to treat gases produced during incineration or pyrolysis of organic waste. The objective is to achieve complete combustion with minimal excess oxygen and residence time, in order to reduce gas throughput and equipment size. The afterburner chamber is a water-cooled metal tube with a 30-kW non-transferred torch located at one extremity. The feed gas enters the chamber radially near the torch. This configuration favours mixing of the incineration gas with the oxygen plasma jet. The other extremity of the tube opens onto a gas cleaning system (Institut National de la Propriété Industrielle 1994).

2.3 Existing Hazardous Waste Incineration Processes

Thermal treatment by fossil fuel combustion is the most widely applicable method of organic waste destruction. The two example processes presented in this section are representative of the current state of thermal treatment technology.

2.3.1 BOVAR Process

BOVAR Waste Management Inc. operates the only integrated waste treatment facility in Canada. Located in Swan Hills (Alberta), the facility includes a high-temperature process suitable for incineration of liquid PCBs and PCB-contaminated materials. This process exemplifies the best available technology for large-scale treatment of hazardous organic materials.

The process consists mainly of a rotary kiln, an afterburner chamber, a quench tower, and a gas cleaning train. The kiln operates at 900-1000°C using natural gas as the auxiliary fuel. A feed mixture of solid and liquid waste burns in the kiln for up to 45 minutes. The residual slagging or ashing solids are stabilized but not vitrified, and are usually fit for landfilling without further treatment. The gas enters an afterburner chamber maintained at 1200°C by combustion of auxiliary fuel and liquid waste. An average residence time of 3 seconds in excess air promotes oxidation of the kiln gas. Combustion efficiency is monitored via CO, CO₂, O₂ and total hydrocarbon (THC) readings. The afterburner gas is quenched in a spray tower with alkali solution. Subsequent gas cleaning steps include a two-stage absorber for pH and temperature control, as well as particulate-removal steps. Dioxin and furan control involves a proprietary method of activated carbon circulation in the wet units.

The outstanding performance of this process is linked to detailed operating plans based on prior knowledge of the feed composition. Waste characterization is an

essential step. The process is fed a prepared waste mixture (called "menu") whose requirements match the thermal and gas throughput capacities of the equipment. The operating plan (temperatures, flow rates, etc.) is developed according to feed characteristics. A computerized control system monitors the process continuously and, if necessary, makes corrections to the plan. The time required for the system to stabilize at new conditions is less than half an hour. Of course, performance is optimal when the system responds as in the original plan (BOVAR Inc. 1999).

2.3.2' Bennett Process

This is a thermal desorption process for the treatment of contaminated soils and sediments. Its flowsheet is similar to that of conventional incineration: primary kiln, secondary combustion chamber, quench and gas cleaning. The thermal desorption kiln operates between 650°C and 980°C in an oxygen-deficient atmosphere. Under these conditions, the organic fraction of the feed volatilizes into a combustible gas in 10 to 15 minutes. The gas is mixed with 50-100% excess air and heated to 1000-1200°C in a secondary chamber where it remains for over 2.8 seconds. The combustion gas is quenched to 150°C, injected with alkali and activated carbon, then filtered for particulate removal. The inorganic soil matrix is reused without further treatment (Bennett Environmental Inc. 1999).

2.4 Novel Aspects of Adaptive Plasma-Assisted Incineration

Most plasma-based waste treatment processes use plasma in the primary stage. The present project investigates the techno-economic feasibility of a plasma reactor as the secondary stage to a conventional incinerator. This process takes advantage of the reliability and economy of a conventional furnace for treating the combustible fraction of the waste. Thermal plasma treatment is applied as needed to eliminate hazardous compounds that resist combustion.

The concept of adaptive operation is original to this project. Whereas most waste treatment processes operate at stable conditions, the proposed process responds to feed requirements. Continuous feedback control of the plasma afterburner is based on real time spectroscopic observations. This adaptive strategy allows one to minimize the operating cost of the afterburner without compromising safety. The plasma heat source provides unprecedented heat transfer capabilities. Built-in flexibility allows cost-effective operation through feed load variations and other disturbances.

The APAI concept is unique in its attempt to integrate thermal plasma technology and adaptive operation into an economically viable waste treatment process. The feasibility of complete organic waste oxidation in laboratory-scale plasma reactors is unquestioned. Destruction efficiencies based on analytical detection limits (in excess of 99.999%) were reported in the treatment of organic liquids, including PCBs, by counter-flow injection into a dc plasma jet (Han *et al.* 1995). The idea of a plasma afterburner for incineration was investigated in modelling and laboratory studies. Demonstrations using an afterburner model monitored by molecular band emission spectroscopy confirmed the importance of optimizing reactant concentrations, power levels and feed loads (Ramasamy *et al.* 1996). In these experimental projects, cost-effectiveness was the main obstacle to large-scale development.

2.4.1 Advantages over Conventional Incineration

This section identifies potential benefits to be gained by operating incineration processes in an adaptive plasma-assisted mode.

Incineration by fuel combustion suffers two major limitations. First is the difficulty in maintaining process conditions that promote complete combustion. The presence of dioxins and furans in post-combustion gas streams and on solid residues is a persistent problem. Existing facilities resort to gas cleaning

techniques and solid immobilization to prevent the release of these highly regulated compounds. The second limitation is a lack in flexibility during operation. The thermal inertia of incinerators imply long transient periods and slow response to disturbances. For this reason, feed homogeneity and prior knowledge of its composition are essential for optimal operation.

The main advantage of plasma technology is its effectiveness at decomposing organic materials. In combustion flames, the formation of toxic organic by-products is linked to incomplete combustion. APAI addresses this problem on two fronts: (1) it provides decomposition into atomic species; and (2) its high oxidizing potential and rapid quench promote recombination of the atomic species into fully oxidized products. Successful plasma-assisted operation would essentially eliminate organic molecule precursors from the combustion gas. This would alleviate reliance on post-combustion gas cleaning operations to meet emission standards.

A key feature of APAI is its flexibility. Fluctuations in feed quality or flow rate are managed by a cost-optimized control response. Through their effects on chemical reaction kinetics, oxygen content and temperature adjustments can compensate for short residence times or stringent feed requirements.

A plasma heat source is advantageous in terms of thermal efficiency and gas throughput. The heat input per unit volume of gas is considerably higher in plasma torches than in fuel burners (Huhn *et al.* 1997). Coupled with a plasma afterburner, a primary incinerator could operate at moderate conditions. This would improve its thermal efficiency and reduce fuel consumption, leading to smaller gas volumes and lower SO_x/NO_x levels. Reductions in gas volume and in by-product formation translate into less expensive gas cleaning systems.

As an upgrading option for existing facilities, APAI would encourage responsible management with respect to environmental protection. Demonstration of the

safety and effectiveness of APAI would facilitate public acceptance of incineration systems. Such qualitative aspects are essential to a complete cost-benefit analysis of the concept. Safety, responsibility and environmentally sound practice are growing priorities. Despite the financial cost of plasma technology, qualitative factors may favour APAI.

3. OBJECTIVES

The general objective of this project was to assess the techno-economic feasibility of Adaptive Plasma-Assisted Incineration (APAI). A practical study of technical feasibility was performed using a laboratory-scale plasma afterburner model. Economic viability was examined in a conceptual study of commercial-scale waste treatment applications.

3.1 Specific Objectives

Nine specific objectives were grouped into four areas: plasma afterburner model, spectroscopic diagnostic, optimization, and techno-economic assessment.

3.1.1 Plasma Afterburner Model

1. Configuration of a laboratory-scale induction plasma system for use as an afterburner model, with simulation of an incinerator flue gas feed;
2. Selection of plasma control variables and definition of an operating space;

3.1.2 Spectroscopic Diagnostics

3. Assembly of an optical detection system for continuous on-line observation of the plasma jet in the model system;
4. Analysis of the emission spectrum of the plasma and formulation of an indicator for the decomposition of organic compounds;

3.1.3 Optimization

5. Development of optimization criteria and programs for cost-effective operation of the afterburner model;

6. Practical demonstration of the system's adaptability to feed requirements and economic factors;

3.1.4 Techno-Economic Assessment

7. Conceptual design of industrial-scale plasma-assisted and conventional incineration processes for three example applications: soil incineration, soil desorption, and liquid waste treatment;
8. Estimation of the capital and operating costs of the afterburner and gas cleaning sections for each case examined;
9. Economic and qualitative comparison of adaptive plasma-assisted and conventional waste incineration, including a study of cost sensitivity to external economic factors and process variables.

4. METHODOLOGY

This chapter describes the instruments and methods pertaining to three essential aspects of the experimental demonstration: plasma afterburner model, optical diagnostics, and optimization.

4.1 Plasma Afterburner Model

4.1.1 Radio Frequency Generator and Induction Plasma Torch

The plasma was generated in an induction torch (Tafa Technologies Inc., model 56, 25 kW) using a radio frequency power supply (Lepel High Frequency Laboratories, model 32*30MC). The generator rectified three-phase 60 Hz AC power (575 V, 36 kW) into DC plate power (up to 30 kW), which the oscillator converted to 4 MHz AC power applied to the induction coil. A grid control variable-impedance inductor matched the characteristics of the oscillator circuit and plasma load for maximum coupling efficiency or energy transfer. Tuning was optimal at the grid setting that best satisfied two opposing criteria: (1) a grid current equal to 10-15% of the plate current, and (2) plate voltage and current at similar levels relative to their maximum. The generator was not equipped for measuring the power dissipated in the plasma and the power reflected through the circuit. Power dissipation was estimated as a fraction of the plate power, which was obtained from plate voltage and current readings:

$$\text{Plasma power} \quad P = P_p * \eta \quad (\text{equation 4.1.1-1a})$$

$$P_p = V_p * I_p \quad (\text{equation 4.1.1-1b})$$

where P_p = plate power; η = coupling efficiency
 V_p = plate voltage; I_p = plate current

An important source of uncertainty was the dependence of the coupling efficiency on gas composition. The inductive characteristics of the load varied with feed composition. Since continual adjustment of the grid setting was impractical, satisfactory operation was maintained by using a limited range of gas composition. Based on literature and on previous calorimetry work on the same instrument (Munz 1974), a torch efficiency of 25-30% was expected.

The torch consisted of a six-turn, 48 mm-diameter induction coil wound around a water-cooled quartz tube. The plasma gas could be distributed among axial, radial and tangential (swirl) injection ports. Following ignition with argon, the gas composition was gradually modified to include an oxidant and a model organic compound. Stable operation was best achieved using a sustaining axial argon flow of 14 slpm (30 scfh), a tangential sheath argon flow of 33 slpm (70 scfh) carrying the oxidant, and no radial flow. An organic model compound was introduced as a substitute for incomplete combustion products in the feed. It entered the plasma through a central injector in a carrier flow of 2.4 slpm (5 scfh) argon, separate from the oxidant.

Propane served as a model compound in the demonstrations. Safety considerations justified the choice of a non-hazardous material over toxic waste. Using a gaseous compound allowed the simulation of a flue gas feed without the complication of liquid atomization. The resistance of the compound to thermal destruction was not a selection criterion: in an actual plasma treatment system, all compounds - persistent or not - should be decomposed. The model compound stood for molecular fragments or recombined products whose presence would signal inadequate control of the process.

The choice of an inductively coupled plasma (ICP) over a non-transferred dc arc plasma was based on laboratory equipment characteristics. Erosion of the tungsten tip cathode in a laboratory-scale dc torch precluded steady operation under oxidizing conditions. Industrial-scale designs use a cylindrical copper

cathode and are not subject to this limitation. An ICP torch has no electrodes and can, in principle, operate over a wide range of gas compositions. The suitability of the ICP as a demonstration model was confirmed in preliminary optical emission studies performed using a 2-kW ICP analytical instrument.

4.1.2 Manipulated Variables

A disadvantage of the induction plasma was the interdependence of composition, plate power and coupling efficiency. Plasma composition depended on the feed gas and on the chemical reactions triggered by power dissipation. In turn, plasma composition determined load impedance and coupling characteristics. Plate and dissipated power varied with oscillator circuit dynamics and coupling efficiency.

Consequently, the preferred manipulated variables - dissipated power and oxidizing potential - were neither independent nor directly controllable. Power dissipation was a function of plate power and coupling efficiency, both of which varied with oxygen concentration. At a fixed oxygen input, power influenced oxidizing potential by controlling molecular dissociation into reactive species. Given these complex interactions, the system was treated as a "black box". Interactions between variables were considered part of the system's response. Plasma stability and reproducibility were key factors in the choice of manipulated variables.

The oxidizing potential was represented by the rate of oxygen addition to a constant argon flow. The manipulated variable was the oxygen flow rate. With the flow console configuration used, the choice of this variable over concentration allowed better reproducibility in torch flow patterns. The composition scale of the operating space was not exactly linear in oxygen concentration. This was inconsequential: the response of the plasma to oxygen concentration was unlikely to be linear.

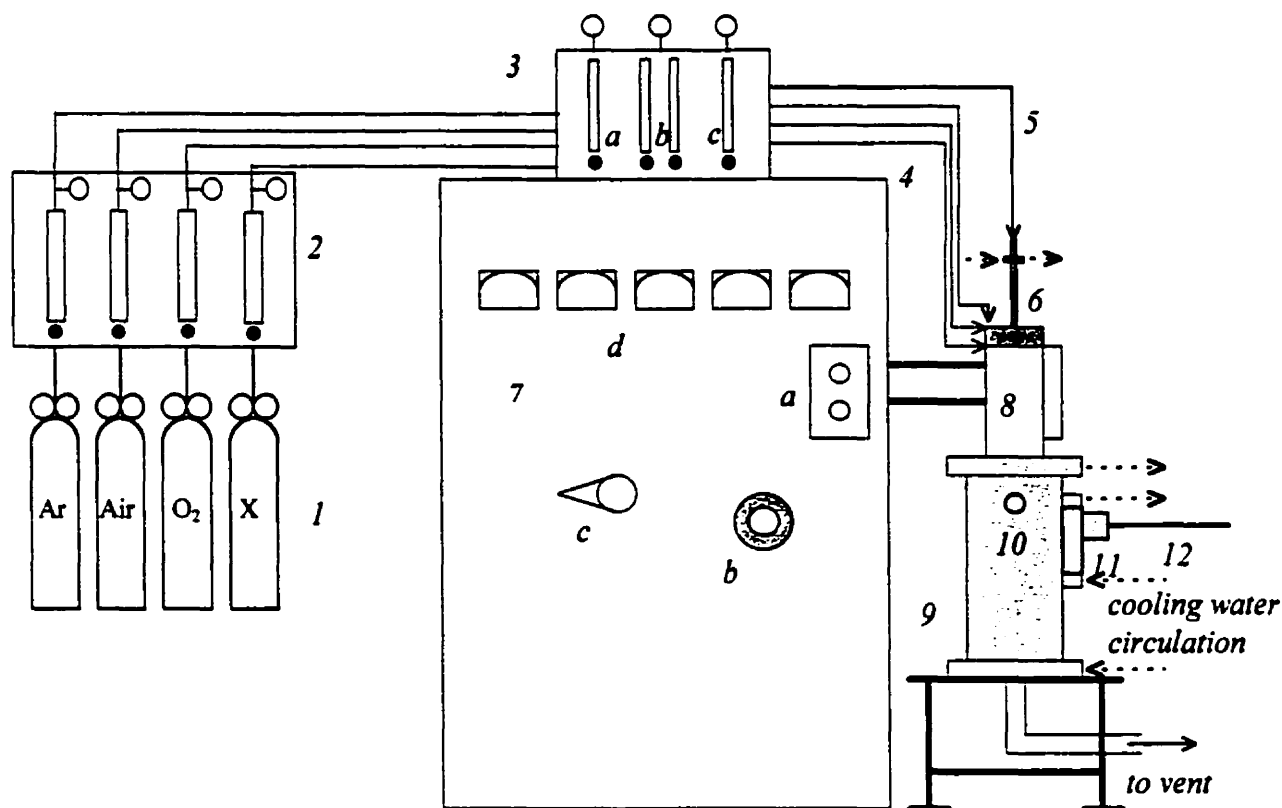
The most reproducible way to control power was to define plate current as the manipulated variable, assuming a constant plate voltage. At a fixed current setting, the voltage varied by less than 7% over the oxygen concentration range. This was acceptable given the uncertainty in energy transfer efficiency from plate power to dissipated plasma power. Due to interdependence among variables, a unique mapping of plate power as a function of plate current was not possible.

4.1.3 Plasma Operation

Figure 4.1.3-1 shows the equipment in its original configuration. The plasma gas was an argon-air mixture supplemented with oxygen. The model organic compound, propane, was introduced at the centre of the torch using a water-cooled stainless steel injector (0.64 cm [1/4"] O.D.). The torch nozzle opened onto a closed water-cooled reactor.

The rationale for attempting to use an argon-air plasma, instead of a typical argon plasma, was the following. Argon was required to ignite and sustain a discharge in the laboratory torch, but an industrial-scale afterburner would operate with air. It was felt that an argon-air model would better simulate the chemistry and optical characteristics of the actual system. However, air was eventually replaced by pure oxygen following difficulties in the operation of the torch.

The fraction of air allowable in the plasma gas was limited by the capacity of the torch to withstand power dissipation: the energy density of the discharge increased with the fraction of polyatomic molecules in the gas. Without a reactor attached, the torch operated successfully using up to 49% air (26.0 slpm [55 scfh] air in 27.4 slpm [58 scfh] argon). With additional oxygen (up to 18.6 slpm [39.5 scfh]), the oxygen concentration ranged from 10.2 % to 33.5%.



- 1 Gas cylinders (argon, air, oxygen, model compound)
- 2 Flow meters (rotameters), valves and pressure gauges
- 3 Flow control console with valves and on-off switches
- 4 Gas lines to axial (a), tangential (b) and radial (c) injection ports
- 5 Model compound injection line
- 6 Water-cooled inserted injector
- 7 Lepel power supply with start/stop buttons (a), power control dial (b), grid control dial (c) and current/voltage indicators (d)
- 8 Plasma torch
- 9 Water-cooled reaction chamber
- 10 Fixed observation window (#9 glass)
- 11 Water-cooled positioning window plate with variable-aperture iris and collimating probe/optical fiber holder
- 12 Fused silica optical fiber (to focusing probe at monochromator entrance slit)

Not shown: computer-controlled optical detection system including monochromator, photomultiplier tube, intensified photodiode array, and data acquisition/processing hardware

Figure 4.1.3-1: Schematic Diagram of the Original System with Torch-Reactor Combination

The presence of air in the plasma gas caused difficulties after attachment of the reactor (Figure 4.1.3-1). Unlike argon plasmas, argon-air plasmas had a propensity to arc to the reactor due to increased power and jet size. Stable operation was limited to low power settings, and the introduction of propane or oxygen was a likely trigger for arcing and extinction. The attachment of a ventilation conduit to the reactor caused additional disturbance, as would a wide conductive surface in the vicinity of the RF field. Operating under these conditions led to overheating and equipment damage.

Measures were implemented to enhance the stability of the discharge and to attenuate the intensity of the external RF field. The air fraction was reduced to 38%; the torch was enclosed in a grounded metal shield; and insulation was improved between the grounded and floating components of the reactor support structure. These changes did not prevent arc formation and plasma extinction.

The six-turn induction coil was temporarily replaced by a four-turn coil to alter coupling characteristics. Shorter solenoids have smaller volumes, higher power densities, and couple better with polyatomic gases. The new coil eased the transition to an argon-air mixture after ignition. It also enhanced stability. Power and composition ranges were unchanged, but there was evidence of better coupling, i.e., higher rate of thermal dissipation at a given plate power setting. Arcing still occurred upon introduction of propane or oxygen. More importantly, the torch cooling could not accommodate the increase in dissipated power. This was signalled by frequent devitrification and failure of the quartz tube. Operating under these conditions proved impractical and unreliable, so the torch was re-equipped with the six-turn coil.

The need for stability and flexibility in composition prompted a change to an argon-oxygen plasma. The removal of nitrogen reduced power requirements for a given oxygen concentration, easing thermal and electromagnetic strain on the equipment. This change was a key factor in improving plasma stability and

making propane injection feasible. The argon-oxygen mixture was introduced tangentially, while an axial flow of pure argon sustained the discharge. Reliable operation was possible over the following window:

Plate current: 3.6 - 4.6 A

Torch gas

Argon: 47 slpm (100 scfh), 30% axial and 70% tangential

Oxygen: 1.8 - 9.8 slpm (3.8 - 20.7 scfh), tangential
(equivalent concentration: 3.5% - 16.5%)

Injector gas

Argon: 2.4 slpm (5 scfh) as a carrier

Propane: 0 - 0.11 slpm (0 - 0.23 scfh)
(equivalent concentration: 0% - \approx 0.2%)

The plate power range varied between \approx 19-27.5 kW and \approx 21-30 kW depending on the gas composition (Figures 4.1.3-2 and 4.1.3-3). In occasional tests, 0.3% or more propane was used to enhance Swan band emission. However, sustained operation at such concentrations was beyond the capabilities of the system as it generally led to failure of the quartz tube.

Initially, the model compound was introduced through a water-cooled injector. Difficulties arose from the injector acting as an antenna within the RF field. The metal tube, floating at the same electrical potential as the torch, became an electrode for argon arcs igniting inside the injector feed line. The problem persisted even after increasing the carrier gas flow and isolating the feed line from the injector with a ceramic tube. The water-cooled injector was therefore replaced by a simple ceramic tube. Without cooling, a refractory material was essential, and insertion into the plasma was no longer feasible. Zirconium oxide tubes (Alfa Aesar, CaO stabilized, 2300°C service temperature) became brittle and broke upon exposure to an analytical plasma of the order of 2000°C. Alumina tubes (Omega, Omegatite 450, 99.8% Al₂O₃, 1950°C service

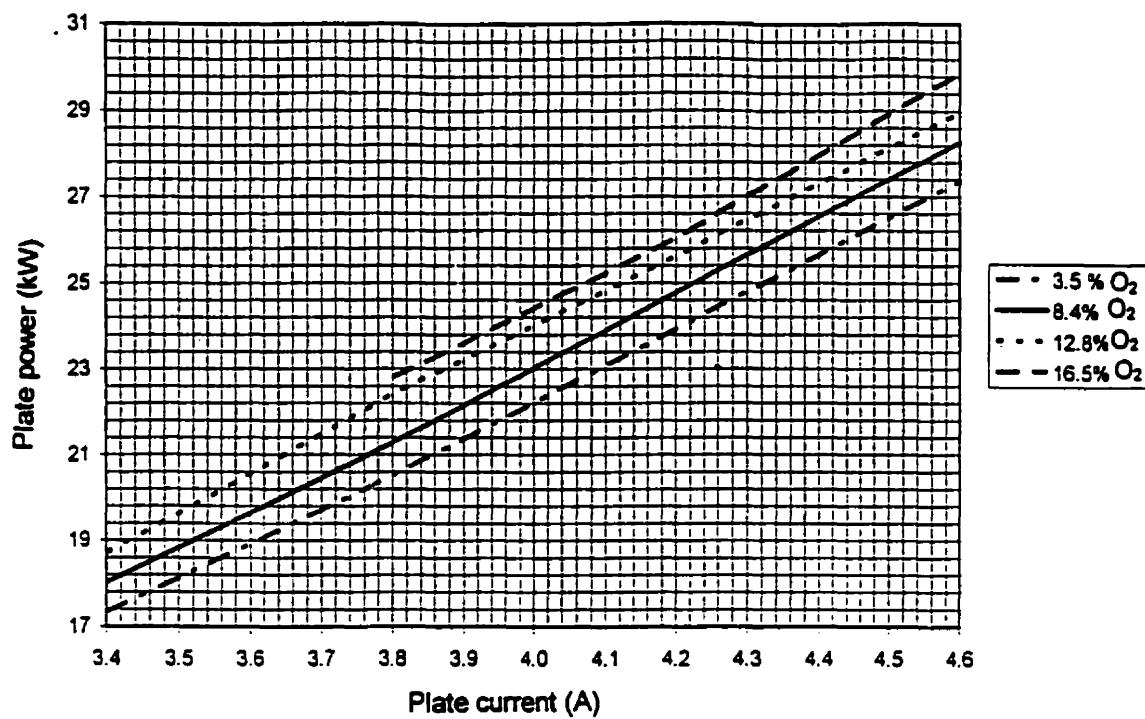


Figure 4.1.3-2: Plate Power vs Plate Current at 0.1% Propane

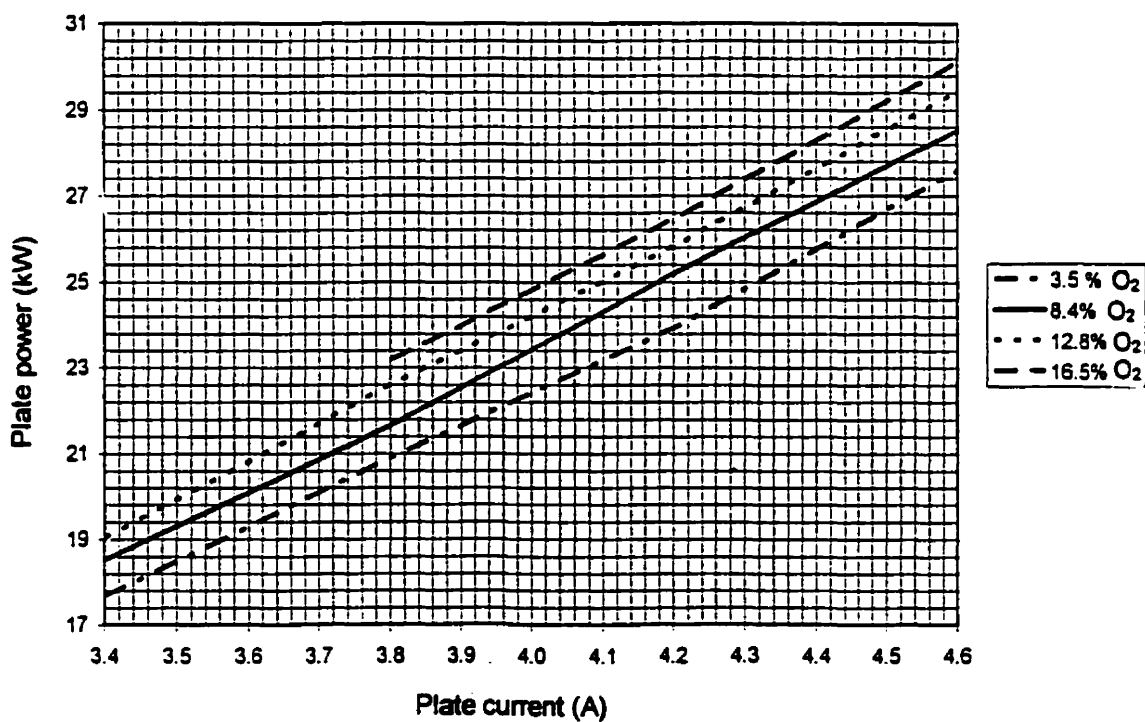
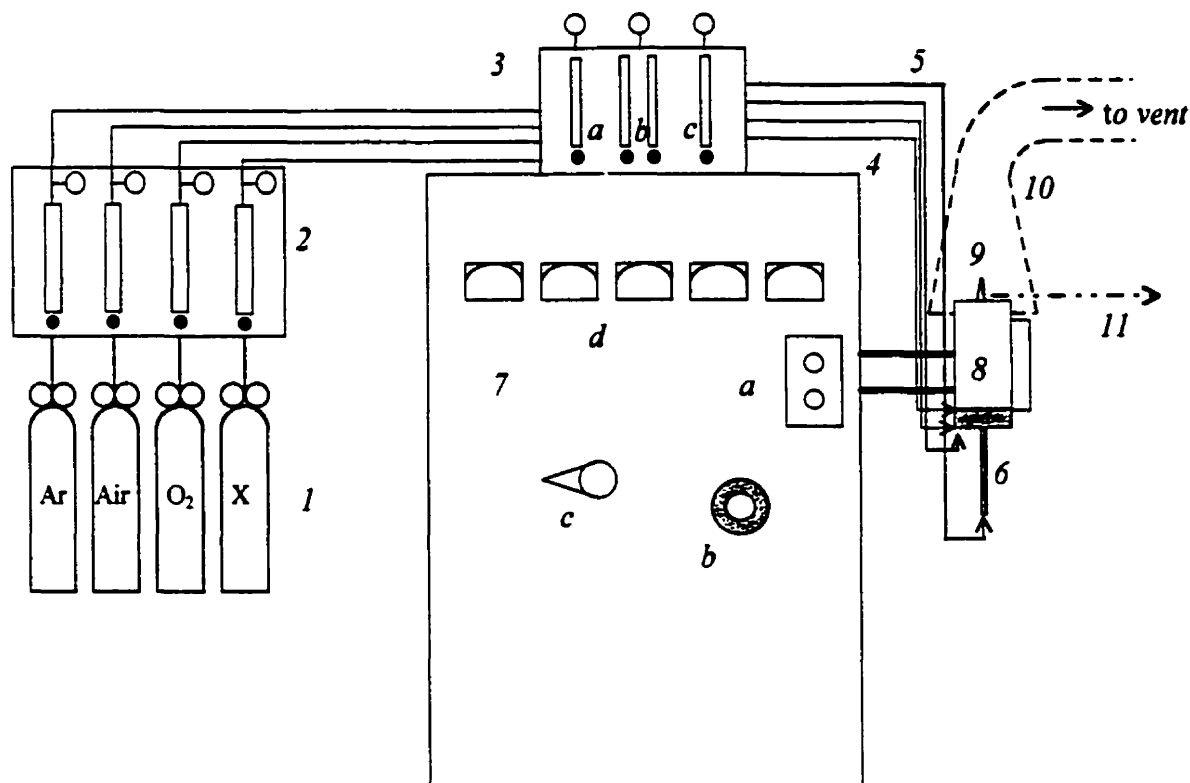


Figure 4.1.3-3: Plate Power vs Plate Current at 0.2% Propane



- 1 Gas cylinders (argon, oxygen, model compound)
- 2 Flow meters (rotameters), valves and pressure gauges
- 3 Flow control console with valves and on-off switches
- 4 Gas lines to axial (a), tangential (b) and radial (c) injection ports
- 5 Model compound injection line
- 6 Alumina tube injector
- 7 Lepel power supply with start/stop buttons (a), power control dial (b), grid control dial (c) and current/voltage indicators (d)
- 8 Plasma torch
- 9 Plasma jet
- 10 Venting tube with non-flammable skirt (open towards imaging system)
- 11 Line-of-sight from imaging system positioned on nearby optical bench

Not shown: computer-controlled optical detection system including monochromator, photomultiplier tube, intensified photodiode array, and data acquisition/processing hardware

Figure 4.1.3-4: Schematic Diagram of the Modified Open System Without Reactor

temperature) withstood insertion just past the gas distributor and were used in all experiments.

The change from argon-air to argon-oxygen had an unexpected consequence. Whereas the visible part of an air-containing plasma jet extended at least 15 cm past the nozzle into the reactor, that of an argon-oxygen plasma jet did not reach the observation window (Figure 4.1.3-1). No useful emission spectrum could be measured from this window. The diffuse light reflected by the brass reactor walls showed none of the optical features sought, perhaps because the light originated from the cool end of the flame. As an open system, without a reactor, the luminous jet was about 5 cm in length, of which a 2 cm-long triangular core was adequate for optical analysis. Severe flicker and rapid cooling by air entrainment made the side and tail regions of the jet unsuitable for optical measurements.

Consequently, the experimental work proceeded using the equipment configuration shown in Figure 4.1.3-4. The plasma exited the nozzle into ambient air. The torch was mounted with the nozzle side up to facilitate gas evacuation. A ventilation tube was placed directly above the nozzle and fitted with a heat-resistant "skirt" to channel the plasma gas into the vent. A safety check on cyanide formation was performed by searching the optical spectrum for the strong violet bands of CN. These tests were carried out at high propane and low oxygen concentrations. The absence of cyanide bands indicated that CN generation by air entrainment into the hot reactive jet was not a problem.

4.2 Optical Diagnostics

4.2.1 Light Collection and Detection

Figure 4.2.1-1 is a diagram of the optical transmission system. Light from the plasma was projected onto an imaging plate by an achromatic lens doublet. The plate was mounted on a translation stage and fitted with an optical fibre

termination nut. At unity magnification, the range of motion of the fibre tip on the plate covered the entire image of the plasma jet. The optical channel was a single fibre of fused silica about 10 m in length. The fibre was 200 microns in diameter and its cone of acceptance included the solid angle subtended by the imaging system. A high imaging F-number justified the assumption of uniform light collection across the depth of the three-dimensional jet. At the image plane, light from the front or back edges of the jet was slightly out-of-focus, hence lower in intensity than at its focal plane. The intensity loss caused by collecting this light off-focus was estimated to less than 8% by a geometric argument presented in Figure 4.2.1-2. This was acceptable for spectral diagnostics using relative intensity measurements. At worst, an analyte present only at the periphery of the jet could still be detected.

The far end of the optical fibre met a two-lens collimating assembly that focused the light onto a spectrometer's entrance slit. The instrument was an $f/8$, one-meter focal length Jobin-Yvon THR-1000 monochromator. A slit width of 20 microns was used for high-resolution scans. (Imperfect slit blade alignment caused transmittance to drop sharply around 10 microns). The spectrometer was equipped with a 1800 grooves/mm grating, which brought the reciprocal linear dispersion close to 0.5 nm/mm and the slit width-limited resolution slightly above 0.02 nm. Experimental determination of the full width at half-maximum (FWHM) gave 0.016 nm using the 313 nm lines of a mercury pen lamp. Around 513-515 nm, a region of interest in this project, a value of 0.022 nm was obtained from P-branch lines of the C_2 Swan band; this estimate could be high since the "lines" consisted of unresolved triplet components.

After wavelength separation, the light was directed to one of two detectors: a photomultiplier tube (Hamamatsu R928 PMT) for high-resolution scans, and a UV-enhanced intensified photodiode array (Princeton Instruments IRY-700S) for short waveband spectra. This optical multichannel array (OMA) contained about

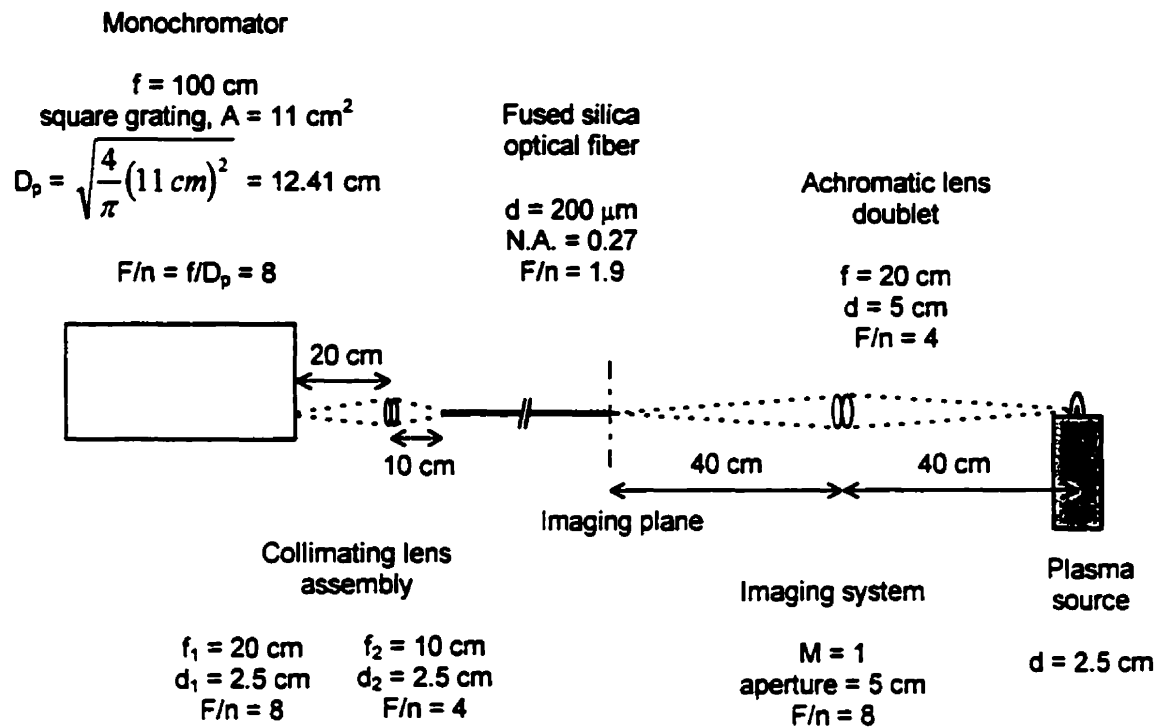
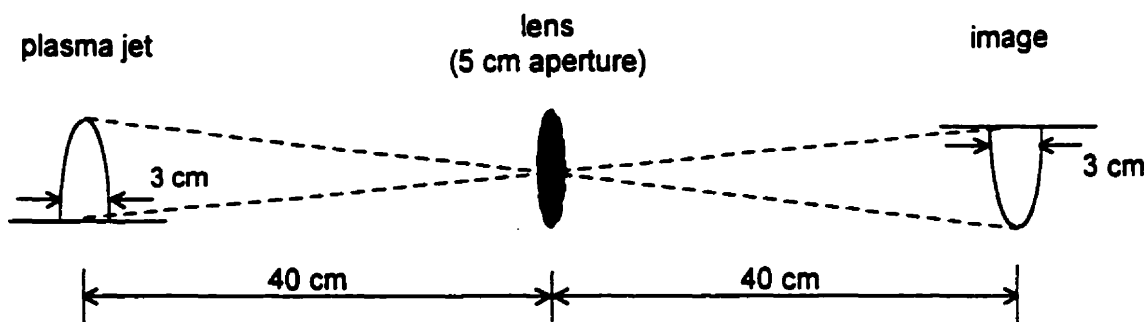


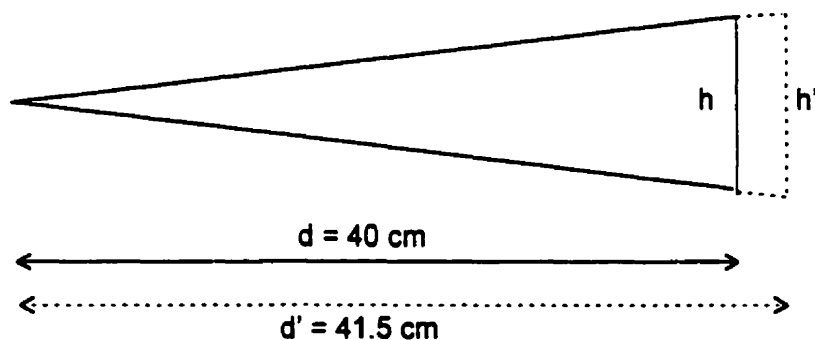
Figure 4.2.1-1: Schematic Diagram of the Optical System (not to scale)

A	area
d	diameter
D_p	equivalent diameter
f	focal length
F/n	F-number
M	magnification
N.A.	numerical aperture



Light focused by a lens disperses into a cone away from its focal point. At the image plane, light originating from the front or back edge of the plasma jet is off its focal point by 1.5 cm. Its intensity is lower than at the focal plane due to dispersion. This figure estimates the intensity loss based on the relative projected area of the source on the plane of a fixed-size detector element (e.g. fibre or entrance slit).

The intensity of the light projected on the imaging plane is assumed inversely proportional to the flat projection area at the extremity of the "cone" of light (solid angle) collected by the lens. Light dispersion at 1.5 cm from the focal plane is represented by an extension of this cone. The loss in measured intensity is estimated from the change in circular area.



F-number of the imaging system: $F/n = 8 = h/d = h'/d'$

Area at focus: $A = (\pi/4)h^2$

Area off-focus: $A' = (\pi/4)h'^2$

Intensity ratio: $\frac{I'}{I} = \frac{A}{A'} = \frac{h^2}{h'^2} = \frac{d^2}{d'^2} = \left(\frac{40}{41.5}\right)^2 = 0.93$ or 93%

Conclusion: off-focus projection causes a 7% loss in intensity.

Figure 4.2.1-2: Approximation of the Intensity Loss Due to Lack of Focus

700 active diodes placed 25 microns apart (23 micron effective width). The theoretical resolution was equivalent to 3 - 3.5 diodes (≈ 0.040 nm), and the array covered an approximate waveband of 8 nm. Experimental measurement of the FWHM gave 0.035 nm using a mercury lamp.

PMT settings and scanning operations were software-controlled (PRISM). The scanning output was a text file processed off-line. The OMA control software WinSpec allowed on-line processing of spectral data (e.g., signal integration over a waveband). Not all WinSpec operations were programmable; in the demonstrations, user input was required for each measurement.

4.2.2 Composition Measurement

Adaptive optimization required fast on-line composition assessment. A simple method was developed for detecting incomplete combustion as inferred by the presence of C_2 molecular fragments. The method used integrated intensity measurements from the OMA in the spectral region of the green C_2 Swan band. A signal-to-continuum ratio was used to assess the relative intensity of the band. Selected wavelength intervals were tested as indicators of Swan and continuum emission. The results of this investigation are presented in section 5.1.2.

4.2.3 Temperature Measurement

The profile of the green Swan band was a function of the statistical temperature associated with molecular rotational movements. As discussed in section 2.1.2.6, the rotational temperature is a good approximation to the mean kinetic temperature in a thermal plasma. Experimental temperature estimates were compared to theoretical estimates. The experimental data were not amenable to an Abel inversion; consequently, the estimated temperature was an average of local values weighted towards regions of strong Swan emission on the optical axis.

4.2.3.1 Temperature Evaluation From High-Resolution Spectra

The green Swan band was free from interference between 513 nm and 515 nm. Slow PMT scans over this region (0.0053 nm steps with an integration time of 1.5 s) gave signal peaks whose full width at half-maximum (FWHM) ranged from 0.020 nm to 0.027 nm. The peaks were P-branch clusters of unresolved triplet lines. They were separated from R-branch triplets down to the background emission level. A propane concentration well in excess of the usual range was needed for Swan signals to exceed background by one order of magnitude. This was explained by the presence of oxygen in the plasma. Given the influence of composition on power dissipation, oxygen was deemed essential to a temperature estimate representative of the conditions during demonstrations.

Boltzmann plots were constructed from the P lines of lower quantum numbers J'' between 46 and 36. The corresponding spectral region was bounded by an argon line past 515 nm and by the $\nu(1,1)$ band head below 513 nm.

The effects of noise on the spectrum were attenuated using the Savitzky-Golay smoothing algorithm. This technique is exactly equivalent to a least-squares polynomial fit procedure. It is formulated as a convolution routine of the moving-average type (Savitzky and Golay 1964). The convolution coefficients are determined by the polynomial order and number of points of the fit. A five-point quadratic average was taken to smooth the spectra without losing P-line resolution.

Peak profiles being uniform in shape, their amplitude (maximum height minus baseline) was usually assumed representative of peak intensity. Alternatively, peak area could be estimated from amplitude (A) and full width at half-maximum (FWHM):

$$I = \sqrt{2\pi} \frac{A(FWHM)}{\sqrt{8(\ln 2)}} \quad (\text{equation 4.2.3-1})$$

4.2.3.2 Temperature Estimates from Unresolved Spectra

This section considers the possibility of estimating temperature from OMA spectra taken during optimization sequences. Simultaneous temperature readings could contribute to the interpretation of destruction efficiency data and to an understanding of the system's behaviour. As an example, Sacchi *et al.* (1996) demonstrated the use of multiple indicators in failure mode diagnostics for an experimental hazardous waste incinerator model. The type of fault responsible for incomplete combustion (flow channelling, insufficient residence time, low temperature, etc.) was successfully identified from a combination of indicators.

As mentioned in section 2.1.2.6, the rotational temperature of a system can be inferred by comparing integrated intensities from two regions of a single vibrational-rotational band. The method compares experimental intensity ratios with theoretical ratios calculated at different temperatures. A computer program was developed to perform a discrete summation of the theoretical intensities of P- and R-branch lines. The program computed intensity ratios for any choice of wavelength intervals.

In the green Swan band, the regions 512.9-516.0 nm and 516.0-516.5 nm are recommended (Bousrih *et al.* 1995). To avoid interference by strong argon lines near 515.1 nm and 516.2 nm, the method was applied to short interference-free wavebands such as 513.0-513.75 nm and 513.75-514.5 nm. The difficulties encountered and results obtained are described in section 5.1.3.2.

Temperature approximation by visual inspection of band profiles - a highly simplified version of the superposition method - was attempted. Experimental

spectra were compared to simulated profiles at different temperatures. This approach is also discussed in section 5.1.3.2.

4.2.3.3 Heat Balance Calculation Tools

Theoretical estimates of the average plasma jet temperature were calculated using a plasma torch simulation program (Hifi23) and a thermodynamic calculation tool (FACT).

Hifi23 is an induction torch simulator developed by members of the Plasma Technology Research Group at the Université de Sherbrooke. Based on equipment specifications and operating conditions (torch dimensions, electrical parameters, gas composition, flow rates, modes of injection, etc.), the program calculates a complete spatial profile of the plasma: temperature, composition, velocity, and electromagnetic characteristics. An average mixing-cup temperature was computed numerically from temperature and velocity profiles at the extremity of the torch, just before the nozzle.

FACT is a commercial thermodynamic database and computation program. It may be used to perform equilibrium calculations and heat balances for chemical reactions. In this project, the energy input required for the plasma to reach a certain temperature was estimated using FACT equilibrium simulations. This heat balance was compared with temperature and dissipated power data from Hifi23 torch simulation results.

4.3 Optimization Techniques and Manual Control

4.3.1 Scaled Variables

The experimental procedure involved four parameters: two manipulated variables (oxygen concentration, plate current), and two dependent variables (efficiency of destruction, operating cost). To simplify the optimization framework, each parameter was normalized on a scale between zero and ten. The normalized parameters were denoted (x_1, x_2) for the manipulated variables, and (X, Y) for the dependent variables. This section explains the basis of the normalizing equations.

4.3.1.1 Manipulated Variables

The available ranges for oxygen concentration and plate current were established empirically. Upper limits were imposed by torch cooling capabilities. Excessive oxygen content and/or current led to torch failure through power dissipation. The lower limit on plate current was the minimum needed to sustain a discharge. The lower limit on oxygen concentration was chosen above zero to maintain the coupling characteristics imparted by a diatomic gas. The system's flexibility range is summarized in Table 4.3.1-1.

In the course of the work, this range proved impractical due to an imbalance in the response of the plasma to oxygen content and to current. The effect of a one-unit change in oxygen content outweighed the effect of a one-unit change in current. Optimization paths were oriented along the axis of the most effective variable. The composition range was therefore modified to balance the scales of the manipulated variables and promote optimization in a two-dimensional space. The range used in the demonstrations is indicated in Table 4.3.1-2.

Table 4.3.1-1: Flexibility Range of the Manipulated Variables

Parameter	Lower limit	Upper limit
Oxygen flow rate (slpm)	1.8	9.8
Oxygen concentration	3.5%	16.5%
x_1 (normalized scale)	0	10
Plate current (A)	3.6	4.6
x_2 (normalized scale)	0	10

Table 4.3.1-2: Operating Space for the Manipulated Variables

Parameter	Lower limit	Upper limit
Oxygen flow rate (slpm)	1.8	5.9
Oxygen concentration	3.5%	10.6%
x_1 (normalized scale)	0	10
Plate current (A)	3.6	4.6
x_2 (normalized scale)	0	10

4.3.1.2 Dependent Variables

The extent of organic compound decomposition was inferred from Swan band intensity, as measured by a signal-to-background optical emission ratio (S/B). The computation of this indicator from spectral data is described in section 5.1.2.1. (S/B) was a relative measure of concentration, whereas destruction efficiency (D.E.) depended on inlet and outlet concentrations. A method for translating (S/B) into absolute concentration was not available (section 5.2.2); D.E. was therefore unknown. To circumvent this problem, the optimization procedure used (S/B), not D.E., to evaluate effectiveness. (S/B) was linked to D.E. in individual optimizations performed at constant input load.

The dependent variables were scaled between zero and ten. For destruction efficiency, a scale ranging from null to complete destruction was not an option. This choice required measuring (S/B) in the absence of destruction - a physically impossible situation in the plasma system. A more practical scale was defined from (S/B) values expected over the operating range of the system. The reference point for the low end of the scale (low destruction) was an upper-bound (S/B) estimate of 1.75. This choice was supported by observations of (S/B) reaching 1.65 under conditions least favourable to decomposition. The top end of the scale was complete destruction as per the detection limit of the optical indicator, where (S/B) equalled one. Thus, the effectiveness parameter X was calculated as:

$$X = 10 + \frac{\left[1.00 - \left(\frac{S}{B}\right)\right]}{0.075} = 23.33 - 13.33\left(\frac{S}{B}\right) \quad (\text{equation 4.3.1-1})$$

With respect to the cost parameter, no attempt was made to calculate the actual costs of the manipulated variables, for two reasons. First, the incremental power consumption corresponding to one plate current unit was not directly measurable. Its closest estimate, based on plate voltage readings, was subject to uncertainty in rectifier/oscillator circuit efficiency. Second, the operating characteristics and costs of the laboratory-scale induction unit were very different from those of an afterburner prototype. The specific costs of the experimental model were irrelevant to the technical feasibility demonstration.

The cost parameter Y was defined in terms of the relative costs of oxygen and plate current units. On a zero-to-ten scale, Y located the overall cost between the minimum and maximum values possible. The zero cost reference point was set at minimum sustaining conditions. The top of the scale corresponded to maximum current and oxygen input. The manipulated variables were assigned fractional weights representing their contributions to the overall cost. By

definition, the fractional weights of current and oxygen added to unity. The cost contribution of each variable was the product of its input setting of by its fractional weight. The cost parameter equation summed the two contributions into an overall cost. Hence, for a given change in destruction efficiency, the economic implications of using one variable over the other were built into the cost parameter.

$$Y = y_1x_1 + y_2x_2 \quad (\text{equation 4.3.1-2})$$

where

- $y_1 \equiv$ fractional weight of one [O₂] unit
- $y_2 \equiv$ fractional weight of one I_p unit
- $x_1 \equiv$ normalized [O₂] setting
- $x_2 \equiv$ normalized I_p setting
- $y_1 + y_2 = 1$ (by definition)

Examples

- a) Units of [O₂] and I_p have equivalent costs: $Y = 0.50x_1 + 0.50x_2$
- b) One [O₂] unit costs twice as much as one I_p unit: $Y = 0.67x_1 + 0.33x_2$
- c) One [O₂] unit costs three times as much as one I_p unit $Y = 0.75x_1 + 0.25x_2$

In an application, economic circumstances would dictate appropriate weights y_1 and y_2 . In the demonstrations, case (c) was most frequently assumed. As mentioned in section 4.3.1.1, the plasma responded more strongly to oxygen than to plate current. Forcing an economic incentive in favour of current helped balance the contributions of each variable to the optimization. The choice of fractional weights was arbitrary and did not affect the validity of the demonstration.

4.3.2 Objective Functions

The goal of optimization is to identify the conditions that best meet the objectives of a process. In practical terms, a progression towards optimal conditions is measured by a numerical criterion. This criterion may correspond to a single variable, such as the yield of a chemical reaction. It may depend on multiple variables, as in the present study. In APAI, the objective is to balance cost and destruction efficiency. The performance criterion is a function of these variables.

The mathematical expression of this criterion is called the **objective function**. It quantifies performance for all possible combinations of efficiency and cost. For example, in waste destruction, efficiency may take priority over economy up to a certain target beyond which the system is said to over-treat and cost becomes important. In this situation, the combination "adequate D.E./low cost" maps to a high objective function value. D.E. levels well below the target give low values irrespective of cost. Over-treatment is assigned a low value when obtained at high cost. Targets, priorities and trade-offs determine the form of the objective function.

The objective function was visualized as a three-dimensional continuous surface over the domain defined by the two dependent variables. Combinations that ranked equivalently by the function formed isometric contours on the surface. Figure 4.3.2-1 is a three-dimensional view of the objective function used in the demonstrations. Figure 4.3.2-2 is a two-dimensional contour plot of the same surface. In keeping with the scaling method adopted for manipulated and dependent variables, the objective function was designed to take values between zero (least desirable conditions: poor destruction at maximum possible cost) and ten (best possible conditions: complete destruction at minimum possible cost). The development of this function is described in section 5.3.1.

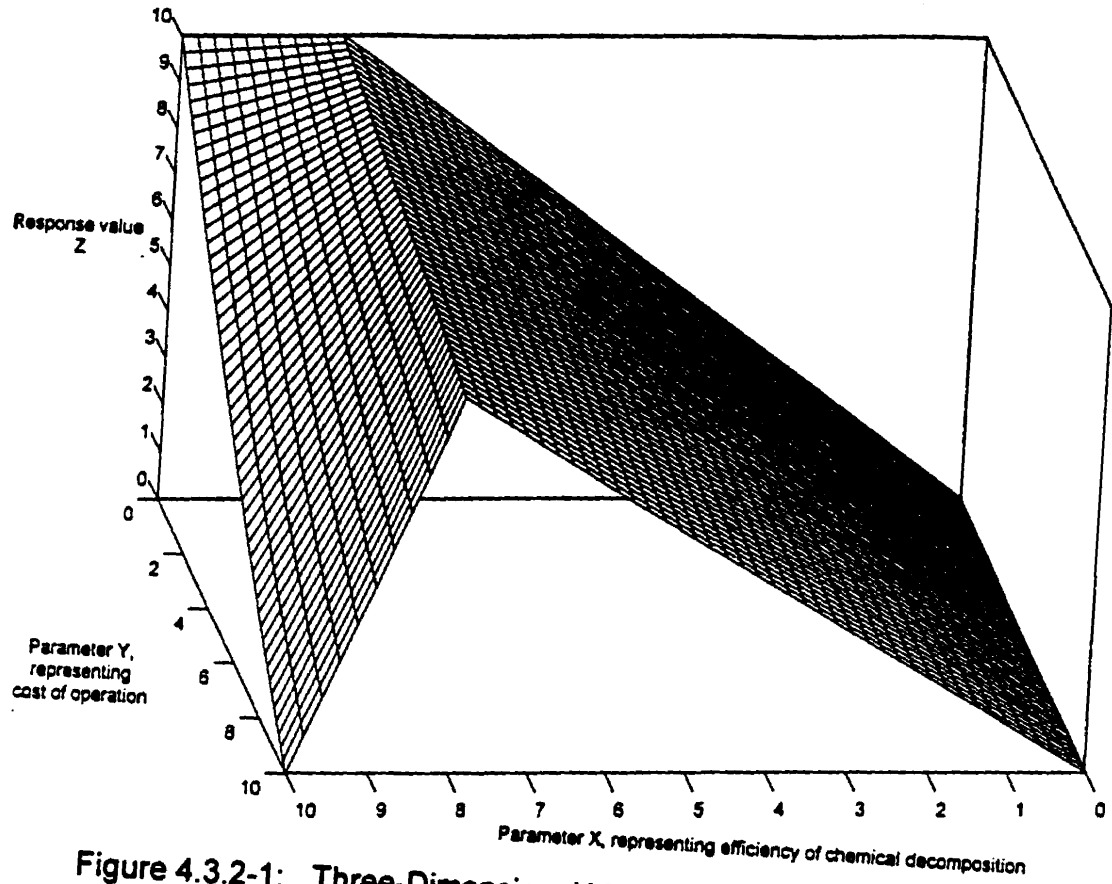
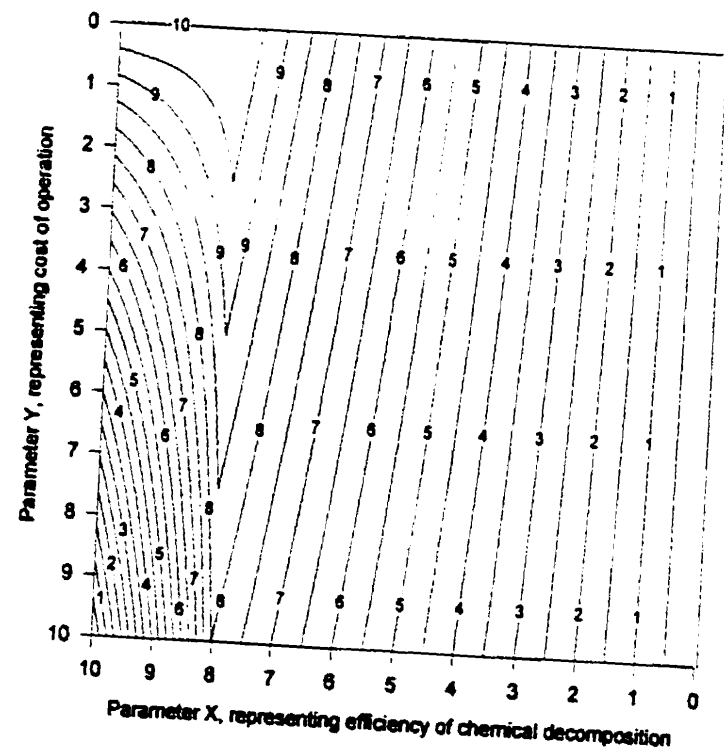


Figure 4.3.2-1: Three-Dimensional View of the Objective Function

Figure 4.3.2-2:
Contour Plot
of the Objective Function



4.3.3 Optimization Programs

As discussed in section 4.1, the experimental system was closer to a "black box" than to a well-defined process. No model described the combined effects of input variables and external factors. Modeling the composition profile and emission patterns of an induction plasma is feasible, but requires extensive computations that integrate thermodynamics, heat and mass transfer, chemical kinetics, and fluid dynamics (Mostaghimi *et al.* 1985, Soucy *et al.* 1994, Zhao *et al.* 1990). The complexity of the problem increases with the number of species present. Even in simple one- or two-gas systems, simultaneous solution of the model equations presents numerical difficulties (Proulx 1995). The development of such a model was beyond the scope of the present project, considering the uncertainty in equipment characteristics and the large number of chemical species. Furthermore, a model of the laboratory equipment would be inapplicable to a pilot-scale dc plasma afterburner prototype.

Among the optimization techniques available, two were selected: a gradient-based method and the Simplex algorithm. These methods complemented each other in aspects deemed important for this application: simplicity (number of parameters, number of measurements, computational requirements); noise sensitivity (e.g., use of differentials); and robustness to system instability (i.e., independence from past measurements). Visual Basic 4.0, an object-oriented programming tool, was used to develop executable graphical-interface programs for optimization by gradient-based and Simplex methods.

User interfaces were similar in all programs. The main window reproduced a control panel. It displayed the operating parameters, optimization settings, sequence history, and contained command "buttons" for user control. During the initialization procedure, the user entered initial manipulated variable settings, objective function value, and optimization parameters. A sequence of optimization steps brought the system to optimal conditions according to the

objective function. At each step, new settings were calculated by the program and implemented by the user. Once the system had stabilized at the new conditions, the program asked for a reading of the response. User intervention was required for spectroscopic measurements and calculation of the destruction efficiency parameter. The efficiency and cost parameters were translated into an objective function value using a programmed calculator.

4.3.3.1 Gradient-Based Program

A preliminary version of this program was limited to the basic rules of the steepest ascent strategy outlined in Appendix VIII. Each step in a sequence involved a gradient computation, and no strategy adjustment was made in the course of the sequence.

The computational procedure was the following. First, the program tested the effects of incremental changes in each manipulated variable. From this information, it calculated the direction of the gradient in the domain defined by the variables. The program then specified the coordinates of the next point along the line of the gradient. If the calculated point fell outside the range of a variable, the new point was placed at the boundary of the space along the line of progression. A message was then displayed to inform the user of which variable was at its upper/lower bound.

If the surface appeared too flat to expect a significant improvement from a move, the program informed the user that no change in operating conditions was justified. The decision to recommend a move or not was set by a minimum threshold on expected response improvement, as predicted from the gradient. A 5% threshold was chosen to match the error in objective function value (see section 5.3.3.2 for error analysis). The program kept a record of current and past operating points which could be saved in text form. The user could modify the current settings and conditions if necessary.

The simple and repetitive structure of the steepest ascent strategy implied time-consuming progressions and limited precision in locating an optimum. To improve flexibility and efficiency, the program was upgraded to offer *optimal gradient* and *gradient prediction* strategy options. The upgraded version also featured automatic or manual step size adjustment, retraction following unsuccessful moves, and identification of near-optimum conditions through response history analysis.

The structure of the program was unchanged, with the exception that surface exploration and gradient computation were not systematically performed at each step. The progression proceeded in the same direction until results showed a need for re-orientation. The difference between the *optimal gradient* and *gradient prediction* strategies was the criterion for re-directing the search. In optimal gradient, the criterion was a decrease in response value. In gradient prediction, it was a deviation from the response predicted by the gradient: if a response fell outside a window around the expected value, the gradient was no longer accurate and a re-evaluation was recommended. A window of $\pm 20\%$ was chosen empirically.

Scale factor adjustment

The scale factor adjustment procedure was also empirical. The scale factor determined the step size. Its default value was 2; its minimum was 1.5. (For reference, a unity scale factor produced a move of the size of the incremental steps taken to calculate the gradient.) The step size must not exceed the range of validity of the linear surface model.

A decrease in response just following a gradient evaluation suggested too large a scale factor; this triggered a reduction of the scale factor by a user-set interval (e.g., 0.5). Conversely, a decrease in response when proceeding in the same

direction could simply indicate a need for re-direction; the scale factor was left unchanged.

When the response increased, the decision depended on the ratio of the change in the last step over the change in the preceding step. A low ratio (below 0.5) suggested a “flattening” of the surface, possibly an optimum; the scale factor was decreased to narrow the search. A high ratio (above 1.5) meant growing improvement in response; the scale factor was increased to accelerate progression in the favourable direction. This algorithm did not apply in the vicinity of an optimum (described shortly), where similar responses could create misleading variations in the ratio of the last response changes.

In cases where none of these rules applied, a marked departure from linearity triggered a reduction in scale factor. If a response fell outside a 30% window around the expected value, the scale of the move exceeded the range of validity of the linear approximation.

Retraction

When a move in the same direction as the previous one was unsuccessful, a full or half step back (user's choice) was implemented. The optimization step ended with a reading of the response at the new point.

Vicinity of an optimum

When changes in the response remained below a threshold and system performance was satisfactory, the progression was assumed to have reached the vicinity of an optimum. An instance of near-optimal operation was defined by three conditions: (1) at least three steps had been taken in the sequence; (2) the response had changed by less than 5% over the last two steps (the threshold was the error in objective function value); and (3) the current operating point satisfied a minimum response value ($Z=8$ in the demonstrations). When all three conditions were met, the user was informed and decided on a course of action:

to continue the search on a finer scale, or to end the sequence at the point of highest response.

4.3.3.2 Simplex Program

The Simplex program worked in a similar fashion as the gradient-based program, using the rules listed in Appendix IX to determine settings for the next point.

During the initialization procedure, the user set three initial vertices. Subsequent points were geometrically determined from the current vertices of the Simplex and their response values. Step size followed from the positions and ranking of vertices. The expansion coefficient, a step size parameter, intervened in the expansion case. Its default value was 2; its minimum was 1.5. (For reference, a unity coefficient superimposed the expansion point on the reflection point.) The geometric procedure did not lend itself to automatic step size adjustment. The expansion coefficient was modified by the user as needed.

If the Simplex extended beyond the range of the manipulated variables, the new point was placed at the boundary along the line of progression. The program displayed a warning, reduced the expansion coefficient by a fixed interval (e.g., 0.1), and modified the rules to prevent further expansion.

Unsuccessful reflections were automatically corrected by the contraction rule. In the case of unsuccessful expansion, the user could retain the reflection point instead of the expansion point. This option is not part of the standard Simplex algorithm, but was added as a means to narrow the search near an optimum.

The response surface could change over time. To cover the possibility that previous points were no longer valid, a command button on the control window allowed the user to check the response at any point, including those retained in

the Simplex. If the response at a point had dropped by more than 10%, re-initialization was recommended.

Instances of near-optimal operation were governed by the same criteria and procedure as in the gradient-based program.

4.3.4 Manual Control Loop

The plasma generator and its gas flow console were operated manually. The oxygen feed was set using a high-precision flowmeter and valve, while DC plate current was adjusted through the generator's power control knob. Changes in manipulated variables occurred at long intervals compared to the system's response time. Steady state was assumed for all measurements.

Figure 4.3.4-1 is a diagram of the manual feedback control loop. The time required to make an optical measurement, interpret the result, enter this information into the optimization program and implement a new set of conditions was of the order of three to five minutes.

4.3.4.1 Optimization Sequence Procedure

The following sequence of steps integrated the variables, programs and loop structure just described into a demonstration of adaptive operation.

Optimization Procedure

- 1) Set the feed of model compound and implement initial settings within the operating space of the manipulated variables (oxygen concentration, plate current).

- 2) Take optical measurements and calculate values for the efficiency parameter (X), cost parameter (Y), and objective function ($Z = f(X, Y)$). Locate the starting point on the response surface. This point simulates process conditions immediately following a disturbance.
- 3) Apply an optimization technique to determine the next input settings. Implement the settings recommended by the program and allow the system to stabilize at its new conditions.
- 4) Take optical measurements; calculate X-, Y- and Z-values.
- 5) Determine whether an optimum has been reached. If not, return to step 3; otherwise, terminate the sequence.

Continuous adaptive operation was simulated by a train of consecutive optimization sequences. Step 1 was replaced by a change in model compound load under fixed oxygen and current settings or, alternatively, by a change in settings under a fixed load. Either case created a process disturbance.

This sequential approach could apply to a continuous process. The optimization procedure would be nested in an iterative loop that took control when an optimum was reached. The outer loop would periodically monitor for changes in system performance, and initiate a sequence when needed. In the demonstrations, the outer loop functions were performed by the user. First, the destruction efficiency was set off-target by a disturbance in feed load or plasma conditions. A sequence was then initiated manually.

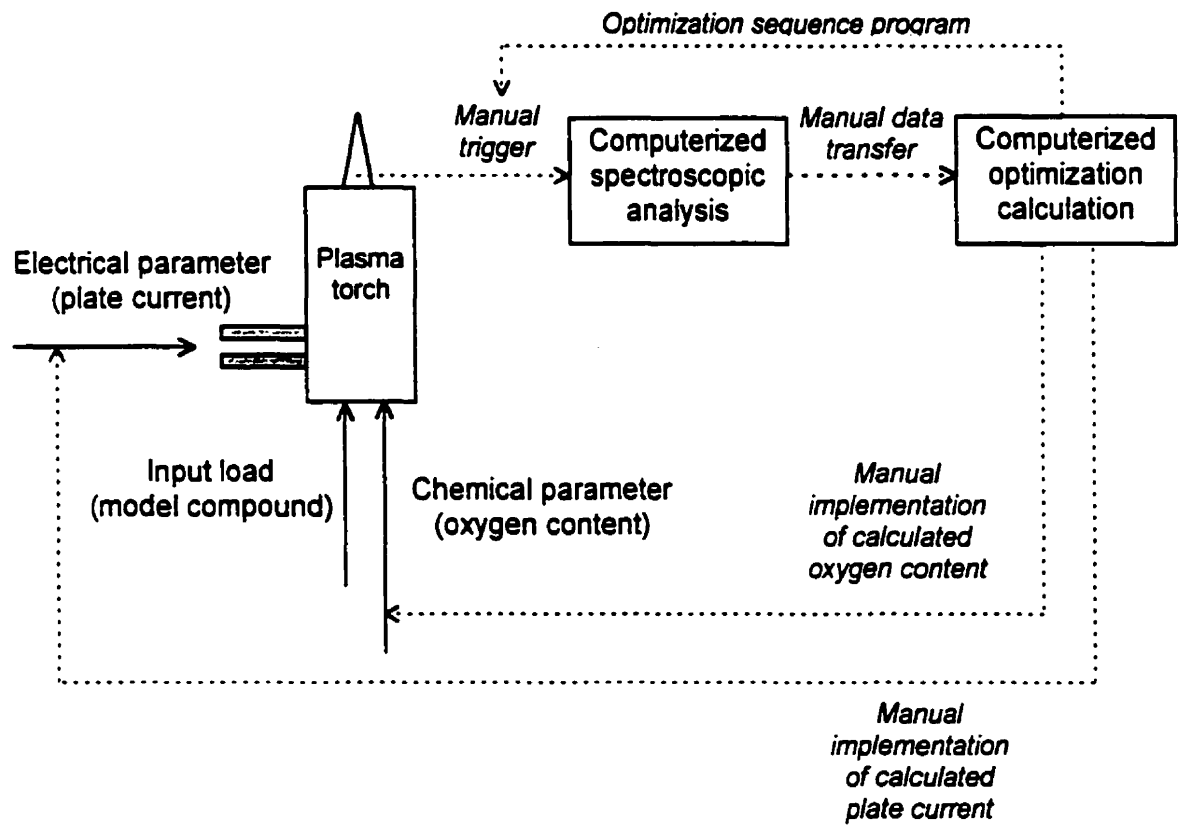


Figure 4.3.4-1: Manual Feedback Control Loop

5. RESULTS AND DISCUSSION

The results are grouped into three sections: optical diagnostic of composition and temperature, characterization of the afterburner model system, and experimental demonstration of an optimization strategy for cost-efficient operation.

5.1 Optical Diagnostics

5.1.1 Spectrum Numerical Simulation

To facilitate the interpretation of experimental emission spectra, theoretical reference spectra were generated from first principles. The $d^3\Pi_g \rightarrow a^3\Pi_u$ Swan band of C_2 was simulated numerically using equations described in Appendices I and III. The theoretical spectra were used to identify band components in measured spectra and to study the influence of temperature on the band profile.

Figure IV-A (Appendix IV) results from a rigorous simulation of P-branch line intensities using the general equations reported by Phillips (rotational energy levels, wavenumbers) and Kovács (line strengths). It is a discrete spectrum where each emission line is represented by a point. Figure IV-B represents the same line intensities as a function of the rotational quantum number instead of wavelength. Figures IV-A and IV-B cover the whole band, while Figures IV-C and IV-D focus on the region of interest for temperature estimation. Figure IV-E shows the correspondence between the quantum numbers and wavelength of P-branch triplet components. In an experimental spectrum, components at closely spaced wavelengths (in groups of three) are detected as a single emission line.

Band simulation from the general equations is computationally intensive. It is common practice to use simplified forms of the equations in certain regions of

their domain (Budó 1937, Herzberg 1950, Phillips 1968). These close approximations are generally adequate for diagnostic purposes. Their applicability was verified by comparing line strengths and rotational energies obtained from the exact method and from Herzberg's simplified formulae (Figures IV-F and IV-G). The values matched closely over the quantum number range of interest ($J' = 34 - 48$). Simplified formulae were applied in subsequent calculations.

A complete simulation of the band, including components of the P, Q and R branches, was programmed by Karen Sum of the Plasma Technology Research Group at McGill University. The MATLAB program could simulate measured spectra by convolving discrete spectra with an apparatus function. The function was modelled by a normal distribution curve with user-specified full width at half maximum (FWHM). Appendix V includes a collection of spectra simulated for different temperatures and apparatus functions. The Fortrat diagram (Figure V-A) was a useful reference for identifying components in the experimental spectra.

5.1.2 Composition Assessment

Figure 5.1.2-1 shows the green emission spectrum of an analytical-scale (2 kW) inductively coupled argon-propane plasma (ICP). The $\nu(0,0) d^3\Pi_g \rightarrow a^3\Pi_u$ Swan band of C_2 (band head located at 516.5 nm) was prominent in the absence of oxygen. Spectra from the afterburner model plasma (25 kW), with and without oxygen, appear in Figure 5.1.2-2. Swan bands were distinguished from other emission features of the plasma by referring to a blank spectrum without organic compound, as in Figure 5.1.2-3.

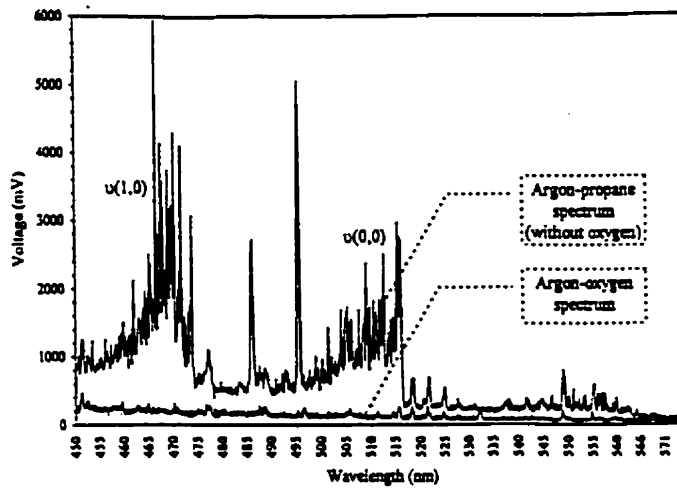


Figure 5.1.2-1:
Plasma Emission Spectrum
in the Swan Band Region

(1.5 kW ICP, 0.3 ml/s
Propane in Argon)

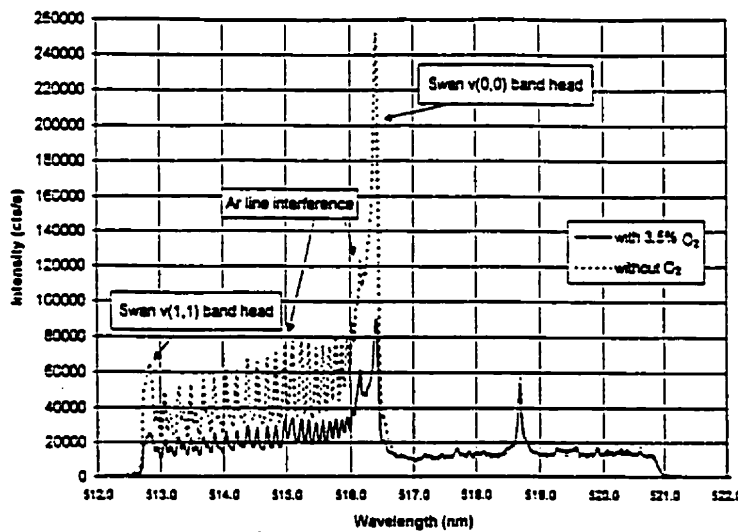


Figure 5.1.2-2:
Afterburner Model Plasma
Emission Spectra

($I_p = 3.8$ A, 0.3% C_3H_8)

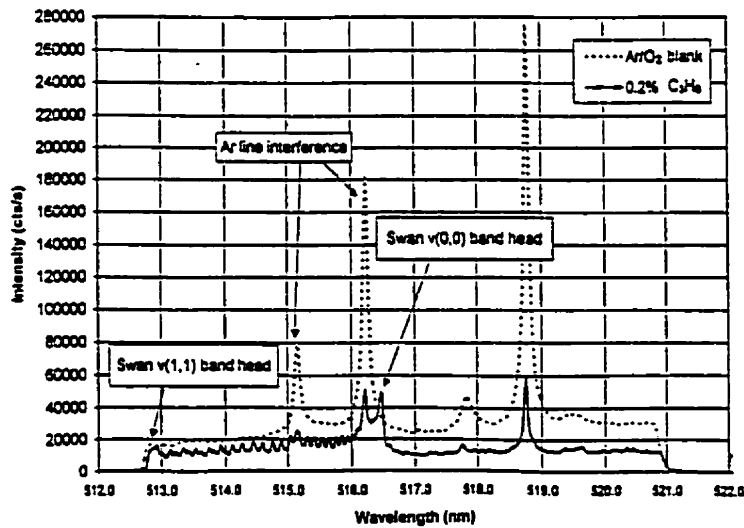


Figure 5.1.2-3:
Swan Band Signal
and Blank Spectra

(3.5% O_2 , $I_p = 3.8$ A)

5.1.2.1 Selection of Spectral Indicators

The effects of oxygen and power on Swan emission intensity are apparent in Figures 5.1.2-4 to 5.1.2-7. The first two figures are medium-resolution spectra from a preliminary study using a low-power (2-kW) analytical ICP. The spectra in Figures 5.1.2-6 and 5.1.2-7 were measured from the afterburner model system. In all cases, an increase in power or oxygen input caused a reduction in Swan band intensity.

Optical emission measurements included three contributions: the Swan band spectrum of C_2 , the spectrum of the argon-oxygen plasma, and the thermal emission continuum (the dark signal was subtracted automatically). The spectrum could have included features emitted by model compound by-products other than C_2 . However, no such structure was identified in the waveband of interest. Figures 5.1.2-8 and 5.1.2-9 present blank spectra (plasma and continuum emissions) measured by the photodiode array (OMA).

Both continuum and argon emissions varied in intensity with plasma conditions. As they originate from different mechanisms, these emission features do not vary proportionally. This is verified in Table 5.1.2-1. In such situations, a standard procedure for isolating an analyte signal is to subtract a blank spectrum measured under identical conditions. In the present case, such identical conditions could not be achieved because of poor operational reproducibility and of the effects of propane on the plasma.

Attempts to isolate Swan signals by subtracting continuum and argon features separately were unsuccessful due to uncertainty in peak area estimation. The procedure was the following. A straight line joining featureless regions at 513 nm, 517 nm and 520 nm was taken as the continuum baseline (Figures 5.1.2-8 and 5.1.2-9). After subtraction of this baseline, emission intensity was integrated over the Swan band region. The area of each interfering argon peak was

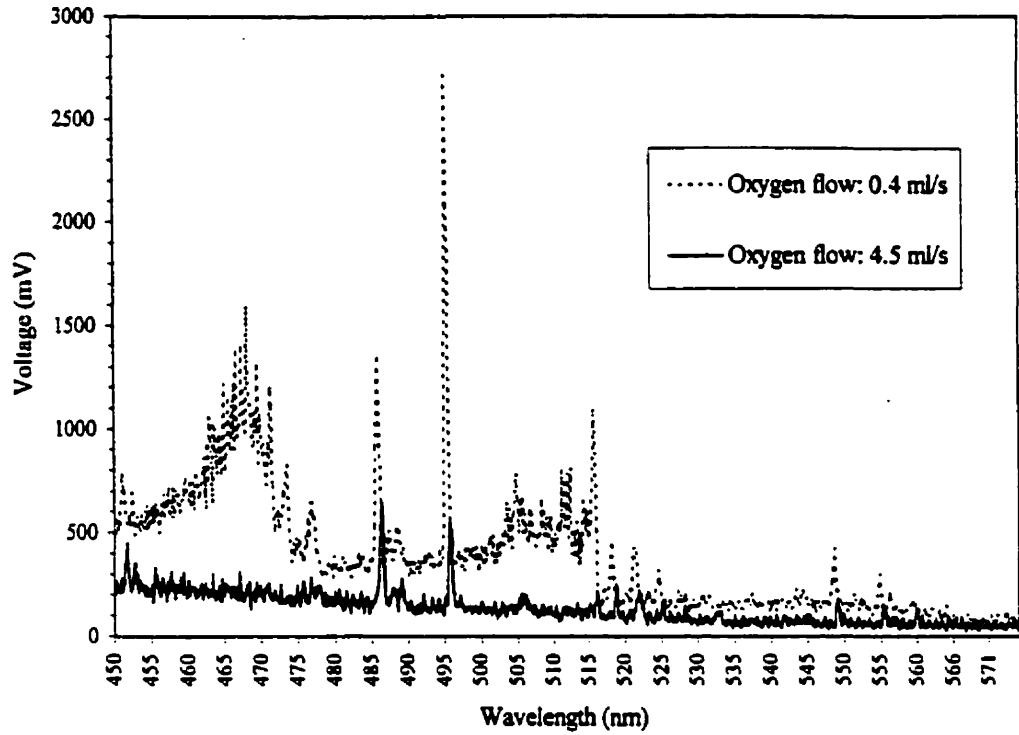


Figure 5.1.2-4: Effect of Oxygen Content on Swan Band Emission

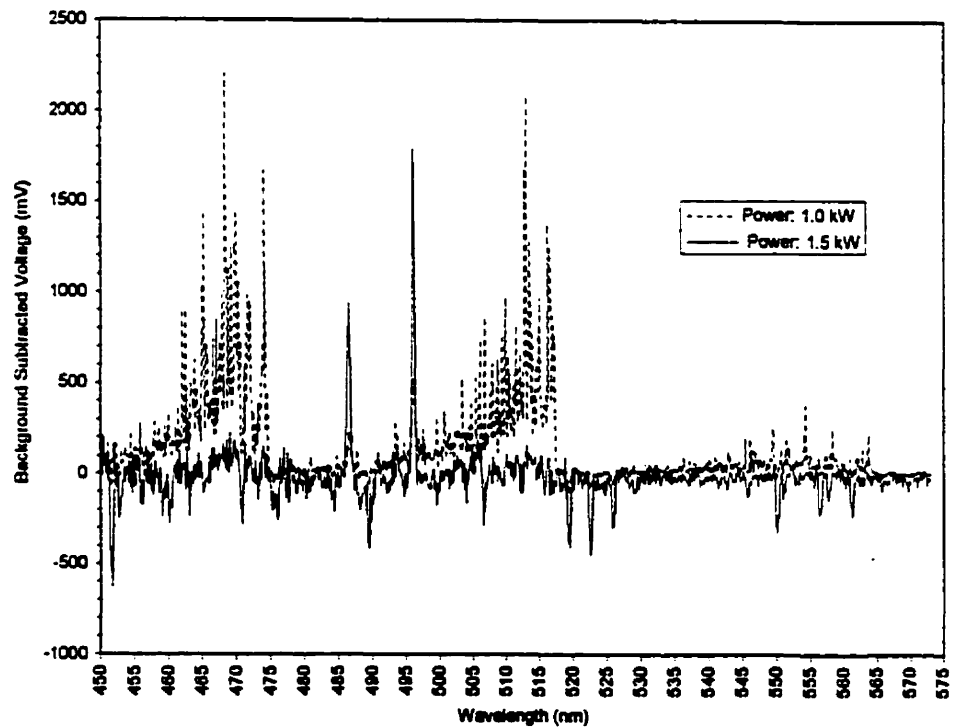


Figure 5.1.2-5: Effect of Power on Swan Band Emission

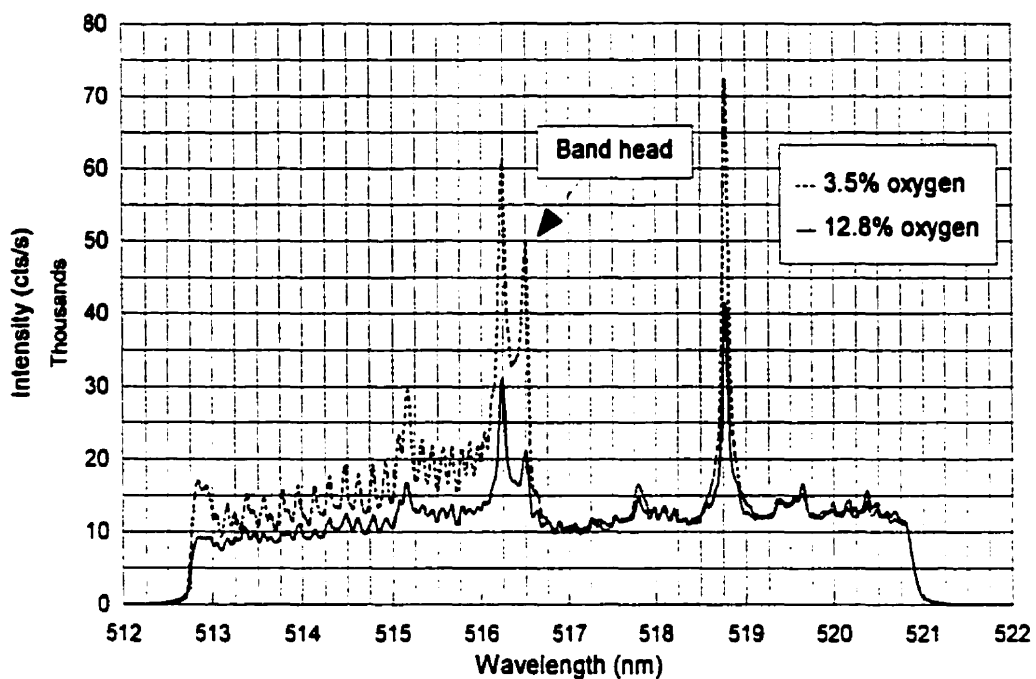


Figure 5.1.2-6: Effect of Oxygen Content on Swan Band Emission
(0.3% propane, 3.8 A plate current)

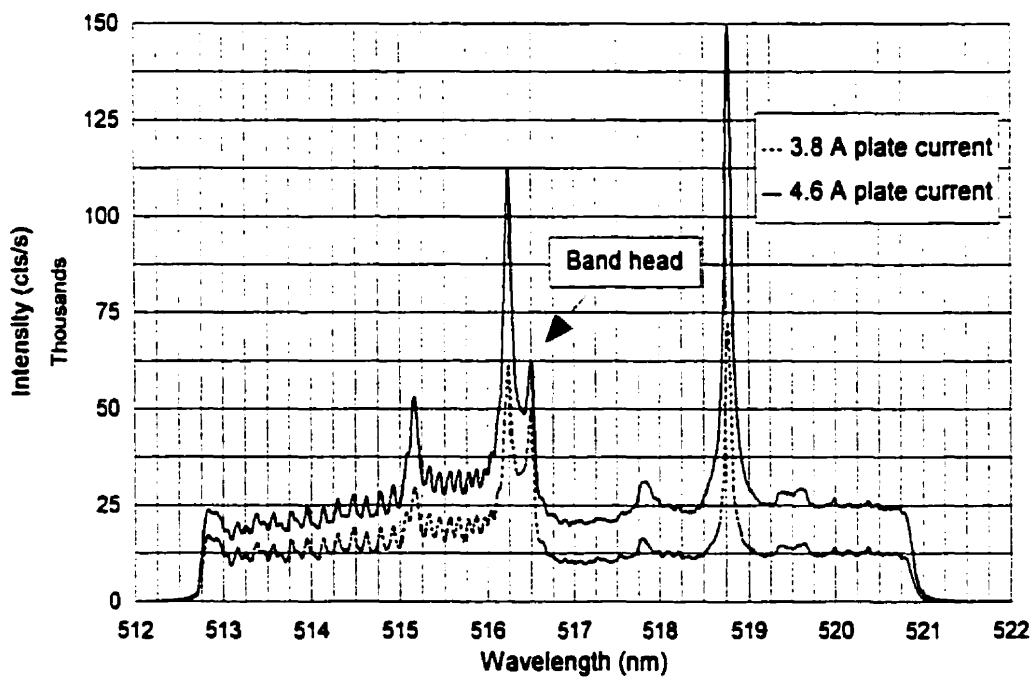


Figure 5.1.2-7: Effect of Plate Current on Swan Band Emission
(0.3% propane, 3.5% oxygen)

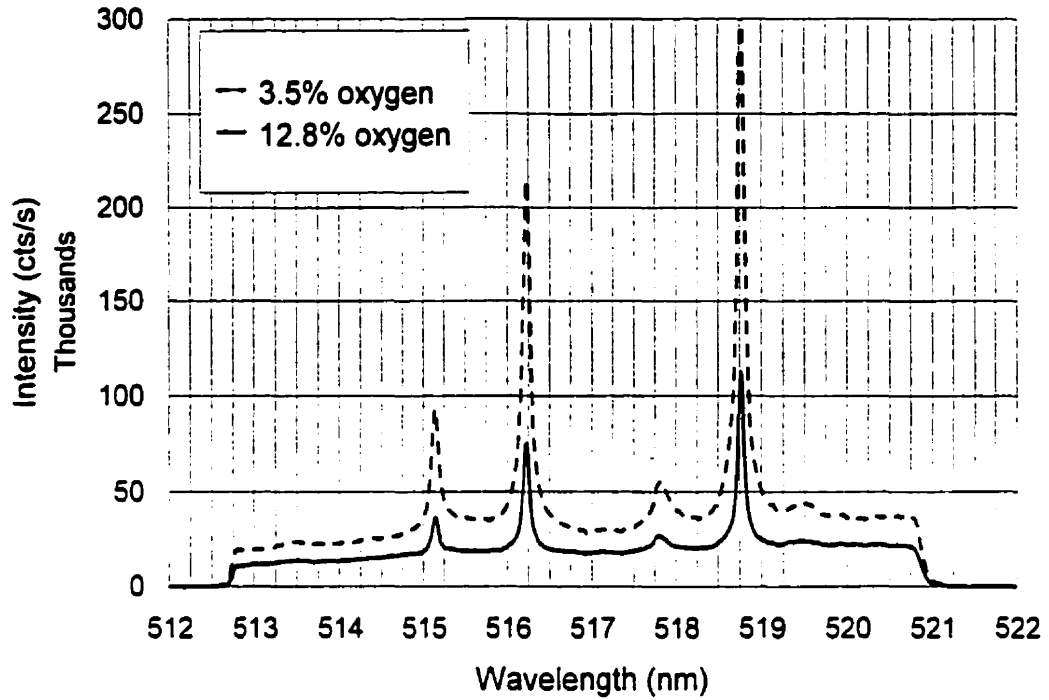


Figure 5.1.2-8: OMA Blank Spectra at Low Power
(3.8 A plate current)

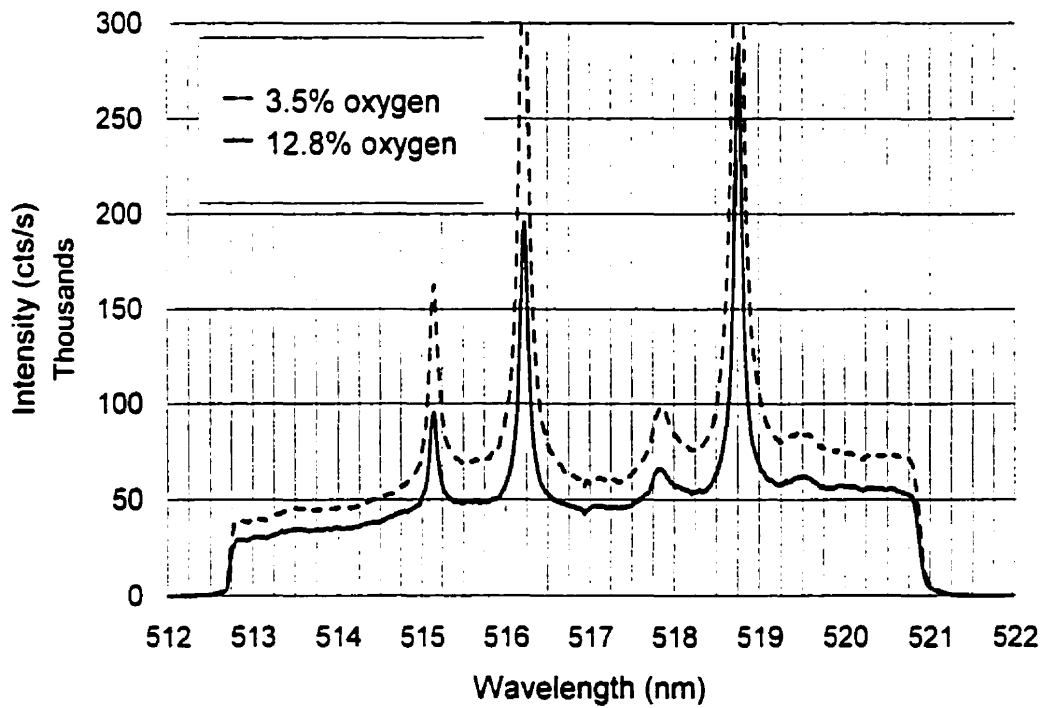


Figure 5.1.2-9: OMA Blank Spectra at High Power
(4.6 A plate current)

estimated from its height, and Swan band intensity was calculated by difference. Peak areas were subject to large errors: transitions between continuum and peak shoulders were unclear and broadened lines were unresolved, as in Figure 5.1.2-9 near 515.5 nm and 518.2 nm. Consequently, this method of isolating Swan signals was felt to be inaccurate.

Table 5.1.2-1: Comparison of Continuum and Argon Emission Intensities

(A)	% O ₂	A Argon at 515.16 nm	B Argon at 516.23 nm	C Continuum at 520 nm	A/C Ratio	B/C Ratio
3.8	3.5	26	72	14	1.9	5.1
3.8	3.5	31	84	16.5	1.9	5.1
3.8	12.8	7.5	21	8	0.94	2.6
3.8	12.8	9.5	26	10	0.95	2.6
4.6	3.5	38	(105)	24.5	1.6	4.3
4.6	12.8	19	52	19	1.0	2.7

An alternative procedure was developed to monitor Swan band intensity. This method presented three advantages: (1) it was rapid and easily implemented on-line; (2) it avoided spectral regions where argon interfered; and (3) it compared each signal to a background reference measured simultaneously. The main limitation of the method was that it assumed proportional variations in Swan and continuum emissivity with changes in plasma conditions. As a consequence of this limitation, no fixed calibration could be established between signals and absolute C₂ concentrations. The procedure did not provide an exact measure of composition but was adequate for the demonstrations. It worked as follows.

Two wavebands were selected: "S" for *signal* and "B" for *background*. The S indicator was the integrated emission intensity over an interference-free region of the green Swan band. The B indicator was the integrated emission intensity over a region of the continuum. (To compare S and B on a common basis, the intensity of each region was divided by the bandwidth.) The regions were close

enough to assume proportional continuum variations. Since continuum intensity was a function of wavelength, B did not equal the background contribution to S; i.e., the ratio (S/B) did not equal unity in the absence of C_2 . A correction was applied to rectify this: B was multiplied by the ratio of continuum emissions in the S and B regions of a blank spectrum. After correction, B represented the background at the signal location. Hence (S/B) was the total signal over its background component. By definition, this corrected ratio equalled one in the absence of Swan emission, and was greater than one otherwise.

Two possible sets of S and B regions were studied: 509.5 - 511 nm (S1), 516.9 - 517.3 nm (B1), 513.1 - 514.6 nm (S2), and 519.8 - 520.3 nm (B2). Both (S1/B1) and (S2/B2) responded to the manipulated variables as would C_2 concentration: they decreased in value with increasing power and/or oxygen input. The background regions avoided minor features that could interfere with background measurement, for example those found at 517.8 nm and 519.2 - 519.7 nm.

S2 and B2 were selected as indicator regions. S2 was preferred over S1 for its higher signal. Whereas B2 appeared flat and clean, B1 was possibly exposed to interference by the shoulders of adjacent argon peaks. Hence the indicator regions were defined as 513.4 - 514.4 nm for S and 519.8 - 520.3 nm for B. Figure 5.1.2-10 delineates these regions in the spectrum.

Table 5.1.2-2 shows the indicator ratio and its relative standard deviation (RSD) at different input conditions and propane loads. The first column of data contains blank measurements (0.0% propane). Overall, the ratio had a standard deviation of the order of 1%. Table 5.1.2-3 presents the results of a time-stability test at fixed input conditions. Measurements spaced in time had standard deviations similar to those of rapid consecutive measurements (Table 5.1.2-2). Hence any drift in the ratio was within uncertainty.

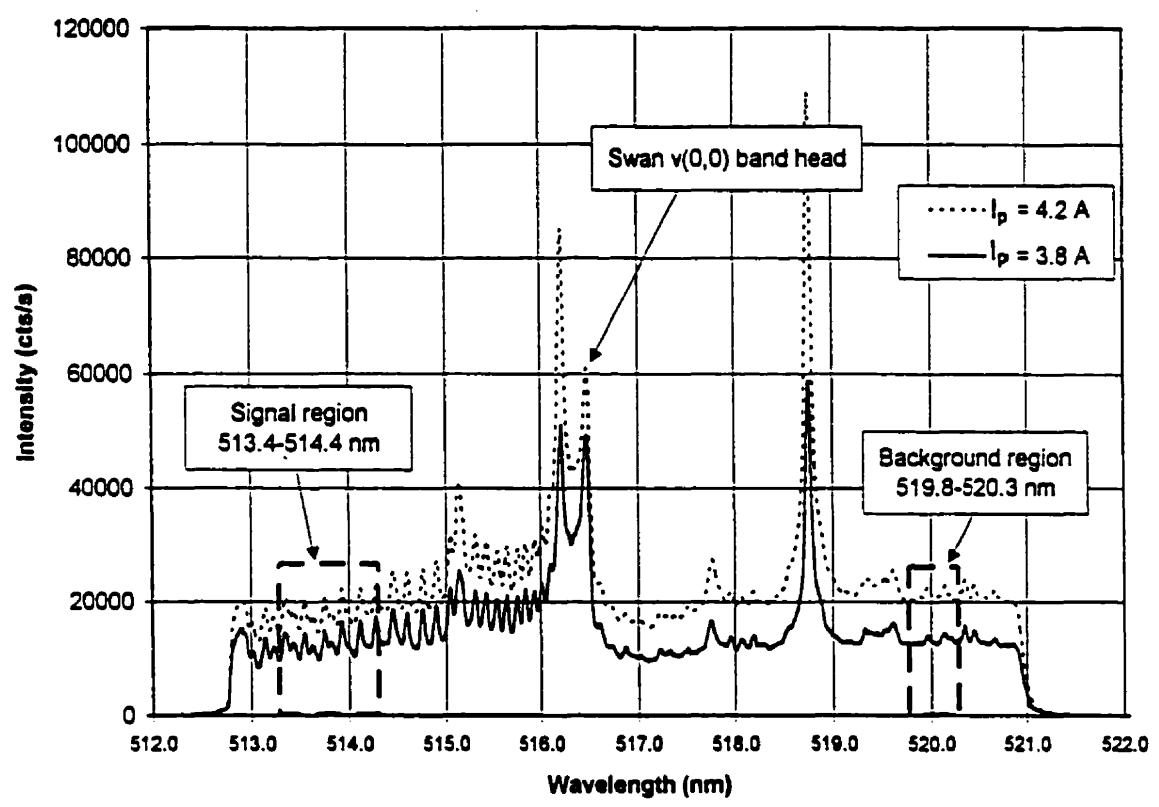


Figure 5.1.2-10: Swan Band Spectra with Selected Indicator Regions
(3.5% Oxygen, 0.2% Propane)

Table 5.1.2-2: (S/B) Indicator and Its Relative Standard Deviation *

C ₃ H ₈		0.0%		0.1%		0.2%		0.3%	
I _p (A)	% O ₂	S/B	RSD	S/B	RSD	S/B	RSD	S/B	RSD
3.8	3.5	1.00	0.3%	1.08	0.7%	1.32	1.1%	1.65	1.1%
3.8	12.8	1.00	0.6%	1.03	1.3%	1.10	1.1%	1.20	0.8%
4.6	3.5	1.00	0.3%	1.05	0.7%	1.16	0.8%	1.36	1.1%
4.6	12.8	1.00	0.4%	1.02	0.5%	1.07	0.8%	1.12	0.6%

* There were three replicates of each measurement.

Table 5.1.2-3: Ten-Minute Stability Test for the (S/B) Indicator *

C ₃ H ₈		0.15%			0.20%		
I _p (A)	% O ₂	S/B	Std dev.	RSD	S/B	Std dev.	RSD
3.6	3.5	1.28	0.010	0.8%	1.47	0.012	0.8%
3.6	7.2	1.14	0.007	0.6%	1.25	0.011	0.9%
4.1	3.5	1.13	0.003	0.3%	1.24	0.010	0.8%
4.1	7.2	1.09	0.003	0.3%	1.15	0.002	0.2%

* Six replicates of each measurement were taken over the ten-minute period.

The assumption of fixed proportionality between continuum emission levels in the two regions was verified: the blank ratio equalled one across the operating range. The correction factor applied to B (the continuum ratio between the regions) had a value of 0.62 and was reproducible from run to run. The correction factor was checked periodically throughout the experimental work; sample test results appears in Table 5.1.2-4a. The correction factor also applied off-centre of the plasma jet (Table 5.1.2-4b). This showed that the indicator ratio was not sensitive to changes in the size and shape of the plasma jet.

Table 5.1.2-4a: Periodic Test of the Proportionality of Continuum Emission

I _p (A)	% O ₂	Blank continuum ratio			Average
3.8	3.5	0.626	0.622	0.626	0.624 = 0.62
3.8	12.8	0.622	0.622	0.618	0.621 = 0.62
4.6	3.5	0.614	0.614	0.616	0.615 = 0.62
4.6	12.8	0.622	0.620	0.620	0.621 = 0.62

Table 5.1.2-4b: Continuum Ratio Off-Centre of the Jet

I_p (A)	% O ₂	Blank continuum ratio	RSD
3.8	3.5	0.64 *	0.6%
3.8	12.8	0.62	0.5%
4.6	3.5	0.62	0.2%
4.6	12.8	0.62	0.1%

* Low plasma intensity caused severe flicker at the observation point.

5.1.2.2 Uncertainty in the Spectral Indicators

The light transmission and detection procedure was not a dominant source of error. The position of the spectrometer grating was reproducible. Drift in the correspondence between wavelength and photodiode array pixels was negligible (up to one pixel out of 700 within an experiment). Because the indicator was a ratio of intensities measured simultaneously from a single source, it was insensitive to flicker, as well as to variations in detector response or light transmission efficiency.

For the data sets presented so far, input settings were not changed between replicate measurements. In Table 5.1.2-2, the average relative standard deviation of the indicator was 0.8%. If one excluded the data at 0.3% propane, which was outside the range of optimization experiments, the average standard deviation was 0.7%.

During optimization experiments, variability in input settings could contribute to the uncertainty in (S/B). To assess the reproducibility of input settings, replicates were taken in a randomized order over a range of settings. The test was jointly performed by the two students who participated in the experiments. Table 5.1.2-5 summarizes the results. Variability due to input settings did not exceed

variability in optical properties at fixed settings: the RSD remained of the order of 1%, averaging 0.7%.

Table 5.1.2-5: Randomized Replicates of (S/B) Readings *

C ₃ H ₈		0.0%		0.1%		0.2%	
<i>i_p</i> (A)	% O ₂	S/B	RSD	S/B	RSD	S/B	RSD
3.8	3.5	1.00	0.6%	1.11	0.7%	1.42	0.7%
3.8	12.8	1.00	0.6%	1.04	0.8%	1.11	1.1%
4.6	3.5	1.00	0.4%	1.06	0.3%	1.21	1.1%
4.6	12.8	1.00	0.6%	1.02	0.6%	1.08	1.0%

* There were three replicates of each measurement.

In analytical chemistry, the **detection limit** (D.L.) is the smallest detectable quantity of an analyte. Described numerically, it is the concentration at which the signal equals the standard deviation of the blank (s_{bk}) multiplied by a confidence factor k (Ingle and Crouch 1988).

$$D.L. \text{ or } C_{DL} = \frac{ks_{bk}}{m} \quad (\text{equation 5.1.2-1})$$

In this equation, m is the slope of the calibration curve. The absolute standard deviation of the blank is used, since that of the signal may be a function of the signal itself. The confidence factor is generally assigned a value of 2 or 3. Assuming a normal error distribution, $k = 3$ corresponds to a 99.73% probability of measurement accuracy within the detection limit; with $k = 2$, the confidence level is 95.45%.

By analogy, a limit of detectable change was defined for (S/B). The minimum significant change or error in (S/B) was assumed equal to a confidence factor times the standard deviation.

$$\Delta(S/B)_{\min.} = ks_{(S,B)} \quad (\text{equation 5.1.2-2})$$

The minimum detectable change was expressed in relative terms, so the relative standard deviation of either signal or blank measurements could be used. From Tables 5.1.2-2 and 5.1.2-5, a conservative RSD value of 1% was assumed. At the chosen confidence level of 95.5%, the relative error in (S/B) was 2% at worst.

$$\frac{\Delta(S/B)_{\min.}}{(S/B)} = k \left(\frac{s_{(S/B)}}{(S/B)} \right) = 2 * (1\%) = 2\% \quad (\text{equation 5.1.2-3})$$

5.1.2.3 Correlation Between C₂ Concentration and Swan Band Emission

An important point to address was whether the absence of Swan emission implied the absence of C₂ molecules. For (S/B) to indicate destruction efficiency, Swan emission by excited species had to correlate with the population of C₂ in the ground state. Furthermore, the temperature at the observation point had to be sufficiently high for vibrational-rotational excitation to occur.

The literature documents the use of Swan band emission to measure rotational temperatures ranging from ≈2000 K to ≈9000 K. Temperature estimates for the plasma jet, presented later, fall within this range (section 5.1.3). Choosing the observation point close to the nozzle, one could assume that any C₂ present underwent sufficient thermal excitation to emit Swan bands.

Goyette *et al.* (1998) published a systematic comparison of $\nu(0,0)$ Swan emission and absolute C₂ concentration, measured by absorption spectroscopy, in argon-hydrogen plasmas at low temperature and pressure. Their findings revealed a two-decade dynamic range correlation between Swan emission and C₂ density (10^{10} - 10^{12} molecules/cm³). It was concluded that Swan band emission was a reliable measure of C₂ concentration. Whether these results apply to the distribution of ground- and excited-state C₂ species in a thermal plasma is

unconfirmed. Yet if $\nu(0,0)$ Swan emission responds strongly to C_2 density at low temperatures, a similar behaviour may be assumed in a thermal plasma where excited levels are highly populated and emitting species are abundant. Operating at atmospheric pressure promotes the dominance of collisional processes and the equilibration of excited states.

Other studies on the spatial distribution of ground- and excited-state C_2 molecules, respectively detected by optical absorption and emission spectrometry, point to a direct correspondence between the lack of Swan emission and the absence of C_2 fragments or species (Reeve and Weimer 1995).

5.1.2.4 Choice of an Observation Point

Assuming that concentration and temperature distributions within the plasma jet maintained steady profiles, a single observation point was adequate for feedback optimization. This assumption was likely to apply near the nozzle; downstream, the jet varied in shape with operating conditions. The intense triangular core of the jet depicted in Figure 5.1.2-11 offered maximal reproducibility and signal-to-noise ratio.

The lateral position of the observation point was chosen on the basis of Abel integral computations for hypothetical profiles. Measurements from the central axis of the jet were shown to be more intense and more sensitive to concentration than measurements from other lateral positions (Filion 1995). This conclusion applied independently of the radial emission profile assumed. Because centreline measurements included contributions from all radial positions, they risked less information loss with changes in jet property distributions.

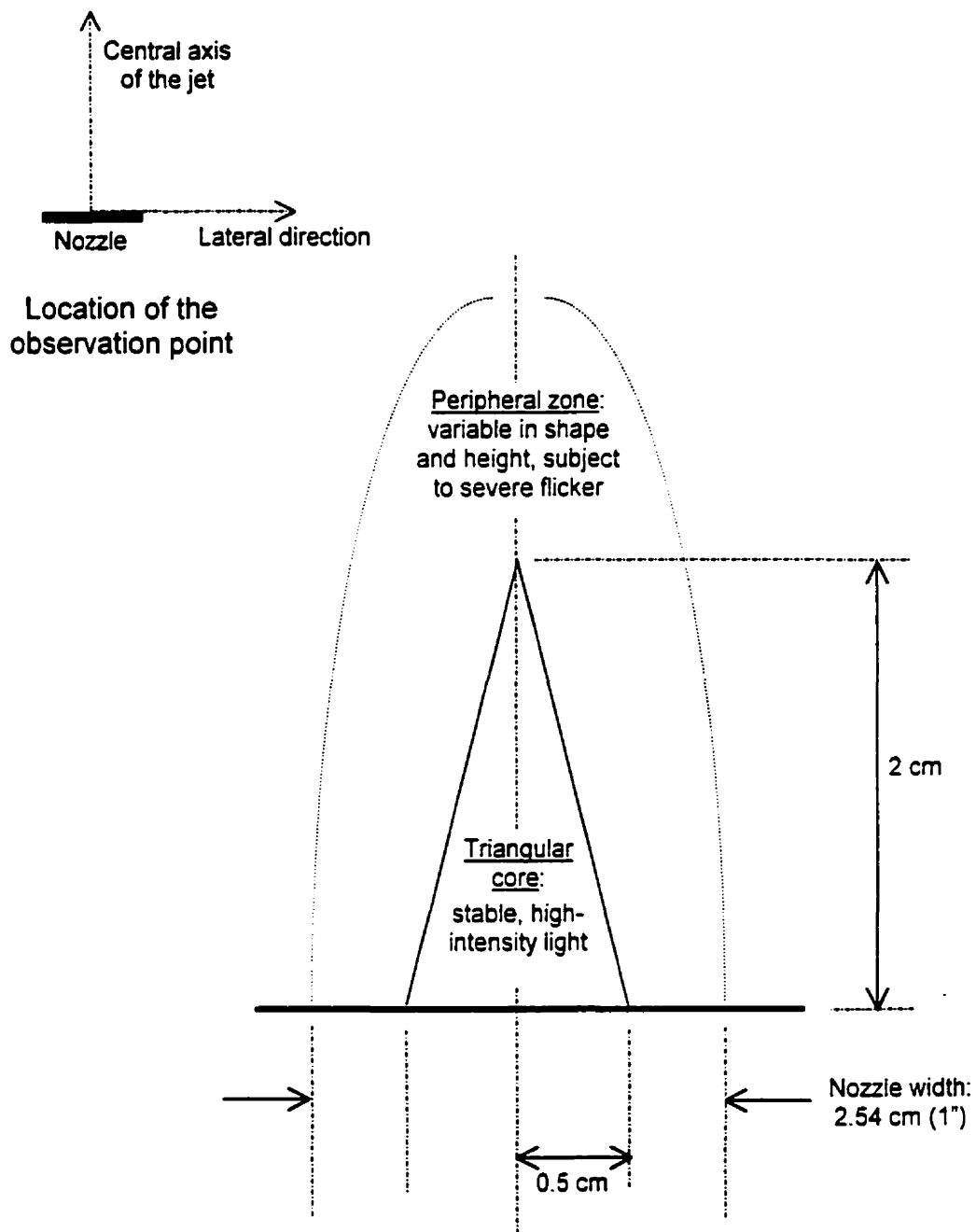


Figure 5.1.2-11: Geometry of the Plasma Jet

The position of the observation point along the axis of the jet was empirically set to maximize light transmission. The projected image was slightly less intense at the nozzle than 1 cm downstream. Unless indicated otherwise, the observation point was located 0.5 cm down the central axis of the jet.

5.1.3 Temperature Estimation

Information on the temperature at the observation point was essential to support the assumption that Swan bands were emitted whenever C_2 was present. Rough estimates were sufficient to show that the temperature is above the 2000-3000 K range (King 1948). Three techniques were used to obtain these estimates: Boltzmann plots using experimental and simulated spectra (for reference), visual comparison of measured and simulated band profiles, and thermodynamic equilibrium heat balance calculations.

5.1.3.1 Boltzmann Plot Method

Figure 5.1.3-1 shows a high-resolution Swan band spectrum for temperature diagnostics. A Boltzmann plot constructed using a range of P-branch lines appears in Figure 5.1.3-2. The slope of this plot indicates a temperature of the order of 7000 K. Temperature estimates at different locations across the plasma jet are shown in Figure 5.1.3-3. The linear regression coefficient (R^2) measured the quality of the linear fit (a unity coefficient denotes perfect fit). For example, a lower coefficient at the side of the jet signalled that the calculated temperature (7500 K) might be inaccurate. Jet flicker and low intensity at this position suggested cooling, hence departure from local thermodynamic equilibrium (LTE). Under such conditions, excited rotational states might not have a Boltzmann distribution or the rotational temperature might overestimate the kinetic temperature of the gas (Chen *et al.* 1994). Fluctuation-related errors at the periphery of a plasma jet often prevail over the measurements themselves (Bousrih *et al.* 1995). Temperature estimates in the core of the jet ranged from

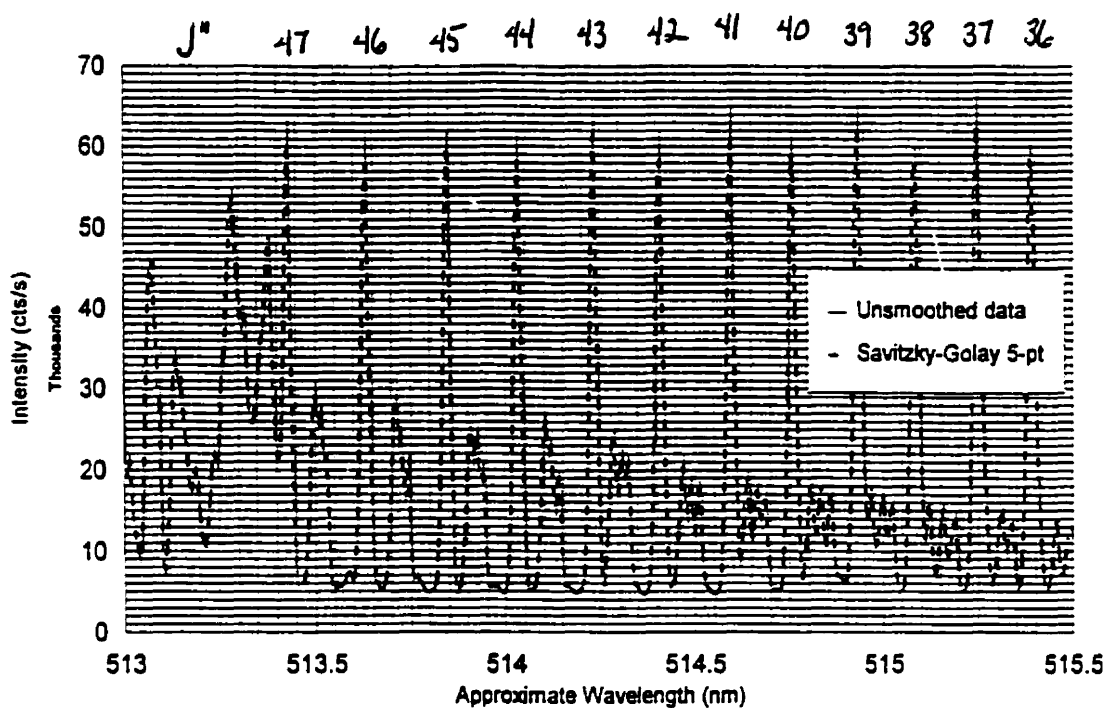


Figure 5.1.3-1: High-Resolution Band Spectrum for Temperature Estimation

Observation point: 0.5 cm down the central axis of the jet
 Operating conditions: 3.5% O₂, 1.4% C₃H₈, I_p = 4.1 A
 Spacing = 0.0053 nm
 PMT voltage = 1200 V
 Integration time = 1.2 s

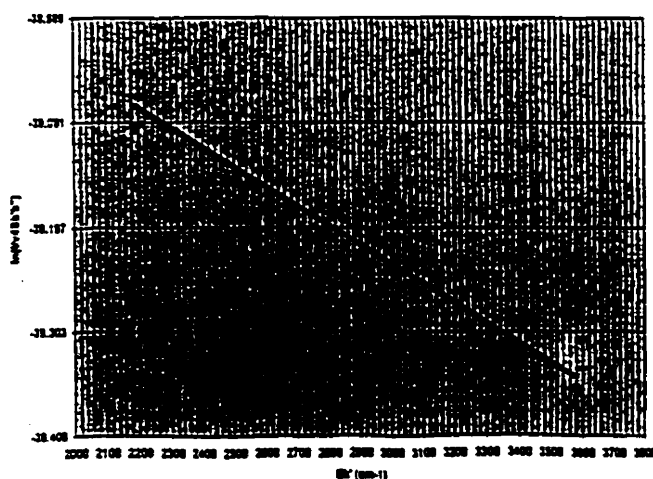


Figure 5.1.3-2: Boltzmann Plot For the Range J'' = 46 - 36 (T ≈ 7300 K, R² = 0.92)

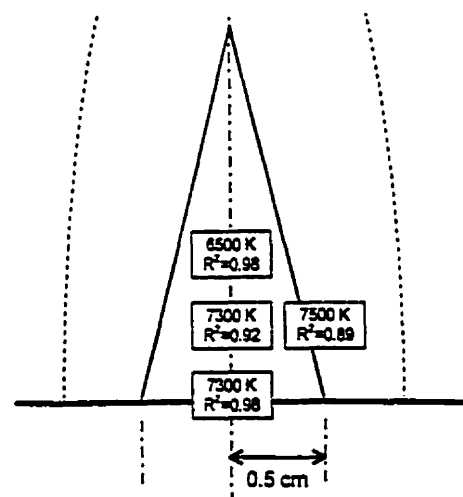


Figure 5.1.3-3:
 Boltzmann Plot
 Temperature Estimates
 Across the Plasma Jet

6500 K to 7300 K. Variations along the central axis were within uncertainty and not representative of a temperature profile.

Instability in the plasma jet was an important source of uncertainty in these measurements. The presence of oxygen in the plasma gas left little carbon in the form of C₂ compounds. A high propane input (1.4%) was needed to produce strong Swan bands. This load increased the plate power required to sustain the discharge by over 3 kW, and resulted in an unstable jet. A long integration time (1.5 s) attenuated the effect of noise but extended the duration of the scans to 13 minutes. PMT readings were sensitive to drift in emission intensity during this period.

The optical resolution of the instruments added considerable uncertainty to temperature estimates. To assess the effect of resolution, Boltzmann plots were constructed from theoretical spectra generated at different resolutions (FWHM). Theoretical peak heights were measured from Figures V-D to V-K of Appendix V. On spectra where the P-triplets were resolved, the tallest component was used. When lines blended, the height of the leftmost peak in each P cluster was used. A FWHM value of 0.001 nm represented an ideal high-resolution case, while a value of 0.15 nm approached the resolution of the experimental system. Spectra generated at FWHM = 0.001, 0.008 and 0.015 nm showed the evolution of P-branch profiles (tall peaks) with decreasing resolution: P-line triplets blended and overlapped with R-branch components (short peaks). Table 5.1.3-1 lists temperature estimates obtained using different resolutions and ranges of emission lines.

Table 5.1.3-1a: Temperature Estimates from Simulated Spectra, $J'' = 46-35$

Simulation T (K)	FWHM (nm)	Calculated T (K)	R^2 (see note)	Error (%)
3000	0.001	2998	0.9999	-0.07
3000	0.008	2587	0.87	-13.8
3000	0.015	2704	0.87	-9.9
4000	0.008	3422	0.81	-14.5
4000	0.015	3544	0.83	-11.4
6000	0.001	5997	0.999	-0.05
6000	0.008	4941	0.70	-17.7
6000	0.015	6656	0.50	10.9

Table 5.1.3-1b: Temperature Estimates from Simulated Spectra, $J'' = 44-35$

Simulation T (K)	FWHM (nm)	Calculated T (K)	R^2 (see note)	Error (%)
3000	0.001	3009	0.9999	0.3
3000	0.008	2451	0.87	-18.3
3000	0.015	2633	0.83	-12.2
4000	0.008	3232	0.82	-19.2
4000	0.015	3422	0.80	-14.5
6000	0.001	6003	0.998	0.05
6000	0.008	4624	0.71	-22.9
6000	0.015	7007	0.38	16.8

Table 5.1.3-1c: Temperature Estimates from Simulated Spectra, $J'' = 46-40$

Simulation T (K)	FWHM (nm)	Calculated T (K)	R^2 (see note)	Error (%)
3000	0.001	2996	0.9997	-0.13
3000	0.008	3129	0.62	4.3
3000	0.015	3077	0.66	2.6
4000	0.008	4340	0.46	8.5
4000	0.015	4128	0.53	3.2
6000	0.001	6097	0.998	1.6
6000	0.008	6641	0.27	10.7
6000	0.015	6493	0.30	8.2

Note: Line broadening and superposition produce an alternating pattern in peak heights. This is exemplified by Figure X-K in Appendix X. On the Boltzmann plots, the points alternate on either side of the line of best fit. This partly explains the poor R^2 values obtained for FWHM = 0.008 nm and FWHM = 0.015 nm.

At extremely high resolution (FWHM = 0.001 nm), the Boltzmann plots gave near-perfect temperature estimates. At lower resolution, estimates were off by about 20% for FWHM = 0.08 nm and 15% for FWHM = 0.015 nm. A lower accuracy for FWHM = 0.08 nm was explained by partial blending of triplet components. Peak heights were based on a single component for FWHM = 0.001 nm and on the entire unresolved triplet for FWHM = 0.015 nm. The contributions to each peak were mixed for FWHM = 0.08 nm.

A comparison of Tables 5.1.3-1a to 5.1.3-1c, summarized in Table 5.1.3-2, illustrates the sensitivity of Boltzmann plot results to spectral measurement error. Temperature estimates varied appreciably with the range of emission line included in the plots. The quantum number ranges (J'') of Tables 5.1.3-1a and 5.1.3-1b are commonly used for temperature diagnostics from Swan bands. Of these two options, the broadest range gave the most accurate temperatures. A shorter quantum number range (Table 5.1.3-1c) was considered after inspection of the Fortrat diagram and theoretical spectra (Appendix V). P- and R-branch components grow closer in wavelength as J'' decreases, and are most likely unresolved below $J'' = 40$. Accordingly, plots restricted to $J'' = 46-40$ were more accurate with simulated, noiseless spectra (Table 5.1.3-1c). However, for experimental estimates, a wide range of points is recommended to attenuate the effect of noise. As seen in Table 5.1.3-3, estimates from the narrow range of points were high for the type of equipment used (temperatures exceeding 7500 K were unlikely based on a heat balance).

Table 5.1.3-2: Temperature Estimates from Simulated Spectra for Different Ranges of Emission Lines (FWHM = 0.015 nm)

Simulation	$T_{\text{calc.}}$ (K)	Error	$T_{\text{calc.}}$ (K)	Error	$T_{\text{calc.}}$ (K)	Error
T (K)	$J'' = 46-35$	(%)	$J'' = 44-35$	(%)	$J'' = 46-40$	(%)
3000	2704	-9.9	2633	-12.2	3077	2.6
4000	3544	-11.4	3422	-14.5	4128	3.2
6000	6656	10.9	7007	16.8	6493	8.2

Table 5.1.3-3: Experimental Temperature Estimates For Different Ranges of Emission Lines (cf. Figure 5.1.3-3)

Observation point	T _{calc.} (K)	R ²	T _{calc.} (K)	R ²	T _{calc.} (K)	R ²
	J" = 46-36		J" = 45-37		J" = 46-40	
Centreline, nozzle height	7300	.98	6800	.97	8300	.99
Centreline, 0.5 cm down	7300	.92	7100	.88	7500	.88
Centreline, 1.0 cm down	6500	.98	6500	.98	6100	.96
0.5 cm to the side, 0.5 cm down	7500	.89	9200	.82	9900	.68

From Table 5.1.3-2, the expected error in temperature for a spectral resolution of FWHM = 0.015 nm was estimated to 15%. Experimental measurements were subject to additional uncertainty due to noise. A combined error margin of 20% was deemed plausible. The jet temperature estimate was therefore 7000 K ± 1500 K.

Boltzmann plot experiments were performed at high propane input. The enhancing effect of propane on power dissipation suggested that temperature was higher than it would be during optimization experiments. An expected temperature difference of 500 K was calculated based on the plate power rise observed when introducing additional propane into the system.

Additional plate power ≈ 3.2 kW

Additional power transferred ≈ (3.2 kW)(0.30) = 0.96 kW

Total gas flow rate ≈ 125 gmol/h

$$\text{Temperature rise} \approx \frac{(0.96 \text{ kJ/s})(3600 \text{ s/h})}{(0.06 \text{ kJ/gmol.K})(125 \text{ gmol/h})} = 460 \text{ K} \text{ or } 500 \text{ K}$$

(equation 5.1.3-1)

Assumptions Torch thermal efficiency ≈ 30%

Plasma heat capacity ≈ 0.06 kJ/gmol.K (Boulos *et al.* 1995)

In conclusion, a plasma temperature estimate of $6500 \text{ K} \pm 1500 \text{ K}$ was inferred under typical experimental conditions. This estimate was based on light originating from all radial positions along the optical axis. It represented an average of local temperatures weighted by their absolute Swan band emissivity. A temperature profile could not be established due to position uncertainty within the jet.

Swan band emission occurs in the 2000-3000 K range and gains in intensity with increasing temperature. The estimated jet temperature supported the assumption that Swan bands emission was assured in the presence of C_2 .

5.1.3.2 Approximate Methods

Superposition method

An approximate temperature was inferred by visually comparing the Swan band rotational emission profile to theoretical predictions at different temperatures. Reference profiles appear in Figure 5.1.3-4. The information of interest was the P-branch profile in the range $J'' = 46-36$. The experimental profile of Figure 5.1.3-1, measured from the central observation point, was visually representative of those measured from other locations. The profile matched a temperature between 6000 K and 7000 K.

Intensity Ratio Method

This method compares an emissivity ratio from two regions of the Swan band with theoretical predictions at different temperatures. This procedure was inconclusive in this project due to difficulties in isolating Swan signals from the remaining spectrum. Emissivity ratios derived from experimental spectra were outside the range corresponding to realistic temperature estimates. Details on the numerical calculations are found in Appendix VII.

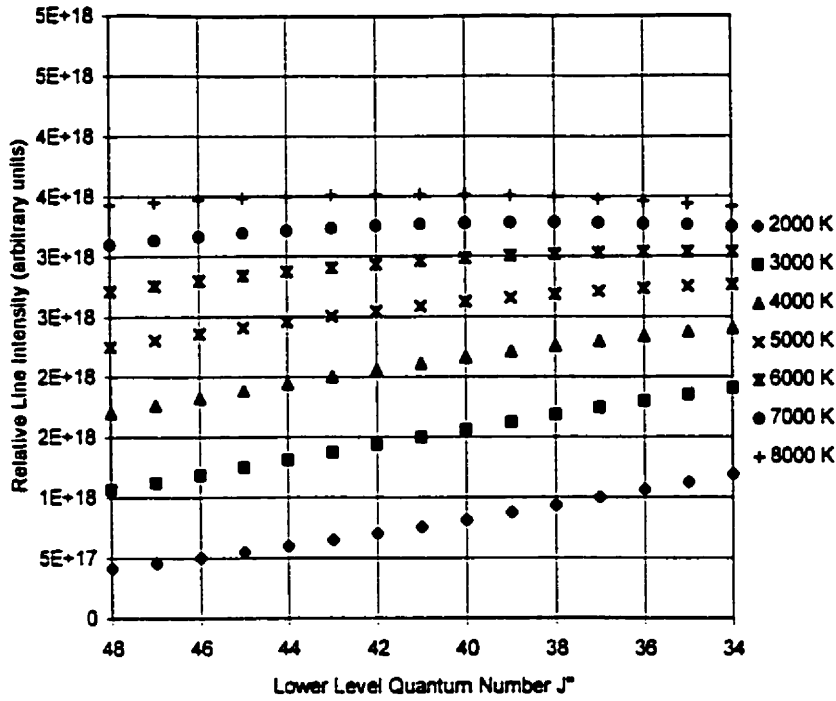


Figure 5.1.3-4: Simulated P-branch Intensity Profiles at Different Temperatures

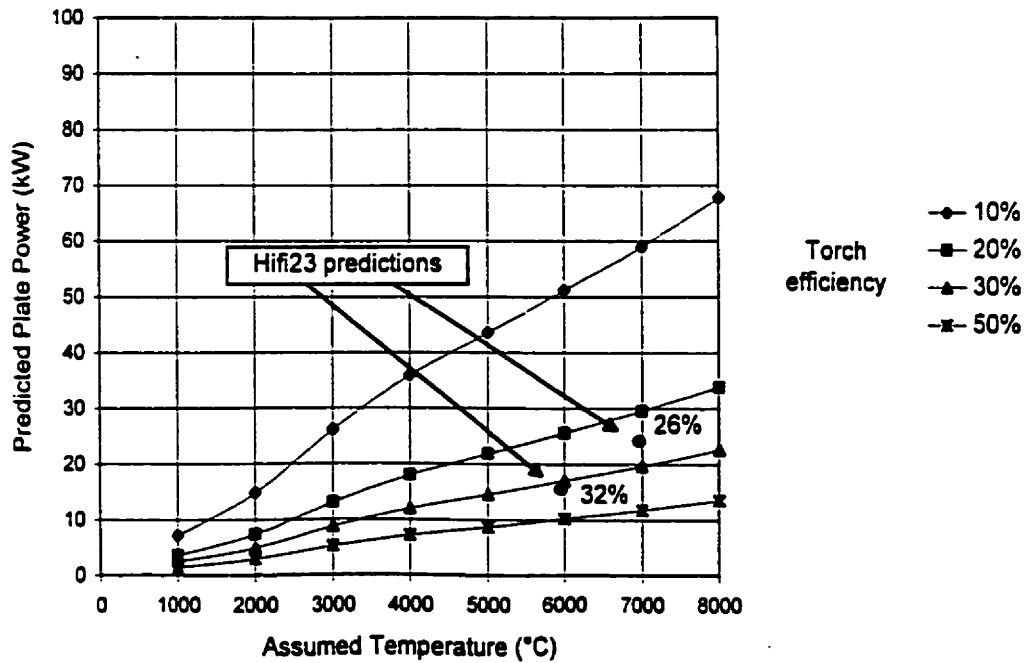


Figure 5.1.3-5: Predicted Plate Power vs Assumed Temperature for an Argon Plasma with 3.5% Oxygen (FACT Equilibrium Calculation)

The presence of strong argon lines within the green Swan band prevented accurate measurement of the band emissivity over the intervals recommended by Bousrih *et al.* (1995): 512.9 - 516.0 nm and 516.0 - 516.5 nm. An attempt to apply the method over two narrow interference-free spectral intervals, namely 513.0 - 513.75 nm and 513.75 - 514.5 nm, was unsuccessful. The selected intervals excluded the band head, which comprises a major fraction of total band emissivity. The temperature dependence of the intensity ratio between two intervals away from the band head is weak. For the narrow intervals used here, the error incurred in subtracting the continuum exceeded the intensity difference between the regions and thus the temperature dependence was lost.

The difficulties encountered with the intensity ratio method were mainly due to the superposition of argon and Swan spectra. A reliable interference correction method should eliminate this problem. The intensity ratio method is a potential diagnostic tool for APAI prototypes. The simplicity of the computation, notably the ease and rapidity with which the information is extracted from on-line emission spectra, are clear advantages over other optical temperature measurement techniques.

5.1.3.3 Heat Balance Computations

The simulation program Hifi23 was used to generate spatial maps of temperature, composition and velocity profiles inside the quartz tube of an induction torch. Numerical results at the exit location, just upstream of the nozzle, allowed the calculation of a mixing-cup temperature. This was performed by dividing the plasma volume into concentric rings matching the numerical simulation grid. Averaging the enthalpy contributions of all rings over the total mass flow gave the mean temperature of a turbulent jet exiting the nozzle.

Hifi23 accepts geometric and dynamic input parameters describing a two-gas plasma in a torch manufactured by Tekna Inc. Unlike the Tafa torch used here,

Tekna torches use tangential injection for the main sustaining gas and axial injection for the sheath. Input flow rates were programmed to match the flow configuration of the Tafa torch as closely as possible. The simulation was run for an argon plasma with oxygen as the secondary gas. The effect of the model compound on the specific heat of the plasma was neglected.

Isotherm contour plots are part of the torch simulation results presented in section 5.2.2-1 and Appendix XV. Temperature estimates at typical operating conditions are summarized in Table 5.1.3-4. Power input data assume a torch efficiency of 30%. The plate power is the product of plate current and plate voltage readings ($P_p = V_p \cdot I_p$).

Table 5.1.3-4: Hifi23 Temperature Estimates at Typical Operating Conditions

% O ₂	I _p (A)	P _p (kW) *	η * P _p (kW)	T _{calc.} (K)
3.5	3.6	16.6	4.98	6250
3.5	4.6	24.0	7.20	7250
12.8	3.6	18.0	5.40	5000
12.8	4.6	25.4	7.62	5850

* Plate power experimentally measured at indicated input settings.

Boltzmann plot experiments used 3.5% O₂ and I_p = 4.1 A. By interpolation, Hifi23 predicted 6750 K at these conditions. This value compared favourably with the Boltzmann plot estimate of 6500 K ± 1500 K.

Equilibrium heat balance calculations were compared with these estimates. Given the initial gas composition and final temperature, FACT could calculate the equilibrium gas composition and energy input. Assuming this input equal to the power dissipated in the plasma gas, plate power values were predicted for different torch efficiencies. Figure 5.1.3-5 plots the predicted plate power (at 3.5% O₂) as a function of assumed temperature and torch efficiency. For comparison, two Hifi23 data points from Table 5.1.3-4 (at 3.5% O₂ and 30% efficiency) are shown on the chart. Next to each Hifi23 point is the torch

efficiency at which the FACT-predicted plate power agreed with the measured plate power. The equilibrium heat balance was satisfied at $\approx 30\%$ torch efficiency. This realistic value supports the validity of the temperature estimates obtained from Boltzmann plots and from torch simulations.

In conclusion, experimental and theoretical estimates suggested a jet temperature of the order of 6500 K, with at least 20% uncertainty. It was reasonable to assume that the temperature at the point of observation was well above the 2000-3000 K range. Therefore, Swan emission could be expected whenever C_2 was present.

5.2 Afterburner Model

This section is to examine the characteristics and limitations of the experimental model system. This information clarifies the applicability of the demonstration results to an APAI prototype.

The laboratory system was not intended to perform routine waste destruction. Rather the project emphasized an experimental demonstration of the adaptive strategy, using a plasma heat source to destroy organic compounds. A diagnostic procedure was developed specifically for the experimental model system. Different techniques and methods would apply to prototype- or industrial-scale systems designed for waste destruction.

5.2.1 Geometry of the Chemically Reactive Zone

Plasma waste treatment studies have confirmed the importance of equipment configuration in relation to destruction efficiency. In experimental systems where a contaminated gas is brought into contact with a plasma discharge, poor mixing is a common cause of low destruction efficiency. The stoichiometric oxygen ratio

and flow patterns in and around the discharge are two critical factors in the destruction of various organic compounds (Sacchi *et al.* 1996, Teplý *et al.* 1995).

The reaction zone in the experimental system comprised the inside of the quartz tube and the core of the jet, where the observation point was located. The configuration of the model system was not suited for complete oxidation. Flow patterns within the torch did not guarantee complete mixing of the model compound with the plasma gas. The injector tip was located at the same level as the main gas distributor. Hence the model compound entered the torch upstream of the high-temperature viscous zone. The introduction of the compound into the plasma relied on the high velocity of the carrier gas against the recirculation patterns induced by electromagnetic pumping. Theoretical evidence from modelling studies predicts laminar flow, hence limited mixing, in the viscous core of induction plasmas (Or *et al.* 1997). Organic molecules entrained into the peripheral stream could bypass the plasma and fail to react completely with oxygen. Alternatively, poor mixing between the central stream and the torch gas could allow undecomposed molecules to escape through the centre.

A Reynold's number of 400 was calculated inside the torch using gas properties near 5000 K. This value indicates laminar flow and limited mixing. Passing the nozzle, the flow assumed an orifice jet profile with some mixing. Previous work using the same laboratory equipment supports the assumption of a uniform profile in the core of the jet (Dlugogorski 1989).

5.2.2 Concentration, Temperature and Velocity Profiles

The response of the C₂ indicator to manipulated variables was determined by their impact on mixing and kinetics in the reaction zone. Property distributions inside the torch were modelled using the simulation program Hifi23. Contour maps of temperature, concentration and axial velocity profiles provided information on the thermal properties and mixing patterns in the reaction zone.

5.2.2.1 Hifi23 Simulations

The Tekna induction torches modelled by the Hifi23 program differ in design from the Tafa torch used here. Yet, with input parameters based on the Tafa configuration, the program produced reasonable maps of the temperature, concentration and velocity profiles in the torch used.

The following characteristics were specified as in the experimental system: number of turns and position of the inductor; electromagnetic frequency, dissipated power (efficiency-adjusted plate power); dimensions of the quartz tube; dimensions and position of the injector; gas flow rates and compositions for the sheath, main and injector streams. Table 5.2.1-1 summarizes the differences between the experimental torch and the simulation model torch. Based on this comparison, predicted and actual profiles could differ on two points.

First, in the experimental torch, swirl injection was used for the sheath gas near the wall. Because the program assumed a swirl motion in the centre, it could overestimate mixing between the injector stream and plasma gas. Second, the presence of propane in the experimental system was neglected by the program. Since the effects of propane on the plasma were similar to those of oxygen, any phenomenon associated with oxygen could be more pronounced in the experimental system than in the simulation. These differences had no consequence on the conclusions of the modelling study.

Appendix XV presents profiles of temperature, oxygen concentration and axial velocity inside the quartz tube. Because oxygen was introduced in the sheath gas only, concentration profiles provided indications of mixing. The contour maps were examined for changes with each manipulated variable. Key observations are summarized in the following discussion.

Table 5.2.1-1: Distinctions Between Experimental and Simulated Torches

Characteristic	Tafa torch (experimentation)	Tekna torch (simulation)
<u>Main sustaining flow</u>		
Injection mode	Axial	Tangential
Torch gas fraction	26-29%	26-29% (25% optimal)
Composition	Argon	Argon
<u>Sheath flow</u>		
Injection mode	Tangential	Axial
Torch gas fraction	71-74%	71-74% (75% optimal)
Composition	Argon, oxygen	Argon, oxygen
<u>Injector flow</u>		
Composition	Argon, propane	Argon

Isotherms showed the typical toroidal shape of induction plasmas surrounding a slightly cooler central channel. Mixing occurred gradually along the length of the quartz tube, decreasing the oxygen concentration gradient between the sheath and the centre. Complete mixing was not achieved within the length of the quartz tube: this would be indicated by flat exit temperature and concentration profiles with steep gradients at the wall. Axial velocity maps show the recirculation zone created by electromagnetic pumping (negative velocities denote an upstream flow). The injector stream decreased in velocity as it encountered and blended into the plasma.

As power increased, the plasma volume expanded towards the wall and upstream. Temperature rose, and both the toroidal high-temperature zone and the central channel widened. Velocities near the wall increased with thermal expansion. The recirculation zone enlarged without much change in upstream velocity. Hence the plasma seemed to "fill" the quartz tube as power increased. This favoured mixing between the injector stream and the plasma. Evidence of improved mixing was found on the concentration maps: oxygen from the sheath gas migrated further upstream toward the centre, and exit concentration profiles became more uniform.

As oxygen content increased, the plasma shrank laterally and expanded axially; i.e., the toroidal region and central channel became longer and narrower. Temperature rose and velocities increased. Raising the oxygen content increased electromagnetic pumping and power density in the toroidal region. Between 3.5% and 12.8% oxygen, the region of negative velocity changed from a toroidal zone around the injector stream to a "shield" of upstream flow in front of the injector. Thus, enhanced electromagnetic pumping steered the injected gas to the outside. This increased the probability of model compound molecules bypassing the core of the plasma. A direct consequence of increased pumping was improved mixing of sheath and sustaining streams over the first third of the length of the plasma. This could attenuate the effects of bypassing.

The axial velocity and concentration contours did not explicitly show the path of the injector stream and its mixing with the surrounding plasma gas. It was assumed that the injector stream would blend into the plasma if it had at least as much momentum as the recirculating flow opposing it. Simulation results for a torch without an injector were used to estimate the axial momentum of electromagnetic pumping under worst case conditions (12.8% O₂, 4.6 A). The momentum of the unopposed upstream flow was compared to that of the injector stream. The result suggested strong impaction of the injected gas onto the plasma - hence some mixing with the sustaining gas. At the point of maximum negative velocity, the injector stream momentum exceeded the local pumping momentum by a factor of twenty.

Two conclusions were drawn from this modelling study. First, complete mixing was not expected inside the torch. Second, the effects of the manipulated variables were not limited to changes in temperature and oxygen concentration. Property profiles and flow dynamics within the torch were strong functions of the manipulated variables. The combined effects of these factors on oxidation reactions governed the destruction of the model compound and thus Swan band

emission in the exiting jet. This contributed to the absence of well-defined reproducible relations between individual variables and measured signals.

The effect of power (or plate current) on destruction efficiency was relatively straightforward: increasing power promoted oxidation by increasing both temperature and mixing. Oxygen might have had opposing effects on oxidation rates. On the one hand, increasing its concentration drove the reaction forward by Le Châtelier's principle. On the other hand, the changes it induced in flow patterns and plasma geometry could facilitate bypassing and incomplete combustion. Yet oxygen did improve destruction efficiency, most likely by increasing power density, temperature and overall mixing. The predicted response of the induction plasma to power and oxygen input agreed with the conclusions of other modelling studies (Or *et al.* 1997).

5.2.2.2 Experimental Observations

Swan emission patterns in the jet were important in the interpretation of (S/B) measurements. Swan band signals were not uniform across the jet diameter. This implied non-uniform C_2 concentration and/or temperature profiles. This section explores the significance of Swan emission at different locations in the jet. This information leads to a more precise definition of what was measured by the (S/B) indicator.

If observed, the presence of C_2 species in the hot core of the jet would signal incomplete oxidation due to poor mixing and/or insufficient residence time. Poor mixing was assumed to dominate, since the oxidation reactions of light hydrocarbons are fast. Experiments performed with acetylene as a model compound supported the hypothesis that the residence time was adequate. In these experiments, weak Swan band emission attested to the rapid thermal decomposition of acetylene into single-carbon species. Yet heavy soot production indicated incomplete combustion. Among the many reactions of

hydrocarbon combustion mechanisms, the rate-limiting steps are those which break the carbon backbone; the oxidation of carbon radicals is comparatively fast (Glassman 1996). Thus, the large amounts of soot were linked to poor mixing between oxygen in the sheath gas and acetylene products at the centre. In all experiments, the oxygen input far exceeded stoichiometric requirements for the propane or acetylene present.

The presence of C_2 at the jet periphery but not at the core would indicate bypassing and/or recombination of molecular fragments and atomic species upon cooling. A bypassing stream would imply a lack of mixing near the water-cooled wall. Recombination would also indicate poor mixing with oxygen from the sheath gas: carbon/hydrocarbon oxidation reactions are typically orders of magnitude faster than reactions involving the formation of a carbon-carbon bond (Glassman 1996).

Past the nozzle, the periphery of the jet developed steep radial temperature and composition gradients due to cold air entrainment. This caused severe departure from the local thermodynamic equilibrium assumed within the torch. Chen *et al.* (1994) studied deviations from LTE in the jet of a dc argon-helium plasma. Their system was similar to the afterburner model in terms of gas flow rates and overall configuration. With the jet exiting onto an atmospheric environment, they found that LTE was confined to a laminar core near the nozzle. Their visual description of the laminar region matched that of the triangular jet core of the afterburner model (Figure 5.1.2-11).

Abel Inversion Procedure

To discriminate between Swan emission from the jet centre and from the periphery, the reconstruction of radial Swan emission profiles by Abel inversion was attempted. The procedure was unsuccessful because of noise and poor spatial resolution in the lateral measurements.

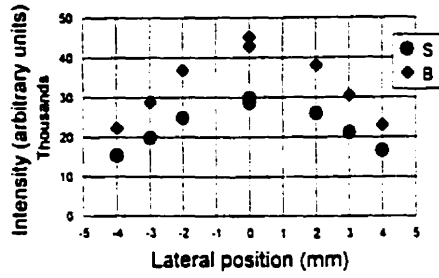


Figure 5.2.2-1a: S and B Profile Set #1

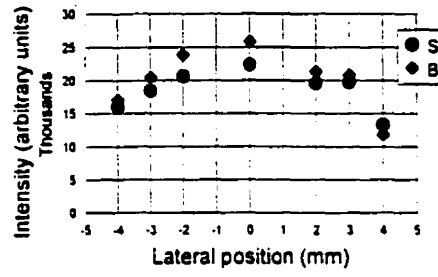


Figure 5.2.2-1c: S and B Profile Set #2

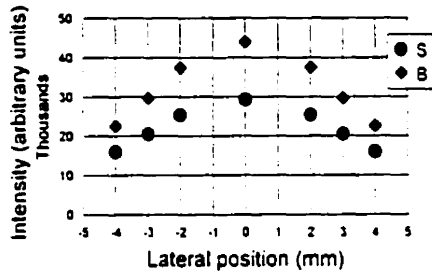


Figure 5.2.2-1b: Averaged Profile #1

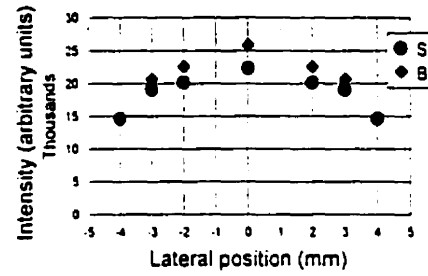


Figure 5.2.2-1d: Averaged Profile #2

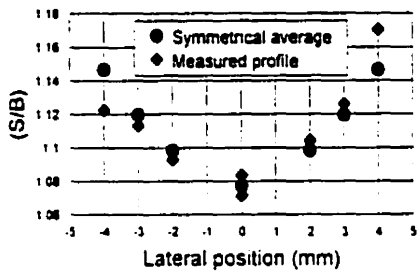


Figure 5.2.2-2a: (S/B) Profile Set #1

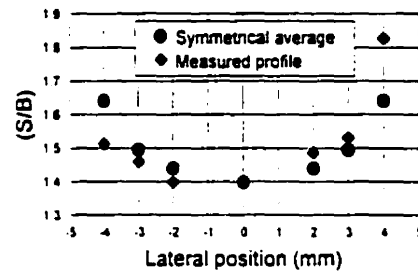


Figure 5.2.2-2b: (S/B) Profile Set #2

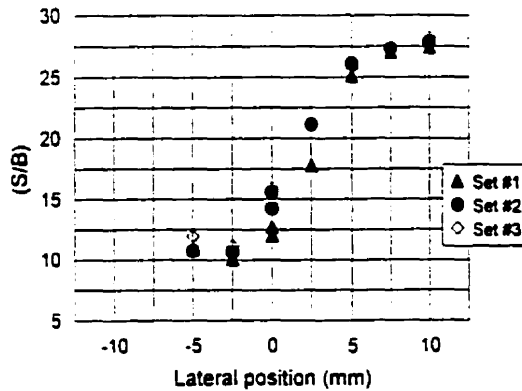


Figure 5.2.2-2c: Measured (S/B) Profile Argon-Propane Plasma Jet (Three Replicate Sets)

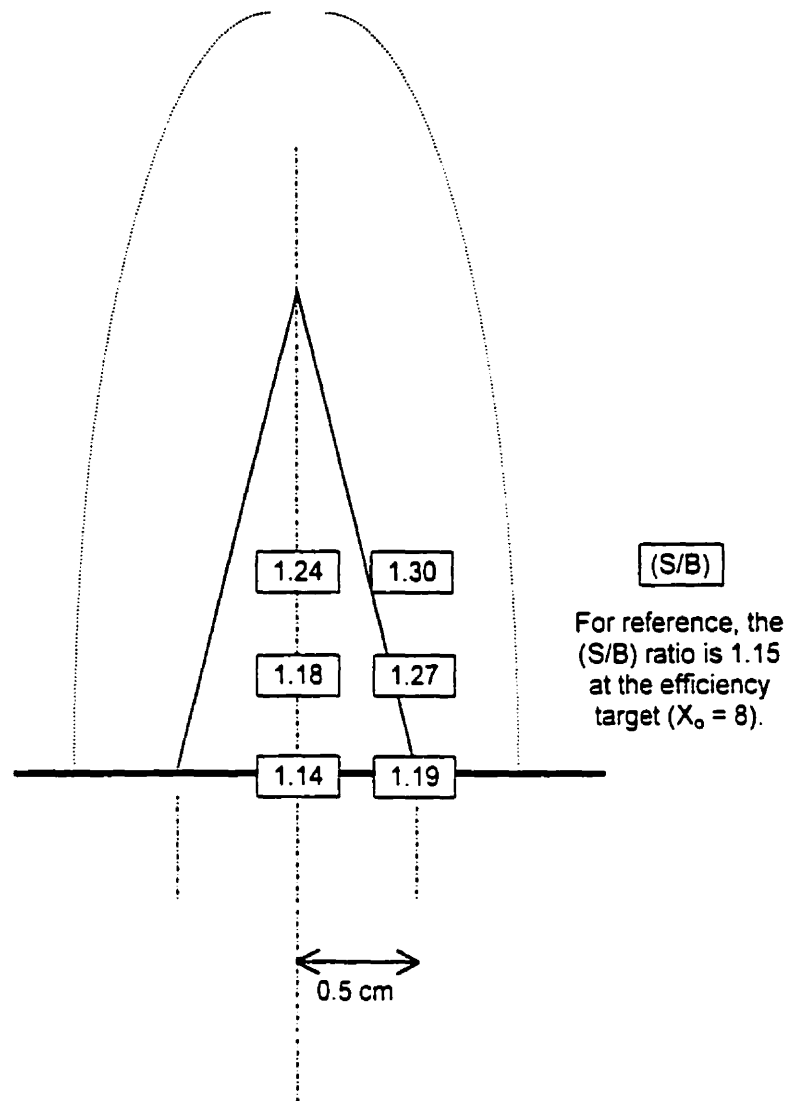


Figure 5.2.2-3: (S/B) Ratio Distribution Across the Plasma Jet

Input conditions

propane:	0.3%
oxygen:	10.6% ($x_1 = 10$)
plate current:	4.1 A ($x_2 = 5$)

The centreline and edges of the jet could not be precisely located due to intense flicker from side to side, asymmetry, and low image intensity at the periphery. At 1:1 magnification, the optical fibre could be positioned within 0.2 cm at best. The luminous core suitable for optical measurements covered 0.5 cm on each side of the centreline. At higher magnification, spatial resolution was improved but light intensity was low so relative noise increased. Variations in jet size and shape impeded reproducibility. Consequently, lateral profile data failed to meet the essential requirements for the Abel inversion procedure: symmetry, a large number of points, low noise and, most importantly, accurate knowledge of centreline and boundary locations.

Lateral profiles of S and B intensity measurements are pictured in Figures 5.2.2-1a to 5.2.2-1d. These measurements were taken at low power ($I_p = 3.8$ A) with low oxygen input (3.5% O_2) to minimize flicker and instability. Two profile sets were measured from plasmas with two different propane concentrations: 0.1% for set #1, and 0.2% for set #2. Figures 5.2.2-1a and 5.2.2-1c show measurements taken across the plasma jet. Values from either side of the centreline were averaged to obtain symmetrical profiles, shown in Figures 5.2.2-1b and 5.2.2-1d. Each profile was modelled by a least-squares fit second-order polynomial. The differential term of the Abel integrand was calculated from the model equations. The boundaries of the jet were estimated from the roots of the polynomials.

The reconstructed S and B profiles decreased in intensity from the centre outward. Their ratio (S/B), however, showed evidence of computational inaccuracy. The shape of the predicted (S/B) profiles varied widely with individual S and B curves. In the absence of accurate centreline and boundary data, the profiles presented numerical singularities at the centre and at the edges. For this reason, numerical predictions of (S/B) at the centre of the jet were not available. It was concluded that error in the measurements, amplified by curve-fitting and

differentiation, was too high for the deconvolution to be accurate. The Abel inversion results were deemed unusable.

For lack of radial profiles, trends in lateral measurements were examined. Figures 5.2.2-2a and 5.2.2-2b present (S/B) profiles computed from the individual S and B measurements of Figures 5.2.2-1a and 5.2.2-1c. (S/B) values increased from the centre of the jet towards the periphery. This lateral profile was verified in an argon plasma with 0.05% propane and no oxygen. These conditions produced intense Swan emission in a wide, green plasma jet 0.5 cm wider than the nozzle in diameter. The profile shown in Figure 5.2.2-2c represents the right-hand side of that jet. Lateral positions were measured relative to the torch centreline. The jet was off-centre of the nozzle.

A distribution of values throughout the jet appears in Figure 5.2.2-3. These values were measured at conditions near the destruction efficiency target of the demonstrations. (S/B) was lowest at the centre near the nozzle. It increased as the observation point moved to the sides and downstream.

These results agree with the hypothesis that some propane bypassed the hot plasma region. Bypassing would cause higher concentration of C_2 species in the outer ring of the jet. The (S/B) patterns observed laterally would be explained by the temperature profile of the jet. In centreline measurements, Swan emission from the outer ring would appear weak against the intense thermal emission of the core. Swan bands would seem stronger when measured against a low-intensity background, such as in cooler regions at the side and downstream.

Alternatively, the concentration of molecular fragments could be uniform throughout the jet due to turbulent mixing at the nozzle or to a low bypass rate. Recombination could cause higher concentration of C_2 species in cooler regions of the jet. This hypothesis could also explain the prevalence of Swan emission at the periphery and down the centreline.

Given the Swan emission patterns observed, uncertainty in temperature profile had no consequence on the validity of the measurements. The highest Swan signals were recorded in the coolest regions. One could confidently expect Swan emission from the jet core if C_2 compounds were present.

5.2.3 Interpretation of Spectral Indicator Values

The detection limit of the (S/B) indicator for C_2 was undefined. The open-system configuration of the afterburner model was not suited to gas sampling for off-line composition analysis. Total hydrocarbon content analyses of samples collected 30 cm above the jet were inconclusive. The composition assessment procedure used in the demonstrations was specific to the model system, and different from that of a prototype system. Its detection limit did not influence the validity of the demonstration.

The (S/B) indicator did not correlate exactly with C_2 concentration. Its numerical value could change with flow dynamics and jet profile variations caused by input settings. For instance, a change in the C_2 concentration profile would be reflected in (S/B) since the emissivity of C_2 molecules depended on their location within the jet. Likewise, a change in the temperature profile would alter the ratio between Swan band and thermal background emissions along the line of sight. Also, because of distinct molecular and continuum excitation mechanisms, local signal (S) and background (B) intensities could respond differently to temperature variations. However, these potential sources of error did not dominate the response of (S/B) to the manipulated variables. Within the operating space of the system, (S/B) consistently decreased with increasing oxygen or current input, as would the concentration of C_2 .

The value of the (S/B) indicator varied in different regions of the jet due to non-uniform thermal emission and C_2 concentration profiles. The optimization

procedure used observations from a fixed reference point. The stable core of the jet offered the highest intensities and signal-to-noise ratios for individual S and B measurements. Thus, the observation point was positioned at the centre of the core to minimize the sensitivity of the (S/B) ratio to profile changes in the jet.

A point of concern was the inability to achieve a (S/B) ratio of 1.00 in the presence of propane. The simplest explanation for this was that complete destruction did not occur in the system. Flow simulation data and experimental observations supported the hypothesis that poor mixing between the injector gas and the oxidizing plasma prevented complete oxidation of the model compound.

In conclusion, the (S/B) indicator was a relative measure of Swan emissivity, and could correctly detect the absence of organic molecules. Although no fixed relationship existed between measured (S/B) values and absolute C_2 concentrations, trends in (S/B) values could be used to direct an optimization towards higher organic compound destruction. The reader should keep in mind the ease and low cost of (S/B) ratio measurements compared to standard analytical techniques such as real time Fourier transform interferometry or atmospheric pressure mass spectrometry.

5.3 Demonstration of Adaptive Plasma Operation

This section presents an experimental demonstration of cost-optimal adaptive operation of the afterburner model. First, it establishes the rules and limitations under which the experiments were carried out: development of an optimization criterion, reliability of the optimization procedure, and uncertainty. Then, it describes optimization experiments simulating different situations on the model system. The discussion of the experimental results concludes with an assessment of the technical feasibility of APAI.

5.3.1 Objective Function Development

The formulation of an objective function (denoted Z) was part of the development of an optimization strategy. The operating range of the system and its response were determinant in the choice of a function. Combinations of equation terms were tested and modified until the objective function showed adequate sensitivity to the dependent variables (efficiency and cost, normalized as X and Y).

Upon examination of process objectives, a compound function with different equations in different zones of the domain appeared necessary. The domain was split into two regions separated by a destruction efficiency target efficiency value X_0 . This threshold marked a limit between under-treatment and over-treatment. In the zone where $X < X_0$, the need to improve effectiveness took precedence over cost considerations. In the zone where $X > X_0$, cost reduction was preferred to over-treatment.

The function that served as a optimization criterion is described by equation set 5.3.1-1. The three-dimensional view and contour plot of its surface were introduced in Figures 4.3.2-1 and 4.3.2-2 (*Methodology*). Below the target X_0 , the surface was a weak function of cost. Above X_0 , the function was highly sensitive to cost, and efficiencies beyond requirements carried a penalty. This penalty was forced to zero as the system approached minimum sustaining conditions (zero cost). The surface presented a ridge along the line $X = X_0$. The position of the optimum on this line depended on the input load. The surface was suited to the domain and precision of the model system. The slopes on either side of the ridge were pronounced enough for the response to vary appreciably around the optimum.

$$a = 10 \quad b = 0 \quad c = 5$$

$$Z(X, Y) = \left(\frac{10 - 0.2Y}{10} \right) \left[\frac{10}{X_0} X \right]; \quad X \leq X_0 = 8$$

$$Z(X, Y) = \left(\frac{10 - 0.2Y}{10} \right) \left[10 - \left(\frac{Y}{2} \right) (X - X_0) \right]; \quad X > X_0 = 8$$

(equation set 5.3.1-1)

The numerical coefficients in these equations (e.g., the efficiency target X_0) could assume values different from the ones assigned here. In general, an objective function is to be adapted to its application.

5.3.2 Optimization Strategy Validation

An optimization strategy was developed for the demonstration of adaptive operation of the plasma afterburner model. Before presenting optimization results, the reliability of the methods and programs used in these demonstrations is addressed.

The relationship between input settings and destruction efficiency (D.E.) was not fixed. At identical settings, D.E. and its sensitivity to oxygen and current, as measured by (S/B), might vary from experiment to experiment. This was caused by variations in electromagnetic coupling due to slight physical changes in system components. For example, routine part replacements in the torch (screws, quartz tube, etc.) might cause changes in plasma response. Alterations in physical or electromagnetic properties (e.g., cooling temperature, circuit impedance, electrical contact, etc.) influenced coupling efficiency and, indirectly, the temperature and chemical reactivity of the plasma.

As a result, the objective function surface was fixed with respect to D.E. and cost but variable with respect to input settings. The optimization programs were designed to continually assess the effect of oxygen and plate current on the

response and to direct the progression accordingly. This empirical approach offered built-in provision against changes in system dynamics.

Results from different experiments could not be compared among themselves or evaluated against a predicted theoretical optimum. Hence the validity of the demonstration depended on the reliability of the optimization procedure. The purpose of this section is to test the effectiveness of the optimization procedure. Optimizations on a known surface provided information on accuracy and on the effect of noise. An artificial response - with and without noise - was simulated by assuming a fixed relationship between input settings and destruction efficiency. In this simulation, the operating space was mapped to the domain of the objective function to generate a fixed response surface.

5.3.2.1 Optimization on a Conical Hill

A preliminary verification of the optimization programs' ability to climb a hill is illustrated in Figure 5.3.2-1. The response surface was a cone whose apex was located at the centrepoint (5, 5) of a 10 x 10 two-dimensional space. The objective of the test was see whether sequences initiated from different points on the surface found the apex. Superimposed on the surface contour plot are the initial and final points of six simulated sequences. The optimal gradient and Simplex methods performed equally well in locating the optimum region. Final conditions were within about half a unit from the apex on the manipulated variable scales. Several factors explain why the sequences failed to converge accurately on the optimum point.

The programs were designed to halt the progression when the response value changed by less than 5% from one step to the next. Thus, in the vicinity of the apex (value = 10), response values were equivalent within ± 0.5 . In addition, the minimum step size was programmed to match the precision of the experimental input settings. As progressions approached the optimum, step size intervals

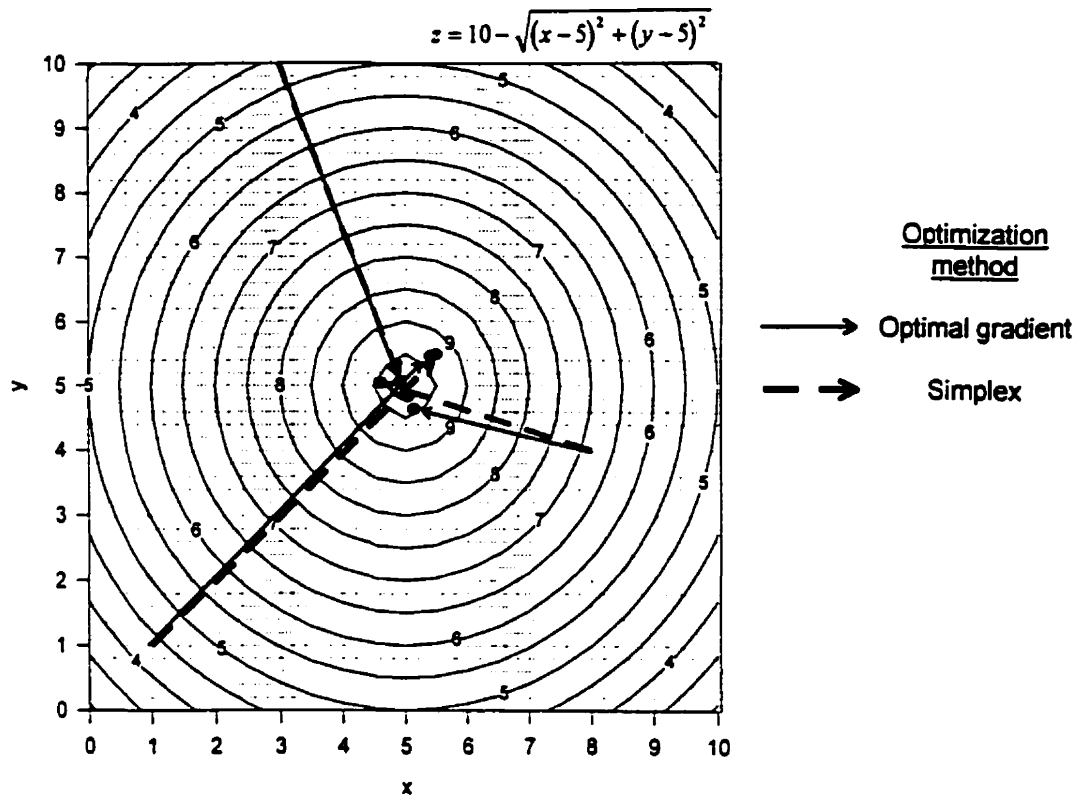


Figure 5.3.2-1: Optimization Paths on a Circular Hill

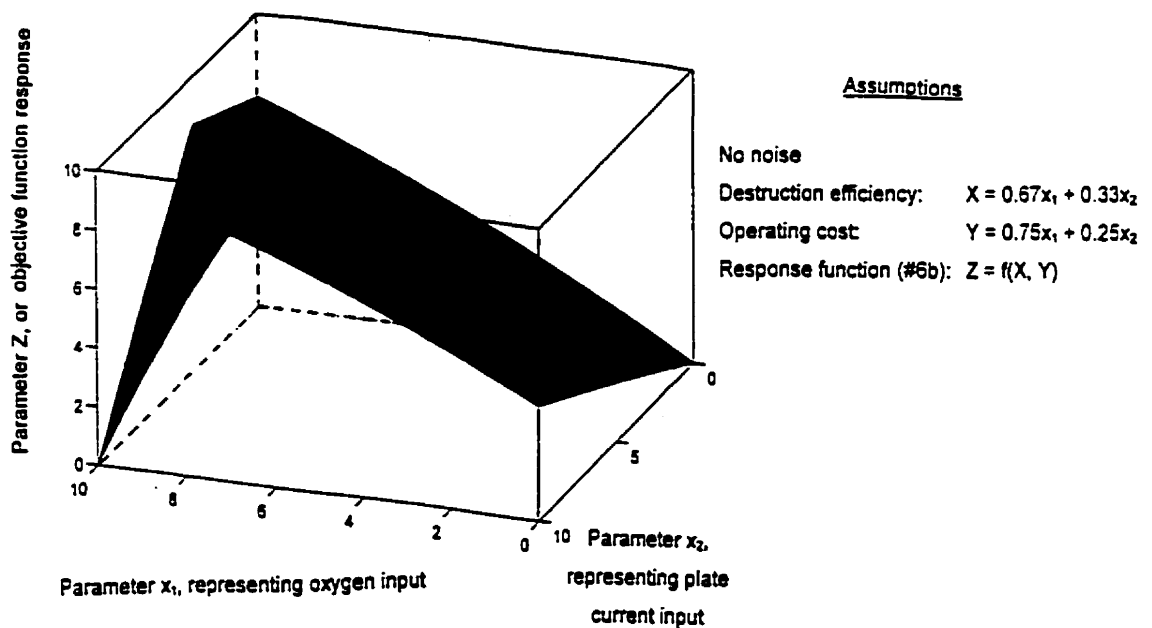


Figure 5.3.2-2: Three-Dimensional View of a Simulated System Response Over the Operating Space

generally decreased. Eventually, the search could no longer narrow onto the optimum with increasingly small steps; rather, it jumped back and forth between equivalent points around the optimum. Had measurement resolution warranted greater precision, sophisticated variations on the optimization techniques could have been programmed. However, the results obtained were adequate in view of experimental measurement uncertainty and system instability.

5.3.2.2 Optimization of a Simulated Noiseless System

The assumption of a fixed correspondence between input settings and destruction efficiency allowed to map the objective function over the operating space. The simulated response surface showed the optimum as a ridge of equally satisfactory input settings. Optimization paths traced on the surface confirmed the ability of the programs to find the best achievable response for the system defined. Unlike this simulation, the response of the experimental system was fluid and could not be mapped.

A relationship was defined between destruction efficiency and the manipulated variables. Based on empirical observations, oxygen was assumed to be twice as effective as plate current. To use the full domain of the objective function, complete destruction was assumed to occur at maximum input ($X = 10, Y = 10$). Zero destruction was referenced at minimum sustaining conditions ($X = 0, Y = 0$). In keeping with the assumption made in the experimental work, oxygen units were assumed to cost three times more than power units. Thus, a response surface was described by the following equations:

Destruction efficiency	$X = 0.67x_1 + 0.33x_2$	
Cost	$Y = 0.75x_1 + 0.25x_2$	(equation set 5.3.2-1)
Objective function	$Z = f(X, Y)$	(equation set 5.3.1-1)

Figures 5.3.2-2 and 5.3.2-3 picture the three-dimensional view and contour plot of the simulated response surface over the operating space. Two distinct regions were separated by a ridge of maximum response. Regions on either side of the ridge corresponded to below-target and above-target zones in the objective function. Differences in surface orientation between the two regions reflected the different priorities within each zone. The ridge was formed of oxygen/current combinations with equivalent results in terms of cost-effectiveness. From this example, it was concluded that points wide apart on the manipulated variable space could produce equally valid optima. This stemmed from a balancing effect in manipulating two variables of which one is more costly but more effective.

Also shown on Figure 5.3.2-3 are the initial and end points of four simulated sequences, all of which successfully reached near-optimal conditions. These sequences demonstrated the influence of initial conditions on sequence end results. Each optimization path followed a direction of ascent toward a point in the optimum region. The location of the end point depended on the initial point. A lesser degree of variability in final conditions was attributed to differences in the computational strategies of the two optimization methods used.

5.3.2.3 Optimization of a Simulated Noisy System

Robustness against noise was essential to the reliability of the optimization strategy. Noise in plasma optical signals caused appreciable uncertainty in the destruction efficiency parameter and, therefore, in the objective response value. To assess the effect of this uncertainty, sequences were simulated on noisy versions of the response surface developed in the preceding section.

The simulation of a noisy response proceeded as follows. Values of destruction efficiency (X) and cost (Y) were tabulated as functions of oxygen and current settings (equation set 5.3.2-1). In other words, X and Y were each expressed as a two-dimensional matrix where each element corresponded to an

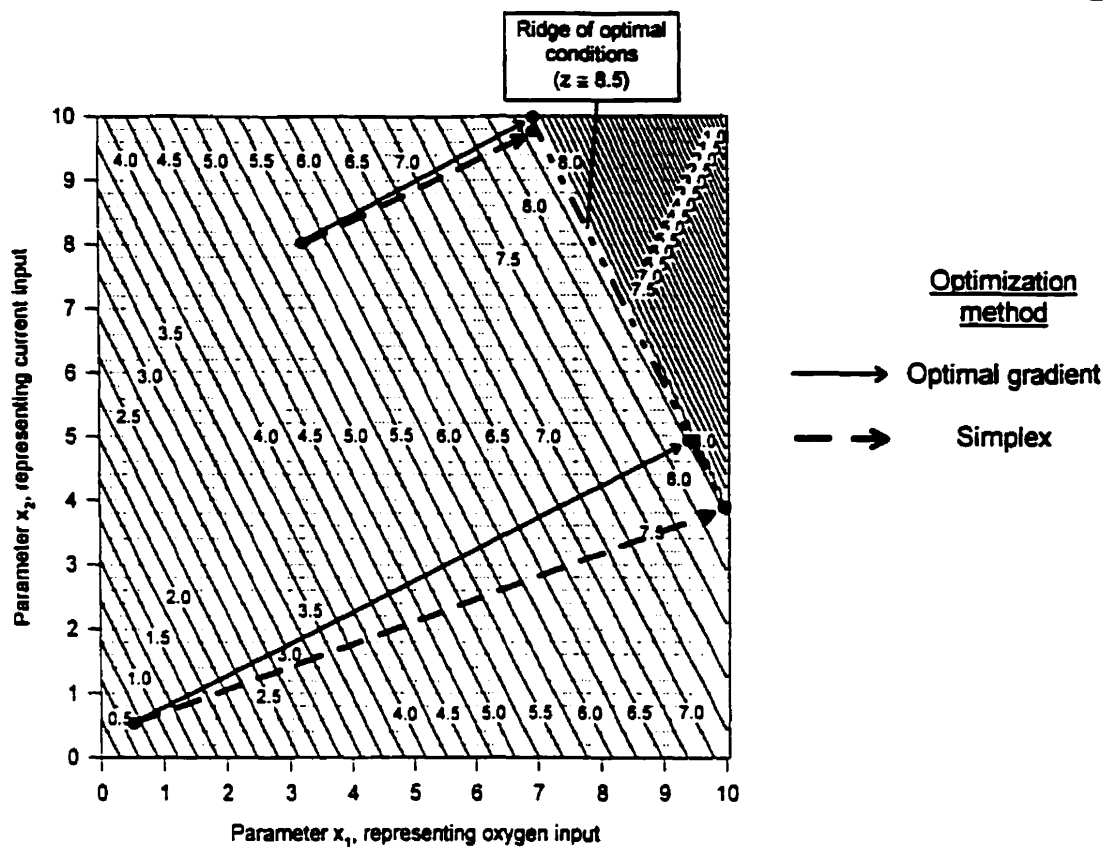


Figure 5.3.2-3: Contour Plot of the Simulated Response with Optimization Paths

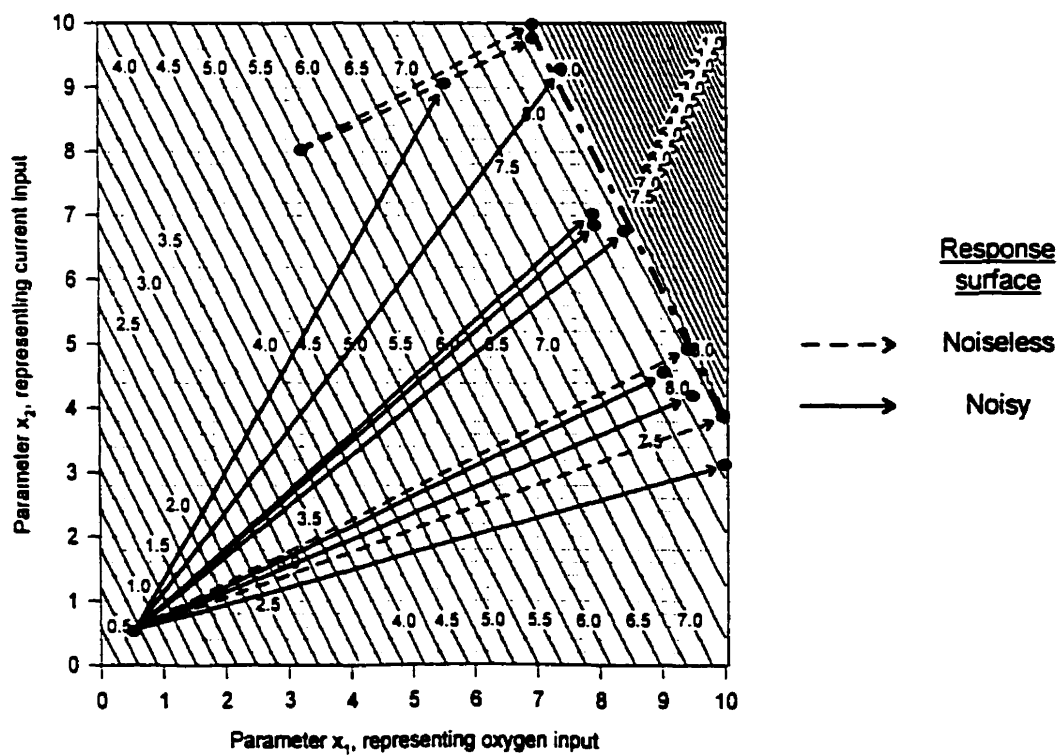


Figure 5.3.2-4: Effect of Noise on Optimization Paths

oxygen/current combination. Uncertainty in X was based on uncertainty in the (S/B) indicator. Uncertainty in Y was estimated from flicker in plate current settings. Uncertainty bounds for X and Y were taken as two standard deviations (95.5% confidence interval in a normal distribution). For each of X and Y, a noise matrix was generated as a set of random numbers with a mean of zero and a matching standard deviation. The noise matrices were added to the tabulated X- and Y-value matrices, producing noisy X and Y matrices. The elements of these noisy matrices served as arguments in the objective function. The outcome was a rough, jagged surface whose overall shape resembled Figure 5.3.2-2. Two types of noise patterns were tested: a uniform distribution, and a normal distribution. A surface was generated for each distribution.

Figure 5.3.2-4 shows the initial and final points of eight sequences simulated on these surfaces - four with each type of noise (the distribution of end points was similar with either type). Comparing these sequences with those performed on a noiseless surface, three observations were made. First, noise scattered the end points around the optimum ridge. Second, it "blurred" the direction of steepest ascent so that sequences with the same starting point ended at different locations along the optimum ridge. Third and most important, noise did not impair the programs' ability to find the region of optimal conditions. It simply reduced accuracy. In all but one case, the final conditions were within about half a unit from an optimum on the manipulated variable scale.

5.3.3 Error Analysis

This section identifies sources of error in the experimental system. Variability in the demonstration results was caused by two types of uncertainty. The first type, called **single-run variability**, related to precision in input settings and optical measurements. This type of error is present in any experimental work. In this project, it defined uncertainty within a single experiment. The second type, called **run-to-run variability**, was caused by variations in system characteristics

between experiments. Factors such as electromagnetic coupling, stability of the plasma discharge, and response to the manipulated variables were not exactly reproducible from one experiment to the next. Consequently, optimizations initiated at similar input load and initial settings gave different results and were not amenable to statistical comparisons.

The present uncertainty analysis examines these two aspects separately. In sections 5.3.3.1 and 5.3.3.2, error propagation calculations establish uncertainty bounds applicable within individual experiments (single-run). These uncertainty limits were used in the formulation of criteria for the optimization algorithms. The propagation of errors through a function was calculated as follows (Holman 1989):

$$\Delta F(x_1, x_2, \dots, x_n) = \sqrt{\left(\frac{\partial F}{\partial x_1} \Delta x_1\right)^2 + \left(\frac{\partial F}{\partial x_2} \Delta x_2\right)^2 + \dots + \left(\frac{\partial F}{\partial x_n} \Delta x_n\right)^2} \quad (\text{equation 5.3.3-1})$$

Section 5.3.3.3 addresses run-to-run variability and its implications for the interpretation of the demonstration results.

5.3.3.1 Uncertainty in Manipulated and Dependent Variables

a) Manipulated variables

The error in plate current was inferred from the flicker range of the needle on the readout dial. Readings were accurate within 0.05 A. This corresponded to 5% of the plate current range, or half a unit in the zero-to-ten operating space.

Propane and oxygen flow rates were set using high-precision control valves and rotameter tubes that provided stable readings. The error in oxygen flow rate was derived from the precision and calibration accuracy of its flowmeter. The readout uncertainty - half the smallest unit on the scale - was equivalent to 0.028 slpm, or

less than 0.5% of the oxygen flow range. The flow rate at a given setting was reproducible within 0.0025 slpm. The cumulative error was 0.031 slpm, or 0.074 unit in the zero-to-ten operating space.

By the same procedure, the uncertainty in propane flow rate was estimated to 0.005 slpm, or $\approx 5\%$ of the propane flow range. This represented less than 0.01% of the total gas flow. Concentration figures (expressed in percentage of the total flow) were precise to 0.01%, taking into account the fluctuations in total flow caused by oxygen input manipulation.

b) Dependent variables

Uncertainty in the destruction efficiency parameter (X) depended on the error in optical indicator values (S/B). Uncertainty in the cost parameter (Y) depended on the uncertainties in oxygen content (x_1) and in plate current (x_2). From section 4.3.1.2, the defining equations for X and Y were:

$$X = 23.33 - 13.33 \left(\frac{S}{B} \right) \quad (\text{equation 4.3.1-1})$$

$$Y = 0.75x_1 + 0.25x_2 \quad (\text{equation 4.3.1-2})$$

It was just established that:

$$\begin{aligned} \Delta x_1 &= 0.074 \\ \Delta x_2 &= 0.5 \end{aligned} \quad (\text{equation set 5.3.3-2})$$

By substitution into equation 5.3.3-1, uncertainty in the cost parameter (on a full scale of 10) was calculated as:

$$\Delta Y = \sqrt{(0.75 * 0.074)^2 + (0.25 * 0.5)^2} = 0.14 \quad (\text{equation 5.3.3-3})$$

Uncertainty in (S/B) was estimated from the data presented in Tables 5.1.2-2 and 5.1.2-3. The relative standard deviation of (S/B) measurements was less than or close to 1%. The absolute standard deviation was of the order of 0.01.

The absolute error was taken as two standard deviations, or 0.02. This definition provides a confidence level of 95.45% if dominant error sources have a normal distribution (Ingle and Crouch 1988).

$$\Delta\left(\frac{S}{B}\right) = 0.02 \quad (\text{equation 5.3.3-4})$$

Using equations 4.3.1-1 and 5.3.3-4, uncertainty in the efficiency parameter (on a full scale of 10) was calculated as:

$$\Delta X = \sqrt{(-13.33 * 0.02)^2} = 0.27 \quad (\text{equation 5.3.3-5})$$

5.3.3.2 Error Propagation Through the Objective Function

Uncertainty in the optimization criterion Z (the objective function defined by equation set 5.1.3-9) was calculated by substituting its partial derivatives ($\partial Z/\partial X$, $\partial Z/\partial Y$) and the contributing errors (ΔX , ΔY) into equation 5.3.3-1. Since the numerical values of the derivatives depended on X and Y, the error in Z was a function of X and Y. Table 5.3.3-1 lists absolute and relative errors in Z over a region of the objective function domain. For reasons of stability, most experiments were restricted to $Y < 6$. The highest Y-values generally occurred at the start of over-treatment sequences.

Uncertainty in Z was most important near the end of an optimization. The decision to terminate a sequence depended on whether the benefit of an additional step exceeded uncertainty in the response. In this situation, the efficiency parameter was close to its target value ($X_0 = 8$). Cost depended on propane input and was usually in the lower third of the range ($Y < 4$). Estimates of the relative error in Z at near-optimal conditions appear in bold characters in Table 5.3.3-1. In this part of the domain, the error was close to or less than 5%. Accordingly, 5% uncertainty was assumed in the response values (Z) as a sequence approached an optimum.

Table 5.3.3-1: Error Propagation Through the Objective Function

X	Y	Z	dZ/dX	dZ/dY	error in X (absolute)	error in Y (absolute)	error in Z (absolute)	error in Z (relative)
X < 8								
4.0	1.0	4.90	1.225	-0.100	0.27	0.14	0.33	6.7%
4.0	2.0	4.80	1.200	-0.100	0.27	0.14	0.32	6.7%
4.0	4.0	4.60	1.150	-0.100	0.27	0.14	0.31	6.7%
4.0	6.0	4.40	1.100	-0.100	0.27	0.14	0.29	6.7%
6.0	1.0	7.35	1.225	-0.150	0.27	0.14	0.33	4.5%
6.0	2.0	7.20	1.200	-0.150	0.27	0.14	0.32	4.5%
6.0	4.0	6.90	1.150	-0.150	0.27	0.14	0.31	4.5%
6.0	6.0	6.60	1.100	-0.150	0.27	0.14	0.29	4.5%
8.0	1.0	9.80	1.225	-0.200	0.27	0.14	0.33	3.3%
8.0	2.0	9.60	1.200	-0.200	0.27	0.14	0.32	3.3%
8.0	4.0	9.20	1.150	-0.200	0.27	0.14	0.31	3.4%
8.0	6.0	8.80	1.100	-0.200	0.27	0.14	0.29	3.4%
X > 8								
8.0	1.0	9.80	-0.490	-0.200	0.27	0.14	0.13	1.4%
8.0	3.0	9.40	-1.410	-0.200	0.27	0.14	0.38	4.0%
8.0	4.0	9.20	-1.840	-0.200	0.27	0.14	0.49	5.3%
8.0	5.0	9.00	-2.250	-0.200	0.27	0.14	0.60	6.7%
8.0	6.0	8.80	-2.640	-0.200	0.27	0.14	0.71	8.0%
8.5	1.0	9.56	-0.490	-0.440	0.27	0.14	0.14	1.5%
8.5	3.0	8.70	-1.410	-0.420	0.27	0.14	0.38	4.4%
8.5	4.0	8.28	-1.840	-0.410	0.27	0.14	0.49	6.0%
8.5	5.0	7.88	-2.250	-0.400	0.27	0.14	0.60	7.7%
8.5	6.0	7.48	-2.640	-0.390	0.27	0.14	0.71	9.5%
9.0	1.0	9.31	-0.490	-0.680	0.27	0.14	0.16	1.7%
9.0	3.0	7.99	-1.410	-0.640	0.27	0.14	0.39	4.8%
9.0	4.0	7.36	-1.840	-0.620	0.27	0.14	0.50	6.8%
9.0	5.0	6.75	-2.250	-0.600	0.27	0.14	0.61	9.0%
9.0	6.0	6.16	-2.640	-0.580	0.27	0.14	0.71	11.5%
9.5	1.0	9.07	-0.490	-0.920	0.27	0.14	0.18	2.0%
9.5	3.0	7.29	-1.410	-0.860	0.27	0.14	0.39	5.4%
9.5	4.0	6.44	-1.840	-0.830	0.27	0.14	0.50	7.8%
9.5	5.0	5.63	-2.250	-0.800	0.27	0.14	0.61	10.9%
9.5	6.0	4.84	-2.640	-0.770	0.27	0.14	0.71	14.7%

Note: estimates in bold characters apply in the vicinity of optima.

Elsewhere in the domain, the uncertainty propagation formula predicted errors exceeding 5%. These figures applied to worst-case scenarios: the analysis assumed fixed upper-bound uncertainty values for X and Y, whereas actual values depended on the stability of the plasma jet. In Table 5.3.3-1, regions where the calculated error exceeds 5% correspond to conditions rarely in effect during the demonstrations. They do not represent operating conditions near an optimum. For example, X-values greater than 9 occurred occasionally at the start of over-treatment sequences, when high propane destruction made the jet stable. In these instances, the X- and Y-error estimates of Table 5.3.3-1 exceeded the actual values. Thus, uncertainty in Z was overestimated in these regions.

5.3.3.3 Run-to-Run Variability in System Response

The result of a sequence was a final combination of destruction efficiency and cost values. The optimization criterion (Z) allowed trade-offs between these variables. Thus multiple combinations could meet a given response value. Points located along isometric lines on the objective function contour plot were equivalent in terms of the criterion. Run-to-run variability resulted in a movable response surface (Z) over the oxygen-current space (x_1 , x_2).

An indication of run-to-run variability was that a fixed oxygen-current combination did not map to the same destruction efficiency state in different experiments. This variability was assessed by comparing initial (S/B) readings among optimization sequences with a common starting point. Table 5.3.3-2 presents three groups of initial points. Within each group, (S/B) values are listed for the starting points of under-treatment and over-treatment simulations. The first two groups had identical input settings but were obtained in different time periods. The third group used different input settings following a major change in system response.

Table 5.3.3-2: Run-to-Run Variability in (S/B) Readings At Similar Input Conditions

Time period	Aug. 6 to Nov. 5, 1998		Dec. 16 to March 14		March 2 to 14, 1999	
Propane input	0.20%	0.15%	0.20%	0.15%	0.26%	0.17%
Sequence type	under-treatment	over-treatment	under-treatment	over-treatment	under-treatment	over-treatment
Starting point (oxygen, current)	(0.5, 0.5)	(5, 5)	(0.5, 0.5)	(5, 5)	(0.5, 0.5)	(5, 5)
(S/B) at the starting point	1.350	1.084	1.436	1.1	1.461	1.082
	1.348	1.073	1.379	1.092	1.468	1.115
	1.242	1.091	1.352	1.098	1.485	1.11
	1.373	1.096	1.271	1.117	1.313	1.104
	1.518	1.088	1.261	1.081		1.124
	1.468	1.097	1.253			1.105
	1.437	1.040	1.291			1.107
	1.493	1.049	1.255			1.104
	1.378	1.034				1.065
	1.474	1.044				1.072
	1.460					
	1.468					
	1.350					
(S/B) average	1.41	1.07	1.31	1.10	1.43	1.10
Standard deviation	0.08	0.03	0.07	0.01	0.08	0.02
Rel. std. dev. (RSD)	5.6%	2.4%	5.2%	1.2%	5.6%	1.7%
(S/B) uncertainty or 2*(std dev.)	0.16	0.05	0.14	0.03	0.16	0.04
Average value of X	4.50	9.07	5.84	8.70	4.24	8.68
Uncertainty in X (cf. equation 5.3.3-5)	2.1	0.7	1.8	0.3	2.1	0.5

Standard deviations in (S/B) measurements between runs averaged 1.8% for over-treatment and 5.5% for under-treatment. The difference is explained by the destabilizing effect of propane on the plasma. Uncertainty in (S/B), defined as two standard deviations, averaged 0.04 and 0.15. By equation 5.3.3-5, the corresponding uncertainties in X were 0.5 unit for over-treatment and 2.0 units for under-treatment. In contrast, the uncertainty in X within a single run was 0.27 unit.

The data of Table 5.3.3-2 applied to under-treatment and over-treatment situations. Optimization sequences did not share a common end point, so no similar data set was available for operating conditions near the optimum. It was deemed valuable to examine how run-to-run variability would manifest itself if one attempted to reproduce the final conditions of an optimization at a given propane load. This required an estimate of the variability near the destruction efficiency target ($X \approx 8$). As an approximation, one could interpolate between the variability observed in the under-treatment and over-treatment situations described in Table 5.3.3-2 (respectively, $\Delta X \approx 2.0$ at $X \approx 4.9$ and $\Delta X \approx 0.5$ at $X \approx 8.8$). This led to an estimated variability of ± 1.0 unit in the observed destruction efficiency at fixed input settings near an optimum.

In the context of the optimization strategy, run-to-run variability in destruction efficiency (X) implied variability in the input settings - and cost - that met the target $X_0 = 8$. The objective function was designed to drive the optimization towards the target. Hence sequence end points approached the line $X_0 = 8$. The spread of points along the cost axis (Y) attested their different oxygen and current settings. At a fixed model compound load, three factors could contribute to the spread in final cost values.

The first factor was the multiplicity of efficiency and cost combinations (X, Y) with the same response value. This would explain a cost difference between points located on an isometric line. The second factor was the multiplicity of oxygen-

current combinations that met a given destruction efficiency. These two contributions were limited by the cost-efficiency objective built into the optimization algorithm: the system sought the least expensive settings at which $X_o = 8$. The third and dominant factor was run-to-run variability in the state and response of the system.

The following example illustrates the effect of this variability on optimization results. Consider a sequence ending with $X \approx 8$ at a given set of oxygen-current settings. If run-to-run variability in X was ± 1.0 unit, the same settings could give anywhere from $X = 7$ to $X = 9$ in subsequent experiments. Consequently, these experiments would approach the efficiency target ($X_o = 8$) at different input settings and costs - hence the dispersion of end points along the cost axis in the demonstrations.

In conclusion, the usual concept of reproducibility did not apply to the optimization sequences presented in the next section. Controllability in the input of a system is essential for the predictability of its response. The experimental system did not meet this requirement. The efficiency of power transfer to the plasma was neither controllable nor measurable. The state and response of the plasma depended on unpredictable interactions between electromagnetic and equipment factors. These considerations were taken into account in the interpretation of experimental results. Sequences were not compared statistically but examined on a case-by-case basis.

5.3.4 Experimental Optimization Sequences

This section presents optimization sequences performed on the afterburner model using both the optimum gradient and Simplex methods. These sequences demonstrated adaptive response to under-treatment and over-treatment.

Under-treatment sequences were initiated with a high model compound load at low current and oxygen settings. Destruction efficiency was below the target at the start of the optimization. Successive steps brought the system to optimal conditions, i.e., target-level efficiency at a minimum cost. Over-treatment sequences started with a light load at high settings. Destruction efficiency initially exceeded the target level. The optimization proceeded toward the efficiency target along the most cost-efficient path.

To facilitate interpretation, selected combinations of propane load and initial settings were used repeatedly. Propane loads were chosen so that the efficiency target would lie within operating limits and above minimum sustaining conditions. Initially, under-treatment and over-treatment sequences used 0.20% and 0.15% propane respectively (August 1998 - February 1999 period). These settings were subsequently replaced by 0.26% and 0.17% following uncontrollable changes in system characteristics (March 1999). Starting points were designated by their coordinates on the manipulated variable space (x_1 , x_2). Under-treatment sequences were usually initiated at (0.5, 0.5); over-treatment ones, at (5, 5).

Two methods were used to represent sequences graphically. The first type of chart mapped optimization steps on the manipulated variable space with oxygen content and plate current settings as the axes. This type provided no information on effectiveness or performance. For this reason, a response value (Z) sometimes appeared next to a point. The second type of chart superimposed the sequence path on a contour plot of the optimization criterion, or objective function (equation set 5.3.1-1). The axes of this chart represented destruction efficiency (X) and cost (Y). The contour lines (Z) indicated response values for (X , Y) combinations in the domain. The purpose of this plot was to illustrate progression from an unsatisfactory state (under- or over-treatment) to one that satisfied the cost-effectiveness objective.

Both the optimal gradient and Simplex optimization methods used exploratory measurements to direct the search. To facilitate visualization, the charts showed only the main optimization steps. The number of measurements in each step depended on the method used and on the response obtained (see Appendices VIII and IX for details on the procedures). In multiple-sequence plots, individual sequences were represented by their initial and final points.

5.3.4.1 Gradient-Based Method

This algorithm found the path of steepest ascent on the response surface. Its *optimal gradient* and *prediction gradient* versions performed equally well in the present application.

Figure 5.3.4-1 maps typical optimal gradient sequences on the operating space. Smooth paths are characteristic of gradient search techniques. Figure 5.3.4-2 shows the corresponding progressions on the objective function surface. Note the change in response value (contour lines) from beginning to end. As intended in the design of the function, the final conditions approached the efficiency target ($X_o = 8$). End point locations depended on the input load. This explains why over-treatment simulations (at low propane input) ended with lower cost and higher response values than under-treatment simulations. Figure 5.3.4-3 pictures a second set of sequences performed with the same propane load and initial settings. The two paths were oriented differently on the manipulated variable space. This means that the system responded differently to the variables in the two experiments.

Generally, one normalized oxygen unit had more impact on destruction efficiency than one plate current unit. This effect was responsible for the preferential use of oxygen in many sequences.

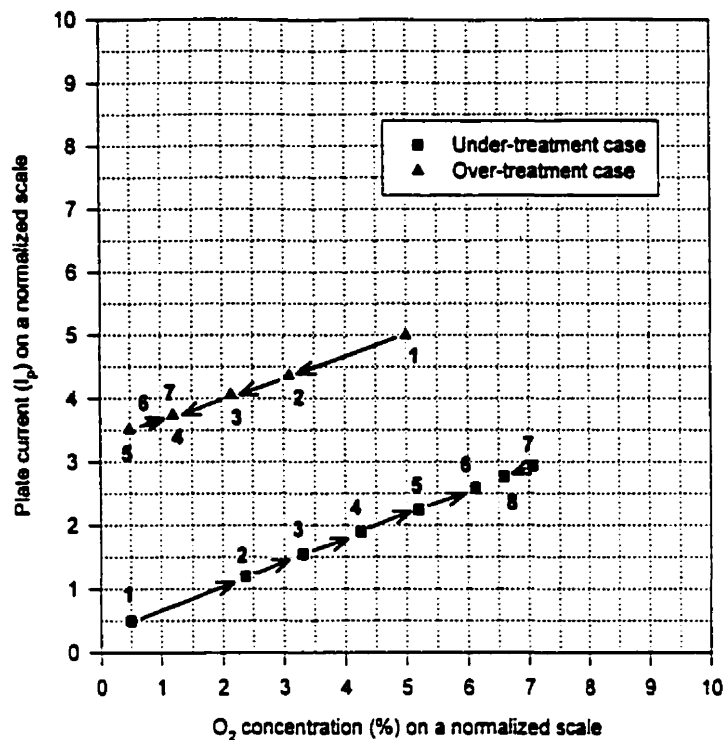


Figure 5.3.4-1: Optimal Gradient Sequence Paths

The numbers indicate optimization steps.

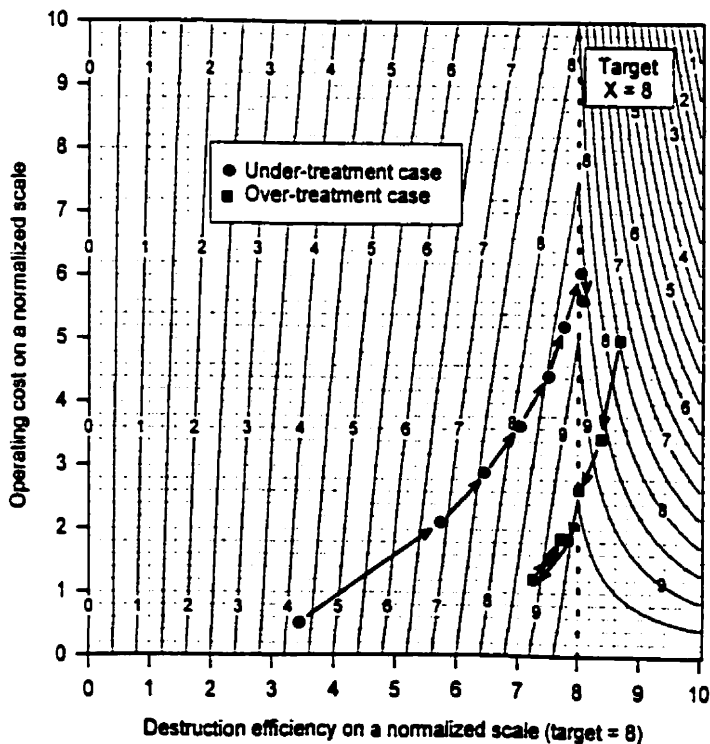


Figure 5.3.4-2: Optimal Gradient Paths on the Objective Function Contour Plot

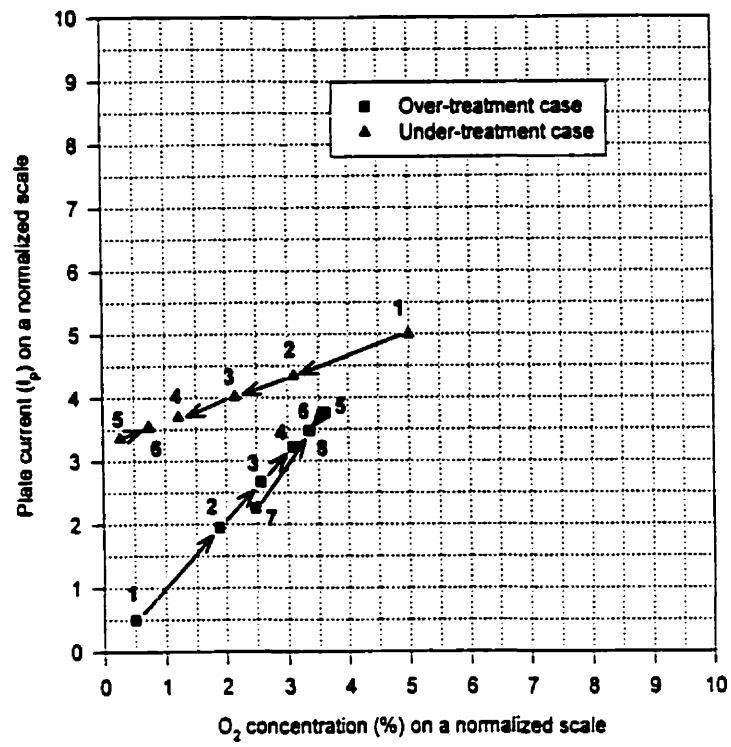


Figure 5.3.4-3: Optimal Gradient Sequence Paths

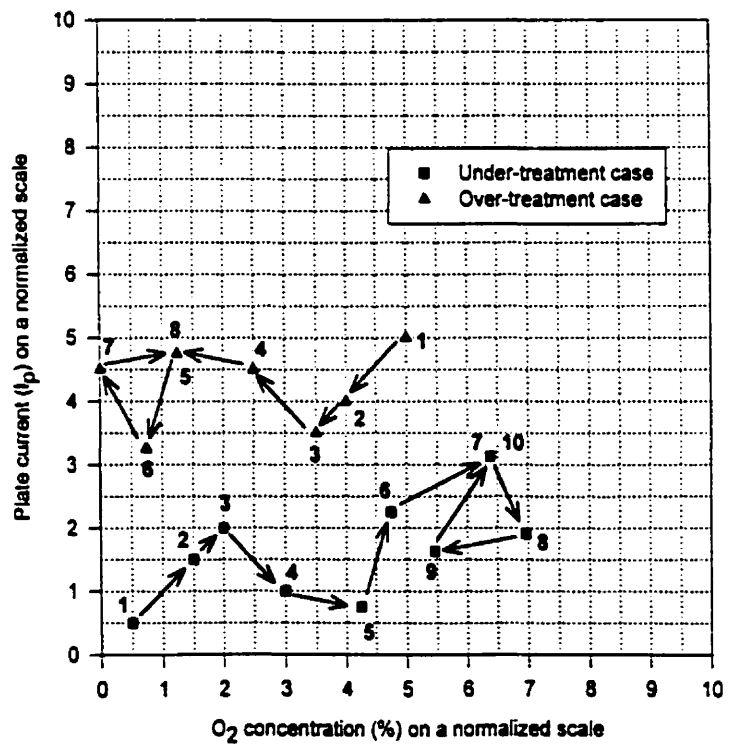


Figure 5.3.4-4: Simplex Sequence Paths

The numbers indicate optimization steps.

The optimization program offered the choice of optimal and prediction gradient strategies. (Recall the difference in decision criteria: optimal gradient used measured responses, while prediction gradient used linear predictions). Given the same operating points and response values, optimal and prediction gradient sequences were practically identical. This confirmed the adequacy of linear surface modeling at the scale of the optimization steps. There appeared to be no advantage in using the prediction gradient strategy for the demonstrations. This method best applies to well-characterized systems where prior information about the response surface guides the choice of decision criteria. The optimal gradient method, based on measurements only, applies regardless of surface characteristics. It is the recommended option for controlled operation of an adaptive plasma afterburner.

5.3.4.2 Simplex Method

While gradient-based methods used linear modelling to find the direction of steepest ascent, Simplex moved by trial-and-error. The empirical search proceeded by selection and rejection of test points whose locations were determined by triangular geometric constructions.

The sequences represented by Figures 5.3.4-4 to 5.3.4-6 were analogous to those of Figures 5.3.4-1 to 5.3.4-3. Initial conditions were identical; only the optimization method differed. The scattered or chaotic appearance of the paths is characteristic of the Simplex technique. Final conditions matched those obtained with the optimal gradient method. The contour plots (Figures 5.3.4-2 and 5.3.4-5) indicate similar performance in both sequence sets.

5.3.4.3 Comparative Evaluation of Optimization Methods

Figure 5.3.4-7 shows a collection of under-treatment sequences. The variability in end point locations is explained in section 5.3.4.4. The interspersion of optimal

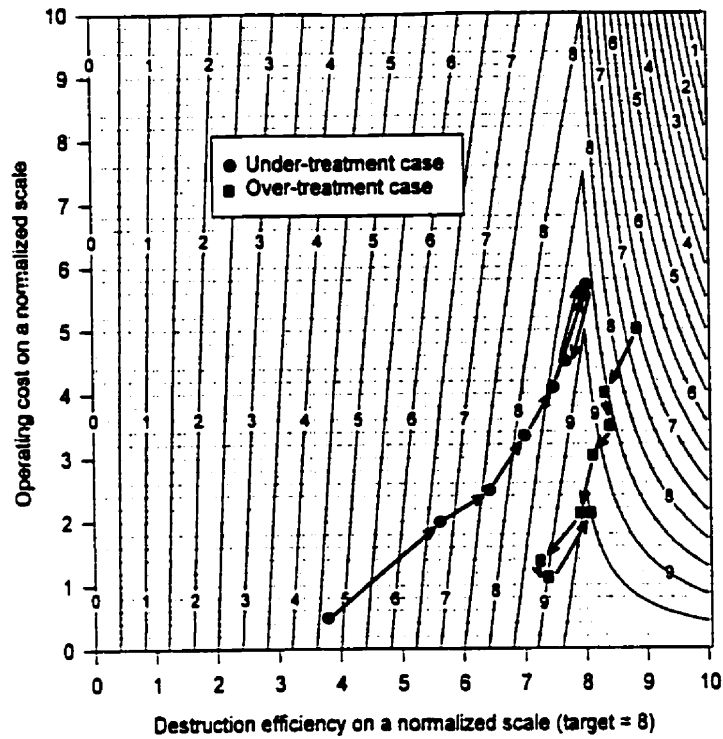


Figure 5.3.4-5: Simplex Paths on the Objective Function Contour Plot

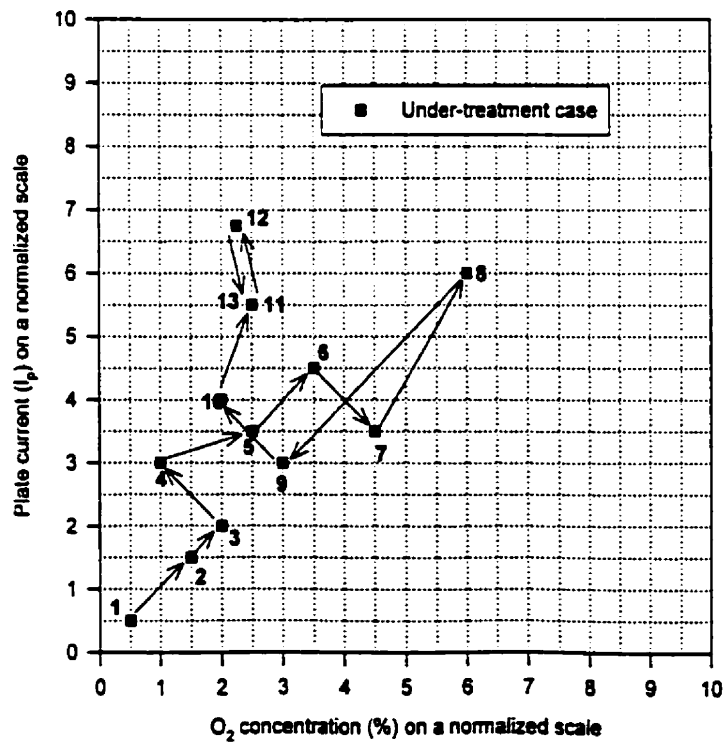


Figure 5.3.4-6a: Simplex Sequence Path

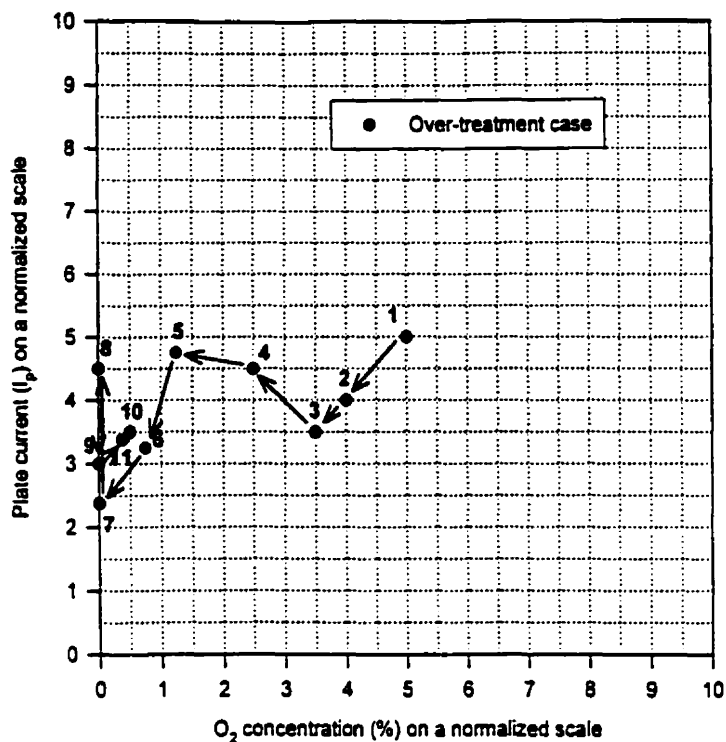


Figure 5.3.4-6b: Simplex Sequence Path

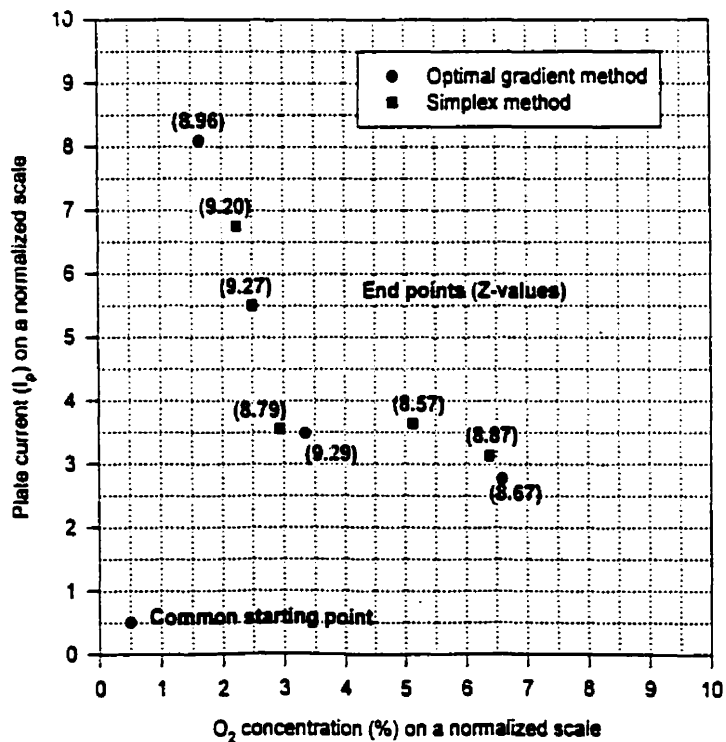


Figure 5.3.4-7: End Point Comparison of Optimization Methods

Under-Treatment Case with 0.2% C_3H_8
Time period: Aug. 31 - Nov. 4, 1998

gradient and Simplex points showed that the choice of method was not a dominant source of variation. End points obtained with either method had similar response values (Z). Figure 5.3.4-8 locates these points on the dependent variable space (the objective function contour lines are omitted for clarity). The starting point mapped to different initial states, signalling run-to-run variability in system response. Again, the interspersed optimal gradient and Simplex points indicated the interchangeability of these methods. This observation also applied to over-treatment situations. The end points in Figure 5.3.4-9 spanned a region of acceptable optima despite apparent scatter. Figure 5.3.4-10 confirms that these points were equally valid with respect to the cost-efficiency objective. There was no evidence of variation due to the optimization method.

Both methods were used, sometimes interchangeably and sometimes to accommodate experimental goals. For example, the effect of assigned cost weights on the use of oxygen and plate current was best seen in the smooth paths of optimal gradient sequences. In most other instances, Simplex was preferred for its robustness under noisy conditions.

Noise and instability affected the orientation of calculated gradients. Irregularities during the first gradient evaluation could launch the sequence in an unfavourable direction. Such errors were corrected over a number of steps by successive re-directions, but carried a cost in efficiency. Since the Simplex algorithm relied on the ranks of test points rather than on response values, it was less sensitive to noise and instability. However, Simplex sequence paths were less directly targeted than gradient paths, as seen in Figures 5.3.4-4 and 5.3.4-6. The initial vertices had to be positioned to promote exploratory moves in both manipulated variables. A poor choice of vertices could narrow the scope of the search.

Like most optimization methods, both optimal gradient and Simplex showed limitations near a ridge. A simple solution to this difficulty was to re-initialize the search on a finer scale in the vicinity of the optimum.

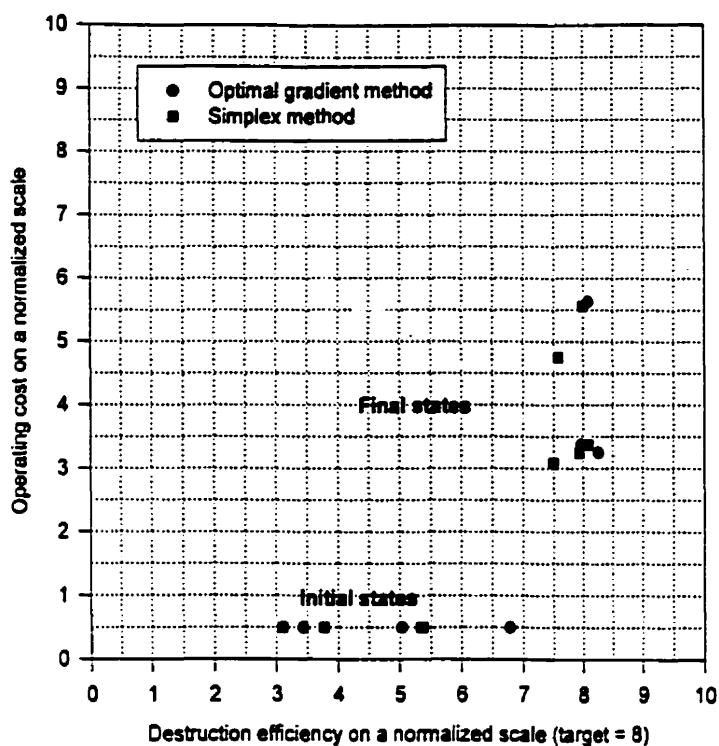


Figure 5.3.4-8: Performance Comparison of Optimization Methods
Under-Treatment Case with 0.2% C_3H_8
Time period: Aug. 31 - Nov. 4, 1998

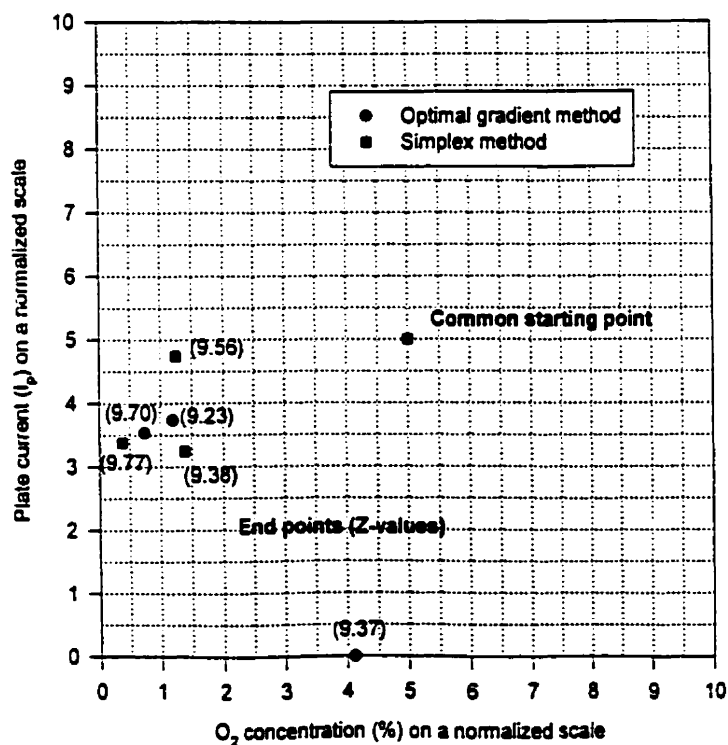


Figure 5.3.4-9: End Point Comparison of Optimization Methods
Over-Treatment Case with 0.15% C_3H_8
Time period: Aug. 31 - Nov. 4, 1998

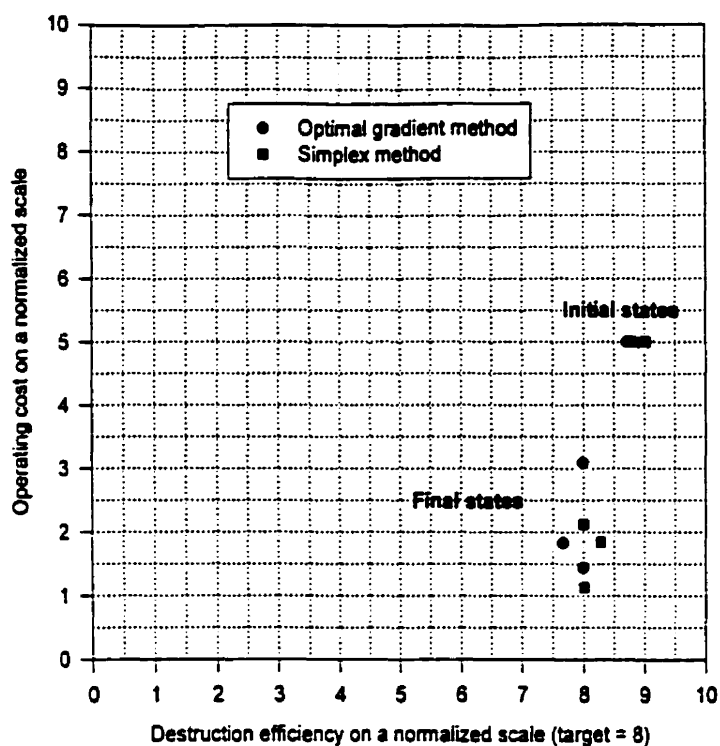


Figure 5.3.4-10: Performance Comparison of Optimization Methods
Over-Treatment Case with 0.15% C_3H_8
Time period: Aug. 31 - Nov. 4, 1998

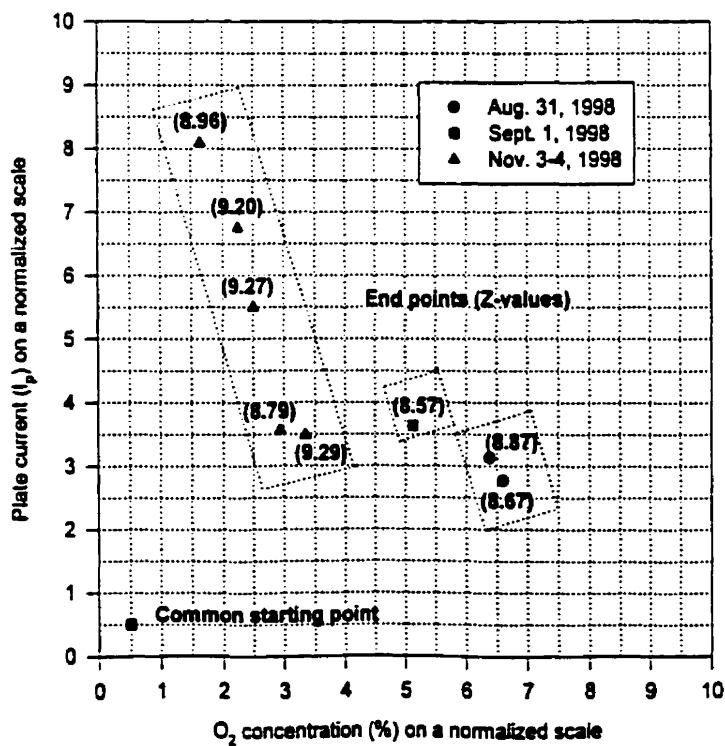


Figure 5.3.4-11: Variations in the Location of the Optimum Region Over Time
Under-Treatment Case with 0.2% C_3H_8

In conclusion, the methods were equally effective as applied in the present work. In other circumstances, for example at higher precision, the methods might perform differently. The investigation of algorithm factors that influence performance, such as initial Simplex size and gradient step size adjustment, was beyond the scope of this project.

5.3.4.4 Reproducibility

Optimal conditions did not correspond to a unique combination of oxygen and plate current settings. The optimum was a set of equivalent combinations along a smooth curve on the operating space. The position of this optimal ridge could vary between experiments. This point is illustrated in Figures 5.3.4-11 and 5.3.4-12, which feature under-treatment sequences with identical feed load and initial settings. The sequences were grouped into three sets. Run-to-run variability was relatively low within each set but was important between sets. Figure 5.3.4-11 demonstrates variability in the location of the optimum region. In Figure 5.3.4-12, each set of end points corresponds to a distinctive cost level. Meeting the destruction efficiency target required different treatment conditions for each set.

The proximity of the end points to the destruction efficiency target varied. This as an unforeseen shortcoming of the methodology. A 5% response change criterion was used to determine the optimum; i.e., sequences were terminated when responses at exploratory points varied by less than 5%. This criterion was based on upper-bound uncertainty estimates for the objective function (section 5.3.3.2). Depending on plasma stability, the 5% interval could exceed actual measurement uncertainty. This could cause early termination of small-scale searches near the optimum, when response changes were less than 5%. This hypothesis was supported by sequence data for the two points located near $X = 7.5$ in Figure 5.3.4-12. In both cases, a 3.3% criterion would have allowed the local search to proceed closer to the optimum. The propagated error near the points in question was calculated to be 3.7% at most (Table 5.3.3-1). Had this

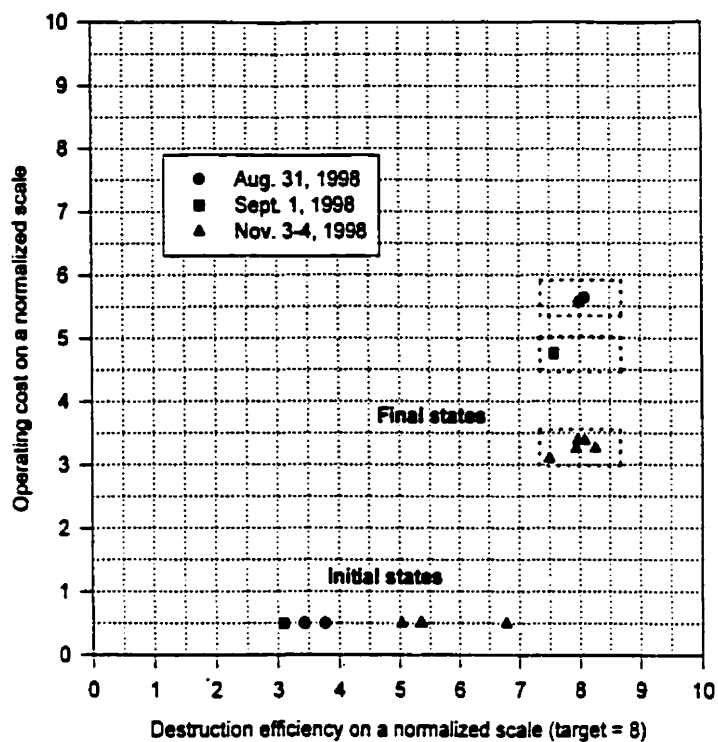


Figure 5.3.4-12: Variations in System Response Under-Treatment Case with 0.2% C_3H_8

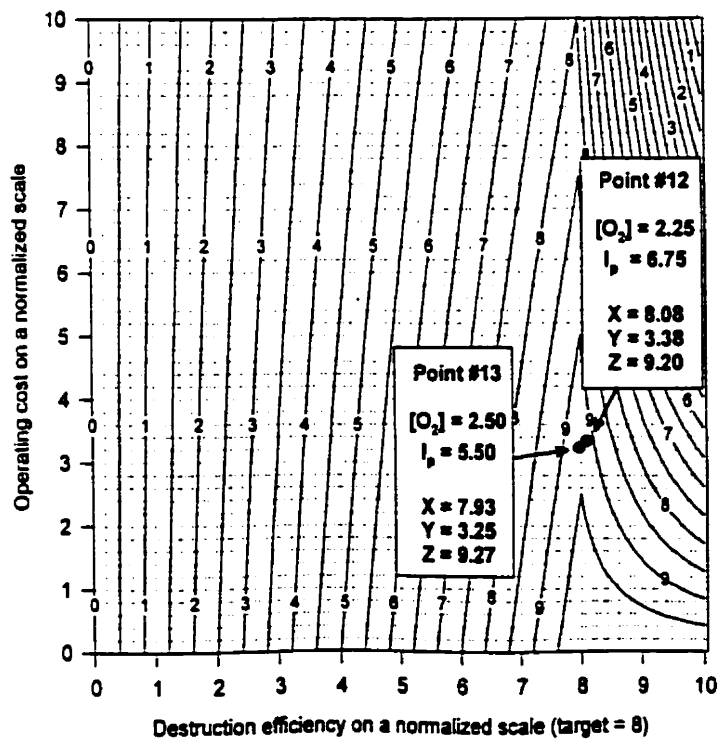


Figure 5.3.4-13: Approaching the Optimum Ridge on the Response Surface Under-Treatment Case with 0.2% C_3H_8

problem been identified early in the work, it could have been alleviated by using a more discriminatory criterion in small-step searches near the optimum. With accurate assessment of error propagation over the domain of the objective function, the criterion could be a programmed function of position in the domain.

Given the multiplicity of optima, variability in end points did not necessarily imply poor reproducibility or poor performance. The decision to terminate a sequence could involve a close call between points that were nearly equivalent yet apart on the manipulated variable space. For instance, Figure 5.3.4-13 provides details on points #12 and #13 of the sequence traced in Figure 5.3.4-6a. Both points closely approached the destruction efficiency target, and their response values were similar enough for the sequence to end at either point.

The location of an end point could depend on the starting position. Figure 5.3.4-14 shows sequences initiated from different points ending at nearby locations in the optimum region. This chart also exemplifies a case of exact equivalence (in destruction efficiency, cost, and response) between two end points. In Figure 5.3.4-15, the interspersing of end points from sequences with different initial states shows that the starting point had no effect on optimization performance. Of course, end point locations could also be influenced by search algorithm parameters such as the choice of Simplex vertices.

A possible contribution to the dispersion of end points within the optimum region is the variability in plasma sensitivity to oxygen content and plate current. The relative effects of these variables determined the orientation of the paths. Figure 5.3.4-16 represents an exceptional set of experiments in which the effect of oxygen was almost negligible compared to that of plate current. Both under-treatment and over-treatment progressions used mostly current because of its predominant impact on destruction efficiency. Oxygen was used in the refined search near the optimum. These examples demonstrate how the optimization strategy adapted to variations in system response.

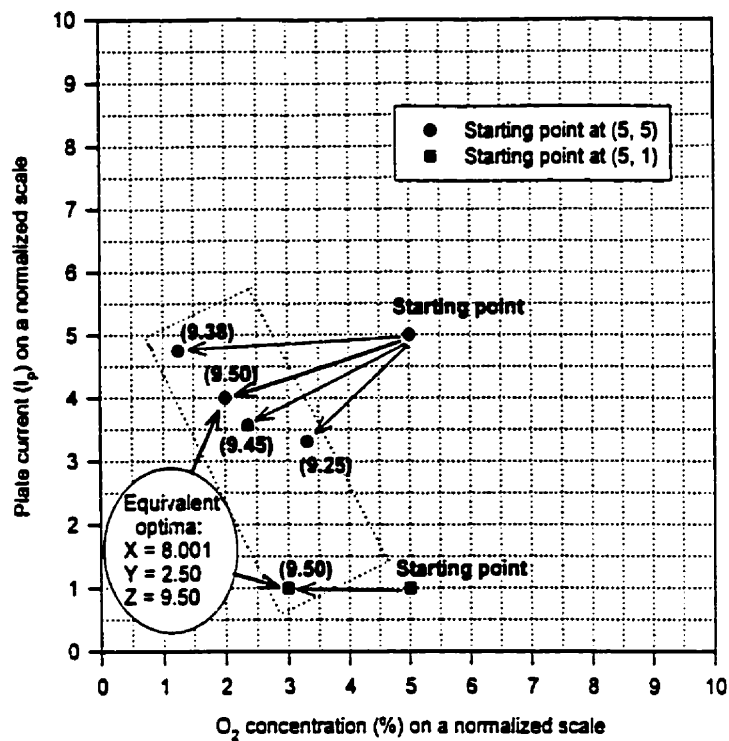


Figure 5.3.4-14: Influence of the Starting Point on the Location of the End Point within the Optimum Region Over-Treatment Case with 0.17% C_3H_8

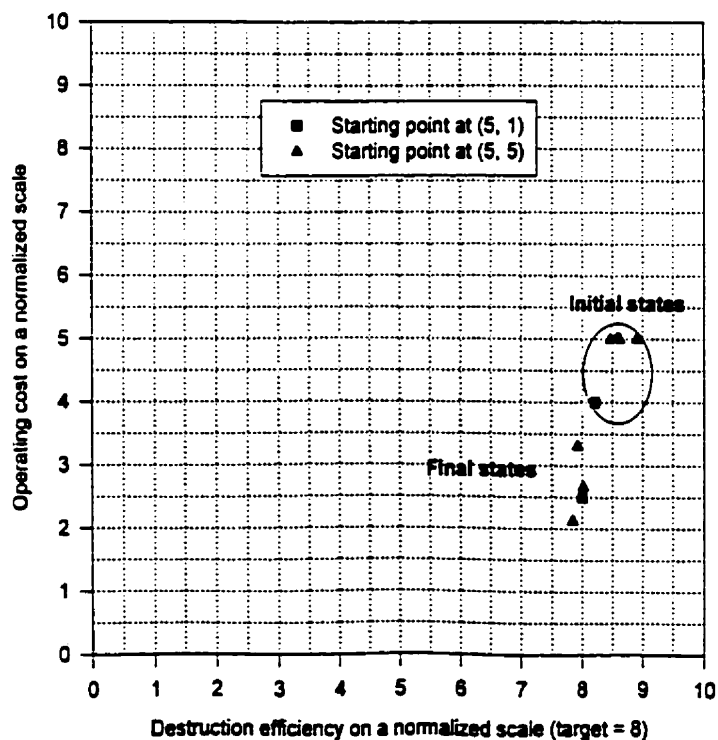


Figure 5.3.4-15: Equivalent Optima Reached From Different Starting Points Over-Treatment Case with 0.17% C_3H_8

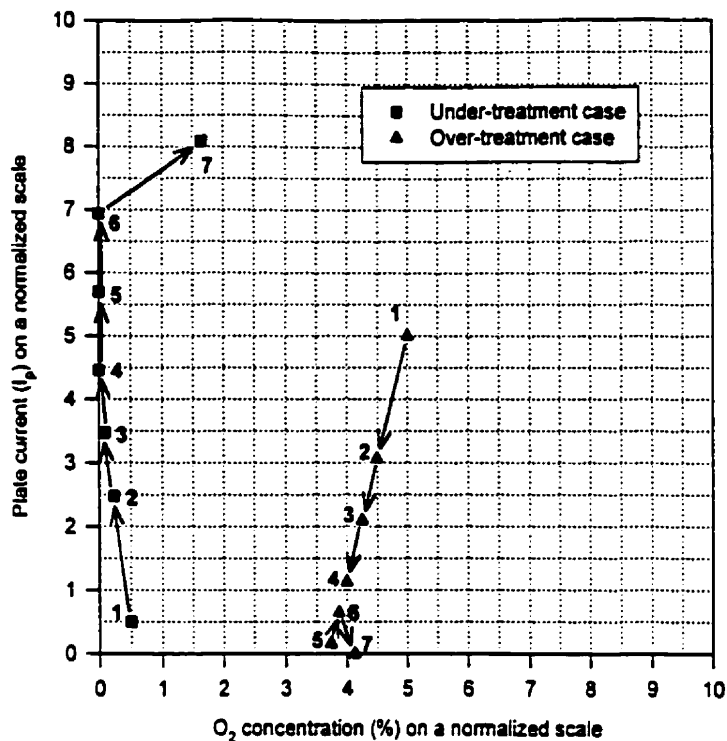


Figure 5.3.4-16: Predominant Effect of Plate Current on Destruction Efficiency
Numbers indicate optimization steps.

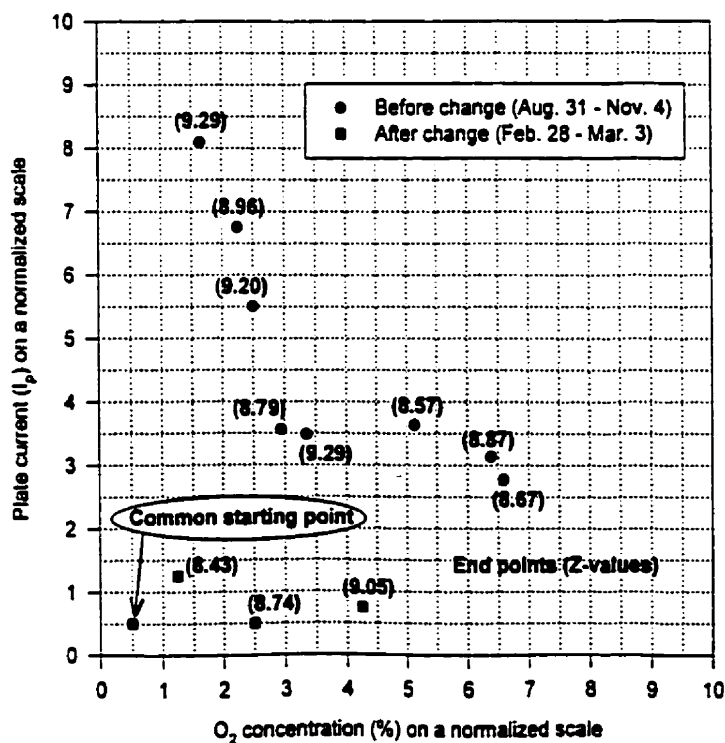


Figure 5.3.4-17: Effect of System Change on Optimization End Points
Under-Treatment Case with 0.2% C₃H₈

Occasionally, clear evidence of change in energy transfer efficiency between the torch and plasma gas was observed. This phenomenon shifted the position of the optimum region and changed the response to the manipulated variables. Figure 5.3.4-17 illustrates the result of an increase in thermal efficiency. The change followed a period when the generator was used for other purposes; its cause was unidentified. As seen on the chart, experiments performed after the change contrasted sharply with previous ones. For the same input load, final conditions were far milder. Unit steps in manipulated variables produced barely detectable changes in response. This low sensitivity reduced the accuracy of the search. Two of the three sequences ended early for lack of change in response. They consequently failed to approach the efficiency target as closely as previous sequences, as seen on the performance chart (Figure 5.3.4-18).

A similar instance of increased thermal efficiency followed a replacement of the quartz tube in the torch. After the repair, an attempt was made to complete the series of experiments of Figure 5.3.4-14 using other starting points. The resulting sequence, traced on Figure 5.3.4-19, showed over-treatment down to the minimum sustaining conditions. The input load of propane was subsequently adjusted to bring the destruction efficiency target within the operating space.

Under exceptionally stable plasma conditions, excellent reproducibility was observed within sets of consecutive sequences. Such circumstances were achieved on three occasions. Figure 5.3.4-20 shows three series of sequences initiated from different points converging onto the same optimum region. The optimum was located precisely and consistently within each series. There was little scatter in final response values, and end points were closely grouped near the efficiency target on the performance chart (Figure 5.3.4-21).

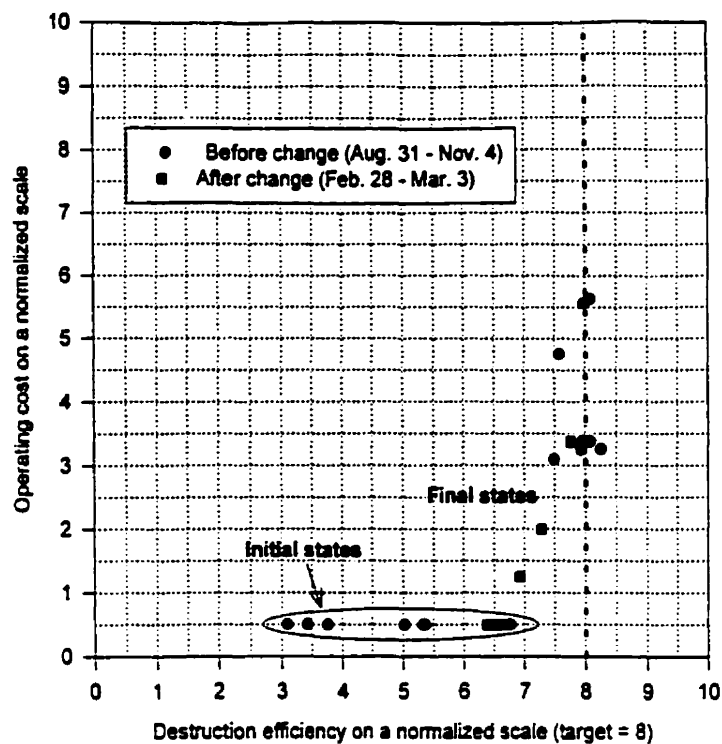


Figure 5.3.4-18: Influence of Response Sensitivity to Manipulated Variables on Optimization Performance Under-Treatment Case with 0.2% C_3H_8

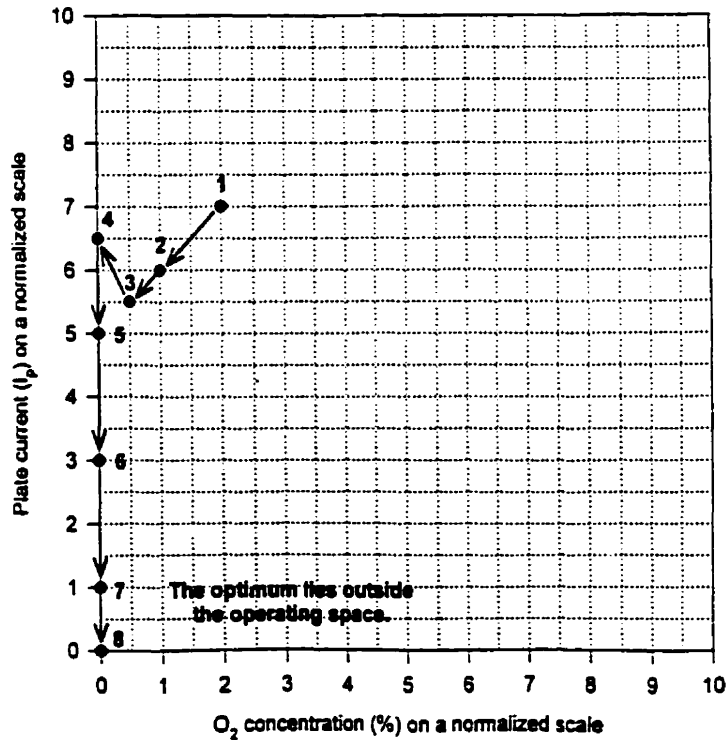


Figure 5.3.4-19: Evidence of Change in Thermal Efficiency Over-Treatment Case with 0.17% C_3H_8

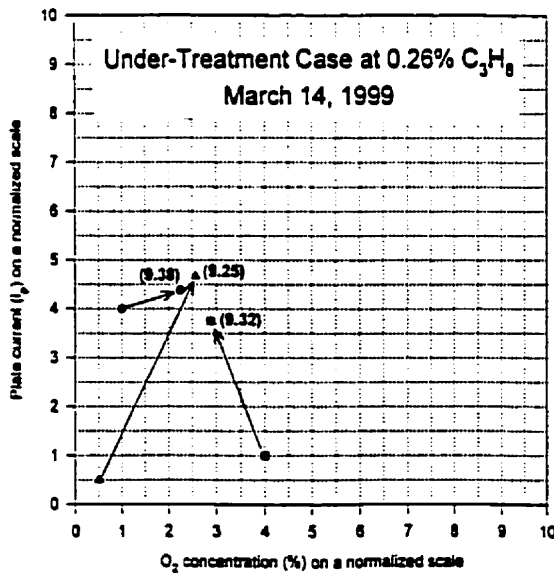
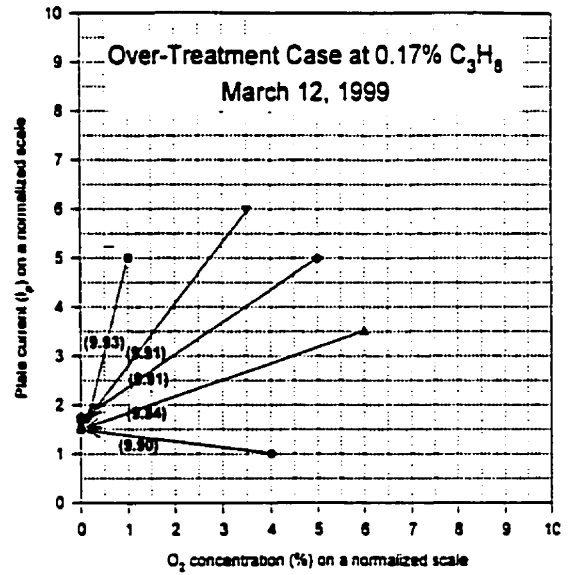
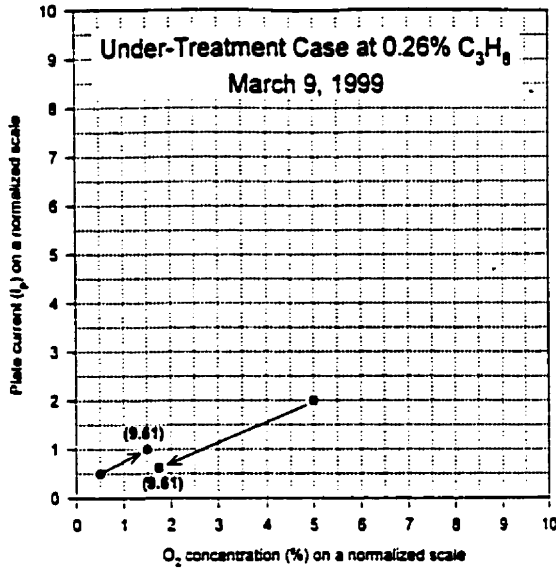


Figure 5.3.4-20: Finding an Optimum Region from Different Starting Points

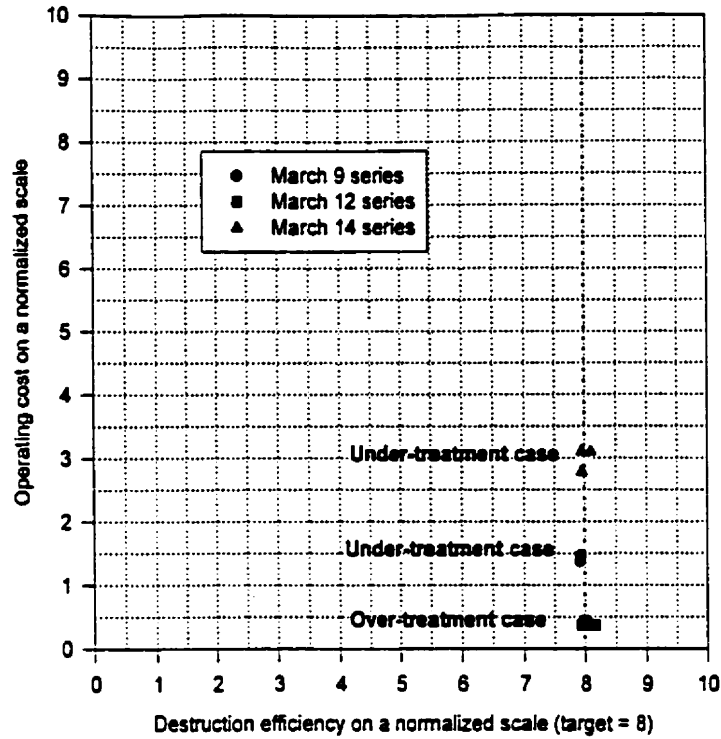
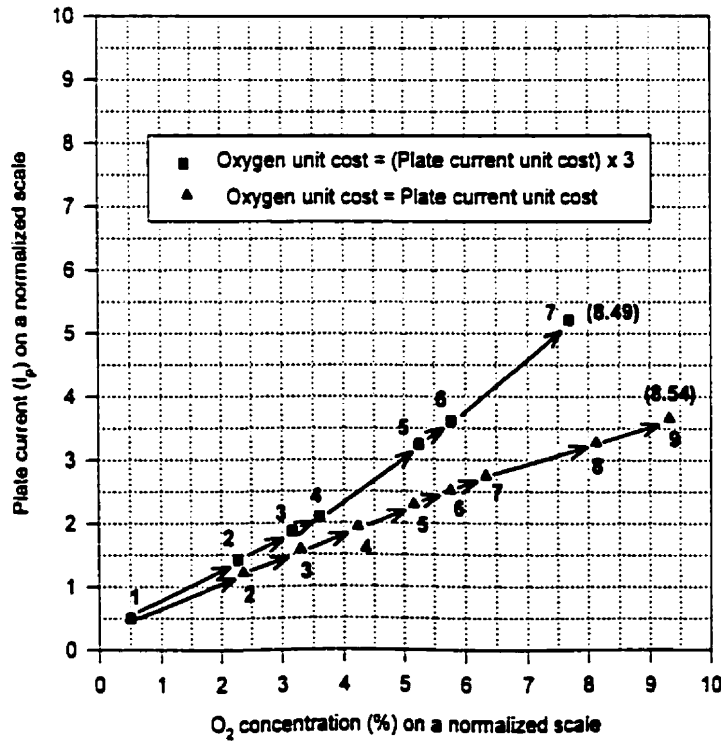


Figure 5.3.4-21: Repeatability of End Results Within Series of Sequences Starting from Different Points



Numbers indicate optimization steps, with final response values in parentheses.

Figure 5.3.4-22a: Influence of the Relative Costs of Manipulated Variables on Optimization Sequence Paths Under-Treatment Case with 0.26% C_3H_8

5.3.4.5 Role of Economic Factors in the Optimization Strategy

The cost-effectiveness of APAI resides in the economic factors built into the optimization criterion. This section demonstrates how the model system responded to simulated changes in economic circumstances.

In the definition of the cost parameter Y (equation 4.3.1-2), economic factors are represented by the fractional cost weights of oxygen and plate current. The impact of these assigned weights on optimization results was investigated. In Figure 5.3.4-22a, a sequence with the unit cost of oxygen three times as high as that of plate current is compared to a sequence with equal unit costs. When oxygen was more expensive, the system used more current and less oxygen. The divergence of the paths was initially small because cost was not a priority in under-treatment situations. In over-treatment cases (Figure 5.3.4-22b), oxygen reduction was emphasized over current reduction when oxygen was more expensive.

To better demonstrate the role of economics in the definition of optimal conditions, limiting cases were studied. Unit costs were assumed to differ by a factor of twenty. Over-treatment simulations, where cost was a priority, were best suited for these experiments. Four sequences, two at high oxygen cost and two at high current cost, appear on Figure 5.3.4-23. As expected, the sequences proceeded by a preferential reduction in the most expensive variable. The end points were equivalent in terms of the optimization criterion, but differed widely in terms of oxygen and current settings. Both pairs of sequences were highly consistent in the location of an optimum.

These sequences also highlight an important aspect of the optimal gradient strategy: the ability to re-direct the path towards an optimum after having moved in the same direction for several consecutive steps. In its first stage, a sequence moved rapidly towards an optimal region (e.g., see points #1 to #5 at high

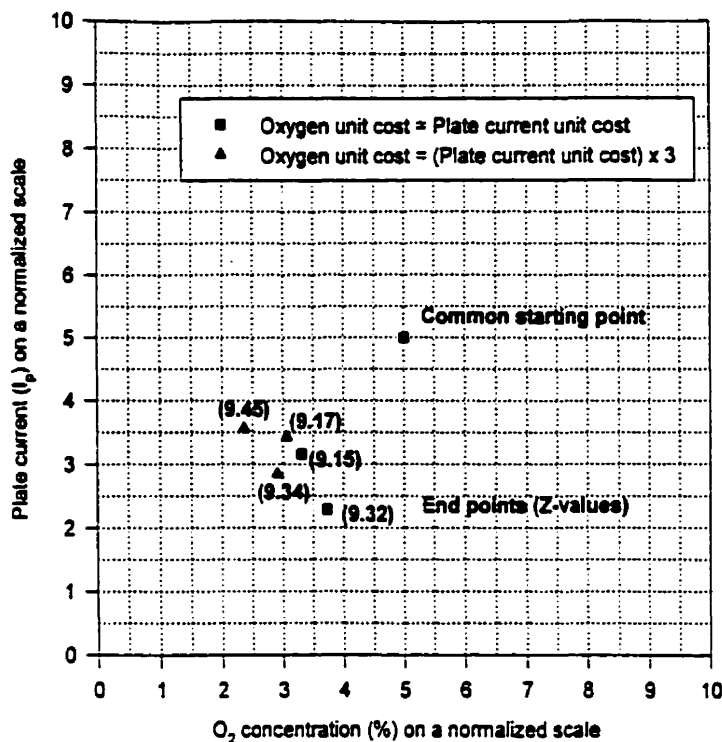
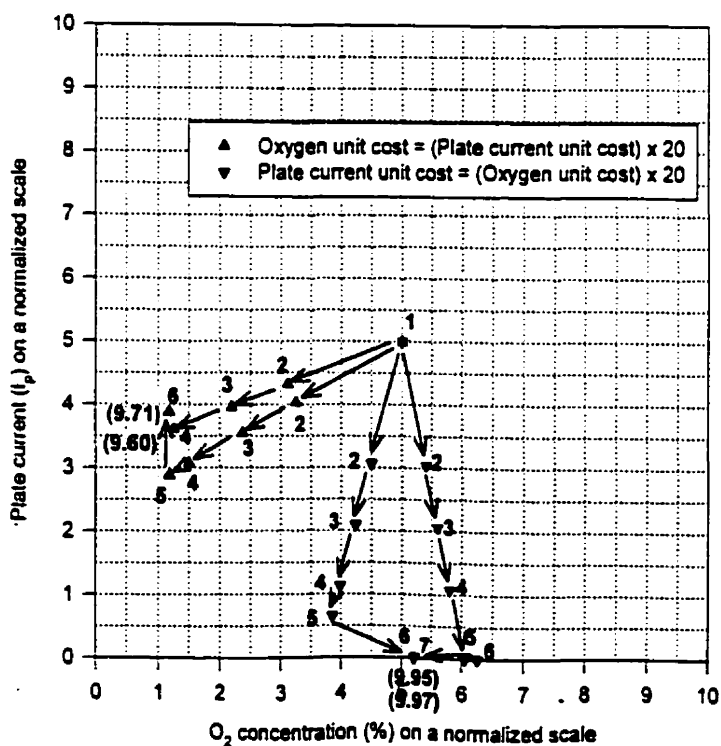


Figure 5.3.4-22b: Influence of the Relative Costs of Manipulated Variables on Optimization Sequence Paths
Over-Treatment Case with 0.17% C_3H_8



Numbers indicate optimization steps, with final response values in parentheses.

Figure 5.3.4-23: Influence of the Relative Costs of Manipulated Variables on Optimization Paths (Limiting Cases)
Over-Treatment Case with 0.15% C_3H_8

current cost in Figure 5.3.4-23). In the second stage, a refined local search either confirmed the adequacy of the point reached or steered the path toward an exact optimum (e.g., points #6 and #7). This two-stage strategy minimized the number of time-consuming gradient evaluations.

5.3.5 Technical Feasibility of the Adaptive Approach

The technical feasibility of APAI was demonstrated within the limitations of the model system. A gas stream contaminated with an organic compound was treated by contact with a plasma heat source. Decomposition and oxidation rates were controlled by adjusting the chemical and thermal properties of the plasma. Optimization programs allowed the system to respond to simulated variations in feed requirements and cost of resources.

Reliability and reproducibility would be essential in a plasma afterburner system designed to treat toxic waste gas. The configuration of the reactor should ideally provide complete mixing. Preliminary work would include a characterization of the flow dynamics and property profiles in the system. This would provide information on the factors affecting the kinetics of oxidation reactions.

For optimal performance of the adaptive strategy, the manipulated variables should be entirely controllable and independent. The preferred variables would be those with a direct impact on the chemical and thermal state of the plasma, such as oxygen concentration and dissipated power.

Composition would be monitored at the exit of the reactive zone using a suitable method. Possible options include emission or absorption spectroscopy, most likely infrared, and mass spectroscopy. Complete oxidation at that stage of the process would be crucial in preventing the recombination of organic fragments downstream. Should precursors be present, optimization of the quench step based on thermodynamics and kinetics could minimize recombination reactions.

6. TECHNO-ECONOMIC EVALUATION

There are fundamental differences in configuration and technology between the demonstration model and a prototype system. The experimental study provides no information on reaction kinetics and destruction efficiency in a plasma afterburner. Hence, rating the performance of a commercial plasma-assisted afterburner is beyond the scope of the project. In the following evaluation, plasma is assumed more effective than fuel combustion in destroying organic waste. This assumption justifies a qualitative discussion of the applicability and benefits of adaptive plasma-assisted incineration.

Waste management generates no revenue. The economic viability of a waste treatment process is assessed by comparison with a competing process or with the consequences of improper waste management. A complete quantitative assessment includes the costs of: environmental protection measures (waste-minimizing process design or end-of-pipe treatment), waste transportation and disposal, insurance coverage of risks and liabilities, non-compliance penalties, and future decontamination requirements. The benefits attached to environmental protection are financially ill-defined but are no less important: health and safety, protection from liability, and public acceptance of industrial activity. A rigorous cost-benefit analysis of the impact of a process on the environment and on the welfare of populations may include far-reaching external effects. For example, electrical power consumption is not exempt from environmental impact, particularly where hydroelectricity is unavailable. Even in the light of relevant scientific information, these aspects do not translate readily into financial figures. For this reason, the present economic analysis is restricted to immediate capital and operating costs. Its purpose is to compare the cost of plasma-assisted waste treatment to the cost of equivalent treatment using combustion heat. This approach assumes adequate destruction efficiency with either technology. The financial figures do not reflect possible differences in the effectiveness or in the thermal efficiency of actual systems.

Sections 6.1 and 6.2 address technical points relative to the design of an APAI prototype. Section 6.3 describes a study-level cost model based on factored estimates. This model is expected accurate within $\pm 40\%$. Section 6.4 describes three example cases where APAI could replace current thermal treatment technology. Section 6.5 presents a comparative cost analysis of APAI and conventional incineration. The qualitative aspects of techno-economic viability are examined in section 6.6.

6.1 Prototype System Design

6.1.1 Configuration

In the demonstrations, the model compound was introduced in the feed gas of the plasma torch in proportions less than 0.3% of the total flow. In an industrial process, the primary combustion gas throughput far exceeds the gas feed to the afterburner torch. The stream to be treated and the heat source enter the chamber separately. The afterburner is designed to promote direct contact and turbulent mixing between the incinerator flue gas and the plasma jet. A single afterburner may be equipped with multiple torches. The optimal geometry and size of the reaction chamber are functions of the system's fluid dynamics, heat and mass transfer properties, and chemical reactions. The afterburner and associated gas cleaning units form a sealed system operating under slightly negative pressure.

The diagnostic tools and methods developed for the model system are unsuitable for a prototype unit. Since contaminants do not enter the system through the plasma, the jet's optical spectrum may not correlate with destruction efficiency. Composition must be assessed downstream of the mixing region. The temperature in the turbulent zone is not intended to exceed 1500°C (2732°F). Under these conditions, thermal emission occurs mainly in the infrared region.

For on-line spectral emission diagnostic, indicators other than the Swan system rotational transitions of C_2 may be required. Infrared absorption spectrum analysis is an option.

6.1.2 Equipment Selection

At the laboratory scale, an electrodeless inductively coupled plasma torch was best suited for work with an oxidizing plasma. At the industrial scale, a non-transferred dc arc torch using oxygen-enriched air is the preferred option. This type of torch is up to 85% efficient in transforming electrical energy into plasma dissipated heat. Commercial units are available in power ratings from 300 kW to 1.5 MW (Phoenix Solutions Co. 1998, Soucy *et al.* 1996).

When technically and financially feasible, on-line mass spectrometry offers a detailed quantitative gas composition analysis. A more affordable and portable alternative for APAI is Fourier Transform Infrared Spectroscopy (FTIR). This technique uses interferometry to measure the infrared absorbance phenomena caused by the bending and stretching of molecular bonds. Absorbance at multiple wavelengths is measured simultaneously using a polychromatic source. An interferogram of signals integrated over all wavelengths is resolved into an absorbance spectrum by Fourier transform calculations. FTIR has been applied in the characterization of plasma systems (Stratton *et al.* 1999), and occupies a strong commercial niche in multi-component gas analysis for environmental applications. Instrument manufacturers have developed rugged on-line systems for real-time detection of organic and inorganic compounds in industrial process flue gas. Detection limits of the order of 0.5 ppm are expected with integration times between five and sixty seconds (Air Quality Analytical Inc. 1999, Nelson 1999).

Adaptive automated operation of an afterburner requires integrated monitoring, optimization and control functions. Interfaces are needed between the

automation program and: (1) the FTIR system's data acquisition and control software, (2) a user-developed or commercial optimization algorithm, and (3) actuators for the manipulated variables.

6.1.3 Optimization Strategy Development

The concept of APAI has the flexibility of a modular structure: each of its three components - thermal treatment, diagnostic, and optimal control - could be upgraded independently. APAI could incorporate new applications in plasma equipment design, analytical chemistry, optimization theory and automated control.

The demonstrated optimization procedure could be refined by the use of an adaptable optimization criterion. This relates to conventional adaptive control, where model parameters are continually updated. Possible options include the use of different objective functions for distinct operating modes, or the modification of the function's adjustable parameters to accommodate immediate priorities. For example, standard 24 hour-average emission targets provide opportunities for short-term variations in control objectives.

The experimental part of the project demonstrated feedback optimization based on empirical information. In an APAI prototype, combined feedforward and feedback control modes should improve adaptive response to feed variations. Recent reports emphasize the benefits of on-line feed characterization for the stability and efficiency of plasma waste treatment (Nazarian 1997). These studies pertain to predictive models that determine operating conditions from feed properties. The development of such models is complex. Alternatively, the field of artificial intelligence offers prospective tools for the interpretation of process information. In APAI, pattern recognition techniques and learning algorithms (e.g., neural networks) could facilitate the search for optimal conditions, allowing the adaptive process to grow more efficient with

"experience". Training sets of optical spectra were successfully used in monitoring toxic metal emissions from plasma vitrification processes (Singh *et al.* 1997).

6.2 Process Flowsheet

Figure 6.2-1 is a generic process flowsheet applicable to both APAI and conventional incineration. The envelope drawn around the afterburner and gas cleaning train defines a versatile system suitable for post-combustion gas treatment and for thermal destruction of liquid waste (afterburners commonly perform both functions simultaneously). The flowsheet compares favourably with the "best available technology" in toxic waste incineration (BOVAR Inc. 1999).

A potential application of APAI is the treatment of waste containing highly toxic components in low concentrations. Thermal remediation of contaminated soil exemplifies this situation, and serves as a model for the conceptual design presented here. Another potential application is the treatment of concentrated organic waste. A liquid waste furnace version of the concept is also studied.

6.2.1 Waste Treatment Section

6.2.1.1 Primary Combustion Chamber

The primary incinerator is typically a rotary kiln. For low-heat, high-silica content waste such as soil, the kiln operates in an ashing mode at temperatures not exceeding 1010°C (1850°F). The residence time is adjusted to obtain complete volatilization of the organic material. Easily combustible compounds burn at this stage, while persistent ones proceed to the afterburner. Fuel consumption is highly variable, depending on the heating value of the material treated and on its moisture content. The fuel value of contaminated soil is usually low, if not

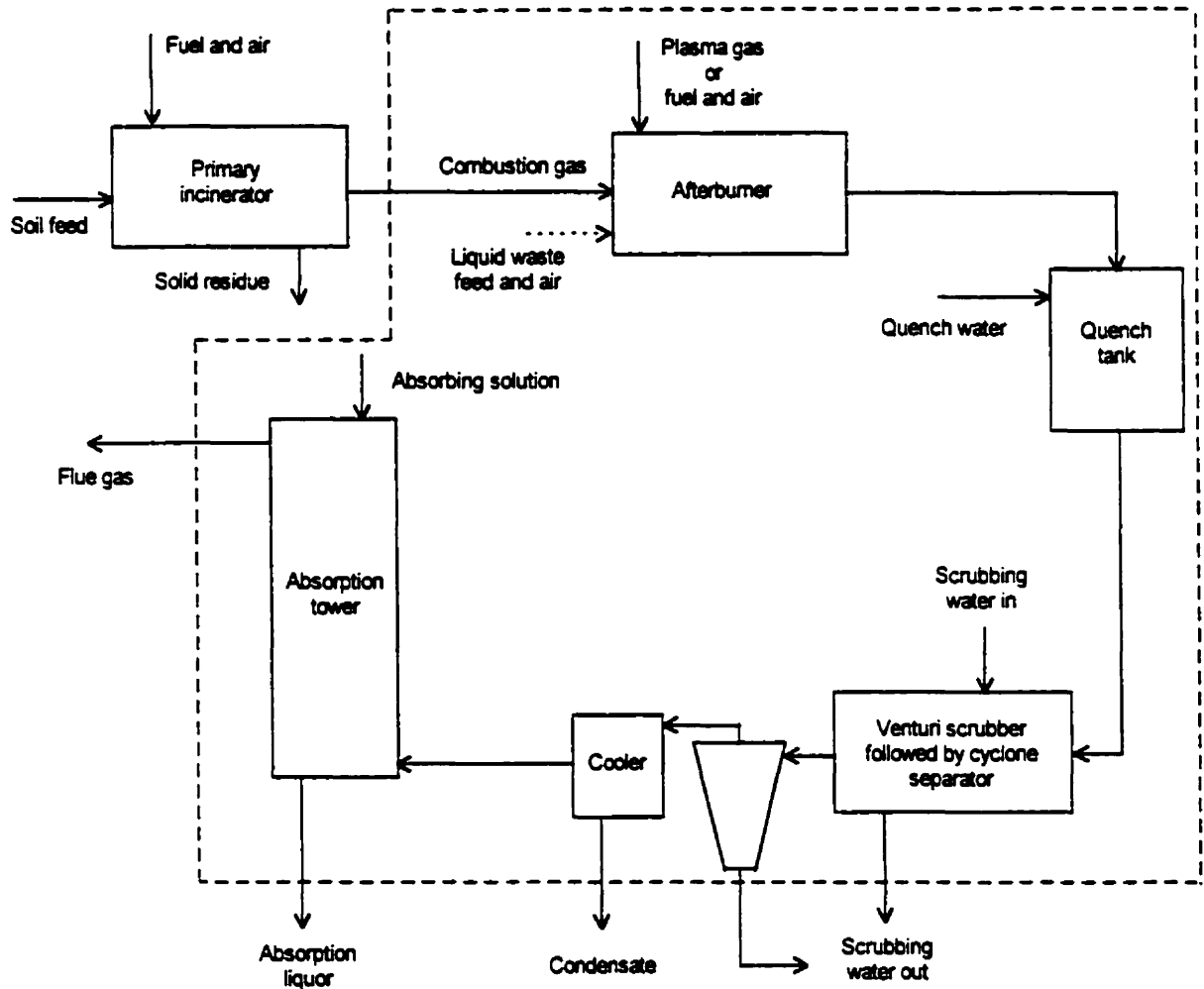


Figure 6.2-1: APAI Process Flowsheet

negligible. In this study, a conservative heat balance is ensured by assuming no heating value for the waste. The kiln feed is assigned 25 wt% moisture (wet basis) and physical properties typical of South-Eastern Quebec soil. Excess air levels are such that the feed to the afterburner contains more oxygen than needed for the combustion of its organic content. Persistent compounds contribute insignificantly to the gas throughput, but their presence is critical due to their toxicity.

6.2.1.2 Afterburner

The post-combustion unit is a refractory-lined tubular chamber equipped with a secondary heat source. Residence time in the vicinity of the heat source is of the order of milliseconds, but thermal decomposition continues in the non-flame zone for a residence time of the order of seconds (Lee and Huffman 1989).

Conventional designs use oil or natural gas burners with excess air to promote complete combustion of the auxiliary fuel. In APAI, the burners are replaced by one or several plasma torches. This change reduces volumetric input to the reactor and simplifies its construction. The base case of the present study assumes the use of a 1.5 MW torch at two-thirds of its rating for minimal electrode erosion. Torch specifications are modelled on equipment manufactured by Phoenix Solutions Co. (1998). The energy transfer efficiency is expected to range from 65% at low flow rates to 85% at high flow rates. The heat balance assumes 75% thermal efficiency at the nominal flow rate of 135 cubic meters per hour. The enthalpy rise in the torch is therefore 750 kW. Thermodynamic calculations predict a jet temperature above 6000 K at these settings. In keeping with the high-temperature capabilities of plasma technology, the afterburner temperature is set to 1370°C (2500°F) for APAI, as opposed to 1200°C (2200°F) in most existing facilities. The plasma gas flow rate is less than 5% of the throughput. This air stream may be oxygen-enriched to enhance the driving force for oxidation reactions.

6.2.1.3 Liquid Waste Furnace

In incineration facilities, the secondary combustion chamber is usually equipped for receiving liquid waste along with the primary combustion gas. If the process is specifically designed to treat liquid waste, no primary chamber is required. The furnace is a relatively simple refractory-lined tubular reactor with supplemental heat input from a plasma jet or fuel combustion flame. High-heat value waste (e.g., organic) is atomized to burn in contact with the heat source in a backmixed zone near the entrance. Low-fuel value waste (e.g., aqueous) is injected in a plug flow zone further downstream (Diemer *et al.* 1997).

A typical application is the destruction of PCB-containing dielectric fluids formerly used in electrical transformers. Waste of this type (generic name Askarel) varies in composition. It may comprise 50-70 wt% PCBs and 30-50% trichlorobenzenes, or may include a highly combustible fraction - e.g., 50% kerosene, 40% PCBs and 10% trichlorobenzenes (Brunner 1996, Manahan 1999). The present study assumes a concentrated feed composed of 40% trichlorobenzenes ($C_6H_3Cl_3$) and 60% tetrachlorobiphenyl ($C_{12}H_6Cl_4$, a compound representative of the PCBs found in dielectric fluids). The heating value of the waste is a significant component of the heat balance. Typically, non-aqueous waste combustion releases twice as much heat as the external source (Brunner 1996).

6.2.2 Gas Cleaning Section

The system proposed here meets basic combustion gas treatment requirements. In the absence of accurate pollutant emission data for plasma-assisted incineration, typical specifications are assumed for three main units: a quench tank, a venturi scrubber with cyclone separator and condenser, and a gas absorber. All three operate near atmospheric pressure.

6.2.2.1 Quench Tank

The tank is a vertical cylindrical vessel where a water spray quenches the afterburner gas from 1370°C to 150°C. The tank is sized for a superficial velocity of 3 m/s based on correlations applicable to gas-liquid separators (Turton *et al.* 1998). Its aspect ratio (length over diameter) has a cost-optimal value of three. Residence times are of the order of seconds. The rate of water evaporation is determined by the heat balance, assuming adiabatic conditions. The pressure drop across the tank is estimated to 0.5 kPa (2 in H₂O).

The choice of construction materials and process conditions must account for potential corrosion problems in the presence of halogens, sulfur or phosphorus. To avoid using specialized corrosion-resistant alloys, temperature is maintained above the saturation point of the gas stream and the dew points of derivative acids. The adiabatic saturation temperature of the afterburner gas is between 60°C and 100°C. The dew point of HCl is below 150°C. There is a risk of chloride corrosion above 300°C when treating chlorinated waste (Brunner 1987).

Thus, a quench temperature window ranging from 150°C to 300°C is available. Over this range, the quench temperature has little effect on volumetric flow rates and on the size of downstream equipment units; this was established through a sensitivity study using computer simulation. The priority goal of post-combustion treatment is to minimize heterogenous formation of dioxins. This requires a quench temperature below 300°C, preferably below 200°C. Accordingly, the tank is designed with an outlet temperature of 150°C.

The present analysis assumes no heat recovery. Air or feed pre-heating is possible after the quench, but the economic benefits of heat recuperation seldom justify its technical requirements in the presence of chlorine (Brunner 1987).

6.2.2.2 Venturi Scrubber

A venturi wet scrubber is the most common choice for post-incineration removal of particulate matter and acid gases. This simple, compact device is designed for throughput flexibility and high-efficiency removal of sub-micron dusts and aerosols. Placed immediately after the quench tank, it prevents fouling in downstream equipment. The venturi also acts as primary absorber for soluble gases. The unit includes a cyclone separator and a small cooler/condenser tower to reduce fan requirements downstream (Niessen 1995). The pressure drop across this type of unit is typically in the range 3.0 - 7.5 kPa (12-30 in H₂O); a value of 5 kPa (20 in H₂O) is assumed (Cooke 1992).

Correlations suggest a liquid-to-gas ratio of 0.8 m³ liquid per 1000 m³ gas (Brunner 1996, Cooke 1992, Vatauvuk and Neveril 1984, Turton *et al.* 1998). The total water input includes the scrubbing liquid volume based on the saturated gas at its dew point ($\approx 87.5^{\circ}\text{C}$), plus the water evaporated in cooling the gas from 150°C to the dew point.

The venturi is followed by a cyclone separator and cooling tray tower with mesh de-entrainment. The cooler is designed for a superficial velocity of 3 m/s and a final temperature of 30°C. The acidic condensate proceeds to a neutralization tank.

6.2.2.3 Absorption Tower

In a typical gas cleaning train, the primary wet scrubber is followed by a secondary absorber for acid gas removal. The unit is usually a packed or tray tower using a caustic scrubbing solution. Its design specifications depend on the composition of the afterburner stream (halogens, oxides, etc.) and on the performance of the primary scrubber.

In computer simulations, the venturi was represented as a single equilibrium stage. Under this simplifying assumption, results predicted an outlet chlorine concentration close to regulatory standards. Quite likely, the simulation overestimated gas-liquid contact and mass transfer within the venturi. In the absence of empirical data, a five-stage packed tower is assumed adequate for acid gas control. The tower is specified according to the following guidelines (Turton *et al.* 1998, Vatauvuk and Neveril 1984): a superficial velocity of 1.2 m/s; the Height of a Transfer Unit (2.5-3.0 ft) set to 0.8 m (2.75 ft); the total height equal to 0.6 m (2 ft) plus 25% of the diameter; a liquid-to-gas ratio of five; and a pressure drop of 0.4 kPa per meter of packing (0.5 in H₂O per foot of packing).

6.2.2.4 Stack and Additional Units

The stack is a major cost component of the gas cleaning section. Its height largely depends on regulations and on meteorological factors. Its capital cost and pressure drop (hence operating cost) are strong functions of dimensions. Considering APAL as a potential addition to existing facilities, the stack is assumed identical for both plasma and conventional versions of the process. As shown by the process envelope of Figure 6.2-1, stacks and neutralization tanks are excluded from the economic evaluation.

Additional gas treatment steps are available if needed. Activated carbon circulation in the wet scrubbing section is highly effective in removing dioxins, furans and other organic by-products (BOVAR Inc. 1999). Selective reduction of nitrogen oxides by ammonia is possible if gas absorption proves insufficient. Electrostatic precipitators and baghouse filters are commonly used to collect salts and fine particulates.

6.2.2.5 Nitrogen and Sulfur Oxide Removal

Based on available information, no specialized units is included for the removal of nitrogen or sulfur oxides. Technology related to these operations is known and applicable if needed (de Nevers 1995, Veerimst 1998).

There are two ways for sulfur to enter the system: through feed waste, and through combustion fuel (the latter source is negligible if using high-grade oil and gas). Unless the sulfur content of the feed is exceptionally high, sulfur oxide emissions should be acceptable past the wet scrubbing units. Conversely, the generation of nitrogen oxides in combustion flames and plasma jets is a potential problem. Different mechanisms contribute to the formation of fuel, prompt and thermal NO_x .

Twenty to fifty percent of the nitrogen present in waste is oxidized to **fuel NO_x** . Low-boiling auxiliary fuel and natural gas are negligible sources of fuel NO_x (de Nevers 1995). **Prompt NO_x** forms by reaction of oxygen and nitrogen with fuel-derived carbon species. This mechanism usually contributes the least to NO_x generation in hot flames (de Nevers 1995). Air plasma jets generate no prompt NO_x . **Thermal NO_x** , which forms upon heating nitrogen and oxygen, predominates above 1400°C . Its production rate increases with peak temperature, residence time at high temperature, and oxygen content. Plasma jets present a risk of thermal NO_x formation due to high peak temperatures.

Methods are available to estimate NO_x , SO_x and CO generation from fossil fuel combustion (Brunner 1996). They were applied to kilns and fuel afterburners in the example cases described in section 6.4. In the absence of guidelines, a plasma afterburner was assumed to produce twice as much NO_x as its conventional counterpart. This estimate appeared realistic: the soil incineration afterburner was assigned 1400 ppm NO_x , while 750-900 ppm were reported for a Retech arc system operated at 1200°C (Gupta 1996). Based on ASPEN process

simulation results, nitrogen and sulfur oxide emissions at the end of the gas cleaning train are expected to meet regulations. This conclusion is supported by process data from the waste incineration facility of BOVAR Inc.

6.2.3 Computer-Aided Process Simulation Using ASPEN

ASPEN calculations of the state and composition of process streams were used in the specification of auxiliary units, in the estimation of utility consumption rates, and in sensitivity analyses. These simulations were subject to uncertainty in the nature and quantity of waste contaminants. Input compositions did not correspond exactly to those of a waste treatment process, for reasons explained below.

Physical property databases are incomplete with respect to highly toxic contaminants such as PCBs. For example, the heat of combustion, heat capacity and heat of vapourization of tetrachlorobiphenyl are unknown. Thermodynamic calculations based on heats of formation (estimated from molecular structures using ASPEN) suggest that such compounds should burn autogenously, or without an external heat source. Clearly, kinetic factors dominate in the combustion of persistent compounds. The complexity of reaction dynamics in the present system precludes accurate prediction of the afterburner gas composition. Furthermore, no model is available to estimate the extent of undesirable reactions (e.g., dioxin formation) in post-combustion sections. Consequently, a simplified approach was adopted. The specific reactions and heat effects of contaminant combustion were excluded from the simulation.

In soil incineration simulations, the composition of the input stream was calculated from combustion stoichiometry in the primary kiln. Volatilized soil components were assumed to contribute negligibly to the gas throughput and combustion heat. The feed flow rate was adjusted according to the heat duty of the afterburner. A common chlorinated compound (m-dichlorobenzene) was

included as a source of chlorine for electrolyte calculations, in an amount equivalent to the estimated chlorine content of contaminated soil. (The heat of combustion of m-dichlorobenzene showed up as excess heat in the afterburner energy balance).

For liquid incineration simulations, the input stream was specified as the stoichiometric combustion products (including excess air) of the liquid treated, plus an assigned combustion heat estimated from empirical guidelines. The heat and mass balance calculations for soil and liquid treatment cases are detailed in section 6.4 under *Example Processes*.

ASPEN calculated the size and cost of pumps and fans, their electrical power requirements, and the water consumption rates of the quench, venturi and absorber units.

6.3 Economic Model

The investment model applied here is an updated version of the factored estimate method of Peters and Timmerhaus (Douglas 1988). All figures are expressed in 1997 US dollars.

The objective of the analysis is to compare the cost of a plasma afterburner system (with gas cleaning) to the cost of an equally effective system that uses fuel combustion as a heat source. The afterburner is intended for secondary gas or liquid treatment within an existing incineration facility. The scope of the analysis is limited to process units most directly affected by the choice of a secondary heat source. The primary incinerator and stack are excluded.

6.3.1 Total Capital Investment

Table 6.3.1-1 outlines the fixed capital investment calculation. Items specified as a fractional range of another cost component are estimated at midrange. Equipment purchase costs are obtained from correlations and converted to 1997 US dollars using the Marshall & Swift Equipment Cost Index. Spare equipment is not included.

The study considers substituting the afterburner heat source in an existing process. The afterburner's share of non-depreciable assets (inventories, accounts payable/receivable, operating cash) is assumed small enough that no additional working capital (WC) is needed. Likewise, the impact of the heat source on start-up costs (S) is assumed negligible. This leads to the simplification:

$$\text{Total capital investment (TCI)} = \text{FCI} + \text{WC} + \text{S} \approx \text{FCI}$$

Table 6.3.1-1: Fixed Capital Investment Breakdown (Douglas 1988)

Cost type	Component items	Calculation
Onsite direct costs	Purchased equipment	PE
	Installation (35-45% PE)	0.40 (PE)
	Instrumentation and controls (6-30% PE)	0.18(PE)
	Piping (10-80% PE)	0.45(PE)
	Electrical equipment & materials (8-20% PE)	0.14(PE)
	Total	2.17(PE) ⁽¹⁾
Offsite direct costs	Buildings, infrastructures & building services	
	Land, yard improvements	
	Service facilities and utilities	
	Total (for plant expansions: 45% onsite costs)	0.45(onsite)
Direct costs	Onsite + offsite	1.45(onsite)
Indirect costs	Engineering and construction (5% direct costs)	0.07(onsite)
	Contingency and fees (20% direct costs)	0.29(onsite)
Total	Fixed capital investment (FCI)	1.81(onsite)

(1) The purchase cost correlations of some equipment items include instrumentation, controls and other related materials or equipment. The onsite direct cost contribution for these items is calculated as 1.23(PE).

6.3.1.1 Equipment Cost Calculations

Plasma afterburner

This unit is modelled as (1) a direct-fired heater of cylindrical construction with a plasma torch in place of fuel burners, and (2) an automated FTIR diagnostic system. The heater cost correlation (Douglas 1988) is corrected for the absence of fuel burners and related equipment by omitting the costs of fans, controls, instrumentation and installation. The cost of the plasma system makes allowance for these items.

As a general rule, the price of plasma equipment is 1,000\$ per kilowatt (Munz 1999, Mustoe 1999). This estimate covers installation, instrumentation, controls, and electrical equipment. Information from Westinghouse Technologies suggests 800\$ per kilowatt for complete systems in the range of 1.0 to 1.5 MW (Soucy 1999). According to these figures, plasma equipment costs for the present application (1.5 MW) reach 1.2 to 1.5 million dollars.

Sophisticated on-line analytical capabilities are essential in APAI. A typical FTIR system designed for waste treatment applications costs 80,000\$ to 95,000\$ (Nelson 1999). The quoted price includes controls, instrumentation, electrical equipment, programmable logic controller, computer interface, software configuration, and development of reference spectra.

Given the uncertainty on plasma equipment costs, a value of 1.5 million dollars is assumed for the plasma and FTIR systems combined.

Fuel afterburner

The cost is based on a correlation for oil-fired gas incinerators with fan, controls and instrumentation but without heat exchanger (Vatavuk and Neveril 1984).

Plasma liquid waste furnace

Similar to the plasma afterburner, this unit is a direct-fired heater of cylindrical construction (Douglas 1988) with auxiliary fuel burners replaced by a plasma torch and FTIR on-line diagnostics. The costing procedure is as described for the afterburner.

Gas liquid waste furnace

A correlation for a direct-fired heater of cylindrical construction (Douglas 1988) applies directly to this unit. Controls and instrumentation are factored separately.

Gas cleaning units

The quench tank is a low-pressure stainless steel-clad vessel (Douglas 1988). Controls and instrumentation are factored separately.

The venturi system is a high-efficiency unit with stainless steel construction. The correlation includes: cyclone separator, cooler/condenser trays, pump, instrumentation and controls (Vatavuk and Neveril 1984).

The cost of the absorber column is estimated from its approximate weight (Vatavuk and Neveril 1984) for a stainless steel shell. Controls and instrumentation are factored separately.

Costs for the quench pump, absorber pump, venturi fan (stainless steel construction) and absorber fan (carbon steel construction) are obtained from ASPEN correlations. Pumps are of the centrifugal type, and fans are class IV blowers (rated for a maximum pressure drop of 3.7 kPa or 15 in H₂O).

6.3.2 Total Annual Operating Cost

Capital investments are written off as operating costs following straight-line depreciation over a ten-year period. Annual cost calculations assume 8400 hours

per year, or 24 hours a day for 50 weeks. Continuous operation is recommended for thermal treatment processes, as frequent temperature cycling shortens the life of refractory materials (Brunner 1987).

To emphasize differences in cost distributions for plasma and conventional processes, cost components are divided into two categories. Table 6.3.2-1 lists the components that depend on utility consumption and on fixed capital investment, i.e., that are affected by the choice of heat source. Fixed charge estimates assume internal financing and no leasing charges within the existing facility or at the site of waste destruction. Costs of the second category (Table 6.3.2-2) are assumed common to both options: operating labour, clerical labour, supervision, laboratory charges, patents and royalties, plant overhead, and general expenses (sales, administration, research and engineering). The two categories combine to give the total annual operating cost.

Plasma technology is a small-market field where equipment prices carry the cost of ongoing development. Relative to associated offsite and indirect costs, the purchase cost of plasma equipment is unusually high. Therefore, standard factors applicable to the chemical industry would overestimate many components of the economic model. Without some adjustments, plasma equipment items would inflate plant cost estimates out of proportion.

In a typical plasma system, the power generator accounts for 80% of the capital cost, yet requires minimal work once it is operational. The present analysis applies the factors for offsite direct costs, indirect costs, maintenance and supplies to 20% of the plasma equipment capital. (Fixed charges and depreciation allowances are based on actual costs.) This adjustment brings the maintenance costs of plasma and conventional processes to similar levels. Economic estimates developed from this type of model agree closely with data from existing plasma waste treatment processes (Soucy 1999).

Table 6.3.2-1: Breakdown of Process-Specific Operating Costs (Douglas 1988)

Cost type	Component items	Calculation
Direct production costs	Utilities	U
	Maintenance & repairs (2-10% FCI)	0.06(FCI)
	Operating supplies (10-20% maintenance)	0.009(FCI)
Fixed charges	Local taxes, insurance (1-5% FCI)	0.03(FCI)
	Depreciation (10% FCI)	0.10(FCI)
Operating costs	Excluding depreciation	U + 0.099(FCI)
Annual costs	Including depreciation	U + 0.199(FCI)

Table 6.3.2-2: Breakdown of Common Operating Costs (Douglas 1988)

Cost type	Component items	Calculation
Manufacturing costs	Operating labour	1 technician, 24 hrs/day
	Direct supervision and clerical labour	5% of operating labour
	Plant overhead	40% of labour, supervision and maintenance (approximate common base)
General expenses	Administrative expenses	5% of labour, supervision and maintenance (approximate common base)
	Executive salaries	
	Legal costs	
	Communications	
Common operating costs		1.05(operating labour) + 0.45(labour, superv. & maint.)

6.3.2.1 Utility Consumption Calculations

The consumption rates of fuel oil, natural gas and electrical power in the afterburner or furnace units are determined from energy balances. No heat recovery is assumed within the process envelope of Figure 6.2-1. In a complete incineration process, heat could be recovered from the afterburner off-gas

(independent of the choice of secondary heat source) to preheat the feed or primary combustion air.

Assuming that cooling water circulates in a closed-loop system, water consumption in the plasma torch and afterburner vessel is negligible. The torch requires dried process air and oxygen compressed to 1 MPa (150 psia). The cost of combustion air for oil and gas burners is assumed negligible. Process water consumption rates in the quench, venturi and absorber units are based on energy balances and on general guidelines pertaining to these units.

Electrical power requirements for centrifugal pumps are based on the calculated water flow rates. Fan power requirements assume pressure drops of 0.5 kPa (2 in H₂O) in afterburner/furnace fans and 5 kPa (20 in H₂O) in venturi and absorber fans. Power consumption rates are obtained from ASPEN simulations.

Table 6.3.2-3 lists the utility market prices assumed in this study. Based on these prices, the unit cost of natural gas energy is nearly half the unit cost of fuel oil energy (Table 6.3.2-4).

Table 6.3.2-3: Unit Cost of Utilities (Turton *et al.* 1998)

Utility description	Cost per common unit (1996 US\$) ⁽¹⁾
Natural gas	0.085 \$/std ⁽²⁾ m ³
Fuel oil #2	170 \$/m ³
Electricity (110, 220 or 440 V)	0.06 \$/kWh
Process cooling water	0.0067 \$/m ³
Pressurized process air	0.023 \$/std m ³
Compressed oxygen ⁽³⁾	0.548 \$/std m ³

(1) The conversion factor to 1997 US\$ is 386.5/382 (Chem. Eng. Plant Cost Index).

(2) Standard conditions are defined as 25°C at 1 atm.

(3) Supplemental oxygen input is a manipulated variable. To avoid underestimation, the oxygen concentration in the plasma gas is assumed to be 40%.

Table 6.3.2-4: Cost of Fossil Fuel Energy

Fuel	Heat available ⁽¹⁾ at 1370°C (MJ/m ³)	Cost per unit volume (\$/m ³)	Cost per unit energy (\$/kJ)
No. 2 oil	10231	170	16.62
Natural gas	9.8736	0.085	8.61

(1) Net heat available at the afterburner temperature, assuming air fractions of 1.2 for oil combustion and 1.1 for gas combustion (Brunner 1996)

6.3.3 Cash Flow and Net Present Value Calculations

In the present study, economic assessments are presented in terms of total annual operating costs (including a 10% capital cost allowance). To facilitate comparison with other projects, annual cash flows and net present value are also computed using the account statement approach described in Appendix XIV. Cash flows depend, among others, on the depreciation method, on financing sources, and on taxation rules. The simplified cash flow model used here assumes the following situation: a uniform marginal tax rate of 40%; sufficient taxable income to absorb tax savings generated by waste destruction expenses; a salvage value that is negligible or offset by dismantling costs; and no additional working capital, i.e., a negligible contribution of the afterburner process to non-depreciable assets such as inventories, accounts payable/receivable, and operating cash.

The presentation of results in terms of annual costs emphasizes the relative importance of cost components and brings out key differences between plasma and conventional processes. A cash flow analysis provides a more exact measure of profitability. Both methods lead to the same general conclusions on the relative costs of plasma-assisted and conventional incineration.

6.4 Example Processes

Techno-economic models were developed for three potential applications of APAI: soil incineration, soil desorption, and liquid organic waste treatment. All three cases use the general flowsheet of Figure 6.2-1.

6.4.1 Case I: Soil Incineration

The first example is the incineration of soil contaminated with hazardous organic compounds. The solids undergo treatment in a primary kiln. The incineration gas proceeds to an afterburner.

The combustion of organic soil components begins in the oil-fired kiln, which operates at 1010°C (1850°F). Persistent compounds and incomplete combustion fragments are oxidized in the afterburner at 1370°C (2500°F). High variability is expected in the quantity and fuel value of the soil's organic fraction. In this example, fuel oil consumption was calculated from the heat required to raise dry soil and its moisture to the kiln temperature. The combustion gas flow rate (per kilogram of soil treated) and its composition were determined from stoichiometry, assuming an air fraction of 1.2 in the oil burners. The throughput of volatilized soil components was assumed small relative to the volume of gas generated by combustion. The heating value of combustible soil components was neglected. Heat lost to cooling air and by radiation was also neglected. These losses are generally less than 5% in total (Brunner 1996).

6.4.1.1 Plasma-Assisted System (Case I)

According to the torch specifications described in section 6.2.1, an afterburner duty of 750 kW is available to bring the system to its final temperature of 1370°C. Of this, 682 kW is absorbed by the kiln gas and 68 kW remains in the plasma gas. Contaminant volume and fuel value were neglected. Based on the

flow rate and composition of the kiln gas per unit mass of soil, the treatment capacity of the plasma afterburner was calculated as 2334 kg wet soil per hour or 56 tonnes a day. For comparison, BOVAR Inc. operates two toxic waste incinerators with respective capacities of 96 and 22 tonnes a day.

6.4.1.2 Conventional System (Case I)

This system is analogous to the one just described, with the exception that the afterburner uses fuel combustion as a heat source. The soil treatment capacity and kiln gas composition are the same as in the plasma-assisted system. The fuel oil afterburner matches the heat duty of the plasma afterburner. Using combustion as the secondary heat source implies different afterburner gas flow rate, afterburner gas composition, and gas cleaning capacity. The rate of fuel oil consumption was calculated from the absorbed heat duty requirement of 682 kW, using the net combustion heat available at the afterburner temperature (1370°C) with an air fraction of 1.2.

6.4.2 Case II: Soil Desorption

The second example is the treatment of contaminated soil by thermal desorption. As in incineration, the gas from a primary kiln proceeds to a high-temperature afterburner. The distinction lies in the temperature of the primary unit: the desorption kiln operates at 260°C (500°F), which is sufficient for volatilization but not combustion of organic soil components. Oxidation occurs mainly in the afterburner, at the same temperature as in the incineration case (1370°C).

The comparison of incineration and desorption applications indicates the sensitivity of the cost analysis to the temperature in the kiln. This information is relevant to the design of plasma-assisted processes, where high effectiveness and flexibility in the afterburner may allow milder conditions in the primary unit.

6.4.2.1 Plasma-Assisted System (Case II)

The heat and mass balance procedure is the same as with soil incineration (case I). The desorption kiln operates at a lower temperature. Fuel requirements and gas throughput are lower in the primary stage but the temperature rise from the kiln to the afterburner is higher. The soil treatment capacity was found to be 1920 kg wet soil per hour or 46 tonnes a day - 18% less than with incineration.

6.4.2.2 Conventional System (Case II)

Again, the soil treatment capacity and fuel oil afterburner heat duty are the same as in the plasma-assisted system. The afterburner gas flow rate and composition were calculated as described in case I.

Afterburner capacity and gas composition calculations for soil incineration and desorption cases are summarized in Appendix X. Each of the three tables pertains to one type of secondary unit: (1) plasma afterburner, (2) fuel oil afterburner, and (3) natural gas afterburner. The tables contain four columns of data corresponding to different primary units (in that order): oil desorption kiln, gas desorption kiln, oil incineration kiln, and gas incineration kiln. Combustion products and kiln outputs were determined from mass and energy balances described in Appendix XI. The compositions listed exclude nitrogen and sulfur oxides, as well as chlorine from contaminants. These compounds were included in ASPEN process simulations.

The techno-economic analysis was applied to fuel oil units, with the understanding that substitution by natural gas would be beneficial in terms of costs and pollutant emissions. Thus, if a plasma afterburner system compared unfavourably with a fuel oil afterburner system, it would not stand comparison with a gas afterburner system. This was confirmed by example case III, where

the conventional system uses natural gas combustion as the secondary heat source.

6.4.3 Case III: PCB Liquid Waste Incineration

The third example is the treatment of concentrated PCB-containing liquid waste. In large-scale facilities, this operation is often combined with solid waste incineration by feeding the liquid to the afterburner stage. Other specialized applications use a single-stage liquid incineration system, as in this example. The flowsheet corresponds to the process envelope traced in Figure 6.2-1, with a liquid waste furnace in place of the afterburner. This type of system is amenable to small-scale and portable operation.

6.4.3.1 Plasma Heating System (Case III)

With concentrated liquid organic waste, treatment capacity depends on the furnace heat available and on the fuel value of the waste. The fuel values of highly toxic compounds such as tetrachlorobiphenyl are not commonly available. The composition of organic liquid waste is application-specific and variable. For these reasons, the heat balance in the preliminary design presented here follows a general guideline for non-aqueous liquid organic waste incineration furnaces: assume a 2:1 ratio between the heat released by waste combustion and the heat supplied by the external source (Brunner 1996). For example, if the torch supplies 750 kW (682 kW net absorbed heat), waste combustion provides 1500 kW. Liquid waste burners use primary air in excess by 30%. Combustion gas volumes and compositions (per unit feed waste) were approximated from the general stoichiometry of PCB-containing liquids. The treatment capacity was determined by varying the feed rate until the net available heat was zero at the desired temperature of 1370°C. Once a treatment capacity was determined, a waste fuel value was back-calculated from the heat release assigned to the waste (here, 1500 kW). This assigned fuel value was compared with an estimate

obtained using a standard formula for hydrocarbon fuel values called *DuLong's approximation*. As detailed in Appendix XII, the assigned values were of the order of, but lower than, DuLong estimates. These results validated the heat release ratio assumption and ensured a conservative analysis where more heat was available than needed.

A single-torch plasma furnace was found to treat 580 kg per hour of tetrachlorobiphenyl ($C_{12}H_6Cl_4$) or 633 kg per hour of a typical Askarel fluid containing 40% trichlorobenzenes ($C_6H_3Cl_3$) and 60% tetrachlorobiphenyl ($C_{12}H_6Cl_4$). Under continuous operation, this system could process 5300 tonnes of fluid annually, or 15 tonnes a day. It compares favourably with other non-transferred arc plasma processes such as PLASCON (1 - 5 tonnes a day using a 150 kW torch) and INDICIS (8 tonnes a day using 250 - 800 kW).

6.4.3.2 Gas Combustion System (Case III)

The natural gas furnace system provides the same heat duty and treatment capacity as the plasma furnace system. The rate of natural gas consumption was determined by the absorbed heat duty requirement of 682 kW, based on the net combustion heat available at the afterburner temperature (1370°C) with an air fraction of 1.1.

6.5 Comparative Cost Analysis

The first part of this section reports on capital and operating costs, comparing plasma and fuel heating options for each of the cases presented above. The second part examines the sensitivity of these cost estimates to design variables and economic factors.

6.5.1 Cost Summaries

Cost summary tables are found in Appendix XIII. These tables detail the calculation of capital and operating costs for each example case. Table XIII-1 outlines the operating costs common to all options. Tables XIII-2 to XIII-7 pertain to soil incineration (case I): XIII-2 to XIII-5 give the initial investment and process-specific operating costs of plasma and fuel afterburner systems, including gas cleaning; XIII-6 and XIII-7 apply to the primary kiln. Tables XIII-8 to XIII-13 repeat the analysis for soil desorption (case II). Tables XIII-14 to XIII-17 apply to liquid waste furnace systems (case III). The essential information contained in these tables is presented graphically throughout the following discussion.

6.5.1.1 Capital Investment

Plasma systems require twice the initial capital investment of conventional systems (Figure 6.5.1-1). For soil incineration, the plasma-assisted process costs 88% more than the conventional system; for soil desorption, 101% more; and for liquid waste incineration, 116% more. In all three cases, the costs of plasma and conventional systems are of the order of 2.5 and 1.25 million dollars respectively.

Capital costs fall into three main components: installed equipment costs (thermal treatment and gas cleaning units considered separately), offsite direct costs (buildings, facilities, etc.), and indirect costs (engineering, construction, contingencies & fees). Figures 6.5.1-2 and 6.5.1-3 show the relative contributions of these costs for the plasma and fuel oil afterburner systems of case I. The distributions are similar for cases II and III. In the conventional system, the dominant element - gas cleaning equipment (34%) - is closely followed by offsite costs (25%), afterburner equipment (21%) and indirect costs (20%). The distribution is far less balanced in the plasma system, where thermal equipment accounts for 61% of the total investment.

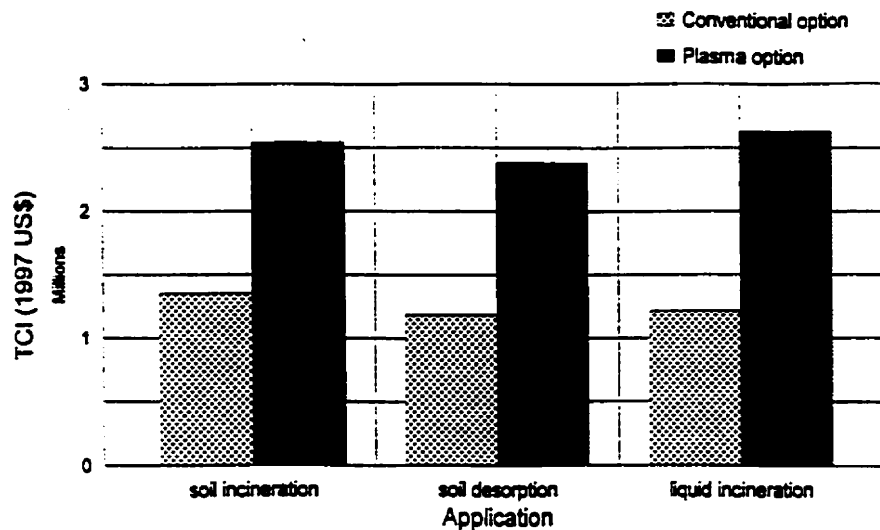


Figure 6.5.1-1: Total Capital Investment (TCI) Afterburner Options Compared

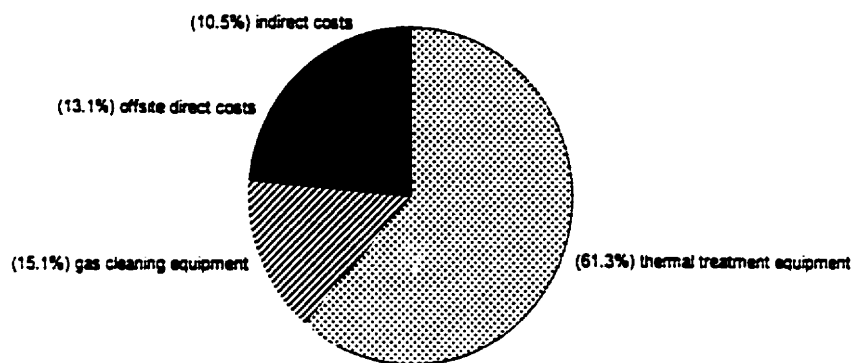


Figure 6.5.1-2: Fixed Capital Investment Breakdown for Soil Incineration with Plasma Afterburner

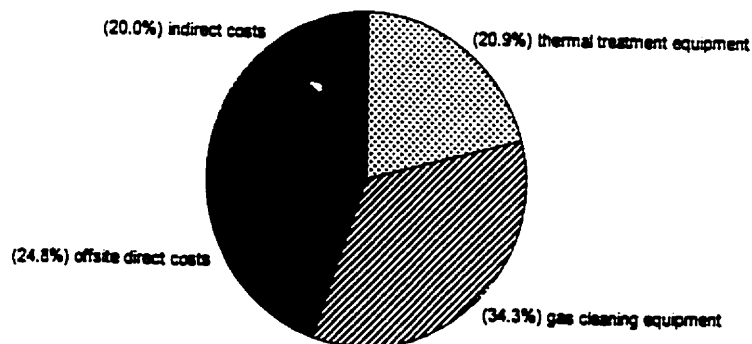


Figure 6.5.1-3: Fixed Capital Investment Breakdown for Soil Incineration with Conventional Afterburner

Figure 6.5.1-4 compares the fractions of the total capital investment allocated to thermal treatment and to gas cleaning for each case and heat source option. The allocation includes the cost of equipment plus factored indirect and offsite costs. Gas throughputs are lower with plasma heating than with fuel combustion. Relative to conventional processes, plasma-assisted processes require 18% less gas cleaning capital for soil incineration, 24% less for soil desorption, and 15% less for liquid waste incineration. Conversely, thermal treatment capital costs are about three times higher with plasma heating than with fuel combustion.

6.5.1.2 Operating Costs

The total annual operating costs include the costs common to all options and the costs specific to each process, including capital cost allowances.

Flexibility in oxygen consumption rates creates a range of operating costs in plasma-assisted processes. For clarity, oxygen costs are represented separately. They correspond to an oxygen concentration of 40% in the plasma gas, and apply only when oxygen enrichment is used.

Figure 6.5.1-5 illustrates the contributions of process-specific and common costs for each case and heat source option. Compared to fuel oil combustion processes, the plasma option is more expensive by 33 - 52% (with 0 - 40% oxygen) in soil incineration, and by 34 - 55% in soil desorption. The difference rises to 69 - 94% for liquid waste incineration with natural gas combustion as the conventional option. This contrast is explained by the relative cost of natural gas and fuel oil energies. Substituting gas for oil in the soil incineration case leads to similar results.

Operating costs are divided into process-specific items (utilities, maintenance and supplies, fixed charges, depreciation) and common items (labour, overhead and general expenses). Figures 6.5.1-6 and 6.5.1-7 illustrate this distribution for

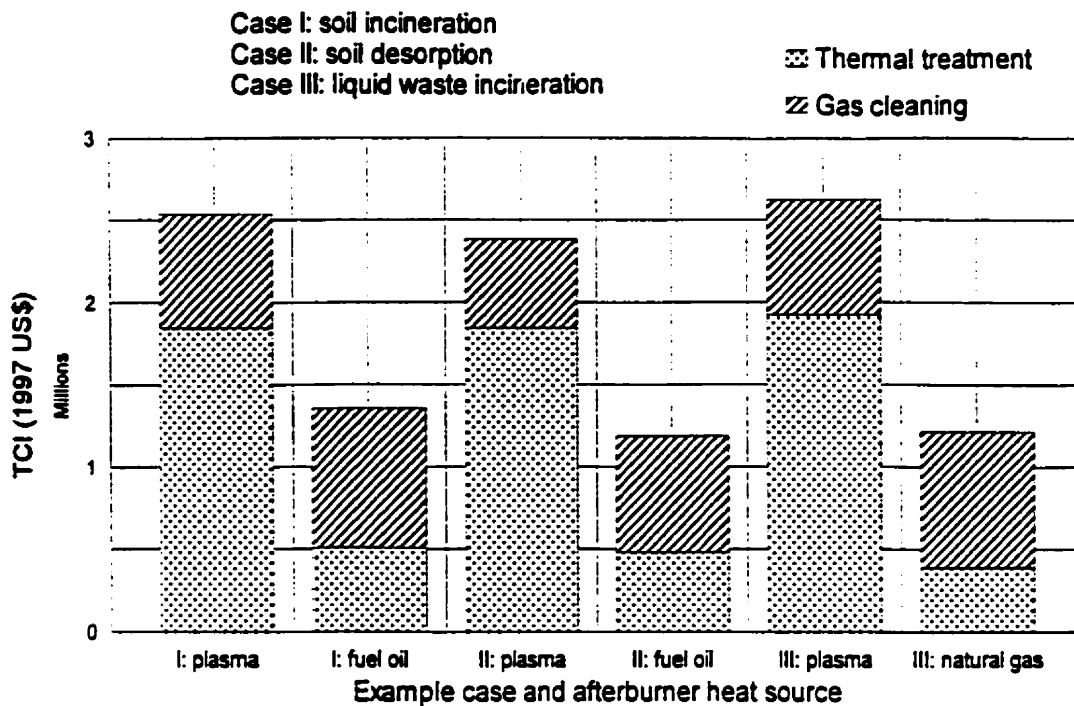


Figure 6.5.1-4: Total Capital Investment (TCI)
Importance of Gas Cleaning Units

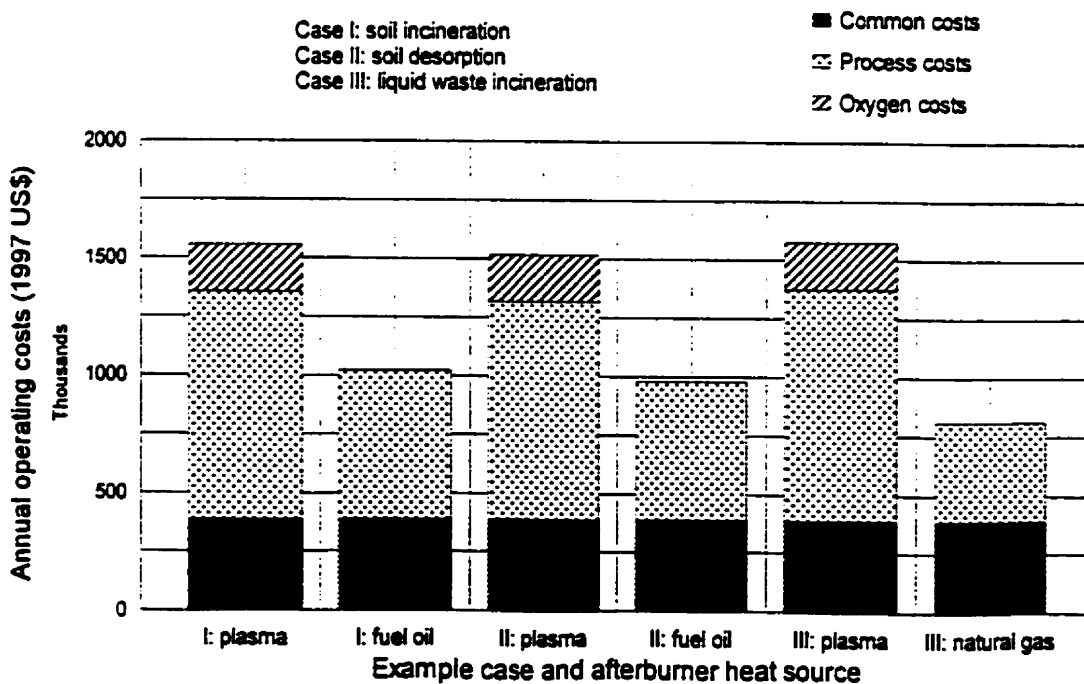


Figure 6.5.1-5: Total Annual Operating Costs
(including depreciation of capital)

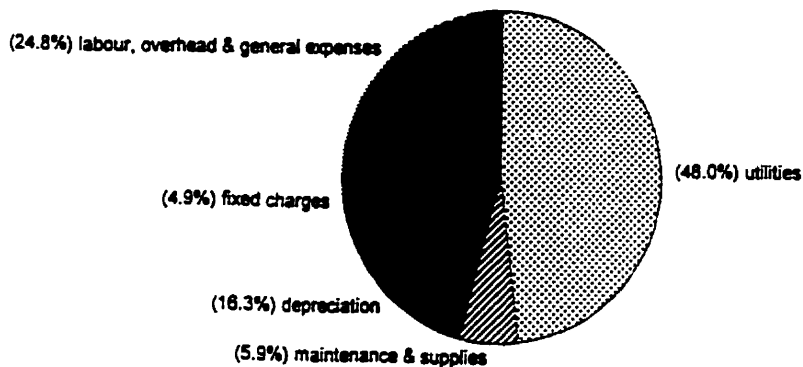


Figure 6.5.1-6: Total Annual Operating Cost Breakdown for Soil Incineration with a Plasma Afterburner

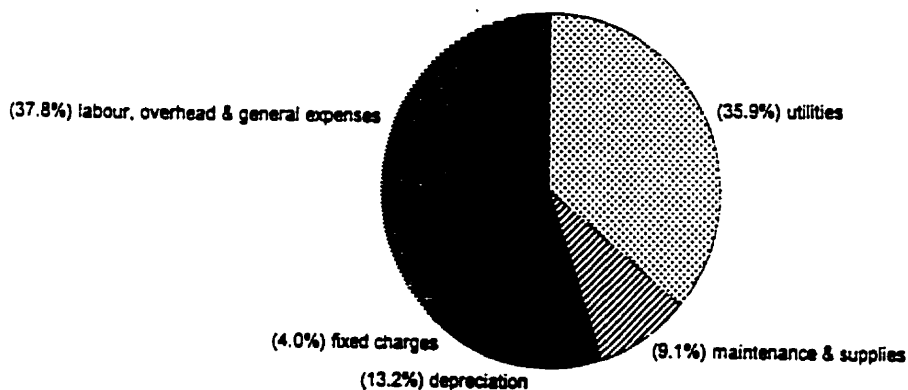


Figure 6.5.1-7: Total Annual Operating Cost Breakdown for Soil Incineration with Conventional Afterburner

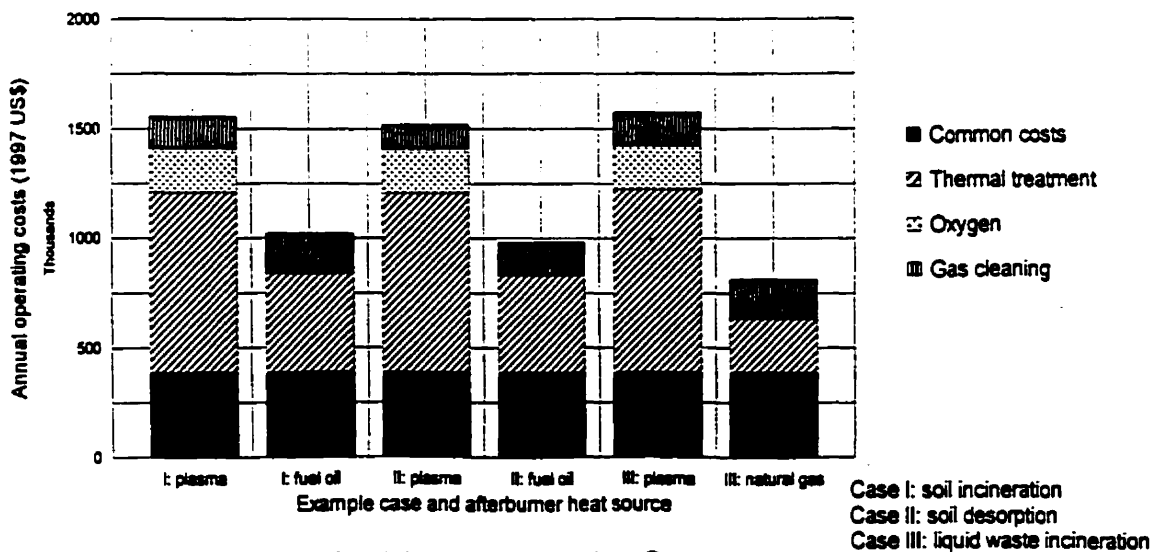


Figure 6.5.1-8: Total Annual Operating Costs Importance of Gas Cleaning Units

Case I: soil incineration
 Case II: soil desorption
 Case III: liquid waste incineration

the plasma and fuel oil afterburner systems of case I. These charts demonstrate the importance of utility and labour costs over capital investment costs. Utilities account for 36% of the total costs in the conventional system, and 48% in the plasma system (including 13% for oxygen enrichment). Despite wide differences in capital investment between the two options, depreciation is near 15% of the annual costs in both cases.

Figure 6.5.1-8 compares the distribution of operating costs among thermal treatment and gas cleaning steps for each case and heat source option. The apportioned costs include the appropriate share of utilities, maintenance, fixed charges and depreciation, but exclude common costs such as labour. Generally, thermal treatment contributes far more than gas cleaning to operating costs. From the tables in Appendix XIII, gas cleaning steps account for less than 10% of utility costs in conventional processes (4% with fuel oil, 8% with natural gas). Gas cleaning contributes 18% of the operating costs in soil incineration, 15% in soil desorption, and 22% in liquid waste incineration. The use of plasma heating lowers gas cleaning costs by about 20% through gas volume reduction. Yet the associated increase in thermal treatment costs far offsets these savings.

6.5.1.3 Net Present Value

An alternative way to evaluate competing options is by their net present values (NPVs). For applications that involve costs without revenues, the NPVs are negative. Figure 6.5.1-9 clearly indicates the overall cost differences between conventional and plasma processes. Figure 6.5.1-10 emphasizes the effects of fossil fuel market prices on the relative standing of these options: the negative NPV of a plasma process is 1.6 times that of a fuel oil process, and twice that of a natural gas process.

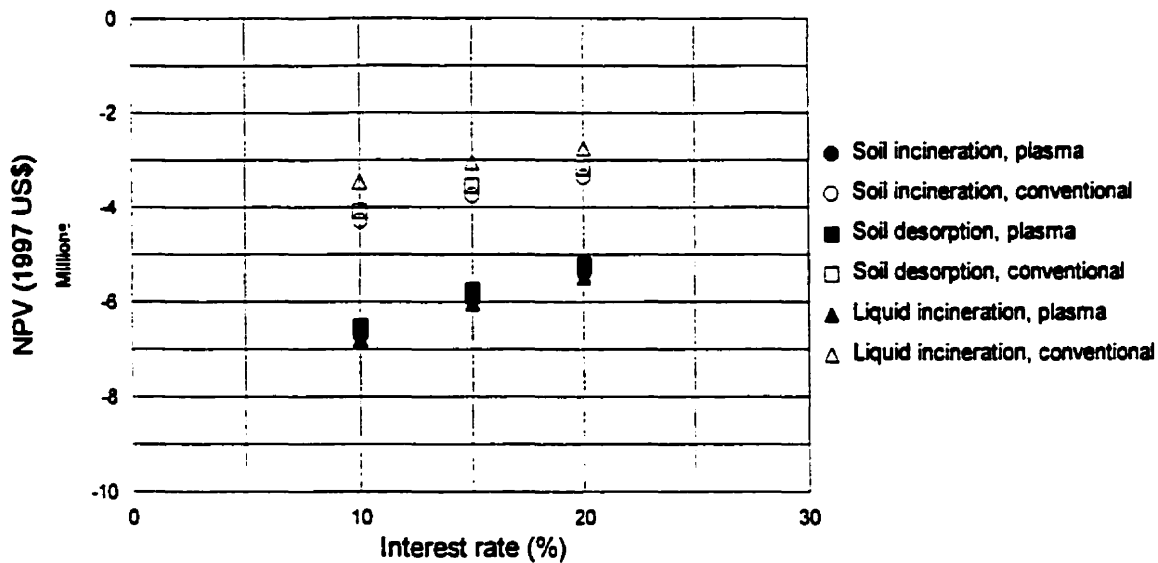


Figure 6.5.1-9: Net Present Value (NPV) of Example Processes Afterburner Options Compared

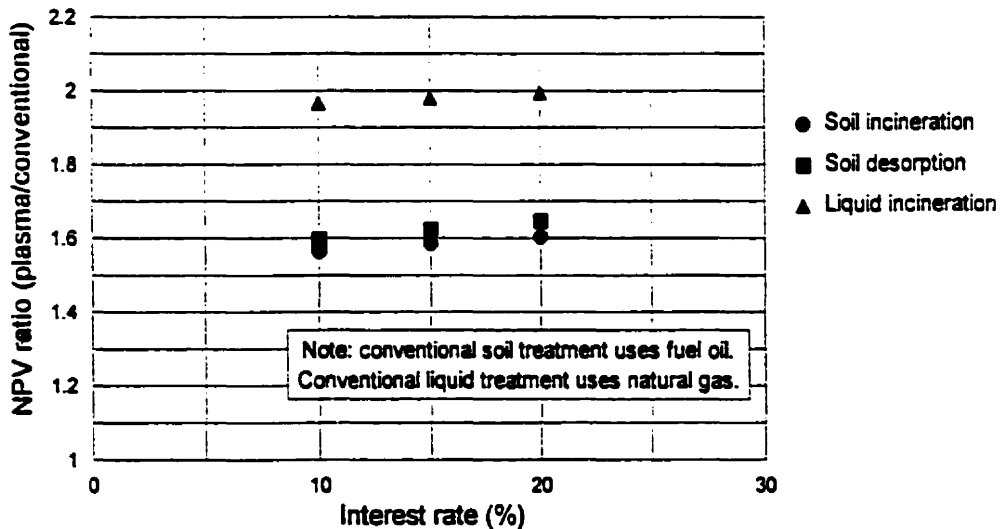


Figure 6.5.1-10: Net Present Value (NPV) Ratio of Competing Options (Plasma-Over-Conventional Heat Source)

6.5.2 Sensitivity Study

6.5.2.1 Process Design Variables

This section addresses the effects of variables such as feed throughput and temperatures on the techno-economic standing of APAI compared to conventional methods.

A potential advantage of plasma heating over fuel combustion is a reduction in gas throughput (Figure 6.5.2-1). Plasma-assisted soil incineration generates 42% less gas per kilogram of soil treated than its conventional counterpart. In desorption, where there is a higher temperature rise from the kiln to the afterburner, plasma heating reduces the throughput by 67%. The lower the kiln temperature, the more significant is the reduction in gas volume for a fixed afterburner temperature. Similarly, the volumetric output of a plasma furnace per kilogram of liquid waste is 39% lower than that of a natural gas combustion furnace. This results in savings on gas treatment costs, but does not ensure the economic viability of APAI. As mentioned in section 6.5.1, thermal treatment dominates over gas cleaning in capital investment and operating costs.

Both plasma and combustion heating generate a fixed amount of gas per unit mass of waste treated. Therefore, the plasma-over-combustion gas throughput ratio is insensitive to soil treatment capacity (Figure 6.5.2-2). The ratio depends on the specific enthalpy rise of the feed gas, so is a function of afterburner temperature (Figure 6.5.2-3). The ratio decreases with increasing temperature. The benefits of plasma are increasingly important as the required operating temperature rises. A plasma heat source also allows operation beyond 1500°C, which is hardly feasible using fuel combustion.

Figure 6.5.2-4 shows the effect of soil treatment capacity on total capital investment in the case of soil incineration. The corresponding charts for soil

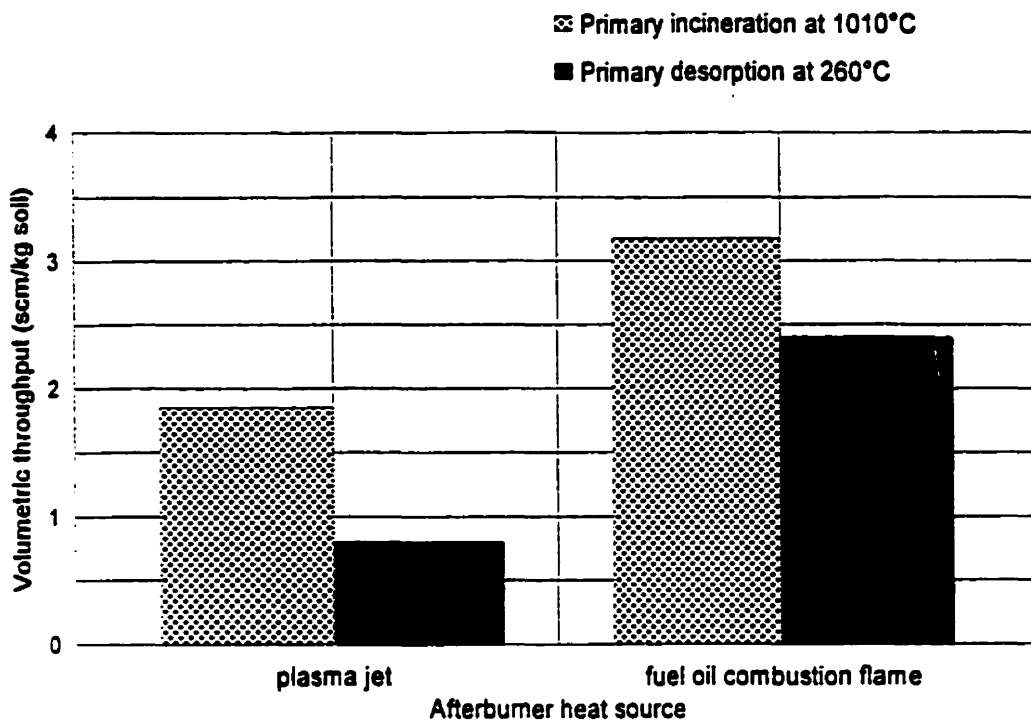


Figure 6.5.2-1: Afterburner Gas Flow Rate per Kilogram of Soil Treated

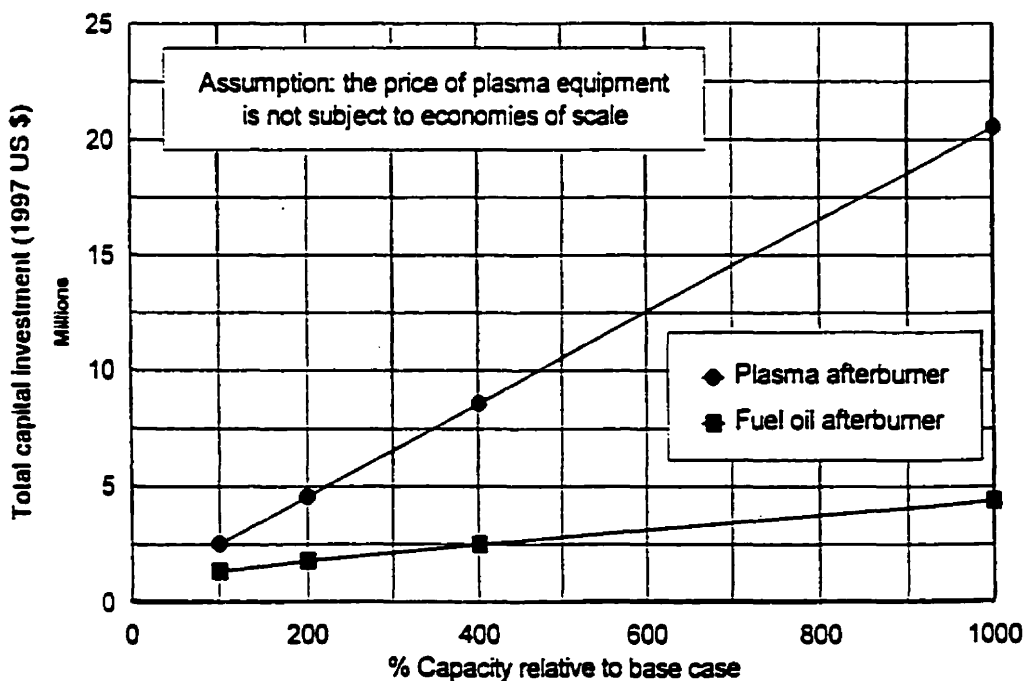


Figure 6.5.2-4: Effect of Soil Treatment Capacity on Capital Investment for Soil Incineration

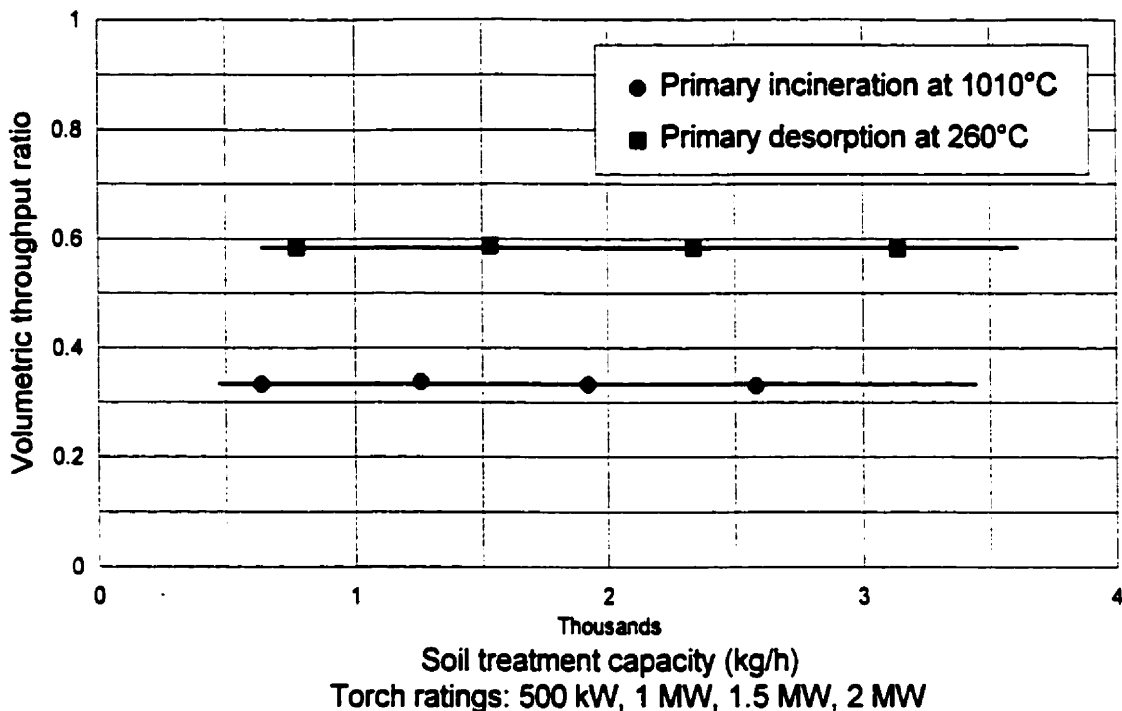


Figure 6.5.2-2: Afterburner Gas Flow Ratio (Plasma-Over-Fuel Oil)
Sensitivity to Soil Treatment Capacity via Torch Power Rating

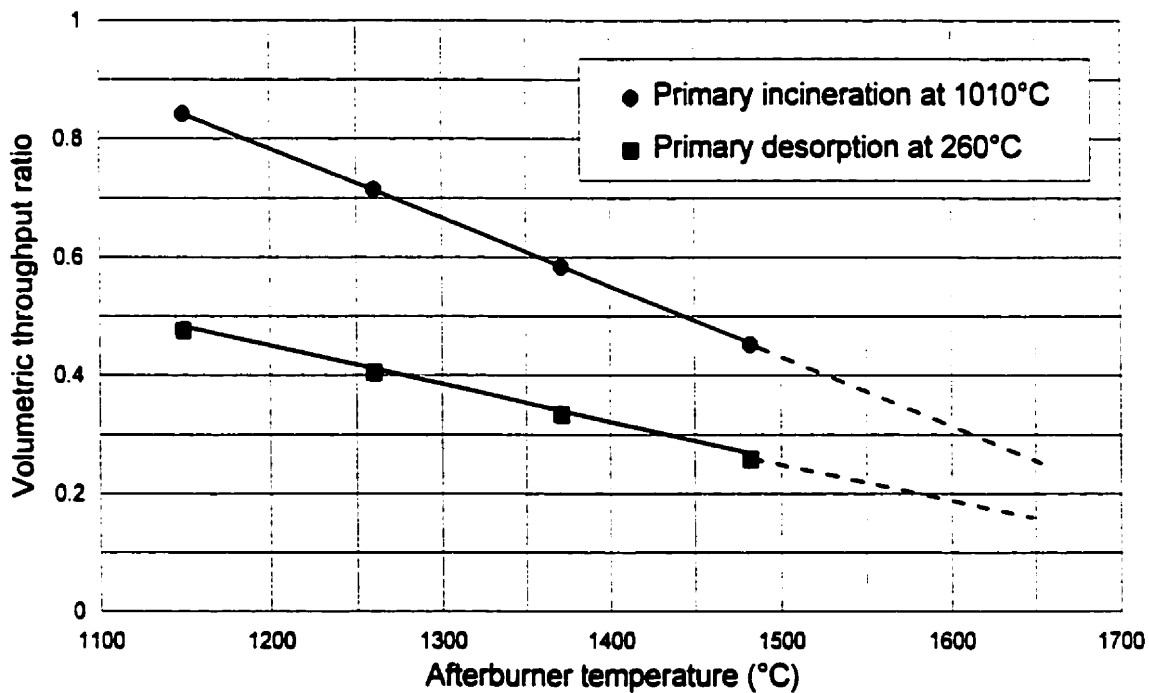


Figure 6.5.2-3: Afterburner Gas Flow Ratio (Plasma-Over-Fuel Oil)
Sensitivity to Afterburner Temperature

desorption and liquid incineration are similar. The data points originate from ASPEN simulations of afterburner systems fitted with one, two, four and ten identical plasma torches rated at 1.5 MW each. Treatment capacity - or heat duty - is proportional to the number of torches. No economies of scale are assumed in the purchase of multiple torch systems for a single afterburner. (The power supply cost [80% of plasma equipment costs] is not subject to economies of scale; the unit cost of a torch might be.) Gas throughput is directly proportional to capacity and determines the size and cost of most process units. Although most costing correlations are non-linear, here overall equipment costs and total capital investment are near-linear functions of capacity, as are utility consumption rates and total annual operating costs (Figure 6.5.2-5). The last two figures demonstrate that the cost of APAI does not depend on the scale of the operation. There would be no disadvantage in applying APAI to a small-scale facility as opposed to a large one.

Curves showing the relative cost of plasma-assisted and conventional processes as a function of capacity appear in Figure 6.5.2-6. These curves represent the total annual cost ratios for plasma options over fuel combustion options. The escalation of the ratio with increasing capacity demonstrates that the viability of APAI does not benefit from scale-up. This conclusion is subject to the limitations of the economic model, including the assumption of direct proportionality between plasma equipment costs and treatment capacity.

A comparison of cases I (soil incineration) and II (soil desorption) informs one on the sensitivity of costs to temperature in the primary kiln. Regarding capital investment (Figure 6.5.2-7), kiln temperature has no significant influence on the comparison between plasma and conventional afterburner options or on the relative costs of primary and secondary units. The relative annual operating costs of plasma and conventional afterburner systems are insensitive to kiln temperature. However, primary treatment costs decrease with the kiln

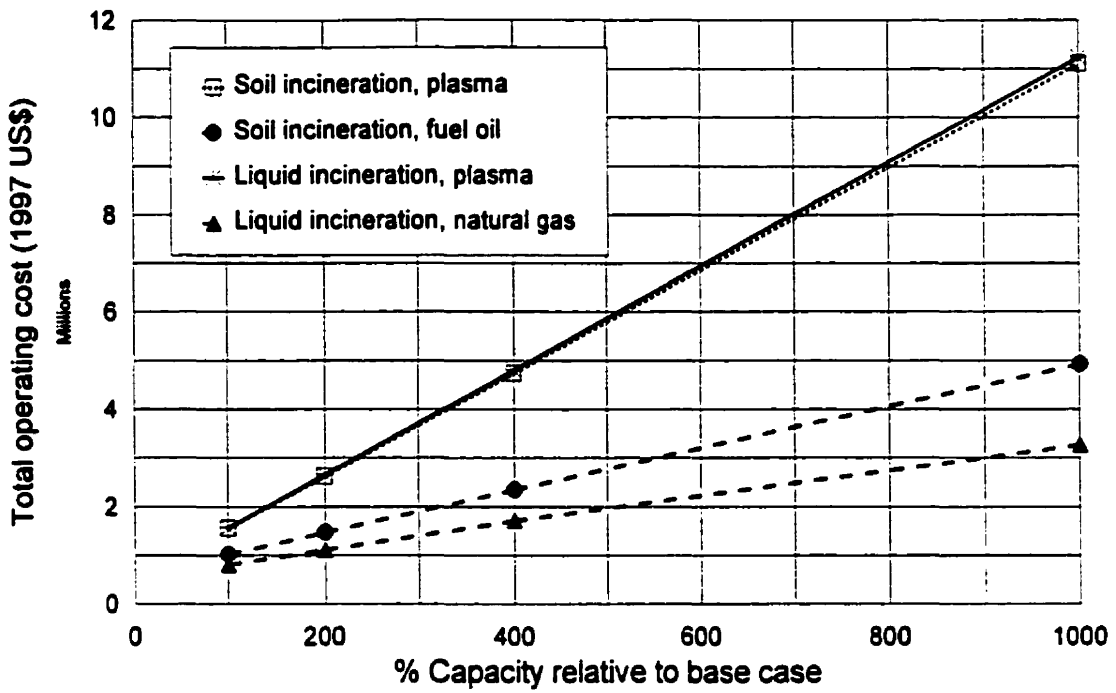


Figure 6.5.2-5: Effect of Scale-Up on the Annual Costs of Competing Options (Plasma vs Conventional Heat Source)

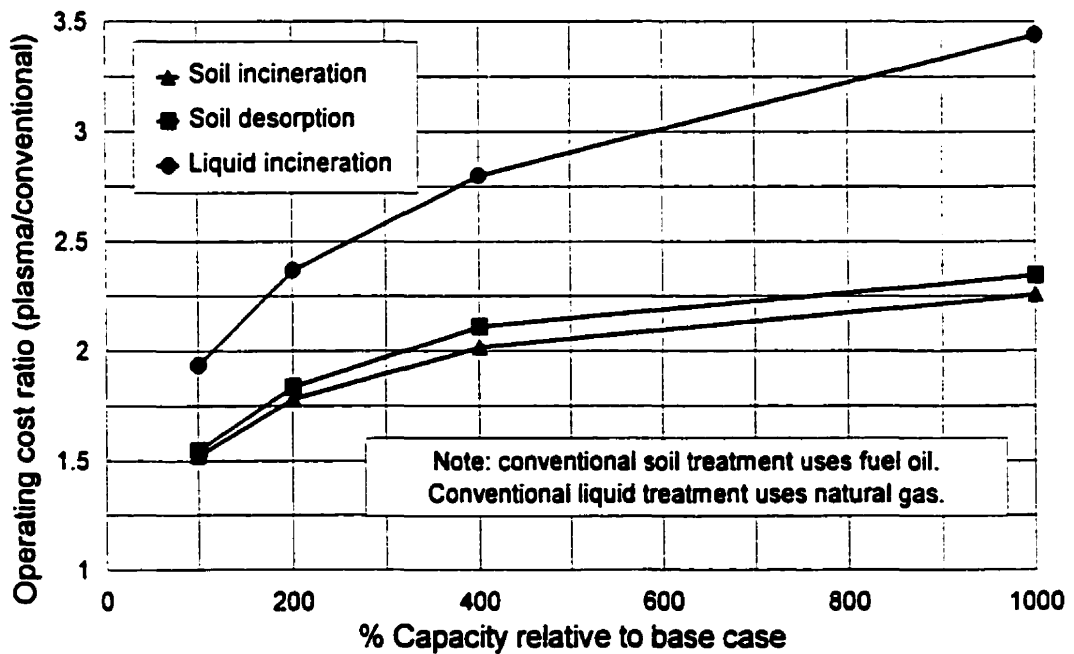


Figure 6.5.2-6: Effect of Scale-Up on the Annual Cost Ratio of Competing Options (Plasma-Over-Conventional Heat Source)

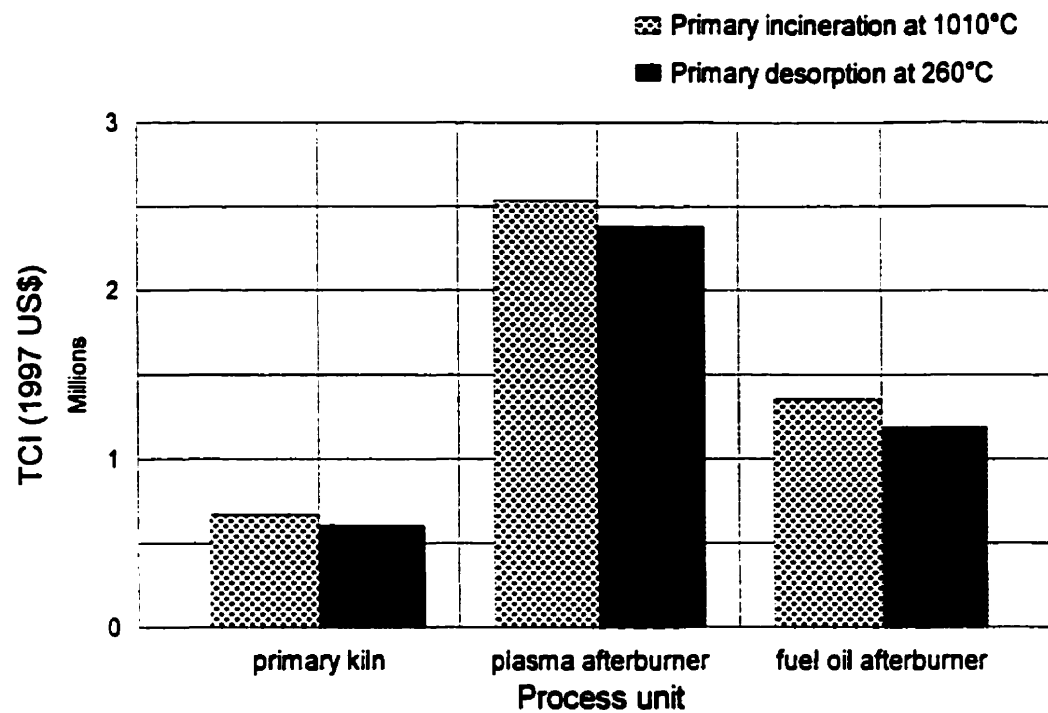


Figure 6.5.2-7: Total Capital Investment (TCI)
 Primary and Secondary Units Compared

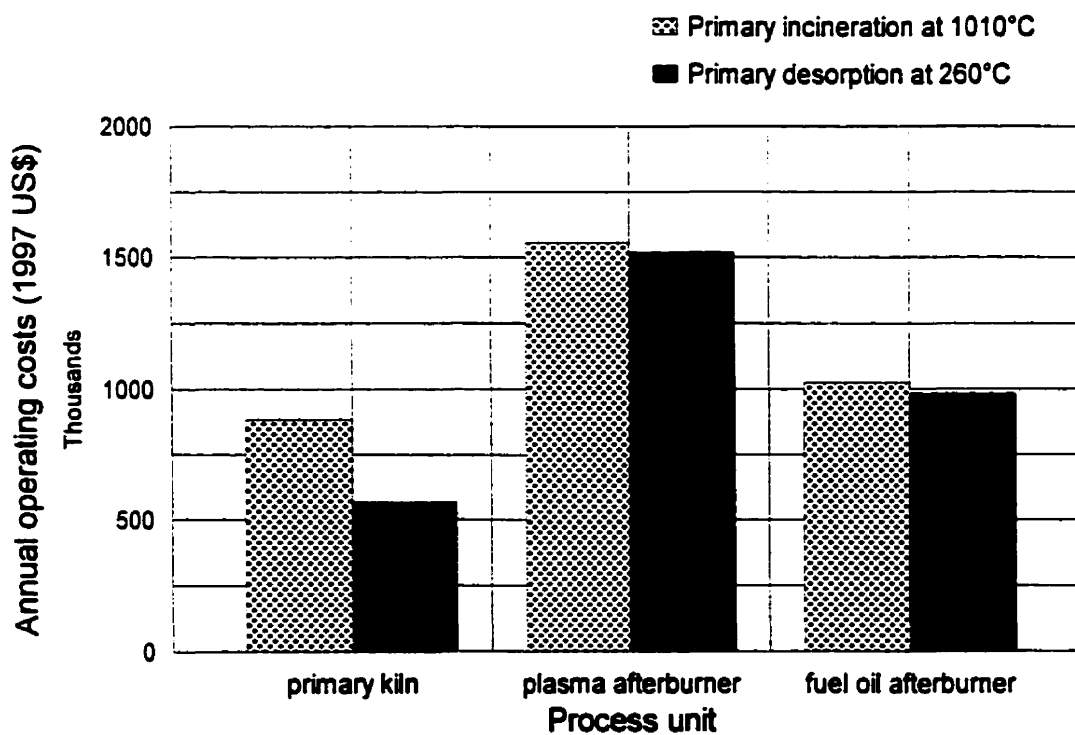


Figure 6.5.2-8: Total Annual Operating Costs
 Primary and Secondary Units Compared

temperature (Figure 6.5.2-8). The thermal capabilities of an APAl afterburner could ease primary treatment requirements and generate savings.

6.5.2.2 External Economic Factors

This section describes how the economic model responds to variations in key market prices. Sensitivity scenarios are developed for cost variables that prominently affect capital or operating costs and are liable to major cost fluctuations. These variables are: the prices of fuel oil, natural gas, electrical power, and the capital cost of plasma equipment. The effect of plasma thermal efficiency, an equipment design variable, is studied here because of its direct link with power consumption. Competing processes are compared in terms of total annual operating costs, which include depreciation of capital.

Fossil fuels

If the price of fuel oil doubled from 170 \$/scm to 340 \$/scm, a soil incineration afterburner would cost the equivalent of a plasma unit without oxygen enrichment (Figure 6.5.2-9). The fuel oil price at which a conventional system would match a plasma system with oxygen is 440 \$/scm, or 2.6 times the current price. A similar analysis for soil desorption gives the same threshold price values. Due to the low cost of natural gas energy, no probable variation in the price of this commodity would make a plasma furnace less expensive to operate than a gas furnace (Figure 6.5.2-10).

Electrical power

A soil incineration plasma afterburner without oxygen enrichment would economically surpass a fuel oil unit given a 67% reduction in electricity price from 6 ¢/kWh to 2 ¢/kWh (Figure 6.5.2-11). At the nominal oxygen consumption level, the plasma system could not compete unless the cost of electricity were negligible. Taking case III as an example (Figure 6.5.2-12), no reduction in

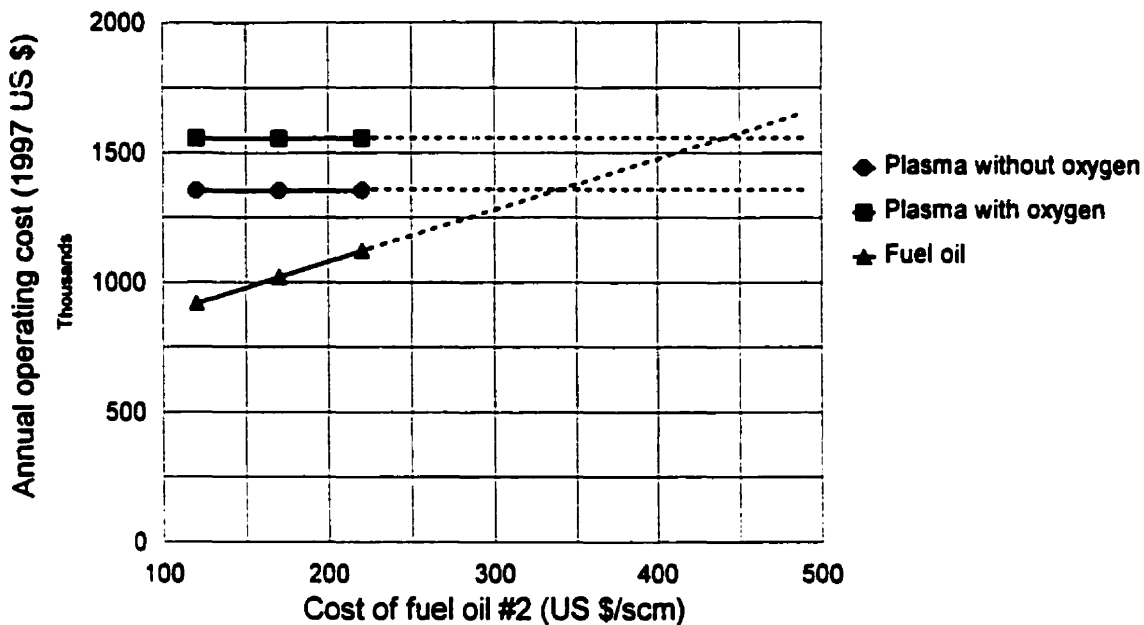


Figure 6.5.2-9: Sensitivity to the Price of Fossil Fuel for Soil Incineration

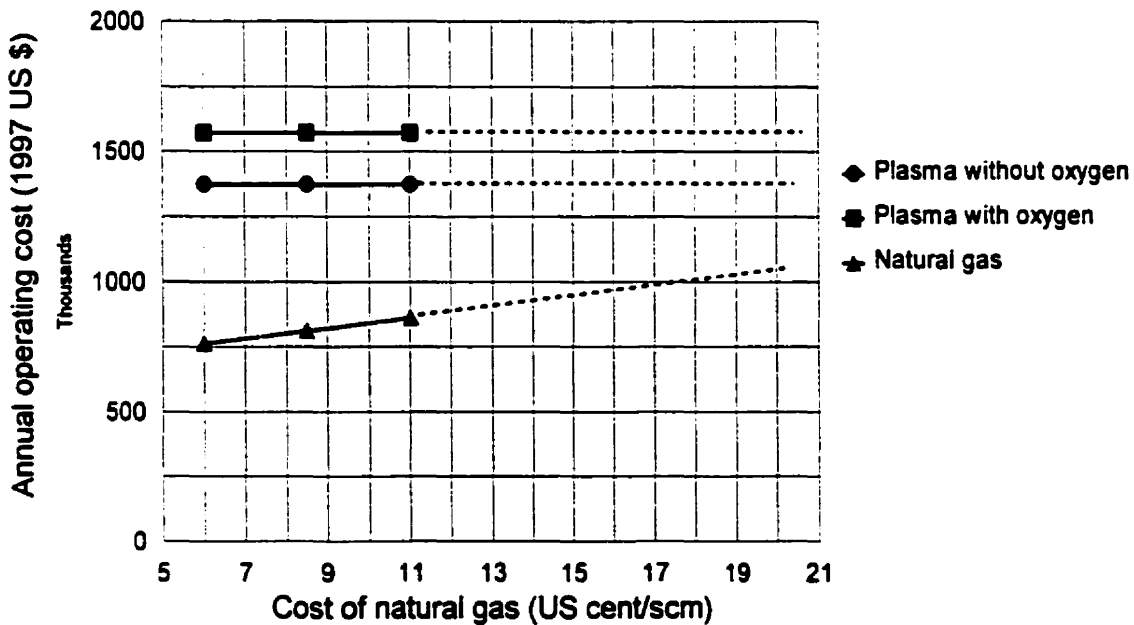


Figure 6.5.2-10: Sensitivity to the Price of Fossil Fuel for Liquid Waste Incineration

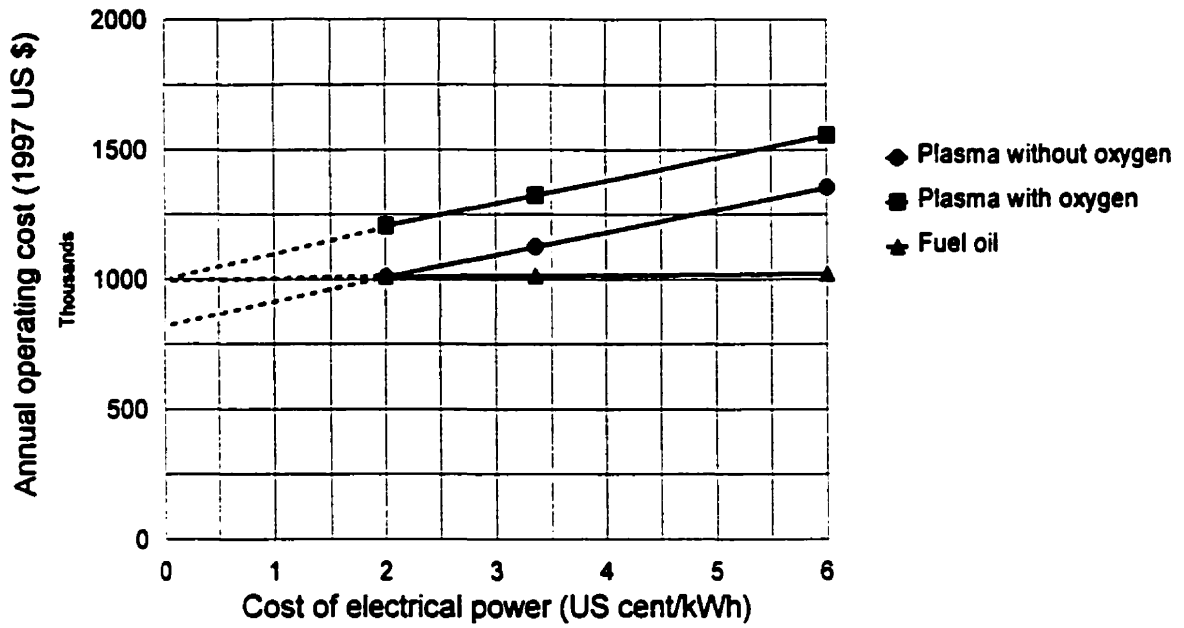


Figure 6.5.2-11: Sensitivity to the Price of Electrical Power for Soil Incineration

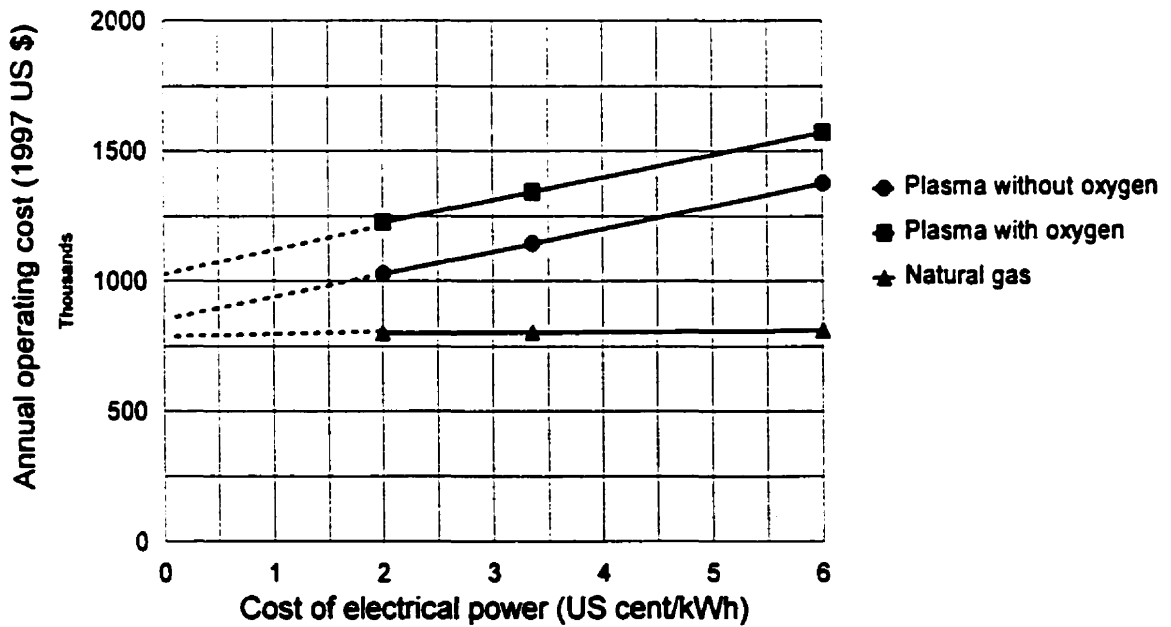


Figure 6.5.2-12: Sensitivity to the Price of Electrical Power for Liquid Waste Incineration

electrical power price could bring the cost of a plasma furnace below that of a natural gas furnace.

Plasma equipment

Based on Figures 6.5.2-13 and 6.5.2-14, a change in the cost of plasma equipment alone could not make APAI more profitable than conventional options. One concludes that utility consumption rates are determinant in the viability of plasma-assisted waste treatment. Power alone accounts for 33% of the annual costs in an oxygen-enriched soil incineration system (69.6% of the utility costs shown in Figure 6.5.1-6). Hence the thermal efficiency of the plasma system is important. For a fixed afterburner duty, overall thermal efficiency sets the rate of power consumption.

A summary chart of economic sensitivity to external factors appears in Figure 6.5.2-15 for a plasma afterburner and in Figure 6.5.2-16 for a fuel oil afterburner (case I). These charts reveal the relative importance of external factors in each process. For example, electrical power price is a dominant factor in APAI, closely followed by thermal efficiency and, less importantly, plasma equipment costs. The conventional process is as sensitive to fuel oil price as the plasma process is to electricity price. This information is summarized in Table 6.5.2-1.

Table 6.5.2-1: Illustrative Figures From the Sensitivity Study

Effect of a 20% increase in ...	In an afterburner system using...	Change in annual operating cost
electrical power price	plasma	+ 6.7 %
overall plasma torch efficiency	plasma	- 5.4 %
plasma equipment cost	plasma	+ 3.4 %
electrical power price	fuel oil	+ 0.4%
fuel oil price	fuel oil	+ 6.9 %

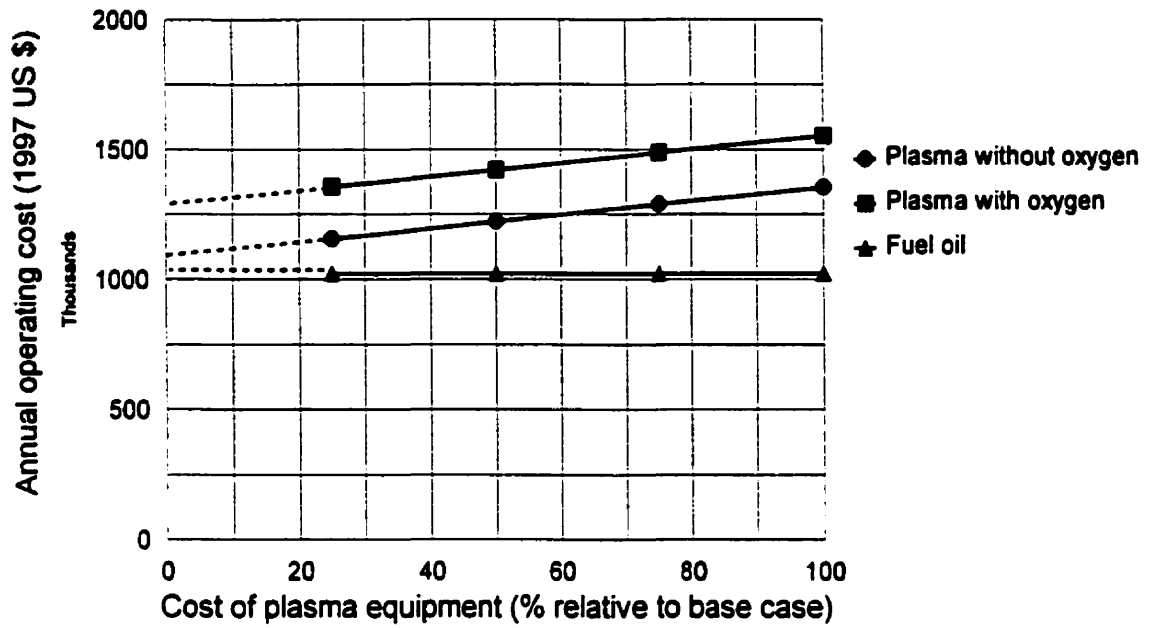


Figure 6.5.2-13: Sensitivity to the Price of Plasma Equipment for Soil Incineration

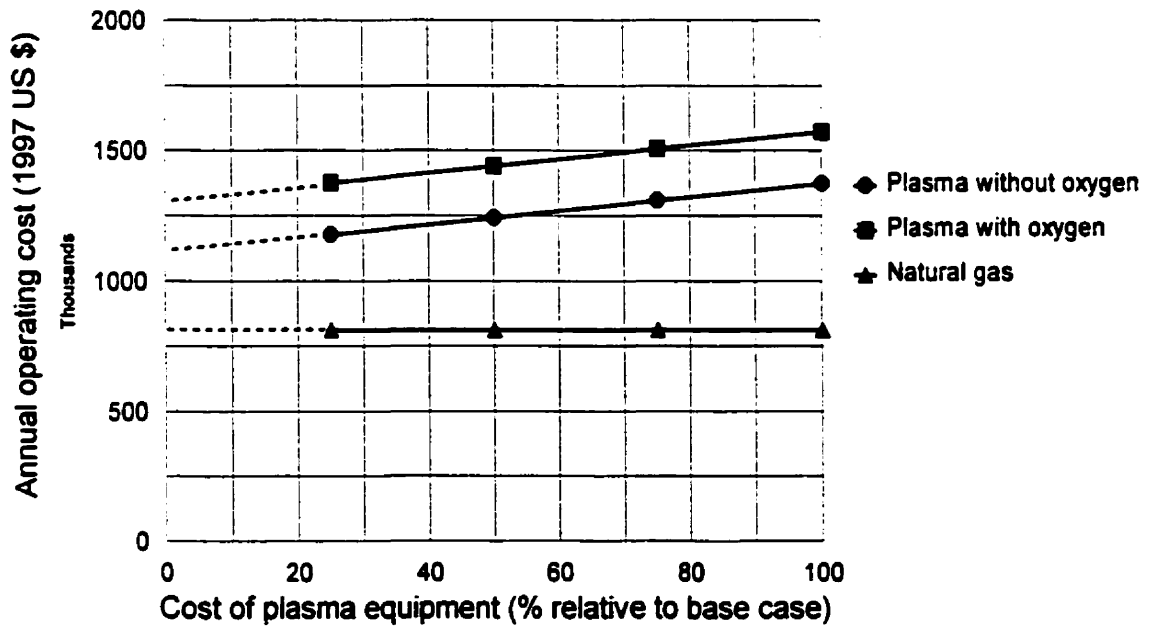


Figure 6.5.2-14: Sensitivity to the Price of Plasma Equipment for Liquid Waste Incineration

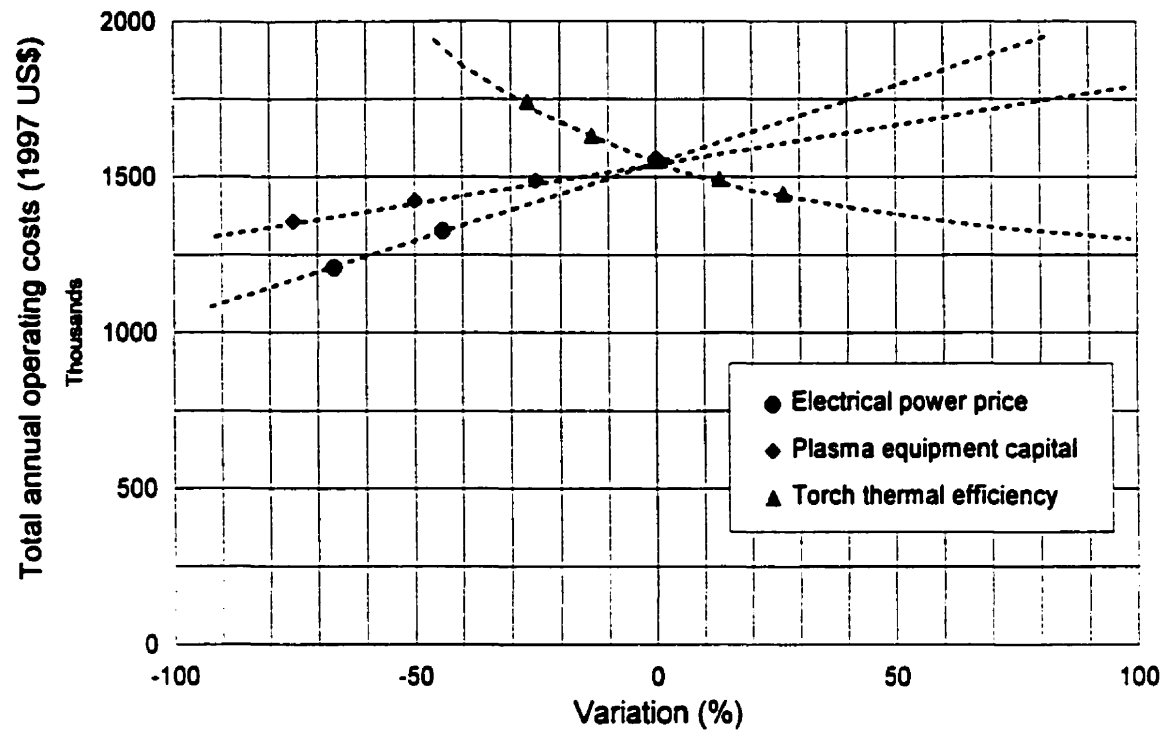


Figure 6.5.2-15: Plasma Process Operating Costs (Including Depreciation) Sensitivity to Market Prices and Torch Efficiency

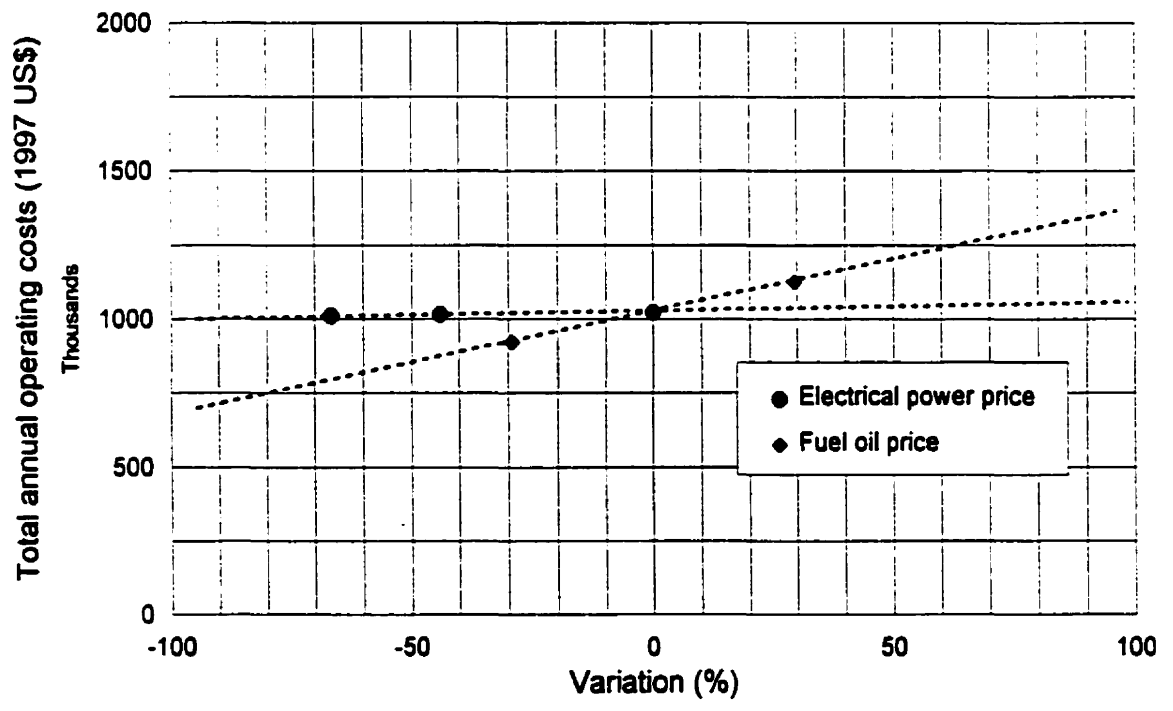


Figure 6.5.2-16: Conventional Process Operating Costs (Including Depreciation) Sensitivity to Market Prices

6.6 Incentives and Potential Market for APAI

This section addresses the viability of APAI in the light of current and emerging trends in environmental management. It complements the economic analysis by discussing factors that are either qualitative in nature or difficult to quantify at this stage of development.

6.6.1 Trends in Environmental Policy

The protection of human health and the environment is beginning to be viewed as a priority obligation. Public scrutiny and involvement in environmental issues denote increasing concern for the safety and sustainability of industrial practices. Ongoing research on the impacts of human activity is prompting changes in environmental policies and guidelines throughout the developed world. These trends highlight three keystones of sound environmental management: public information, technological and regulatory change, and prevention. The following paragraphs examine these three aspects in further detail.

The public acceptance of a project or technology calls for the accessible information about its safety. *Right-to-know legislation* has been implemented on specific issues, e.g., the Toxics Release Inventory in the United States in 1987 and the National Pollutant Release Inventory in Canada in 1993 (CEC 1998). Public demands, including proposals for citizens' monitoring initiatives (Jackson 1996), encourage progress through communication of accurate information. The following case exemplifies the pitfalls of misinformation.

BOVAR Waste Management Inc. owns a toxic waste incineration facility in Swan Hills, Alberta. Following a 1996 accidental release of PCBs, dioxins and furans, aggressive measures were implemented to improve emergency response and bring fugitive emissions well below safe limits. The company's environmental record has been outstanding since. Somehow, until recently, residents wrongly

assumed that fugitive emissions had been eliminated entirely. When marginal PCB levels in snow due to fugitive emissions were brought to public attention, BOVAR suffered unfavourable media exposure (Maclean Hunter 1998). Company officials acknowledged the existence of fugitive emissions, explaining that the observed levels posed no risk. Yet the surprise raised public suspicion, prompting demands for an independent assessment of the situation. BOVAR's initial failure to offer complete, clear information allowed media and activists to turn acceptable monitoring results into a sensational disclosure.

New scientific information justifies regulatory change which, in turn, drives technological development. For example, the addition of dioxins to the list of known carcinogens in 1997 by the World Health Organization (WHO) spurred dioxin-related health and safety research worldwide. The WHO's statement greatly increased public awareness, as attested by an ensuing wave of "dioxin scares," and led to enhanced monitoring efforts.

Japan's agricultural sector fell into turmoil in February 1999 when reports of contamination in soil and vegetables triggered public debate over environmental regulations. The Japanese government responded by proposing regular updates of its emission policies, inspection systems and tolerable daily intake values. A dioxin emission threshold set for 2002 has initiated a shift toward novel incineration technologies, as existing facilities fail to meet the new standards (Bureau of National Affairs 1999). In France, dioxin emissions from waste incinerators dropped by 40% from 1997 to 1998 due the closure of several facilities in the wake of contamination reports. Since 1997, new waste incinerators are subject to revised dioxin and furan emission norms which only six of the country's seventy-two largest established facilities can meet (Bureau of National Affairs 1999). These two examples point out the need for the development of techniques which can meet stricter regulatory standards.

Present uncertainty about the global effects of human activity demands a prevention-oriented approach that values flexibility and potential for improvement. To encourage preventive management, environmental strategists propose expanding the scope of regulatory action beyond bans and limits. Positive incentives envisaged as instruments of change include: (1) benchmarking efficiency standards to encourage technological improvement; (2) setting targets beyond current best practice to promote innovation; (3) adopting strict liability structures (i.e., independent of fault) to favour the control of risk, waste and pollution; and (4) adjusting material prices through taxation to account for environmental and social externalities (Jackson 1996).

The objectives of APAI fit within current environmental trends. APAI offers unique waste destruction capabilities suited for the challenge of future legislation. It provides an alternative to the complete shut-down of existing incineration facilities. The adaptive strategy is an asset in the context of prevention and safety. Pollutant emissions are kept under control as the system rapidly detects and responds to disturbances. This inherent flexibility ensures appropriate action in a wide range of situations. Continuous monitoring provides sustained evidence of the operation's safety. These circumstances should facilitate public acceptance of this application.

6.6.2 Full Cost Accounting and Total Life Cycle Analysis

Full Cost Accounting (FCA) is an investment appraisal strategy whose goal is to report all relevant costs and benefits, in financial terms whenever possible. Full cost accounting guidelines help in the identification of probable and potential costs or benefits. Table 6.6.2-1 compares plasma and conventional afterburner processes along guidelines listed by Jackson (1996). The table indicates the probable standing of each process with respect to specific cost elements. The comparison assumes that plasma allows higher destruction efficiency, lower toxic emission rates, and minimal exposure to future liabilities. A qualitative

appreciation of the factors listed suggest a net advantage in favour of the plasma option.

Table 6.6.2-1: Qualitative Comparison Using FCA Guidelines

FCA Elements	Plasma Afterburner	Fuel Afterburner
Capital costs	equipment: higher start-up training: higher	equipment: lower start-up training: lower
Operating costs	capital-related: higher utility: slightly higher start-up/shut-down: lower gas cleaning: lower wastewater treatment: lower	capital-related: lower utility: slightly lower start-up/shut-down: higher gas cleaning: higher wastewater treatment: higher
Overhead charges		
re. toxic emissions	emission fees: lower liability insurance: lower fines and penalties: lower legal fees: lower	emission fees: higher liability insurance: higher fines and penalties: higher legal fees: higher
re. approval	new technology certification, testing: higher	established process, appropriated rights: lower
Indirect costs		
re. public relations	public acceptance: lower corporate image on environmental issues: lower	NIMBY syndrome: higher long-standing image as pollution generator: higher
re. innovation	flexibility, "best available technology": lower	adaptation to regulations, feasibility limitations: higher

The comparison could extend to further-reaching indirect costs ("externalities") linked to environmental damage. **Total Life Cycle Analysis (TCLA)** assesses the environmental costs of a process, product or activity through systematic examination of resource use, waste release, associated impacts, and improvement opportunities. This includes accounting for broad-ranging consequences such as environmental burdens from the production of materials and utilities. These burdens are not necessarily reflected in market costs, and lie outside the boundaries of typical accounting frameworks. The main difficulty of this approach is the uncertainty in cost values assigned to externalities.

A comprehensive examination modelled on TLCA highlights other advantages of APAI over incineration:

1. A plasma is a more efficient heat source than a combustion flame, increasingly so as temperature rises. An energy transfer efficiency of 75-85% is expected between the plasma and the medium to be heated (including losses to walls and such). In contrast, the heat available from a flame is 26% of the fuel value at the afterburner temperature (1371°C), and 46% at the kiln temperature (1010°C).
2. A plasma afterburner substitutes electrical energy for fossil fuel energy. Electricity is generally recognized as renewable whereas petroleum products are not.
3. Unlike fossil fuel combustion, a plasma discharge generates no carbon oxides (greenhouse gases), and its gas output is low. This statement applies within the boundary limits of a waste treatment facility. Outside this envelope, the externalities of electricity generation must be considered.
4. Lower gas volumes in the plasma process mean lower scrubbing water consumption, lower wastewater volumes, and therefore lower material and energy requirements in gas and wastewater treatment units.
5. The use of a plasma is expected to reduce the formation of dioxins and furans by minimizing the amount of precursors and by promoting oxidation reactions. This would ease the social, financial and environmental burdens attached to toxic emissions from waste treatment facilities.

6.6.3 Techno-Economic Niche for APAI

Based on the economic model, APAI appears uncompetitive. It requires twice as much capital investment as an equivalent conventional process, and costs 50% more to operate. This statement implies the major assumption that combustion systems as effective as APAI are indeed available.

Economic appraisal in the environmental sector requires a concept of profitability that extends beyond direct return on investment. Carrying environmental protection costs to the retail price of goods and services is not the only means of recovering this type of investment. Benefits derived from protection measured can be viewed as "non-market goods" or "profits". A company's environmental profile reflects on public opinion and market share. The influence of market forces on corporate policies is seen in the recent emphasis on environmentally friendly technologies and products. Environmental responsibility is no longer a strict economic burden: it provides strategic opportunities to increase competitiveness and expand market share. Concurrently, antipollution laws shift the focus of process viability away from economic considerations. Attesting to this is the controversial "technology forcing" approach of the American government, whereby "... legislative or administrative standards compel industry to implement the 'best available' or 'most suitable' technology for achieving lowered emission standards, regardless of (or putting strikingly low weight upon) economic feasibility or internal cost-benefit calculations" (Koplow 1997). These trends in environmental policy announce a context in which the benefits of APAI could justify the financial investment.

Environmental protection costs fall into four classes: (1) *prevention costs*, including end-of-pipe measures; (2) *appraisal costs* linked to monitoring and auditing; (3) *internal failure costs* of corrective measures applied before external damage is incurred; and (4) *external failure costs* which include fines, liability

charges, clean-up charges, and impact on public image (Madu 1996). Sound environmental management emphasizes prevention and appraisal, responds efficiently to internal failure, and aims to avoid external failure. APAI focuses on the first three categories, or proactive costs, to minimize the detrimental costs of external failure. In this respect, APAI fits the economic framework of responsible environmental management.

In industrial practice, a common strategy is to effect minimum treatment or prevention (as per regulations) using the most affordable means. Another strategy is to surpass mandatory requirements using technology designed to meet higher standards. The additional cost can be carried to products and services within an acceptable margin known as "WTP", or what customers are "Willing To Pay" for added benefits (Pearce and Brisson 1995). A third alternative is to make waste minimization a process objective. The last two strategies imply higher capital and operating costs, but enhance the process in terms of prevention and flexibility. APAI complies with both these approaches.

Unlike conventional incineration, APAI is not a broad-purpose solution to waste management problems. Its applicability pertains to waste likely to generate intractable volatile compounds that are toxic, incineration-resistant and severely regulated, as in the following situations:

1. Restoration of contaminated soil, when the nature or quantity of contaminant justifies incineration of the soil matrix;
2. Treatment of PCB-contaminated materials, often combined with destruction of PCB-containing liquids as in electrical transformer decommissioning operations;

3. Incineration processes where difficult combustion produces high concentrations of incomplete oxidation products at the primary stage;
4. Treatment of mixtures where hazardous contaminants are non-homogeneously distributed;
5. Incineration processes for treating organohalogenated liquids in concentrated form.

A specific example of possible application is the demilitarization of aging chemical weapon stockpiles. Following ratification of the Chemical Weapons Convention Treaty in 1993, the United States' Army has operated a prototype facility for permanent dismantling of chemical weapons (Koplow 1997). Among potential technologies under development at the time of the treaty, only incineration was deemed sufficiently advanced to allow demilitarization of the designated stockpiles within the time frame of the program. The process developed at the Johnston Atoll facility involves four incineration units, each of which includes an afterburner and a pollution abatement system. A *deactivation furnace* handles explosive components in a rotary kiln at 550-1000°C, with post-combustion at 1200°C. Toxic chemical agents are burned in a *liquid incinerator* at 1480°C. Recyclable casings and containers are decontaminated in a *metal parts furnace*, while miscellaneous packaging/waste materials go to a *dunnage incinerator*. The development of the program was slowed by technical difficulties and by controversial reports on the performance and safety of the facility. Among other issues, accidental and fugitive releases of unacceptable chemicals were of major concern to opposition groups. The implementation of APAI could alleviate such problems, notably in the high-temperature liquid incineration process.

7. CONCLUSIONS

This project examined the potential benefits of combining plasma technology and conventional incineration in the treatment of toxic organic waste.

APAI is a promising option for the complete destruction of the most persistent hazardous contaminants. Its thermal and adaptive capabilities answer a need for safe balance between effectiveness and cost. The conclusions of this study support the feasibility of APAI and its potential as an advanced method of hazardous waste treatment.

- 1 - The expected benefits of APAI reside in unsurpassed effectiveness, safety and flexibility. In principle, APAI could meet almost any destruction efficiency requirement for organic components, regardless of feed characteristics. With thermal capabilities in excess of actual needs, compliance with new regulations could be as simple as altering the settings of a control program.
- 2 - Efficient operation is achievable by continuous feedback optimization using an algorithm that integrates the destruction efficiency target and cost of resources.
- 3 - The adaptive plasma-assisted approach to incineration is more costly than conventional methods. APAI requires twice the capital investment and costs 30% more to operate than fuel combustion incineration.
- 4 - The economic standing of APAI relative to conventional incineration will not change significantly with fluctuations in the price of utilities.
- 5 - APAI could find a commercial niche in the treatment of waste containing persistent compounds and subject to severe regulatory control. Potential applications range from the destruction of concentrated hazardous liquids

(e.g., PCB oils) to the remediation of soil contaminated with toxic industrial chemicals.

7 - APAI is equally suitable for small-scale and large-scale operation.

Original contributions to knowledge

- 1 - The technical feasibility of the APAI concept was demonstrated experimentally using a plasma afterburner model system.
- 2 - Plasma power and oxygen content were confirmed to be effective variables for controlling the destruction of organic compounds.
- 3- Rapid on-line monitoring was achieved by optical detection of distinctive emission features using a simple low-cost technique.
- 4 - The cost of APAI relative to conventional methods was modelled for soil incineration, soil desorption and liquid organic waste treatment.
- 5 - A range of applicability was proposed for APAI based on its expected benefits and economic constraints.

Recommended future work

- 1 - Further research is needed to verify the efficiency of hazardous organic waste destruction in laboratory- and pilot-scale plasma afterburners. The configuration of these units should provide sufficient control over temperature, mixing and residence time in the afterburner chamber.

- 2 - The adaptive optimization approach should be tested on a dc plasma system where independent control of the manipulated variables provides stable and reproducible operation.
- 3 - The experimental system used optical emission measurements in the visible spectrum. In an APAI prototype, alternate spectroscopic techniques should be investigated for composition monitoring in and downstream of the afterburner, where visible emission is reduced.
- 3 - The limitations of the open-system model did not permit measurement of absolute concentrations in the product gas. The exhaust gas of a prototype system should be analyzed at steady state to establish a correspondence between spectroscopic measurements and composition.
- 4 - The optimization strategy developed for this project was limited to manual feedback control using standard optimization algorithms. The control system of an automated prototype could use advanced techniques such as learning algorithms. On-line feed characterization could allow feedforward control action. Hence the optimization strategy could integrate operating record information and knowledge of waste decomposition chemistry to enhance the adaptive response.

8. BIBLIOGRAPHY

- Air Quality Analytical Inc. (1999), Technical literature and personal communication with Mr. Mark R. Nelson.
- Alder J.F. and J.M. Mermet (1973), "A Spectroscopic Study of Some Radio Frequency Mixed Gas Plasmas," *Spectrochimica Acta*, **28** (B), 421-433.
- Bennett Environmental Inc. (1999), Commercial literature.
- Betteridge D., A.P. Wade and A.G. Howard (1985), "Reflections on the Modified Simplex - I," *Talanta*, **32** (8B), 709-722.
- Betteridge D., A.P. Wade and A.G. Howard (1985), "Reflections on the Modified Simplex - II," *Talanta*, **32** (8B), 723-734.
- Beulens J.J., C. Gastineau, N. Guerrassimov, J. Koulidiati and D.C. Schram (1994), "Atomic and Molecular Emission Spectroscopy on an Expanding Argon/Methane Plasma," *Plasma Chemistry and Plasma Processing*, **14** (1), 15-42.
- Bleekrode R. and W.C. Nieuwpoort (1965), "Absorption and Emission Measurements of C₂ and CH Electronic Bands in Low-Pressure Oxyacetylene Flames," *The Journal of Chemical Physics*, **43** (10), 3680-3687.
- Boulos M.I., P. Fauchais and E. Pfender (1994), *Thermal Plasmas*, vol. 1, Plenum Press, New York.
- Bousrih S., E. Ershov-Pavlov, S. Megy and J.M. Baronnet (1995), "Hydrogen/Argon Plasma Jet with Methane Addition," *Plasma Chemistry and Plasma Processing*, **15** (2), 333-351.
- BOVAR Waste Management Inc. (1999), Technical literature and personal communication with Mr. Harold Krenkel and Mr. Ian Glew.
- Brunner C.R. (1996), *Incineration Systems Handbook*, Incinerator Consultants Inc., Reston VA.
- Brunner C.R. (1987), "Incineration: Today's Hot Option for Waste Disposal," *Chemical Engineering*, Oct. 12, 96-106.
- Budó A. (1937), "Intensitätsformeln für die Triplettbanden," *Zeitschrift für Physik*, **105**, 579-444.

- Bureau of National Affairs, Washington DC (1999), "News," *International Environment Reporter*, **22** (5), 180-210.
- Cavadias C., J. Amouroux, L. Hochard, and A. Ricard (1995), "Determination of C-Atom Density Downstream an Ar-CH₄ RF Plasma Torch," *Plasma Chemistry and Plasma Processing*, **15** (2), 221-230.
- Chen W.L.T., J. Heberlein and E. Pfender (1994), "Diagnostics of a Thermal Plasma Jet by Optical Emission Spectroscopy and Enthalpy Probe Measurements," *Plasma Chemistry and Plasma Processing*, **14** (3), 317-332.
- Commission for Environmental Cooperation (1998), *Taking Stock: North American Pollutant Releases and Transfers 1995*.
- Cooke N.E. (1992), Class notes for course no. 302-472A: Industrial Air Pollution Control Engineering, McGill University, Canada.
- Czernichowski A., P. Labbé, F. Laval and H. Lesueur (1995), "Plasma-Assisted Cleaning of Flue Gas from a Sooting Combustion: Case of Organic Nitrates," *Emerging Technologies in Hazardous Waste Management V*, American Chemical Society, 144-154.
- Czernichowski A., P. Jogensen, H. Lesueur, J. Chapelle and K. Meguernes (1990), "Destruction et valorisation complète de l'hydrogène sulfuré par des procédés plasma-chimiques," *Colloque de physique C5*, **51**(18 suppl.), 65-71.
- Czernichowski A. (1987), "The Rotational Temperature Evaluation from Partially Resolved 516.5 nm C₂ Band," *Proceedings of the ISPC-8*, Tokyo, 437-448.
- de Nevers N. (1995), *Air Pollution Control Engineering*, McGraw Hill, USA.
- Diemer R.B., G.D. Silcox, J.S. Lighty and D.W. Pershing (1997), "Incineration," *The Wiley Encyclopedia of Energy and the Environment*, vol. 2, eds. A. Bisio and S. Boots, John Wiley & Sons, USA.
- Dlugogorski B.Z. (1989), *The Treatment of Vacuum Distilled Residue from the Canmet Process in Argon/Hydrogen Plasmas*, M. Eng. Thesis, McGill University, Canada.
- Douglas J.M. (1988), *Conceptual Design of Chemical Processes*, McGraw Hill, USA.

- Eddy T.L., B.D. Raivo, P.T. Eddy, N.R. Soelberg and B.C. Benefiel (1996), "Plasma Arc Melters for Conversion of Waste to Value-Added Products," *Proceedings of the 17th Biennial Waste Processing Conference*, ASME, 375-392.
- Eduljee G.H. (1995), "Organic Micropollutant Emission from Waste Incineration," *Issues in Environmental Science and Technology - (2) Waste Incineration and the Environment*, eds. R.E. Hester and R.M. Harrison, Royal Society of Chemistry, UK.
- Electricité de France (1991), *Les plasmas dans l'industrie*.
- Environmental Protection Service (1985), "Le Programme National d'Essais et d'Evaluation des Incinérateurs: Sommaire des Essais à l'Incinérateur à Combustion en Deux Etapes de Parkdale, Ile-du-Prince-Edouard," *Rapport SPE 3/UP/1*, Environment Canada.
- Eschenbach R.C., R.E. Haun and T.F. Yeast (1994), "A Portable Vitrification System for Waste Treatment," AICHE 1994 Summer Meeting, Retech Inc.
- Farmer, T. (1999), "Thermal Plasma Waste Treatment," *ISPC-14*, Prague.
- Filion J. (1995), "A Study of the Interpretation and Sensitivity of Lateral Emission Profiles Measured from an Inductively Coupled Plasma," Project report for course no. 302-541B, McGill University, Canada.
- Filius K.D. and C.G. Whitworth (1996), "Emissions Characterization and Off-Gas System Development for Processing Simulated Mixed Waste in a Plasma Centrifugal Furnace," *Hazardous Waste and Hazardous Materials*, **13** (1), 143-152.
- Gaydon A.G. (1968), "Chapter 1: Theory of Atomic and Molecular Spectra," *Dissociation Energies*, 3rd ed., Chapman and Hall, London.
- Gaydon A.G. and H.G. Wolfhard (1950), "Spectroscopic Studies of Low-Pressure Flames - III. Effective Rotational Temperatures and Excitation Mechanism for C₂ Bands," *Proceedings of the Royal Society (A)*, **201**, 561-569.
- Georgiev I., Z. Bulgaranova and K. Kumanova (1995), "Plasma Chemical Process for Treatment of Hazardous Wastes," *International Journal of Materials and Product Technology*, **10** (3), 522-529.
- Gifford G.G. (1991), "Applications of Optical Emission Spectroscopy in Plasma Manufacturing Systems," *SPIE Proceedings Series - Advanced Techniques for Integrated Circuit Processing*, **1392**, 454-465.
- Glassman I. (1996), *Combustion*, 3rd ed. Academic Press, USA.

- Government of Canada, Minister of Supply & Services (1990), *Canada's Green Plan for a Healthy Environment*.
- Goyette A.N., J.E. Lawler, L.W. Anderson, D.M. Gruen, T.G. McCauley, D. Zhou, A.R. Krauss (1998), "C₂ Swan Band Emission Intensity as a Function of C₂ Density," *Plasma Sources Science and Technology*, **7**, 149-153.
- Greenfield S., H. McD. McGeachin and P.B. Smith (1976), *ICP Information Newsletter*, **2** (6), 167-173.
- Guillet C. and I. Causse (1994), "Destruction de déchets spéciaux par torche à plasma: le procédé INDICIS," International Symposium on the Stabilization and Valorisation of Ultimate Waste - Plasma and Other Processes, September 12-14, Soretel Inc.
- Gupta A.K. (1996), "Thermal Destruction of Solid Wastes," *Journal of Energy Resources Technology*, **118**, 187-192.
- Han Q.Y., Q.D. Zhuang, J.V.R. Heberlein and W. Tormanen (1995), "Chapter 11: Thermal Plasma Destruction of Hazardous Waste with Simultaneous Production of Valuable Coproducts," *Emerging Technologies in Waste Management V*, eds. D. William Tedder and Frederick G. Pohland, ASC Symposium Series 607, American Chemical Society, Washington DC.
- Harrad S.J. (1996), "Chapter 16: The Environmental Behaviour of Toxic Organic Chemicals," *Pollution: Causes, Effects and Control*, 3rd ed., ed. R.M. Harrison, Royal Society of Chemistry, UK.
- Harrison R.M. (1996), "Chapter 8: Chemistry of the Troposphere," *Pollution: Causes, Effects and Control*, 3rd ed., ed. R.M. Harrison, Royal Society of Chemistry, UK.
- Heberlein J.V.R. (1993), "Thermal Plasmas for the Destruction of Hazardous Wastes," *Industrial Applications of Plasma Physics*, eds. G. Bonizzoni, W. Hooke and E. Sindoni, SIF, Bologna.
- Herzberg G. (1950), *Spectra of Diatomic Molecules*, van Nostrand, New Jersey.
- Hill R.D. and R.A. Olexsey (1989), "Overview of the Superfund Innovative Technology Evaluation (SITE) Program," *JAPCA*, **39** (1), 16-21.
- Himmelblau D.M. (1990), *Process Analysis by Statistical Methods*, Alphagraphics, Austin TX.
- Holman J.P. and W.J. Gajda Jr. (1989), *Experimental Methods for Engineers*, 5th ed., McGraw Hill, USA.

- Huhn W.A., H.R. Zwi, A. Lynn, R. Dickman, A. Wong, C. Behr-Andres and E. Hemmick (1997), "Radio Frequency Plasma Treatment of Organic Hazardous Waste," *Practice Periodical of Hazardous, Toxic, and Radioactive Waste Management*, **1** (3), 107-112.
- Hutchinson I.H. (1987), *Principles of Plasma Diagnostics*, Cambridge University Press, USA.
- Inaba T., Y. Watanabe, M. Nagano, T. Ishida and M. Endo (1998), "Ar Torch Plasma Characteristics and Its Applications to Waste Treatment," *Thin Solid Films*, **316**, 111-116.
- Ingle J.D. Jr. and S.R. Crouch (1988), *Spectrochemical Analysis*, Prentice Hall, New Jersey.
- Institut National de la Propriété Industrielle (1994), demande de brevet no. 2695985 (FR).
- Itatani R. (1993), "Studies on Toxic Waste Destruction with Plasmas in Japan," *ISPP-13 'Piero Caldirola' Industrial Applications of Plasma Physics*, eds. G. Bonizzoni, W. Hooke, E. Sindoni, SIF, Bologna.
- Jackson T. (1996), *Material Concerns: Pollution, Profit and Quality of Life*, Stockholm Environment Institute, Routledge GB.
- Joseph M.F., T.G. Barton, and S.C. Vorndran (1986), "Incineration of PCBs by Plasma Arc," *Proceedings of the 33rd Ontario Industrial Waste Conference*, June 15-18.
- Kiely G. (1997), *Environmental Engineering*, McGraw Hill, USA.
- King R.B. (1948), "Relative Transition Probabilities of the Swan Bands of Carbon," *Astrophysical Journal*, **108**, 429-433.
- Kini K.S. and M.I. Savadatti (1977), "Investigation of the C_2 ($A^3\Pi_g-X^3\Pi_u$) Band System Excited in a Discharge through Carbon Monoxide," *Journal of Physics - B: Atomic and Molecular Physics*, **10** (6), 1139-1149.
- Koplow D.A. (1997), *By Fire and Ice: Dismantling Chemical Weapons While Preserving the Environment*, Gordon and Breach, Amsterdam.
- Koulidiati J., A. Czernichowski, J.J. Beulens et D.C. Schram (1990), "Evaluation des températures de rotation et de vibration à partir du spectre d'émission $A^2\Lambda-X^2\Pi$ de la molécule CH," *Colloque de physique C5*, **51**(18 suppl.), 297-303.
- Kovács I. (1966), "Formulae for Rotational Intensity Distribution of Triplet Transitions in Diatomic Molecules," *Astrophysical Journal*, **145**, 634-647.

- Kovács I. (1969), *Rotational Structure in the Spectra of Diatomic Molecules*, American Elsevier, New York.
- Lambert D. and T.F. McGowan (1996), "NO_x Control Techniques for the CPI," *Chemical Engineering*, June, 98-101.
- Lee C.C. and G.L. Huffman (1989) "Incineration of Solid Waste," *Environmental Progress*, **8** (3), 143-151.
- Lee T.H., G.E. Adams and W.M. Gaines (1968), *Computer Process Control: Modeling and Optimization*, John Wiley & Sons, New York.
- Maclean Hunter Publishing Ltd. (1998), "New Study Shows Swan Hills Continues to Leak," information downloaded on March 25, 1999 from <http://www.plant.ca/Content/1998/980907/pla090798.html>.
- Madu C.N. (1996), "Chapter 8: Quantitative Tools for Environmental-Quality Management," *Managing Green Technologies for Global Competitiveness*, Quorum Books, London.
- Malchow D.S. (1992), "Industrial Process Control with Array Spectroscopy," SPIE Conference on Instrumentation used in Spectroscopy, Process Control, and Color Measurement, March 24.
- Manahan S.E. (1999), *Industrial Ecology: Environmental Chemistry and Hazardous Waste*, Lewis - CRC Press, Boca Raton FL.
- Marwick R. (1995), "Automated Simplex Optimization of an Inductively-Coupled Plasma Atomic Emission Spectrometer for Use in a Complete Autonomous Instrument Package," Project thesis for course no. 180-480/490D, McGill University, Canada.
- McAllister T. (1995), "Thermochemistry and Kinetics of Plasma Waste Destruction," *Proceedings of the ISPC-12*, Minneapolis.
- Mermet J.M. (1987), "Chapter 10: Spectroscopic Diagnostics - Basic Concepts," *Inductively Coupled Plasma Emission Spectroscopy - Part II. Applications and Fundamentals*, ed. P.W.J.M. Boumans, John Wiley & Sons, New York.
- Mostaghimi J., P. Proulx and M.I. Boulos (1985), "Computer modelling of the emission patterns for a spectrochemical ICP," *Spectrochimica Acta*, **40B**, 153-166.
- Munz R.J. (1999), Personal communication.
- Munz R.J. (1974), *The Decomposition of Molybdenum Disulphide in an Induction Plasma Tailflame*, Ph.D. Thesis, McGill University, Canada.

- Mustoe T. (1999), Personal communication (Callidus Technologies Inc.).
- Nazarian A. (1997), "On-Line, Input-Stream Process Control Sensor for High Temperature Process, *ICHEME Symposium Series*, **143**, 149-155.
- Nelder J.A. and R. Mead (1965), "A Simplex Method for Function Minimization," *The Computer Journal*, **7**, 308-313.
- Nelson M.R. (1999), Personal communication (Air Quality Analytical Inc.).
- Niessen W.R. (1995), *Combustion and Incineration Processes: Applications in Environmental Engineering*, 2nd ed., Marcel Dekker, New York.
- Omenetto N. et al. (1980), "Relative Spatial Profiles of Barium Ion and Atom in the Argon Inductively Coupled Plasma as Obtained by Laser Excited Fluorescence," *Spectrochimica Acta*, **35**, 507-517.
- Or D.T., N.S. Subramanian, J.V.R. Heberlein and E. Pfender (1997), "Modeling of High-Pressure, High-Frequency (RF) Oxygen Plasmas," *IEEE Transactions on Plasma Science*, **25** (5), 1034-1041.
- Park C.S., K.C. Porteous, K.F. Sadler and M.J. Zuo (1995), *Contemporary Engineering Economics: A Canadian Perspective*, Addison-Wesley, Canada.
- Pasek R.J., D.P.Y. Chang and A.D. Jones (1996), "Investigation of Thermal Decomposition of Chlorinated Polymers, *Hazardous Waste and Hazardous Materials*, **13** (1), 23-38.
- Pearce D.W. and I. Brisson (1995), "The Economics of Waste Management," *Issues in Environmental Science and Technology - (3) Waste Treatment and Disposal*, eds. R.E. Hester and R.M. Harrison, Royal Society of Chemistry, UK.
- Pearse R.W.B. and A.G. Gaydon (1965), *The Identification of Molecular Spectra*, 3rd ed., Chapman and Hall, London.
- Pellerin S., K. Musiol, O. Motret, B. Pokrzywka and J. Chapelle (1996), "Application of the (0,0) Swan Band Spectrum for Temperature Measurements," *Journal of Physics D: Applied Physics*, **29**, 2850-2865.
- Pfender E. (1999), "Thermal Plasma Technology: Where Do We Stand and Where Are We Going?," *Plasma Chemistry and Plasma Processing*, **19** (1), 1-31.
- Phillips J.G. (1948), "An Extension of the Swan System of the C₂ Molecule," *Astrophysical Journal*, **108**, 434-452.

Phillips J.G. and S.P. Davis (1968), *Berkeley Analyses of Molecular Spectra: The Swan System of the C₂ Molecule / The Spectrum of the HgH Molecule*," University of California Press, Berkeley and Los Angeles.

Phoenix Solutions Co. (1998), Technical literature.

Prasad C.V.V. and P.F. Bernath (1994), "Fourier Transform Spectroscopy of the Swan System of the Jet-Cooled C₂ Molecule," *Astrophysical Journal*, **426**, 812-821.

Proulx P. (1995). Lecture given as part of course no. 302-541B, McGill University, Canada.

Rae G.W. (1995), "Recovering Energy from Waste: Emissions and Their Control," *Issues in Environmental Science and Technology - (2) Waste Incineration and the Environment*, eds. R.E. Hester and R.M. Harrison, Royal Society of Chemistry, UK.

Ramasamy V., T.-Z. Li, K. Saito, C.J. Cremers, and V. Majidi (1996), "Combustion By-Products Destruction by Arc Plasma," *Hazardous Waste and Hazardous Materials*, **13** (1), 131-141.

Reeve S.W. and W.A. Weimer (1995), "Plasma Diagnostics of a Direct-Current Arcjet Diamond Reactor - II. Optical Emission Spectroscopy," *Journal of Vacuum Science and Technology (A)*, **13**(2), 359-367.

Rosen B., ed. (1970), *Spectroscopic Data Relative to Diatomic Molecules Series: International Tables of Selected Constants*, Pergamon Press, Oxford.

Sacchi G.F., C. Procaccini, J.P. Longwell and A.F Sarofim (1996), "Experimental and Numerical Studies of PIC Formation During Chlorocarbon Combustion: Development of a Failure Mode Diagnostic System for Hazardous Waste Incinerators," *Hazardous Waste and Hazardous Materials*, **13** (1), 39-49.

Savitzky A. and M.J.E. Golay (1964), "Smoothing and Differentiation of Data by Simplified Least Squares Procedures," *Analytical Chemistry*, **36** (8), 1627-1639.

Schlienger M.P. (1993), "Plasma Arc Processing of Solid and Liquid Wastes," *NATO ASI Series, G34* (Part A), eds. B.M. Penetrante and S.E. Schultheis, Springer-Verlag, Berlin Heidelberg.

Seborg D.E., T.F. Edgar and D.A. Mellichamp (1989), *Process Dynamics and Control*, John Wiley & Sons, New York.

- Simek M., G. Dilecce, and S. De Benedictis (1995), "On the Use of the Numerical Simulation of the First Positive System of N₂: I. Emission and LIF Analysis," *Plasma Chemistry and Plasma Processing*, **15** (3), 427-449.
- Simek M. and S. De Benedictis (1995), "On the Use of the Numerical Simulation of the First Positive System of N₂: II. Fast T_{rot} Estimation from the Partially Resolved (3,0) Band," *Plasma Chemistry and Plasma Processing*, **15** (3), 451-463.
- Singh J.P. , F.-Y. Yueh, H. Zhang and R.L. Cook (1997), "Study of Laser-Induced Breakdown Spectroscopy as a Process Monitor and Control Tool for Hazardous Waste Remediation," *Process Control and Quality*, **10**, 247-258.
- Snyder H.R. and C.B. Fleddermann (1997), "Decomposition of Dichloroethane in a Plasma Arcjet Reactor: Experiment and Modelling," *IEEE Transactions on Plasma Science*, **25** (5), 1017-1022.
- Soucy G. (1999), Personal communication.
- Soucy G., L. Fortin and M.I. Boulos (1996), "Toxic Waste Destruction by Thermal Plasma Technology," 18th Canadian Waste Management Conference, Oct. 21-24, Winnipeg, Canada.
- Soucy G., J.W. Jurewicz and M.I. Boulos (1994), "Mixing Study of the Induction Plasma Reactor: Part I. Axial Injection Mode," *Plasma Processing and Plasma Chemistry*, **14** (1), 43-58.
- Soucy G., J.W. Jurewicz and M.I. Boulos (1994), "Mixing Study of the Induction Plasma Reactor: Part II. Radial Injection Mode," *Plasma Processing and Plasma Chemistry*, **14** (1), 59-71.
- SRL Plasma Ltd. (1995), *PLASCON Technology Fact Sheets*, Croydon, North Victoria, Australia.
- Stratton B.C., R. Knight, D.R. Mikkelsen, A. Blutke and J. Vavruska (1999), "Synthesis of Ozone at Atmospheric Pressure by a Quenched Induction-Coupled Plasma Torch," *Plasma Chemistry and Plasma Processing*, **19** (2), 191-216.
- Teply J., M. Dressler, J. Janca and C. Tesar (1995), "Destruction of Organic Compounds in a High Frequency Discharge Plasma at Reduced Pressure," *Plasma Chemistry and Plasma Processing*, **15** (3), 465-479.
- Theodore L. and J. Reynolds (1987), *Introduction to Hazardous Waste Incineration*, John Wiley & Sons, New York.

- Thörnblom J. and K.J. Roihjert (1992), "Utilizing Plasma Technology for Chemical Reactions in Controlled Atmosphere," *Pure and Applied Chemistry*, **64** (5), 671-676.
- Thorne A.P. (1974), *Spectrophysics*, Chapman and Hall, London.
- Turton R. et al. (1998), *Analysis, Synthesis and Design of Chemical Processes*, Prentice Hall, USA.
- Tyte D.C., S.H. Innanen and R.W. Nicholls (1967), *Identification Atlas of Molecular Spectra - 5. The $C_2 A^3\Pi_g - X^3\Pi_u$ Swan System*, York University Centre for Research in Experimental Space Science and Department of Physics, Toronto, Canada.
- UIE - International Union for Electroheat (1988), "Chapter 8: Plasma Destruction of Wastes," *Arc Plasma Processes*, UIE, France.
- Valy Y. and C. Guillet (1995), "Plasma Torches for Waste Destruction," *Proceedings of the ISPC-12 Workshop on Industrial Applications of Plasma Chemistry - Volume B: Thermal Plasma Applications*, Minneapolis.
- Vatavuk W.M. and R.B. Neveril (1984), "Section IV: Costs of Equipment - Data and Estimating Methods," *Modern Cost Engineering: Methods and Data*, vol. II, ed. J. Matley, McGraw Hill, New York.
- Veerimst F. (1998), "La traque aux dioxines," *Décision Environnement*, **67**, 59-65.
- Walters F.H., L.R. Parker, S.L. Morgan, and S.N. Deming (1991), *Sequential Simplex Optimization: A Technique of Improving Quality and Productivity in Research, Development, and Manufacturing*, CRC Press, Boca Raton FL.
- Williams P.T. (1995), "Pollutants from Incineration: an Overview," *Issues in Environmental Science and Technology - (2) Waste Incineration and the Environment*, eds. R.E. Hester and R.M. Harrison, Royal Society of Chemistry, UK.
- Zhao G.Y., J. Mostaghimi and M.I. Boulos (1990), "The Induction Plasma Chemical Reactor: Part I. Equilibrium Model," *Plasma Chemistry and Plasma Processing*, **10** (1), 133-150.
- Zhao G.Y., J. Mostaghimi and M.I. Boulos (1990), "The Induction Plasma Chemical Reactor: Part II. Kinetic Model," *Plasma Chemistry and Plasma Processing*, **10** (1), 151-166.

9. APPENDICES

- Appendix I Molecular Band Emission Intensity Equations
- Appendix II The Swan Band Spectrum of the C_2 $d^3\Pi_g \rightarrow a^3\Pi_g$ Transition
- Appendix III Band Spectrum Simulation Equations for the $d^3\Pi_g \rightarrow a^3\Pi_g$ $\nu(0,0)$ Transition of C_2
- Appendix IV Rigorous Simulation of the P-branch $\nu(0,0)$ Swan Band
- Appendix V Complete Simulation of the $\nu(0,0)$ Swan Band
- Appendix VI Temperature Estimation Using the Boltzmann Plot Method
- Appendix VII Temperature Estimation Using Integrated Band Intensities
- Appendix VIII Steepest Ascent Optimization Strategies and Equations
- Appendix IX Simplex Optimization Principles and Rules
- Appendix X Energy and Mass Balances for Soil Treatment Afterburners
- Appendix XI Energy and Mass Balances for Combustion Reactions and for Primary Incineration
- Appendix XII Fuel Value Estimation for a PCB Dielectric Fluid
- Appendix XIII Capital and Operating Cost Summaries
- Appendix XIV Incremental Cash Flow Model
- Appendix XV Hifi23 Torch Simulation Contour Maps

Appendix I Molecular Band Emission Intensity Equations

The total energy of an electron is the sum of its electronic, vibrational and rotational energies:

$$E = E_e + E_v + E_r \quad (\text{equation I-1})$$

It is common practice to express energy levels in terms of wavenumber, with units of reciprocal length. $G(v)$ and $F(J)$ are standard notation for vibrational and rotational energies, respectively.

$$\nu = \nu_e + \nu_v + \nu_r = \nu_0 + \nu_r \quad (\text{equation I-2})$$

$$\text{or } \nu = \nu_e + G(v) + F(J) \quad (\text{equation I-3})$$

The quantity ν_0 (called *band origin* or zero line) is constant for a specific vibrational transition. The radiation wavenumber associated with a rotational line of the transition is:

$$\nu = \nu_0 + F'(J') - F''(J'') \quad (\text{equation I-4})$$

Assuming a Boltzmann equilibrium among upper state rotational levels, the emission intensity of a rotational line is given, in general form, by the following equation (Bousrih *et al.* 1995, Pellerin *et al.* 1996):

$$I_{\nu'\nu''J'J''} = C \frac{N(T)}{Q(T)} \nu^4 S_{\nu'\nu''} \frac{s_{J'J''}}{g'(2J'+1)} \exp\left(-\frac{hc}{kT} [\nu_e' + G(\nu') + F(J')]\right) \quad (\text{equation I-5})$$

where C = a constant

N(T) = total population number density

Q(T) = internal partition function

$S_{\nu'\nu''}$ = band strength

$s_{J'J''}$ = Hönl-London factor

g' = upper level electronic degeneracy

ν_e' = electronic energy of the upper level

G(ν') = vibrational energy of the upper level

F(J') = rotational energy of the upper level

The emission band strength is the sum of line strengths starting from a given J' in ν' (upper level) and ending on various J'' in ν'' (lower levels). Conversely, absorption line strengths refer to a single lower level and multiple upper levels. Individual line strengths are related to the band strength by the Hönl-London factor, a parameter that can be reliably calculated for most transitions (Thorne 1974). By convention, the Hönl-London factor is normalized against $g'(2J'+1)$, the statistical weight of the upper level multiplied by the degeneracy, so that its sum over all branches equals unity.

$$S_{\nu'\nu''J'J''} = \frac{s_{J'J''}}{g'(2J'+1)} S_{\nu'\nu''} \quad (\text{equation I-6})$$

$$\sum_{\text{sub-levels}} \sum_{J''} \frac{s_{J'J''}}{g'(2J'+1)} = 1 \quad (\text{equation I-7})$$

Numerical values for the line strength can be calculated from formulae tabulated by Kovács, Herzberg and Budó and described in Appendix III.

When considering the rotational lines of a single band, the total population density, partition function, electronic energy and vibrational energy can be included in the constant, and equation I-5 simplifies to:

$$I_{v'v''J'J''} = A \nu^4 S_{v'v''J'J''} \exp\left(-\frac{hc}{kT} F(J')\right) \quad (\text{equation I-8})$$

$$\text{where } A = C \frac{N(T)}{Q(T)} \exp\left(-\frac{hc}{kT} [v_e' + G(v')]\right)$$

Appendix II The Swan Band Spectrum of the $d^3\Pi_g \rightarrow a^3\Pi_u$ Transition of C_2

Note: A brief explanation of Hund's cases and Λ -type doubling is provided at the end of this appendix.

The Swan bands are of the $^3\Pi \rightarrow ^3\Pi$ type. The upper ($d^3\Pi_g$) and lower ($a^3\Pi_u$) levels are respectively located at 2.48 eV and 0.09 eV above the ground level of the $\Lambda = 1$ electronic state. A typical energy level diagram for this type of vibrational-rotational transition is presented in Figure II-A.

A $^3\Pi \rightarrow ^3\Pi$ transition has three sub-bands, each of which shows a strong P branch, a strong R branch, and a very weak Q branch whose intensity falls rapidly with increasing J because $\Delta\Lambda = 0$. Each level splits into two components due to Λ -type doubling. Because of the zero nuclear spin of the carbon atom, the C_2 molecule misses alternate lines so this doubling is not apparent (Phillips and Davis 1968). The existence of six strong branches is predicted whether the two states involved belong to Hund's cases (a) or (b) or to a transitional intermediate case going from (a) to (b). In case (b), the three P sub-branches and the three R sub-branches lie close together and appear as triplets in the spectrum. The band thus presents a single head. In case (a), splitting is larger and each sub-band produces a separate head (Herzberg 1950).

The electronic states involved in the Swan bands belong to the intermediate case, approaching case (b) as the rotational quantum number increases. Indeed, triplet splitting decreases rapidly with increasing J-values (Phillips and Davis 1968); for the P branch, the transition to case (b) occurs around $J = 4$ (Prasad and Bernath 1994). The Swan system lies in the wavelength range 340-780 nm and comprises over 45 bands, of which those of the sequences $\Delta v = -1, 0, 1$ are most commonly observed (Tyte *et al.* 1967). The system is dominated by four single-headed bands degraded to violet (i.e., with the band head located on the

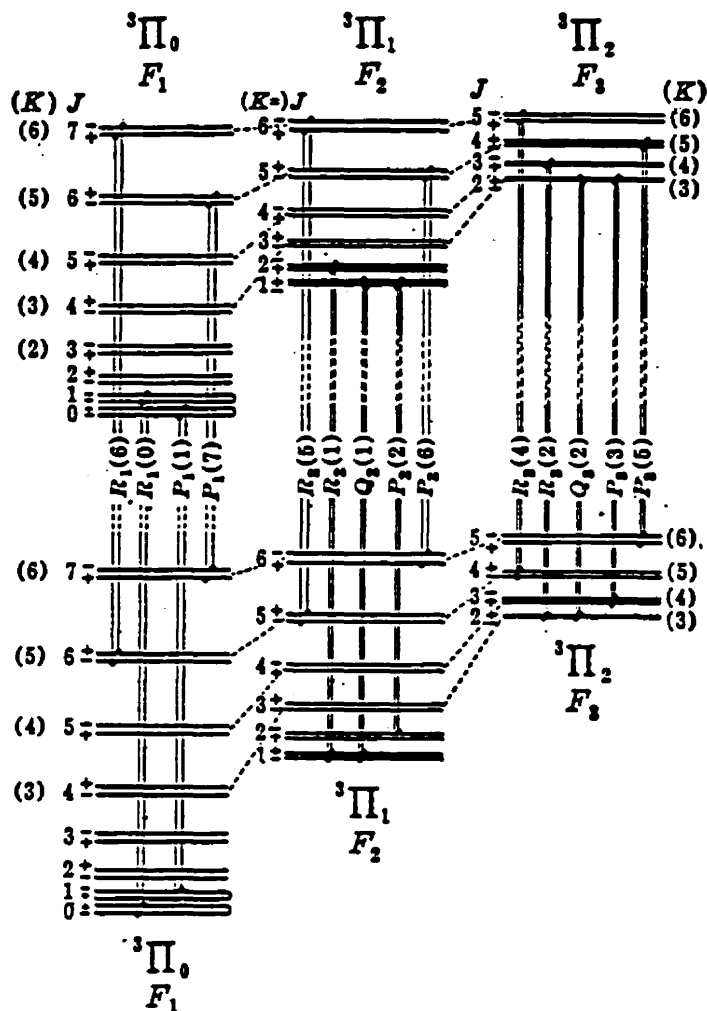


FIG. 128. Energy Level Diagram for a ${}^3\Pi-{}^3\Pi$ Transition. For the upper as well as the lower state a very rapid transition from case (a) to case (b) is assumed. The A-type doubling is greatly exaggerated. The first line of every branch, as well as one line with a larger J value, is shown except for the Q branches, which are not observed for higher J values. It is seen how for larger J the triplet R and triplet P branches arise. The K values are not given for the lowest levels, since they are not defined in case (a). Of course, formally it is possible to continue the K values from the higher levels to the lower, but the K values thus obtained do not always correspond to the true K values that one would obtain if a transition to case (b) were actually carried out. For example, strictly speaking, the three lowest levels of ${}^3\Pi_0$ belong to $K = 1$.

Figure II-A: Energy Level Diagram for a ${}^3\Pi \rightarrow {}^3\Pi$ Transition
(Herzberg 1950)

upper-wavelength side). These are the $\nu(0,2)$ band at 592.3 - 619.1 nm, the $\nu(0,1)$ band at 547.0 - 563.6 nm, the $\nu(0,0)$ band at 509.8 - 516.5 nm, and the $\nu(1,0)$ band at 467.8 - 473.7 nm (Greenfield *et al.* 1976, Pearse and Gaydon 1965). Other bands, less commonly observed, are listed in Table II-1. Figure II-B shows a low-resolution scan of the $\nu(1,0)$ and $\nu(0,0)$ bands within the visible spectrum, in an argon-oxygen plasma subject to air entrainment. The "green band" is widely used for diagnostic purposes in plasma systems.

Hund's cases (Gaydon 1968)

Several modes of coupling between the different angular momenta are possible, giving rise to variations in rotational electronic structure. A description of five limiting cases, first developed by Hund, was reported and used by Herzberg and many others to aid in the mathematical formulation of rotational structures. Hund's cases are not fully discussed here. Only the two most important ones, relevant to the present work, are described: case (a), where interaction of the nuclear rotation with electronic motion is weak but spin coupling is large, and case (b), characterized by weak interaction of the nuclear rotation with electronic motion and a weak spin component along the internuclear axis. Actual states can belong to an intermediate case or a transition case which switches from one model to the other with increasing J-value. In physical terms, coupling of the angular momentum to the internuclear axis weakens with increasing rotation. Deviations from these ideal cases may arise from interactions that are neglected in the models. These interactions become significant at high rotational speed. For instance, when $\Lambda \neq 0$, interaction with nuclear rotation - neglected in both cases (a) and (b) - causes a fine splitting of the double degeneracy into two components of slightly different energy for each J-value. This phenomenon is called *Λ -type doubling*.

Quantum mechanics principles state that electronic transitions from one level to another are subject to restrictions as to which combinations of upper and lower

C₂

Appearance. Degraded to violet. Single-headed. Sequences well marked.

Transition. A ³Π_g → X ³Π_g.

References. R. C. Johnson, *Phil. Trans. Roy. Soc. A.*, 226, 157 (1927).

W. Jevons, *Report on Band Spectra of Diatomic Molecules*, The Physical Society, 1932.

λ	I	v', v''	λ	I	v', v''
6677.3	1	2, 5	5501.9	4	3, 4
6599.2	1	3, 6	5470.3	2	4, 5
6533.7	2	4, 7	5165.2	10	0, 0
6480.5	2	5, 8	5129.3	6	1, 1
6442.3	2	6, 9	5097.7	1	2, 2
6191.2	3	0, 2	4737.1	9	1, 0
6122.1	4	1, 3	4715.2	8	2, 1
6059.7	3	2, 4	4697.6	7	3, 2
6004.9	3	3, 5	4684.8	4	4, 3
5958.7	2	4, 6	4678.6	2	5, 4
5923.4	1	5, 7	4668.7	1	6, 5
5635.5	8	0, 1	4382.5	2	2, 0
5585.5	8	1, 2	4371.4	4	3, 1
5540.7	6	2, 3	4365.2	5	4, 2

J. G. Phillips (*Astrophys. J.*, 108, 434 (1948)) has observed some "tail bands." The following heads are degraded to the red, λλ4996.7 (13, 12), 4911.0 (12, 11), 4836.1 (11, 10), 4770.1 (10, 9), and there are headless bands with origins at λλ4734 (9, 8) and 4395 (8, 6).

Table II-1: Band Heads of the C₂ Swan System
(Pearse and Gaydon 1965)

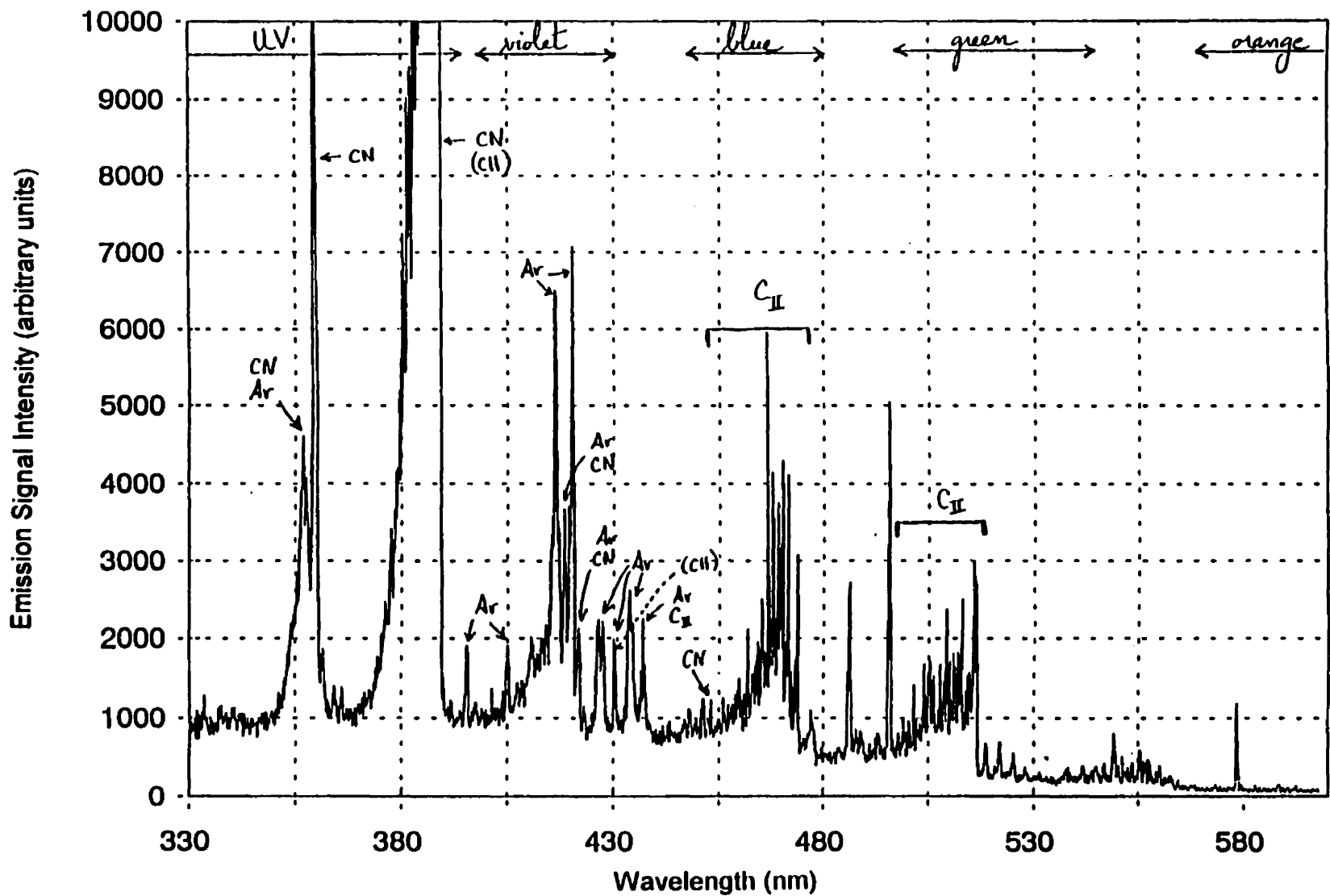


Figure II-B: Optical Emission Spectrum of an Inductively Coupled Plasma
(1.5 kW analytical ICP, 0.3 ml/s propane in argon)

levels are likely. This translates into selection rules that designate *allowed* and *forbidden* transitions. The following selection rules apply generally:

- $\Delta J \equiv J' - J'' = 0, \pm 1$ (except for $J = 0 \rightarrow J = 0$);
- positive terms combine with negative terms, and vice-versa;
- (anti-)symmetric terms combine with (anti-)symmetric ones;
- even electronic states combine only with odd ones.

Other selection rules hold when both levels belong to Hund's cases (a) or (b). Yet other rules apply when both levels belong strictly to case (a) or case (b). The reader is referred to a reference source such as Herzberg for details about these rules and their meaning in terms of spectral features.

Appendix III Band Spectrum Simulation Equations

for the $d^3\Pi_g \rightarrow a^3\Pi_u$ $\nu(0,0)$ Transition of C_2

(Budó 1937, Herzberg 1950, Kovács 1966, Kovács 1969, Phillips 1948, Phillips and Davis 1968, Rosen 1970)

From equation I-8 in Appendix I, three quantities must be calculated to simulation a band spectrum: the upper level rotational energies, the line wavenumbers, and the line strengths. Calculation methods for each of these quantities, of varying complexity as reported by different authors, are outlined below.

A) Rotational energy levels

Herzberg

This simple form of the rotational energy level equation is based on the non-rigid vibrating rotator model of a diatomic molecule. It gives the combined rotational energies of the triplet components.

$$F(J) = B_v J(J+1) + (A - B_v)\Lambda^2 - D_v J^2(J+1)^2 + \dots$$

The second term is constant for a given vibrational level of a given electronic state. It can be neglected if ν_0 in equation I-4 of Appendix I is chosen so that $F(J)$ is measured relative to the $J = 0$ level (which is usually the case). The first term derives from the rigid rotator model of a diatomic molecule. The third term corrects for a slight increase in internuclear distance due to the centrifugal force in a non-rigid molecule. It is a small correction ($D_v \ll B_v$, always) and is often neglected for simplicity. The values of the rotational constants for the $\nu(0,0)$ Swan band are $B_v = 1.7455 \text{ cm}^{-1}$ and $D_v = 6.853e^{-6} \text{ cm}^{-1}$.

Phillips

A more advanced treatment of electronic structures following the vibrating rotator model leads to equations for the rotational energies of individual triplet components. The centrifugal effect correction term is included, and different molecular constants apply for levels with even and odd J-values to account for Λ -type doubling. These expressions, originating from the works of Kovács and Phillips, were used by Pellerin *et al.* (1996) to produce accurate simulations of the $\nu(0,0)$ Swan band spectrum.

$$F_1(J) \approx B_v \left(J(J+1) - [Y_1 + 4J(J+1)]^{1/2} - \frac{2Y_2 - 2J(J+1)}{3Y_1 + 4J(J+1)} \right) - D_v \left(J - \frac{1}{2} \right)^4 \quad (J \geq 0)$$

$$F_2(J) \approx B_v \left(J(J+1) + \frac{4Y_2 - 2J(J+1)}{3Y_1 + 4J(J+1)} \right) - D_v \left(J + \frac{1}{2} \right)^4 \quad (J \geq 1)$$

$$F_3(J) \approx B_v \left(J(J+1) + [Y_1 + 4J(J+1)]^{1/2} - \frac{2Y_2 - 2J(J+1)}{3Y_1 + 4J(J+1)} \right) - D_v \left(J + \frac{3}{2} \right)^4 \quad (J \geq 2)$$

$$Y_1 = \Lambda^2 Y(Y-4) + \frac{4}{3}$$

$$Y_2 = \Lambda^2 Y(Y-1) - \frac{4}{9}$$

Table III-A: Molecular Constants for the $\nu(0,0)$ Swan Band

state	constant	even J	odd J
$d^3\Pi_g$	B_v (cm^{-1})	1.74557	1.74544
	D_v (cm^{-1})	$6.85e^{-6}$	$6.856e^{-6}$
	Y	-9.399854	-9.399854
$a^3\Pi_u$	B_v (cm^{-1})	1.6237	1.62370
	D_v (cm^{-1})	$6.40e^{-6}$	$6.40e^{-6}$
	Y	-10.70294	-10.62889

B) Wavenumbers

Herzberg

The following expressions for individual line wavenumbers result from Herzberg's formulation of rotational energy levels. The band origin, ν_0 , is listed at 19389.44 cm^{-1} ($\lambda = 515.745 \text{ nm}$).

$$\nu = \nu_0 + F'(J') - F''(J'')$$

$$\nu = \nu_0 + [B_v' J'(J'+1) - D_v' J'^2 (J'+1)^2 + \dots] - [B_v'' J''(J''+1) - D_v'' J''^2 (J''+1)^2 + \dots]$$

$$P(J'') = \nu_0 + F'(J') - F''(J'') = \nu_0 + F'(J''-1) - F''(J'')$$

$$Q(J'') = \nu_0 + F'(J') - F''(J'') = \nu_0 + F'(J'') - F''(J'')$$

$$R(J'') = \nu_0 + F'(J') - F''(J'') = \nu_0 + F'(J''+1) - F''(J'')$$

Substituting,

$$P(J'') = \nu_0 - (B_v' + B_v'')J'' + (B_v' - B_v'')J''^2$$

$$Q(J'') = \nu_0 + (B_v' - B_v'')J'' + (B_v' - B_v'')J''^2$$

$$R(J'') = \nu_0 + 2B_v' + (3B_v' - B_v'')J'' + (B_v' - B_v'')J''^2$$

Phillips

These wavenumber equations for each triplet component of the P, Q and R branches following from Phillips' rotational energy equations. The branch name replaces the line wavenumber for clarity. The band origin, σ_0 , is calculated to be $\approx 19380.5210 \text{ cm}^{-1}$ ($\lambda \approx 515.982 \text{ nm}$) from the transition's electronic state (both vibrational levels are at ground).

$$P_i(J'') = \sigma_0 + F_i'(J''-1) - F_i''(J'')$$

$$Q_i(J'') = \sigma_0 + F_i'(J'') - F_i''(J'') \quad (i = 1, 2, 3)$$

$$R_i(J'') = \sigma_0 + F_i'(J''+1) - F_i''(J'')$$

C) Line strengths

Herzberg

Herzberg's simplified *Hönl-London formulae* for $\Delta\Lambda = 0$ give the combined line strengths of triplet components as a single value. They provide a simple yet adequate representation of the spectrum for applications where resolution of the triplet components is unnecessary or impractical. For emission, $J = J'$; for absorption, $J = J''$.

$$S_J^P = \frac{(J+1+\Lambda)(J+1-\Lambda)}{(J+1)}$$

$$S_J^Q = \frac{(2J+1)\Lambda^2}{J(J+1)}$$

$$S_J^R = \frac{(J+\Lambda)(J-\Lambda)}{J}$$

Budó

A relatively simple set of equations for the strength of ${}^3\Pi \rightarrow {}^3\Pi$ transition lines were introduced by Budó. Different expressions apply whether the upper and lower levels obey Hund's case (a) or (b) or transitional (a) \rightarrow (b). Over the typical J-value range useful in plasma diagnostics, both states in the $d^3\Pi_g \rightarrow a^3\Pi_u$ transition of C_2 approximate closely to Hund's case (b). The corresponding equations are given below. For emission, $J = J'$; for absorption, $J = J''$.

Table III-B: Line Strength of ${}^3\Pi(b) \rightarrow {}^3\Pi(b)$ Transitions

Branch	${}^3\Pi(b) \rightarrow {}^3\Pi(b)$
$P_1(J)$	$\frac{(J-2)J(2J+1)}{(J-1)(2J-1)}$
$Q_1(J)$	$\frac{(J+1)(2J+1)}{J^3}$
$R_1(J)$	$\frac{(J-1)(J+1)(2J+3)}{J(2J+1)}$
$P_2(J)$	$\frac{(J-1)^2(J+1)^2}{J^3}$
$Q_2(J)$	$\frac{(2J+1)(J^2+J-1)^2}{J^3(J+1)^3}$
$R_2(J)$	$\frac{J^2(J+2)^2}{(J+1)^3}$
$P_3(J)$	$\frac{J(J+2)(2J-1)}{(J+1)(2J+1)}$
$Q_3(J)$	$\frac{J(2J+1)}{(J+1)^3}$
$R_3(J)$	$\frac{(J+1)(J+3)(2J+1)}{(J+2)(2J+3)}$

Kovács

These are general equations applied in rigorous band spectra calculations. The transition is treated as an intermediate between Hund's cases (a) and (b), with an inverted electronic state. Λ -type doubling is taken into account by using different sets of molecular constants for even and odd J-values (Table III-A). For emission, $J = J'$; for absorption, $J = J''$.

Table III-C: Line Strength of Triplet Transitions for $\Delta\Lambda = 0$ in General Form

Branch	${}^3X(\text{int}) \rightarrow {}^3X(\text{int})$
$P_1(J)$	$[(J-\Lambda)(J+\Lambda)/16JC'_1(J-1)C''_1(J)][(J-\Lambda+1)(J+\Lambda-1)u'_1{}^+(J-1)u''_1{}^+(J) + (J-\Lambda-1)(J+\Lambda+1)u'_1{}^-(J-1)u''_1{}^-(J) + 8(J-\Lambda-1)(J-\Lambda)(J+\Lambda-1)(J+\Lambda)]^2$
$P_2(J)$	$[4(J-\Lambda)(J+\Lambda)/JC'_2(J-1)C''_2(J)][\Lambda^2(Y'-2)(Y''-2)/2 + (J-\Lambda-1)(J+\Lambda+1) + (J-\Lambda+1)(J+\Lambda-1)]^2$
$P_3(J)$	$[(J-\Lambda)(J+\Lambda)/16JC'_3(J-1)C''_3(J)][(J-\Lambda+1)(J+\Lambda-1)u'_3{}^-(J-1)u''_3{}^-(J) + (J-\Lambda-1)(J+\Lambda+1)u'_3{}^+(J-1)u''_3{}^+(J) + 8(J-\Lambda)(J-\Lambda+1)(J+\Lambda)(J+\Lambda+1)]^2$

where Y' and Y'' are upper and lower level molecular constants (Table III-A) and

$$u_1{}^\pm(J) = [\Lambda^2 Y(Y-4) + 4J^2]^{1/2} \pm \Lambda(Y-2)$$

$$u_3{}^\pm(J) = [\Lambda^2 Y(Y-4) + 4(J+1)^2]^{1/2} \pm \Lambda(Y-2)$$

$$C_1(J) = \Lambda^2 Y(Y-4)(J-\Lambda+1)(J+\Lambda) + 2(2J+1)(J-\Lambda)J(J+\Lambda)$$

$$C_2(J) = \Lambda^2 Y(Y-4) + 4J(J+1)$$

$$C_3(J) = \Lambda^2 Y(Y-4)(J-\Lambda)(J+\Lambda+1) + 2(2J+1)(J-\Lambda+1)(J+1)(J+\Lambda+1)$$

The transition involves inverted terms, so Y is assigned a negative sign and $(-\Lambda)$ is substituted for Λ in $C_1(J)$ and $C_3(J)$. Simpler forms corresponding to Hund's cases (a) and (b) are obtained by substituting $Y \rightarrow \pm \infty$ and $Y \rightarrow 0$, respectively. Corrections associated with centrifugal terms and interaction between rotation and spin are neglected.

Appendix IV Rigorous Simulation of the P-branch $\nu(0,0)$ Swan Band

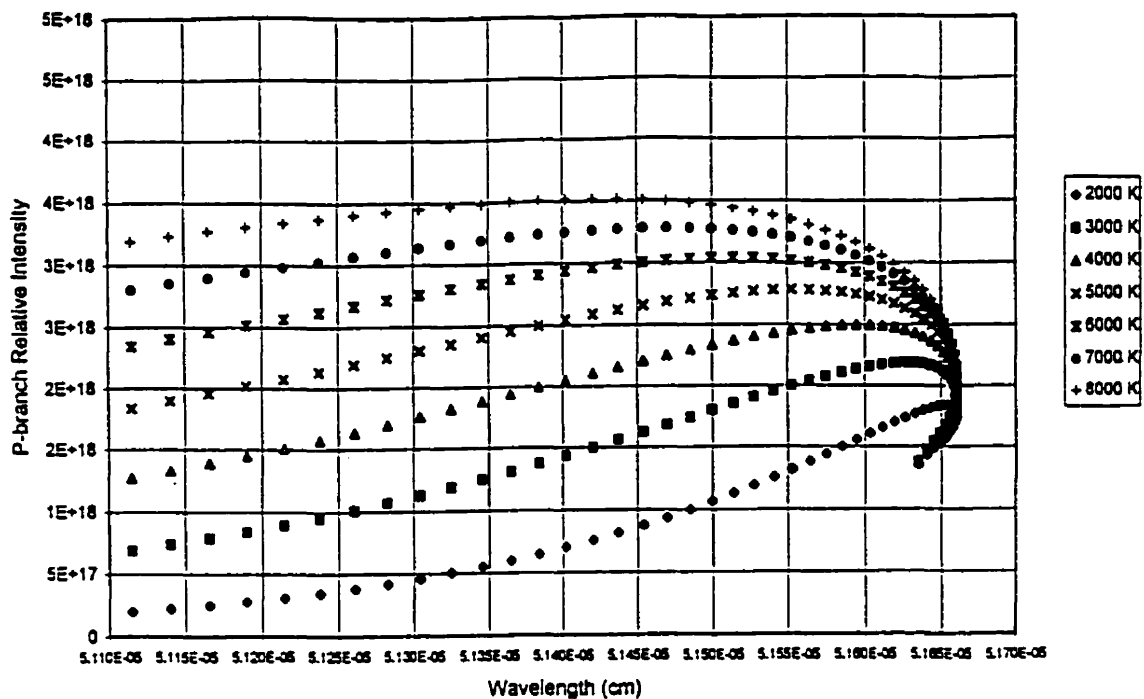


Figure IV-A: P-Branch Relative Line Intensity vs Wavelength

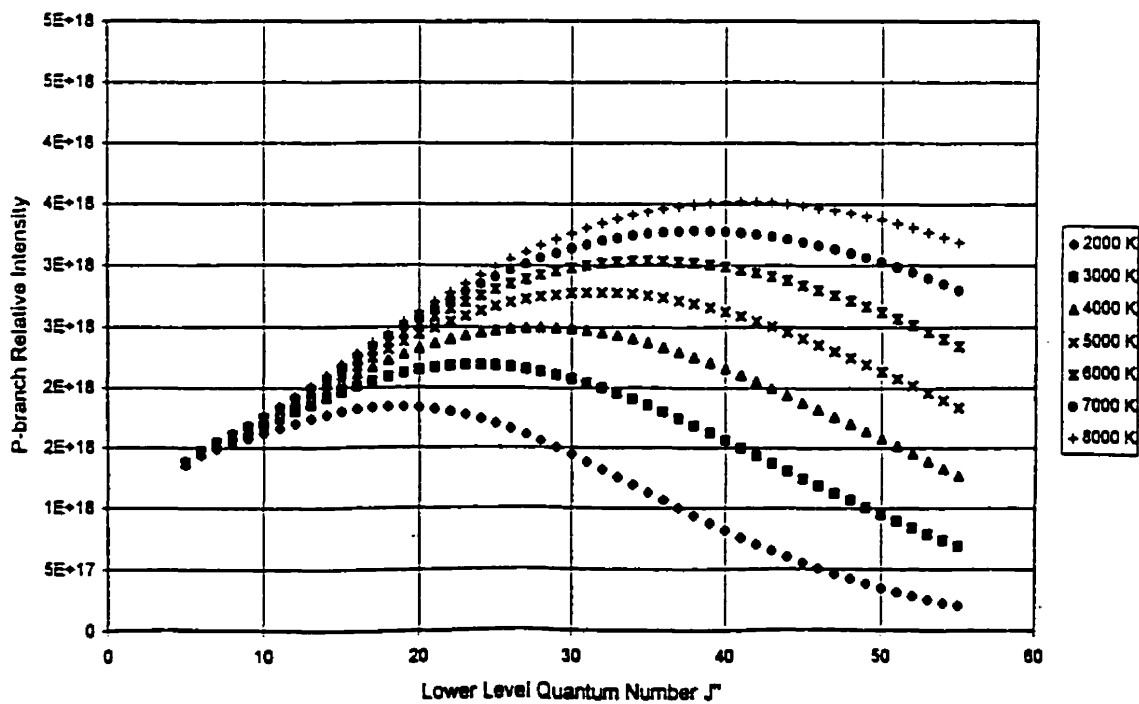


Figure IV-B: P-Branch Relative Line Intensity vs Quantum Number

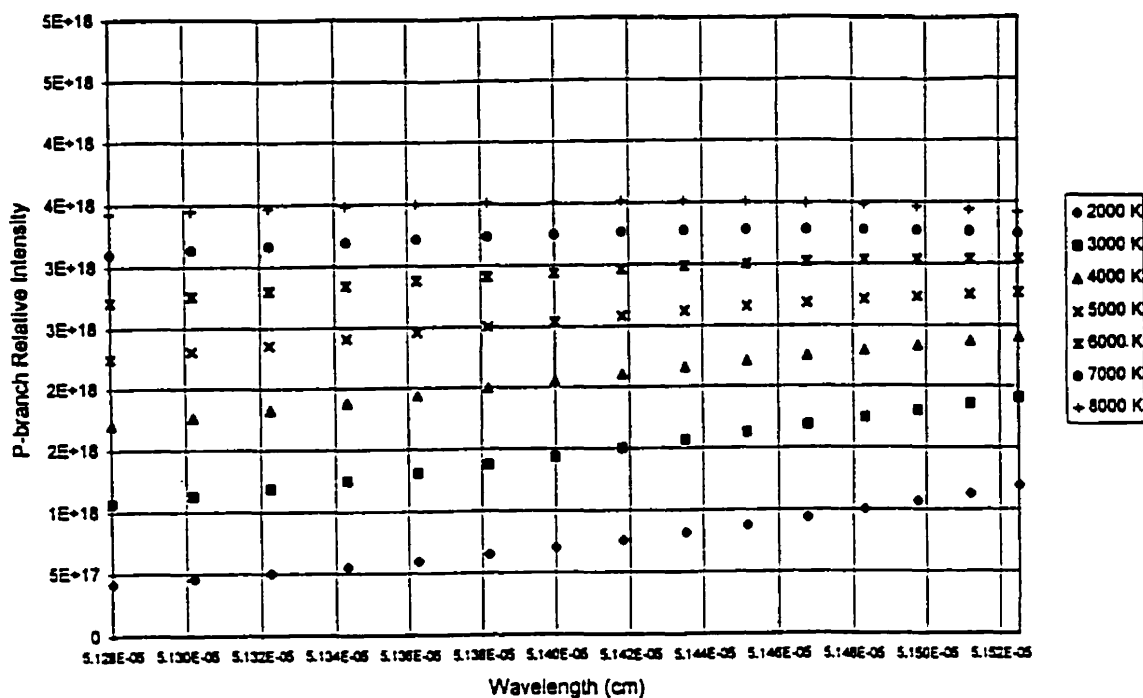


Figure IV-C: P-Branch Relative Line Intensity vs Wavelength

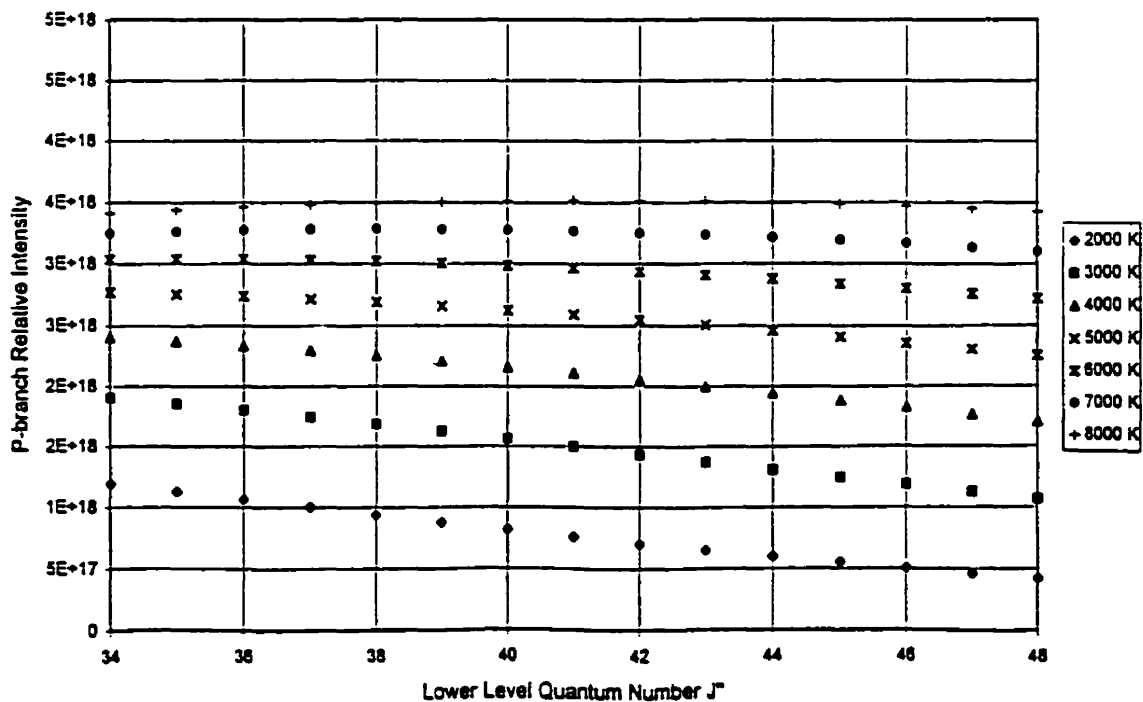


Figure IV-D: P-Branch Relative Line Intensity vs Quantum Number

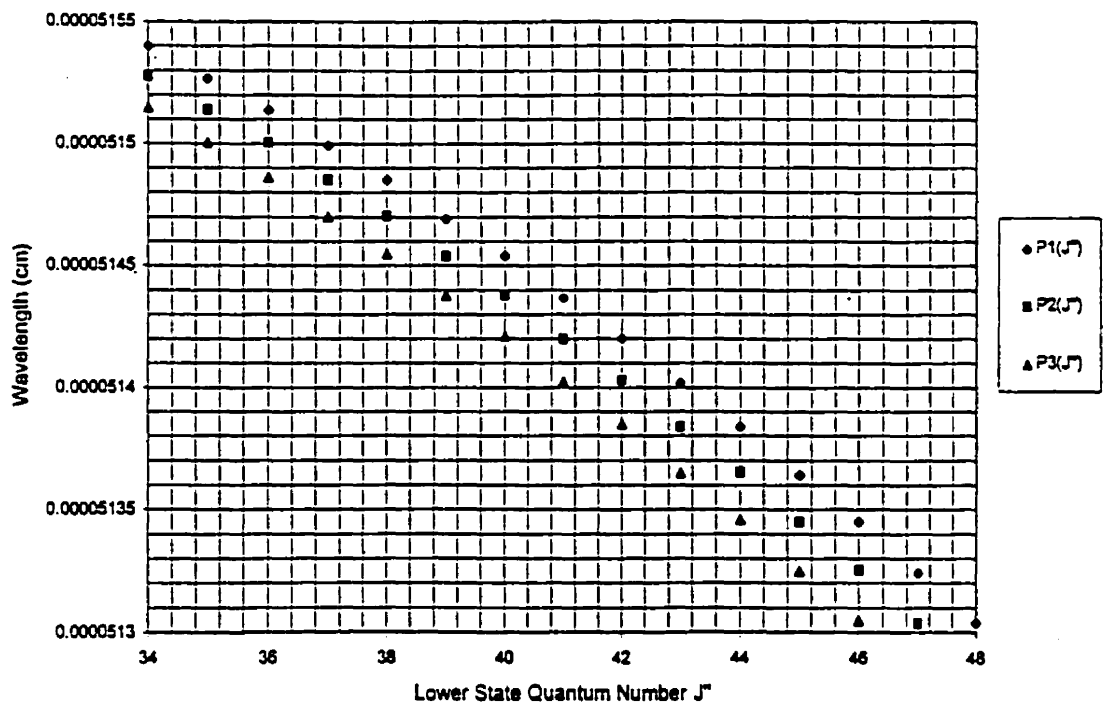


Figure IV-E: P-Branch Component Wavelengths

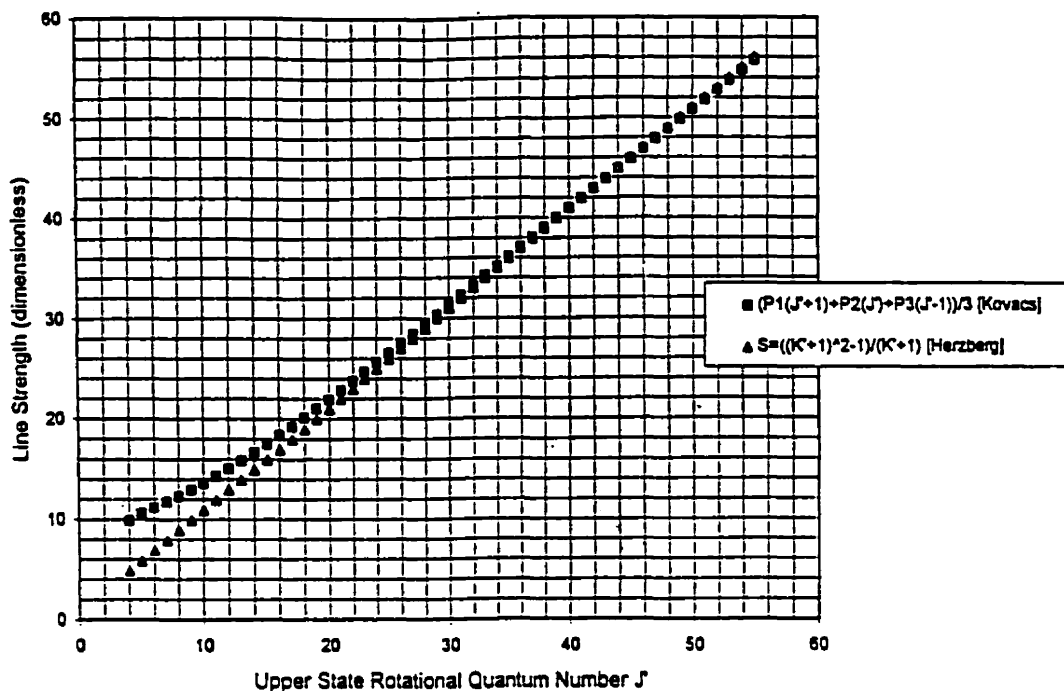


Figure IV-F: P-Branch Component Line Strengths

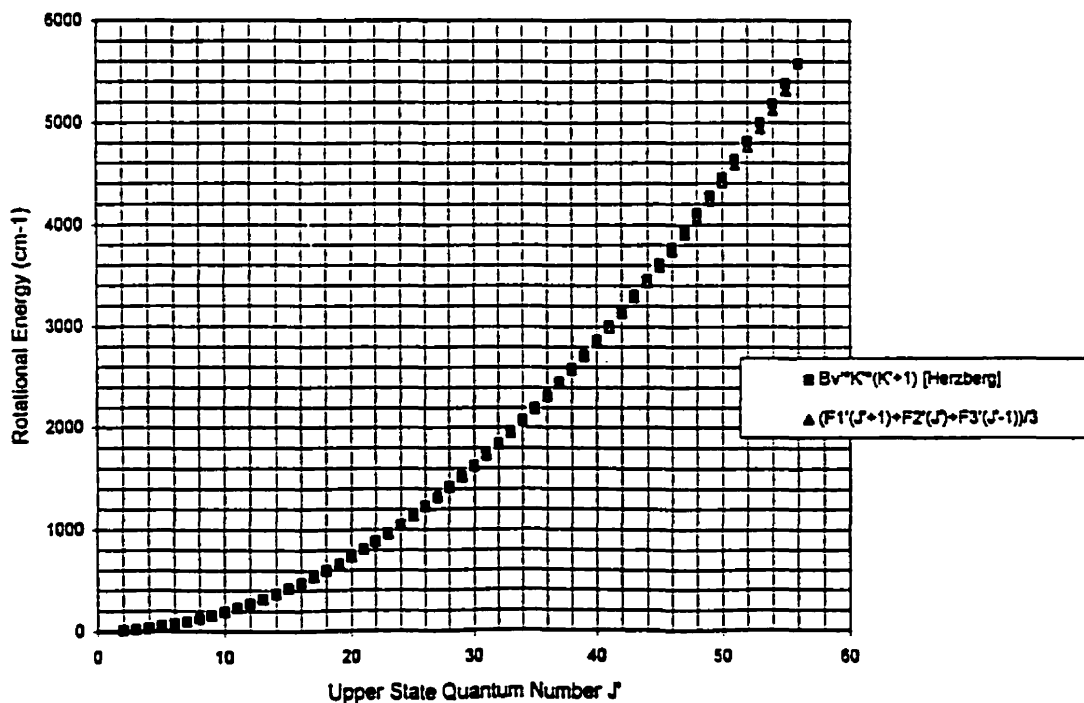


Figure IV-G: P-Branch Rotational Energy Levels

Appendix V Complete Simulation of the $\nu(0,0)$ Swan Band

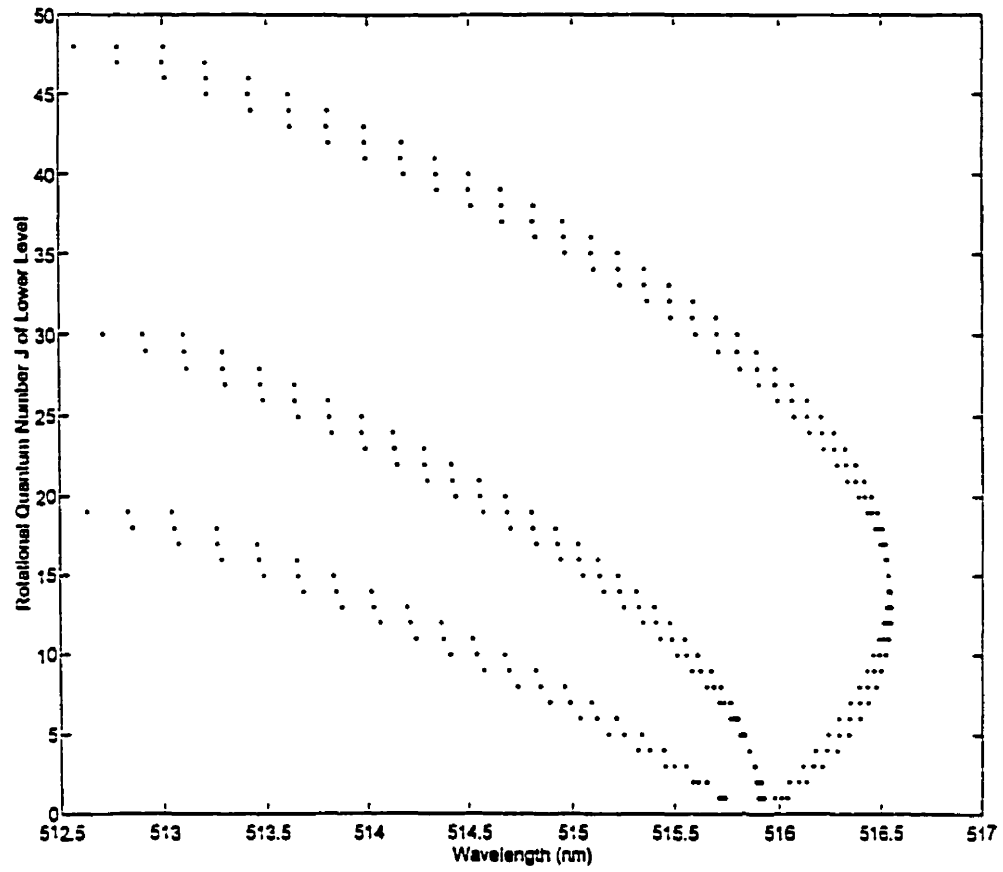
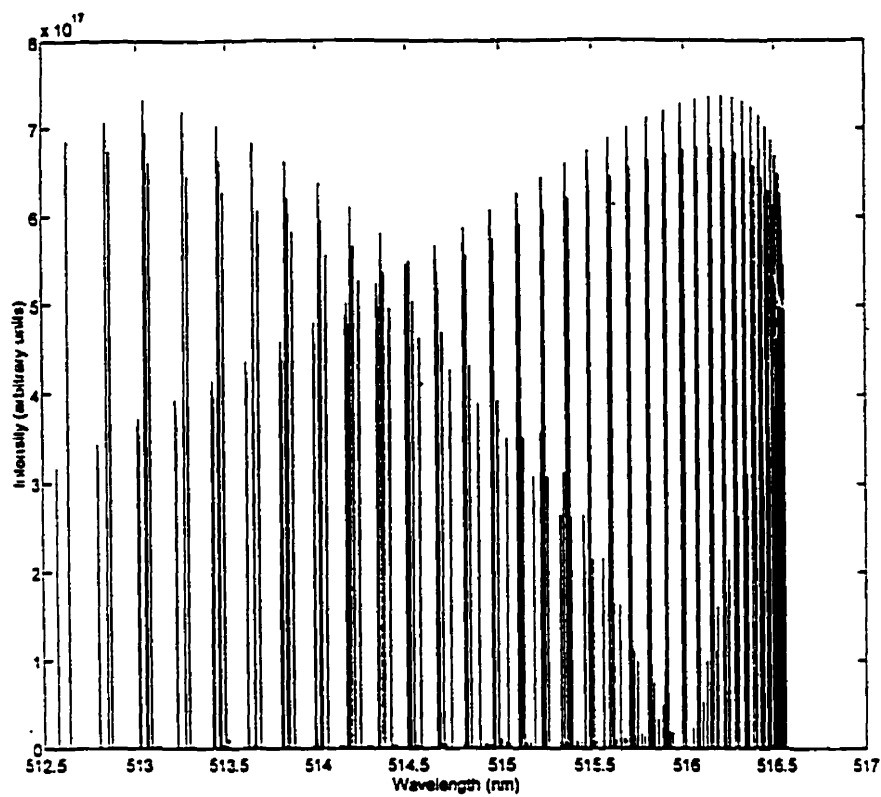
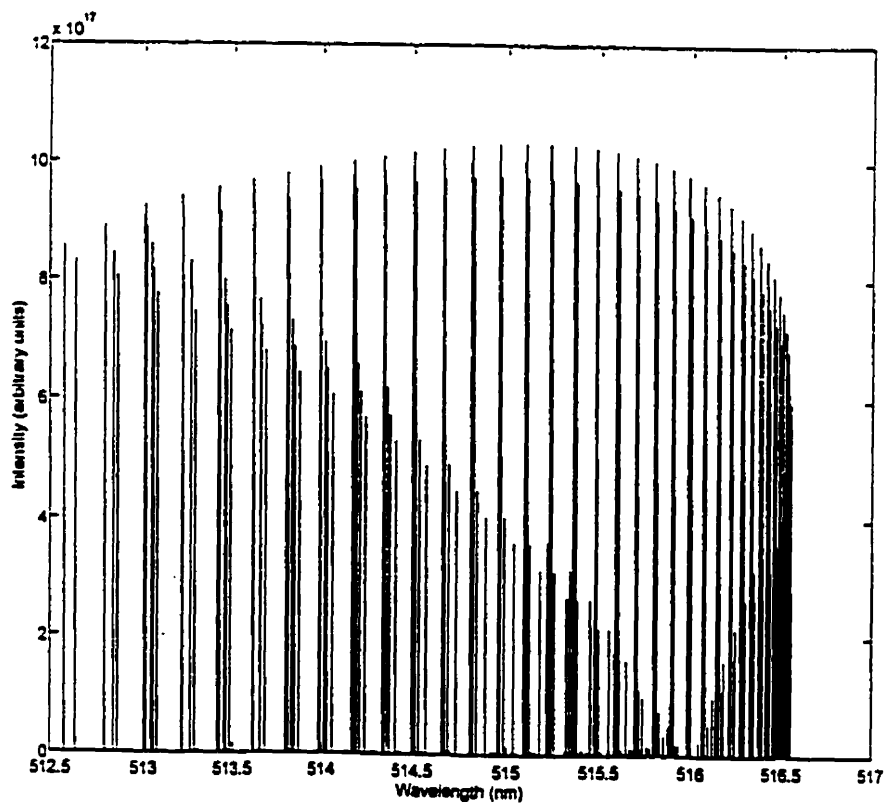


Figure V-A: Fortrat Diagram of the (0, 0) Band of the Swan System

Figure V-B: Discrete Spectrum at $T = 3000\text{ K}$ Figure V-C: Discrete Spectrum at $T = 6000\text{ K}$

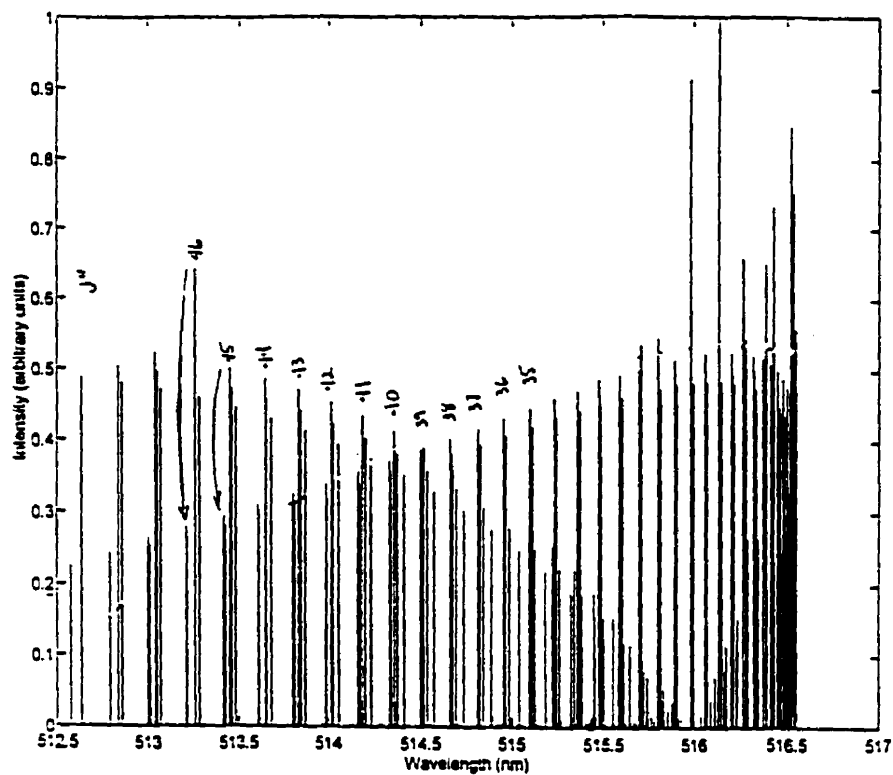


Figure V-D: Simulated Spectrum at $T = 3000$ K and $\text{FWHM} = 0.001$ nm

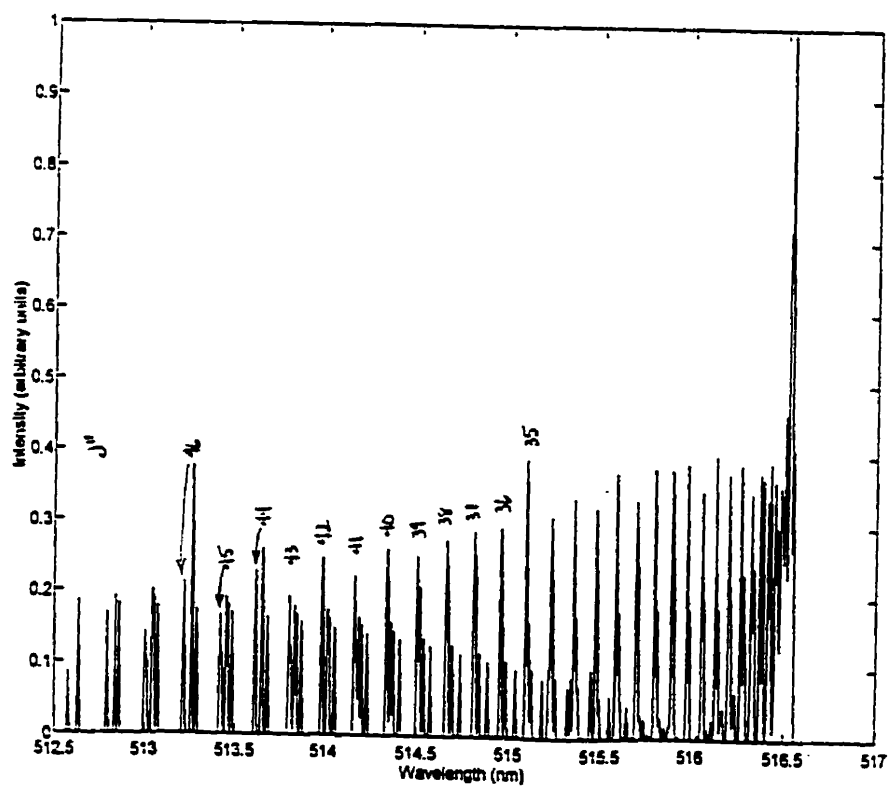


Figure V-E: Simulated Spectrum at $T = 3000$ K and $\text{FWHM} = 0.008$ nm

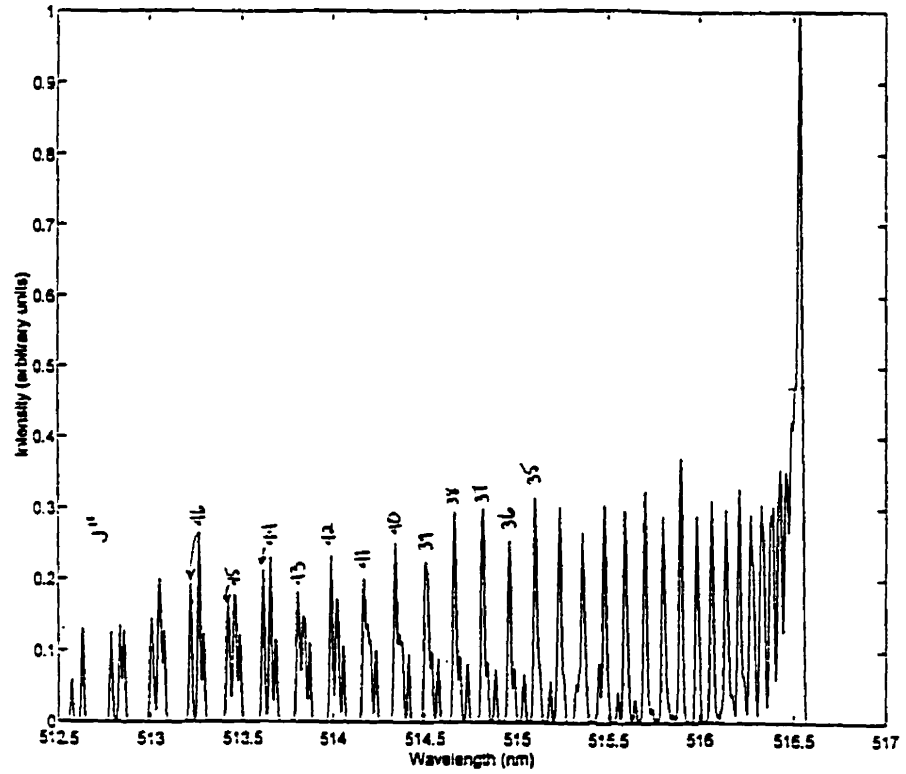


Figure V-F: Simulated Spectrum at T = 3000 K and FWHM = 0.015 nm

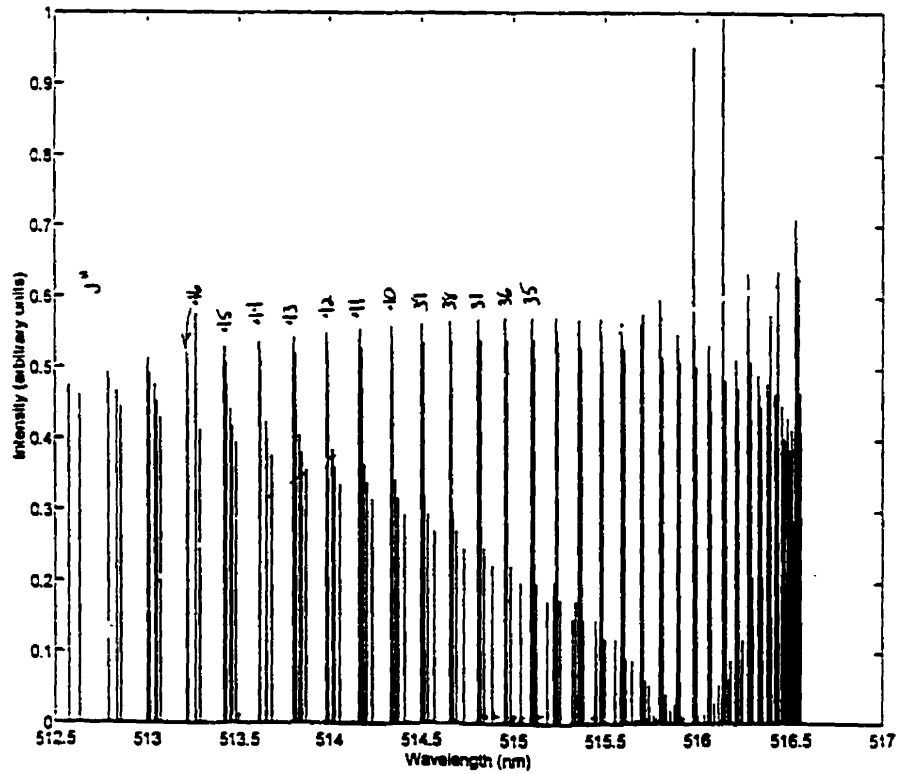


Figure V-G: Simulated Spectrum at T = 6000 K and FWHM = 0.001 nm

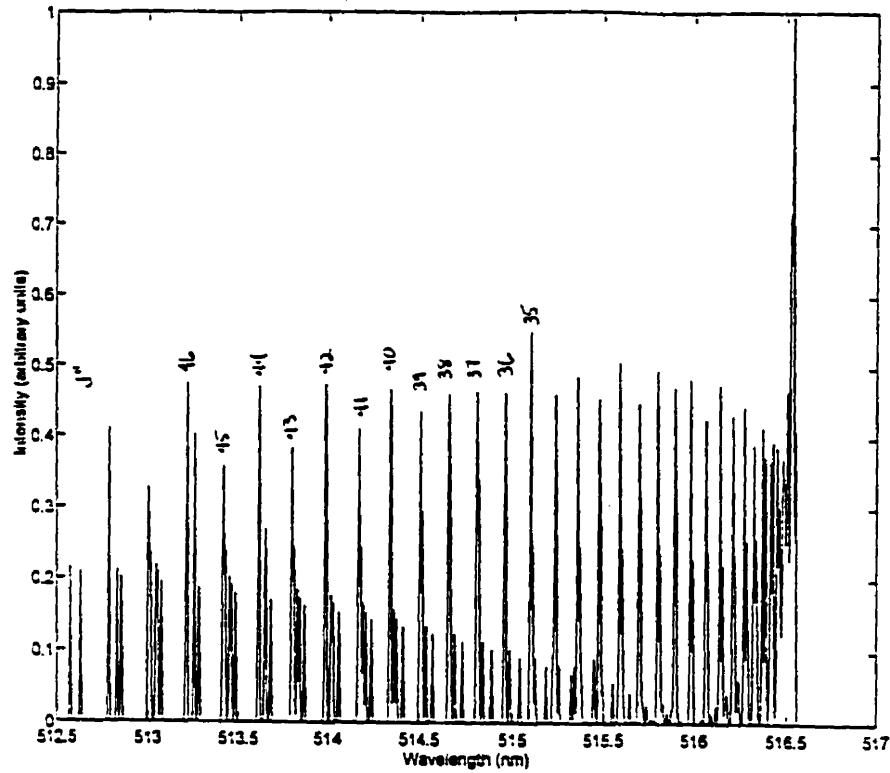


Figure V-H: Simulated Spectrum at $T = 6000$ K and $\text{FWHM} = 0.008$ nm

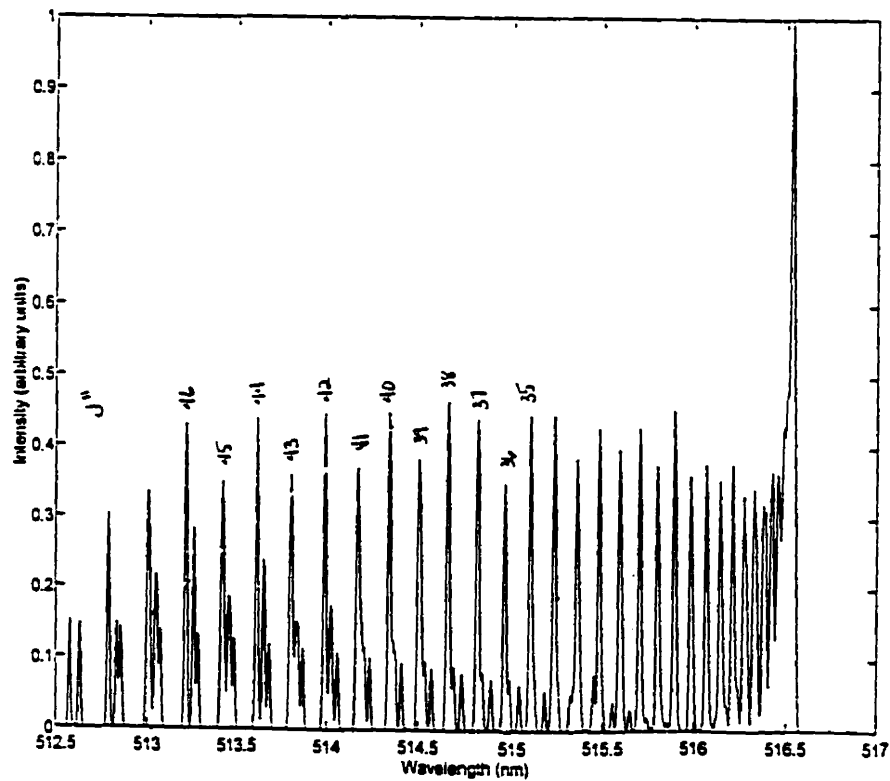


Figure V-I: Simulated Spectrum at $T = 6000$ K and $\text{FWHM} = 0.015$ nm

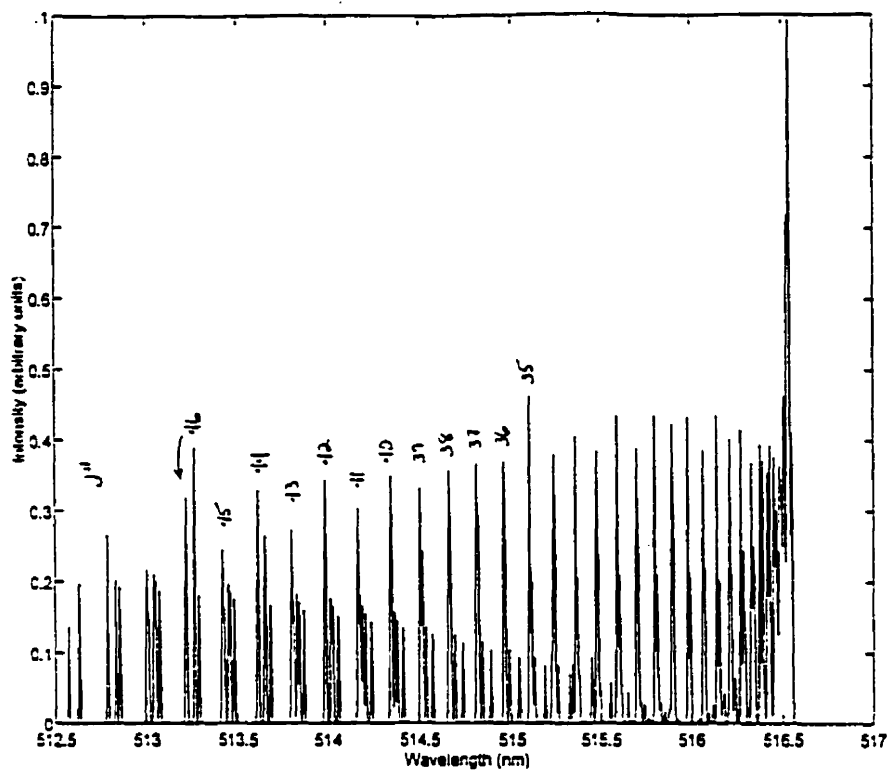


Figure V-J: Simulated Spectrum at $T = 4000\text{ K}$ and $\text{FWHM} = 0.008\text{ nm}$

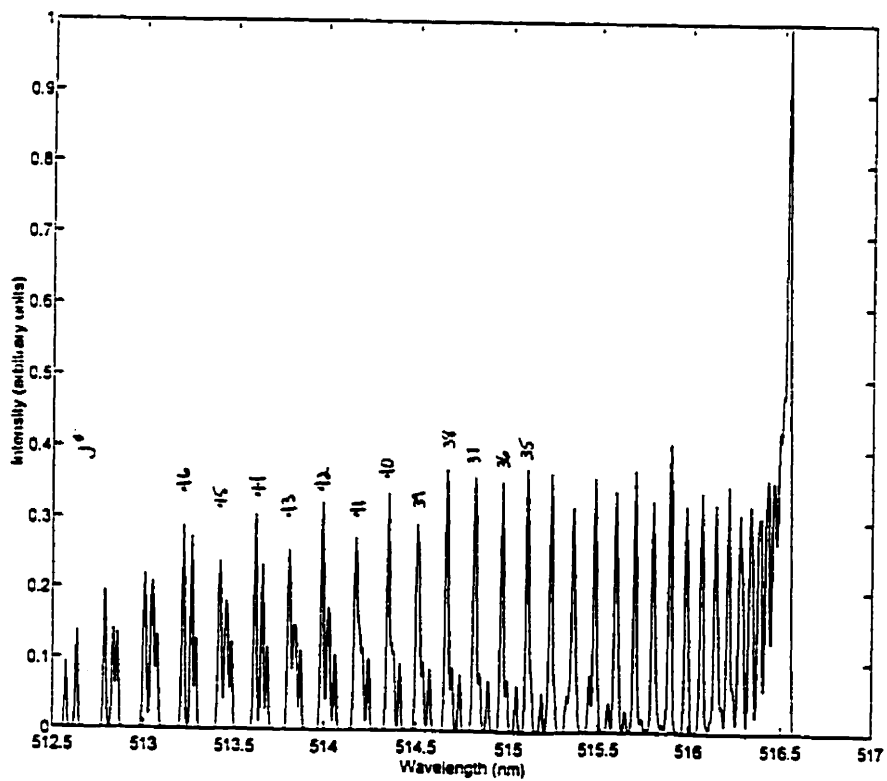


Figure V-K: Simulated Spectrum at $T = 4000\text{ K}$ and $\text{FWHM} = 0.015\text{ nm}$

Appendix VI Temperature Estimation Using the Boltzmann Plot Method

The kinetic temperature of the plasma's heavy species is assumed close to the rotational temperature (T_r) of the $d^3\Pi_g \rightarrow a^3\Pi_u$ $v(0,0)$ transition of C_2 . Assuming a Boltzmann equilibrium among the rotational energy states of the upper level, T_r is estimated from relative line intensity measurements.

$$I_{v'v''J'J''} = A v^4 S_{v'v''J'J''} \exp\left(-\frac{hc}{kT_r} F(J')\right) \quad (\text{equation I-8})$$

$$\frac{I_{v'v''J'J''}}{A v^4 S_{v'v''J'J''}} = \exp\left(-\frac{hc}{kT_r} F(J')\right)$$

$$\ln\left(\frac{I_{v'v''J'J''}}{A v^4 S_{v'v''J'J''}}\right) = -\frac{hc}{kT_r} F(J')$$

$$\ln\left(\frac{I_{v'v''J'J''}}{v^4 S_{v'v''J'J''}}\right) = \ln(A) + \left(\frac{-hc}{kT_r}\right) F(J') \quad (\text{equation VI-1})$$

Since A is a constant, a plot of $\ln\left(\frac{I_{v'v''J'J''}}{v^4 S_{v'v''J'J''}}\right)$ against $F(J')$ is linear with a slope equal to $\left(\frac{-hc}{kT_r}\right)$.

Experimental intensity values for the P-branch lines of the selected transition between $J'' = 46$ and $J'' = 36$ (unresolved triplet components) were measured from emission scans. The lines $P_1(J'+1)$, $P_2(J')$ and $P_3(J'-1)$ were very close in wavelength. This is seen in the Fortrat diagram (Figure V-A), in standard band analysis tables (Phillips and Davis 1968, Prasad and Bernath 1994), and in experimental spectra (Czernichowski 1987). These groups of lines were

assumed to form single peaks on the measured spectra. The rotational energies, wavenumbers and strengths of the lines were evaluated using equations from Phillips and Kovács (Appendix III). A line of best fit was determined in the least squares sense, and its slope was used to estimate T_r .

$$\begin{aligned} \text{Taking } k &= 1.380662e^{-23} \text{ J/K} \\ h &= 6.626176e^{-34} \text{ Js} \\ c &= 2.99792458e^{10} \text{ cm/s} \\ \text{and } F(J') &[\text{=}] \text{ cm}^{-1} \end{aligned}$$

one obtains $T_r [\text{K}] \approx 1.43879 / (-\text{slope})$.

Appendix VII Temperature Estimation Using Integrated Band Intensities

Let ϵ_{00} be the absolute emission intensity integrated over a molecular band, specifically the $\nu(0, 0) d^3\Pi_g \rightarrow a^3\Pi_u$ transition of C_2 (equation I-8 in Appendix I). Let $\epsilon_\nu(J)$ be the absolute intensity of a line in the band. The relative integrated intensity over a waveband (λ_1 to λ_2) corresponding to quantum numbers J_1 to J_2 (with different values for different branches) is defined as:

$$\alpha = \frac{\sum_{P,Q,R} \sum_{J_1}^{J_2} \epsilon_\nu(J)}{\epsilon_{00}} \quad (\text{equation VII-1})$$

From equation I-8,

$$\epsilon_\nu(J) = A\sigma^4 S_{\nu\nu'J'J''} \exp\left(-\frac{hc}{kT} F(J')\right) \quad (\text{equation VII-2})$$

where the factor $A\sigma^4$ is assumed constant over short wavebands, and where $F(J') \approx B_\nu J'(J'+1)$.

The ratio of relative integrated intensities over two intervals A and B within the same band simplifies to:

$$\frac{\alpha_A}{\alpha_B} = \frac{\left[\frac{A\sigma^4 \sum_{P,R} \sum_{J_{A1}}^{J_{A2}} S_{\nu\nu'J'J''} \exp\left(-\frac{B_\nu hc}{kT} J'(J'+1)\right)}{\epsilon_{00}} \right]}{\left[\frac{A\sigma^4 \sum_{P,R} \sum_{J_{B1}}^{J_{B2}} S_{\nu\nu'J'J''} \exp\left(-\frac{B_\nu hc}{kT} J'(J'+1)\right)}{\epsilon_{00}} \right]}$$

$$\frac{\alpha_A}{\alpha_B} = \frac{\sum_{P,R} \sum_{J_{A1}}^{J_{A2}} S_{\nu\nu'J'J''} \exp\left(-\frac{B_\nu hc}{kT} J'(J'+1)\right)}{\sum_{P,R} \sum_{J_{B1}}^{J_{B2}} S_{\nu\nu'J'J''} \exp\left(-\frac{B_\nu hc}{kT} J'(J'+1)\right)} \quad (\text{equation VII-4})$$

The integrated band intensity method works as follows. Line strengths for the P and R branches (the Q branch being negligible) are given by Herzberg's simplified formulae (Appendix IV). For any two intervals within the band, a relative intensity ratio value is predicted as a function of temperature. A temperature estimate is then inferred by matching calculated and measured ratios. A MATLAB program was developed to perform the numerical integration described by equation VII-4.

To calculate experimental ratios, the Swan band emission had to be isolated from continuum and argon line emissions. This was performed by subtraction of a blank spectrum scaled using a reference background measurement (B). However, continuum and argon emissions were not proportional, and the subtraction procedure was questionable for intervals including argon lines. A more accurate correction was expected over band intervals free from argon interference.

Attempts at estimating temperature by this method, using the two sets of interval described in Table VII-1, were unsuccessful. Table VII-2 contains experimental ratios for the wavebands proposed by Bousrih *et al.* (1995), which cover the whole band (512.9 nm to 516.5 nm). Table VII-3 gives the corresponding theoretical values. Table VII-4 contains experimental ratios for short wavebands free from argon interference. The corresponding theoretical values appear in Table VII-5. In either case, the measured values were outside the expected range. Possible explanations for these discrepancies are discussed in section 5.1.3.2.

Table VII-1: Interval Sets #1 and #2 (Wavelengths in nm)

	#1	#2
λ_{A1}	512.9	513.0
λ_{A2}	516.5	513.75
λ_{B1}	516.0	513.75
λ_{B2}	516.5	514.5
J'_{PA1}	46	46
J'_{PA2}	1	42
J'_{RA1}	20	19
J'_{RA2}	1	15
J'_{PB1}	26	42
J'_{PB2}	1	38
J'_{RB1}	---	15
J'_{RB2}	---	11

Table VII-2: Measured Ratios for Interval Set #1

Spectrum	Ref. B	Integrated I_A	Integrated I_B	α_A/α_B
Blank (3.5% O ₂)	15384	114553	35771	---
Signal (0.2% C ₃ H ₈)	6596	63174	16892	9.0
Signal (0.3% C ₃ H ₈)	7059	92338	25611	4.3

Table VII-3: Theoretical Ratios for Interval Set #1

T (K)	1000	2000	3000	4000	5000	6000	7000	8000
α_A/α_B	1.977	2.284	2.540	2.724	2.860	2.962	3.042	3.106

Note: For intervals ranging from a wavelength λ^* to the band head ($J^* \rightarrow 1$), the ratio is computed as $[(1-\alpha_A^*)/(1-\alpha_B^*)]$, where α^* is defined as the relative integrated intensity from λ^* to the band tail ($J^* \rightarrow 100$ for the purpose of numerical integration). This procedure is preferred since the equations used in modelling line intensities are less accurate at low J-values.

Table VII-4: Measured Ratios for Interval Set #2

Spectrum	Ref. B	Averaged I _A	Averaged I _B	α_A/α_B
Blank (3.5% O ₂)	15384	18096	19816	---
Signal (0.2% C ₃ H ₈)	6596	11569	13508	0.76
Signal (0.3% C ₃ H ₈)	7059	16722	19627	0.82

Note: Intervals A and B being of identical size, integrated intensities and averaged intensities (i.e., integrated then averaged over the bandwidth by the data acquisition software) were interchangeable.

Table VII-5: Calculated Theoretical Ratios for Interval Set #2

T (K)	1000	2000	3000	4000	5000	6000	7000	8000
α_A/α_B	0.925	0.986	1.010	1.031	1.047	1.060	1.070	1.078

Appendix VIII Steepest Ascent Optimization Strategies and Equations

(Lee *et al.* 1968)

Gradient-based methods work by successive moves along the gradient of a response surface. Local approximations to the surface indicate the direction of steepest ascent, which is re-evaluated as needed. This section presents a mathematical description of the procedures and a summary of the decision rules which govern gradient-based optimization.

Gradient approximation by the difference equation

General case $F(X_1, X_2, \dots, X_n)$ = function to be optimized
 p (as a subscript) = current operating point
 ΔX_i = incremental change in the i^{th} parameter

$$\left. \frac{\partial F}{\partial X_i} \right|_p \approx \left. \frac{\Delta F}{\Delta X_i} \right|_p$$

With one measurement:

$$\Delta F_i = F[X_1, X_2, \dots, (X_i + \Delta X_i), \dots, X_n] - F[X_1, X_2, \dots, X_i, \dots, X_n]$$

With two measurements:

$$\Delta F_i = F[X_1, X_2, \dots, (X_i + \frac{\Delta X_i}{2}), \dots, X_n] - F[X_1, X_2, \dots, (X_i - \frac{\Delta X_i}{2}), \dots, X_n]$$

Particular case: $F(O, P)$ = objective function
 O = oxygen flow rate
 P = plasma power

$$\left. \frac{\Delta F}{\Delta O} \right|_p = \frac{F(O_p + \Delta O, P_p) - F(O_p, P_p)}{\Delta O} = F'_O$$

$$\left. \frac{\Delta F}{\Delta P} \right|_p = \frac{F(O_p, P_p + \Delta P) - F(O_p, P_p)}{\Delta P} = F'_p$$

$$\bar{\nabla} F(O, P) = \frac{\partial F}{\partial O} \mathbf{i} + \frac{\partial F}{\partial P} \mathbf{j} \quad \text{where } \mathbf{i} = \text{unit basis vector along the } O \text{ axis}$$

and $\mathbf{j} = \text{unit basis vector along the } P \text{ axis}$

$$\bar{\nabla} F = F'_O \mathbf{i} + F'_P \mathbf{j}$$

The **directional vector** is the normalized (unit length) form of the gradient. Hill-climbing by the gradient method involves moving in this direction by a step whose magnitude is given by the **scale factor** M , an arbitrary parameter. The move is effected by applying to each variable a change equal to the projection of the normalized vector along its axis multiplied by the scale factor. This procedure is summarized in mathematical form by the **recurrence equation of a step**.

$$\text{Directional vector} = \frac{F'_O \mathbf{i} + F'_P \mathbf{j}}{\sqrt{F'^2_O + F'^2_P}}$$

$$\text{Change in oxygen flow rate} = \frac{MF'_O}{\sqrt{F'^2_O + F'^2_P}}$$

$$\text{Change in plasma power} = \frac{MF'_P}{\sqrt{F'^2_O + F'^2_P}}$$

Recurrence equation of a step

X_i^p = value of i^{th} control variable at point p

X_i^{p+1} = value of i^{th} control variable at point $(p + 1)$

\mathbf{D}^p = normalized gradient evaluated at point p

D_i^p = gradient component along axis i

H_i^p = scale factor operating on gradient component i at step p

$$\Delta X_i^p = X_i^{p+1} - X_i^p$$

$$X_i^{p+1} = X_i^p + (H_i^p)(D_i^p)$$

or, in matrix notation, $\mathbf{X}^{p+1} = \mathbf{X}^p + \Delta\mathbf{X}^p = \mathbf{X}^p + \mathbf{H}^p\mathbf{D}^p$

Gradient Strategies

Variations on the basic method have been developed to improve gradient optimization or adapt it to particular situations. Here are three common strategies.

A) Steepest Ascent

This is the basic version of the gradient method. At every step, the directional vector is determined from the gradient. The scale factor is constant and equal for all variables. Convergence is relatively slow. Difficulties arise near a ridge or an optimum.

B) Optimal Gradient

The same directional vector and scale factor are used for successive steps as long as the response increases. At the first sign of decrease in response, the last step is retraced by a full or half step and a new gradient is computed. Optionally, the step size can be modified to refine the search near an optimum or to speed up convergence in other regions (see *Technique for modifying the step size* below). The method does not require computation of the gradient at every step.

C) Gradient prediction

The same directional vector and scale factor are used for successive steps until the response falls outside a range of values predicted from the gradient. When the response differs significantly from the prediction, the last step is retraced by a full or half step and a new gradient is computed. Again, the step size may vary.

F^p = actual response surface value at point p

\bar{F}^{p+1} = predicted response surface value at point $(p + 1)$

ΔF^p = actual change in response surface value for step p

$\Delta \bar{F}^p$ = predicted change in response surface value for step p

\mathbf{G}^p = gradient vector used at step p

\mathbf{D}^p = directional vector for step p

K_3 = arbitrary limit

$$\bar{F}^{p+1} = F^p + \mathbf{G}^p (\mathbf{H}^p \mathbf{D}^p)$$

$$\Delta \bar{F}^p = \bar{F}^{p+1} - F^p$$

$$\Delta F^p = \sqrt{\sum_{i=1}^n (X_i^{p+1} - X_i^p)^2 (G_i^p)^2}$$

$$|\Delta F^p - \Delta \bar{F}^p| < K_3 \Rightarrow \text{gradient / directional vectors unchanged}$$

$$|\Delta F^p - \Delta \bar{F}^p| \geq K_3 \Rightarrow \text{compute new gradient / directional vectors}$$

Technique for modifying the step size

The purpose of this procedure is to accelerate progression when moves in the direction of steepest ascent strongly improve the response, and to slow it down otherwise. When changes in response value become less important, the step size decreases; as they grow more pronounced, the step size increases. The standard algorithm suggested by Lee *et al.* is as follows:

R^p = ratio of differences in response surface value for two successive steps

$$R^p = \frac{\sqrt{\sum_{i=1}^n (X_i^{p+1} - X_i^p)^2}}{\sqrt{\sum_{i=1}^n (X_i^p - X_i^{p-1})^2}}$$

K_1 = lower limit on R^p (arbitrary)

K_2 = upper limit on R^p (arbitrary)

$K_1 < |R^p| < K_2 \Rightarrow$ scale factor unchanged

$|R^p| \leq K_1 \Rightarrow$ decrease scale factor

$|R^p| \geq K_2 \Rightarrow$ increase scale factor

When tested experimentally, this algorithm worked well on monotonic surfaces but was inadequate near an optimum. For instance, upon crossing a ridge, a marked drop in response could follow several close readings. This would make R^p large and cause an increase in step size, whereas smaller steps were needed to refine the search on one side of the ridge. Therefore, additional guidelines were developed to suit the needs of the present project:

- 1) The algorithm described above applies only when responses increase over successive steps.
- 2) A decrease in response just following evaluation of the gradient indicates that the scale factor is too large relative to the scale of applicability of the linear model. This situation triggers a reduction in scale factor, regardless of the magnitude of R^p .
- 3) A decrease in response just following a step in the same direction as the previous one signals a need for re-orientation, and calls for a gradient evaluation with no change in the value of the scale factor.

- 4) The algorithm does not apply in the vicinity of an optimum, where similar responses could cause R^p to vary widely. This situation is identified by comparing response changes over the last few steps.
- 5) A marked departure from linearity following a gradient evaluation (i.e. an important difference between the measured response and that estimated by a linear model) suggests too large a scale factor compared to the scale of applicability of the model. This triggers a reduction in scale factor provided a first adjustment was not implemented under rule #2 or the basic algorithm. In case of conflicting outcomes, the algorithm takes precedence over rule #5.

Appendix IX Simplex Optimization Principles and Rules

(Betteridge *et al.* 1985, Marwick 1995,
Nelder and Mead 1965, Walters *et al.* 1991)

The Simplex algorithm is applicable in the optimization of any function of n variables. A Simplex is a geometric figure with $(n+1)$ vertices, each vertex corresponding to an operating point at which the value of the response to be optimized is measured. The choice of initial vertices is arbitrary. The basic principle of the method is to compare responses at these vertices and reflect the point with the worst response in the hyperplane formed by the remaining points, thus forming a new Simplex. For example, on a two-dimensional surface, the Simplex is a triangle whose vertices are labeled B (best), N (next best), and W (worst) based on their responses. A new Simplex is formed by reflecting point W across the mean of B and N, denoted P (see Figure XI-A), and a response is measured at the new point (R).

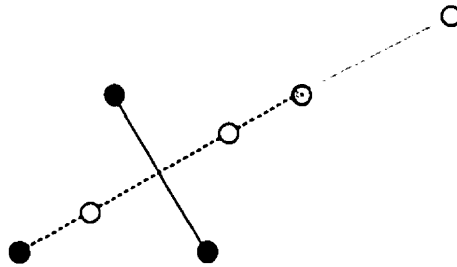


Figure IX-A: Illustration of Basic Simplex Concepts

In the simple algorithm developed by Nelder and Mead, the next step is determined as follows. Fixed step-size reflection (Figure IX-A) is the default option, but the position of the reflected point may be adjusted according to the quality of the response obtained. The resulting variations in step size speed up the optimization, allowing the Simplex to extend toward good response areas and to retract from poor ones. A variable step-size Simplex is less likely to

become stranded on a ridge or to converge prematurely in a region that excludes the optimum. There are three possible cases:

- 1) $R > B$ (i.e. the response at R is better than that at B)
Use the expansion rule described below.
- 2) $B \geq R \geq N$ (default case)
B remains B', R becomes N', N becomes W', and W is dropped.
- 3) $N > R$
Use the contraction rule described below.

Expansion rule

When $R > B$, extend the Simplex by a factor k - the **expansion coefficient**, usually assigned a value of two - from P to obtain E (Figure IX-A); measure the response at E:

$$E = P + k*(P - W) = P + 2*(P - W) = R + (P - W)$$

If $E \geq B$, then E becomes B', B becomes N', N becomes W', and W is dropped.

If $E < B$, then R becomes B', B becomes N', N becomes W', and W is dropped.

Contraction rule

If $R > W$, retract from R by a half step (contraction with reflection):

$$C_R = P + (P - W)/2$$

If $R < W$, retract from P by a half step (contraction without reflection):

$$C_W = P - (P - W)/2$$

If C_R or $C_W \geq B$, then C becomes B', B becomes N', N becomes W', and W is dropped.

If C_R or $C_W < B$, then B remains B', C becomes N', N becomes W', and W is dropped.

An expansion point may or may not replace the reflection point depending on its response, but a contraction point is retained regardless of its response. The ranking rules are designed so that N becomes W' and W is dropped, always. Hence C is assigned the label N' even when $C < N$. Were C allowed to become W' , difficulties might arise when $R < N$. For example, straddling a ridge, the Simplex may go into "partial oscillatory collapse," as illustrated in Figure IX-B: the Simplex reflects back and forth across the ridge, slowly closing in on it through successive contractions. Near a saddle point, the Simplex might undergo "catastrophic oscillatory collapse," shown in Figure IX-C, and fail to reach an optimum.

Should oscillatory behaviour occur despite application of the contraction rule, re-initialization with translation or compression of the Simplex might be in order. Another option, proposed by Walters *et al.*, is to reflect N across the centroid of R and B , i.e. to take N as W' and R as N' (an application of the "Next-to-Worse" rule described below). This offers a possibility of reorientation and satisfies the general requirement that vertex N in a Simplex be rejected in the next Simplex, regardless of the response at R .

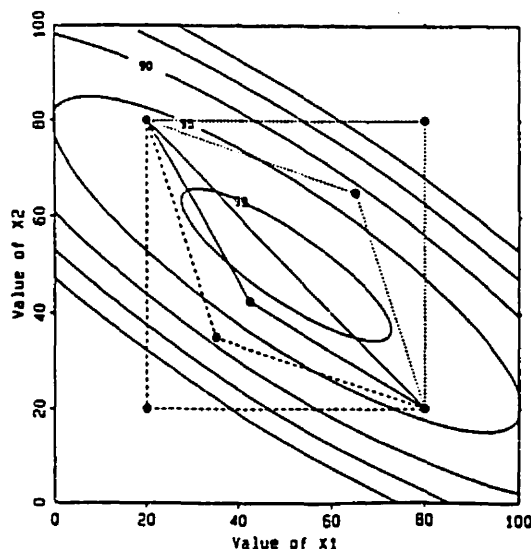


Figure IX-B:

Partial Oscillatory Collapse
(Walters *et al.* 1991)

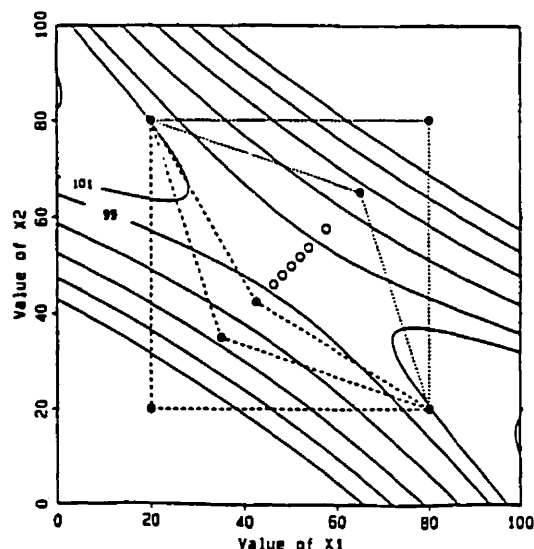


Figure IX-C:

Catastrophic Oscillatory Collapse
(Walters *et al.* 1991)

Additional rules

Researchers have modified the Nelder and Mead algorithm to improve its performance or adapt it to particular optimization problems. Here is a summary of the most common rules which have been shown to improve the efficiency of Simplex optimization.

A) Weighted centroid

Reflect point W through a centroid weighted towards the better point(s), e.g. towards point B in two dimensions. This rule helps when the region of the optimum is unknown; unweighted exploration is preferable near the optimum.

B) Variable expansion coefficient

An expansion coefficient of two is most often used. A deterioration in search efficiency has been observed with coefficients greater than two.

C) Comparison of expansion and reflection

If $E \geq R$, then E becomes B'

If $R > E > B$, then R becomes B'

Part of the well-known *Composite Modified Simplex (CMS)* developed by Betteridge *et al.* (1985), this variation focuses on retaining the highest response. It may prove a disadvantage in the early stages of a search, where it is desirable to explore as far and as rapidly as possible over potential response areas.

D) "Next-to-worse" rule

When $R < N$, start a new cycle treating N as if it were W . Although there is little effective difference between this alternative and the contraction rule, it provides an opportunity for reorientation.

E) Polynomial fit

Introduced in the *Super-Modified Simplex (SMS)* of Routh *et al.* reviewed by Marwick (1995), this technique has similarities with gradient methods. It involves quadratic fitting between points P, R and F, where point F is the maximum of the curve defined by points W, P and R.

F) Fitting and squashing to boundaries

Whenever points fall outside a parameter boundary, adjust the reflection or expansion move (either for out-of-bound variables only, or for all variables) such that all points are within the operating range. The effect of this procedure is to “flatten” the Simplex into a lower-dimensional search along boundaries. Alternatively, a point outside the range may be artificially assigned a poor response value, forcing a contraction without reflection.

G) Suboptimal redirection

If both $R < W$ and $C_W < W$, move in the second most favourable direction by applying the Next-to-Worst rule. If $R < W$ and $C_W < W$ in the new Simplex also, reflect B across the centroid of N and W (denoted P') with a coefficient of -2. If the new point $S \geq W$, then reject N (which could be near a local optimum). If $S < W$, reflect B across P' with a coefficient of 1, and contract if necessary. In the absence of improvement, take B as the optimum.

Choice of initial vertices

The performance of a Simplex optimization depends, to some extent, on the size, orientation and position on the initial vertices. In general, a large Simplex is more efficient in the early stage of a search, as it spans a wider area on the response surface. When the initial Simplex is too small, time is wasted in expanding the design to find the region of the optimum and then contracting it to locate the optimum. Too large a Simplex will not work; the initial vertex should be allowed to reflect once. The starting points are usually default settings, unless

practical reasons justify a particular choice. For instance, initial vertices may be points where the response is known, points that correspond to preferred starting conditions, or points that provide desirable information. Alternatively, an algorithm may be used to standardize the initial Simplex. The *tilted algorithm* leads to an equilateral design (in two dimensions, a triangle) of controllable initial step size. The *corner algorithm* yields a set of orthogonal vertices that fit in the corner defined by the axes, allowing to change one variable at a time. The corner algorithm is generally preferred over the tilted algorithm.

Effects of noise and outliers

The Simplex will wander if response differences among vertices are of the same order as the uncertainty in the response. An estimate of this uncertainty can be obtained by replicating the best and worst vertices before initiating the first step.

An erroneously low response will be rejected within two iterations, and is of little consequence save for a temporary disturbance in the direction of progression. An erroneously high response, however, may cause the Simplex to converge around a false optimum. To prevent this situation, the following rule has been proposed by Walters *et al.*: the response at a vertex that has been in a n -dimensional Simplex for $(n+3)$ steps without rejection should be re-evaluated. It is also recommended to monitor stability by periodically measuring the response at a reference point (usually the best vertex of the initial Simplex). A new Simplex should be initialized following appreciable change in the response surface.

Appendix X - Table 1: Heat and Mass Balance and Soil Treatment Capacity for a Plasma Afterburner

Heat Balance

Basis: 1 kg wet soil

Afterburner T (°C)		1371	(2500°F)		
		Thermal desorption		Conventional incineration	
		fuel oil	nat. gas	fuel oil	nat. gas
Kiln gas (kgmol)		0.030	0.029	0.073	0.070
	% CO2	6.5%	4.5%	9.8%	6.9%
	% H2O	52.1%	57.0%	27.3%	34.6%
	% O2	1.8%	0.9%	2.7%	1.4%
	% N2	39.7%	37.5%	60.2%	57.1%
	Initial T (°C)	260	260	1010	1010
	Final T (°C)	1371	1371	1371	1371
Cp (kJ/kgmolK)	CO2	51.10	51.10	57.22	57.22
	H2O	41.85	41.85	45.82	45.82
	Air	32.71	32.71	34.50	34.50
Enthalpy rise (kJ)	CO2	109	76	148	101
	H2O	721	779	330	403
	O2	19	10	24	12
	N2	430	401	549	501
	Total	1280	1265	1052	1016
Torch gas (scm/h dry air)		135	135	135	135
	(kgmol/h dry air)	5.615	5.615	5.615	5.615
	Initial T (°C)	10	10	10	10
	Final T (°C)	1371	1371	1371	1371
	Cp (kJ/kgmolK)	32.02	32.02	32.02	32.02
	Enthalpy rise (kJ/h)	244697	244697	244697	244697
Calculation of the soil treatment capacity					
	Torch power rating (kW)	1200	1200	1200	1200
	Operating power (kW)	1000	1000	1000	1000
	Overall thermal efficiency	75%	75%	75%	75%
	Effective power (kW)	750	750	750	750
	Available enthalpy (kJ/h)	2455303	2455303	2455303	2455303
	Soil treatment capacity (kg/h)	1919	1941	2334	2417
Mass balance and output composition					
Output (kgmol/h)	CO2	3.697	2.594	16.752	11.768
	H2O	29.766	32.501	46.642	58.842
	O2	2.185	1.697	5.736	3.527
	N2	27.135	25.846	107.298	101.573
	total	62.78	62.64	176.43	175.71
	(scm/h)	1535	1532	4314	4297
	(scfh)	54218	54093	152360	151739
	(scm/min.)	25.6	25.5	71.9	71.6
	(scfm)	903.6	901.6	2539.3	2529.0
Composition	CO2	5.9%	4.1%	9.5%	6.7%
	H2O	47.4%	51.9%	26.4%	33.5%
	O2	3.5%	2.7%	3.3%	2.0%
	N2	43.2%	41.3%	60.6%	57.8%

Appendix X - Table 2: Heat and Mass Balance for a Fuel Oil Afterburner

Basis: soil treatment capacity determined for a plasma afterburner (Table 1)
 Assumptions: fuel oil #2, air fraction of 1.2

		Thermal desorption		Conventional incineration	
		fuel oil	nat. gas	fuel oil	nat. gas
Heat balance and fuel requirement					
Capacity	(kg soil/h)	1919	1941	2334	2417
Enthalpy rise	(kJ/h)	2455303	2455303	2455303	2455303
Heat available	(Btu/gal.)	36706	36706	36706	36706
at 2500°F	(kJ/gal.)	38728	38728	38728	38728
Fuel required	(gal./h)	63.399	63.399	63.399	63.399
Mass balance and output composition					
Secondary combustion gas	(lbmol/gal.) (lbmol/h)				
H2O	0.486	30.81	30.81	30.81	30.81
CO2	0.551	34.92	34.92	34.92	34.92
N2	3.382	214.40	214.40	214.40	214.40
O2	0.150	9.50	9.50	9.50	9.50
	(kgmol/h)				
H2O		13.97	13.97	13.97	13.97
CO2		15.84	15.84	15.84	15.84
N2		97.25	97.25	97.25	97.25
O2		4.31	4.31	4.31	4.31
Kiln gas	(kgmol/kg soil)	0.030	0.029	0.073	0.070
H2O		0.016	0.017	0.020	0.024
CO2		0.002	0.001	0.007	0.005
N2		0.012	0.011	0.044	0.040
O2		0.001	0.000	0.002	0.001
	(kgmol/h)	57.17	57.02	170.81	170.09
H2O		29.77	32.50	46.64	58.84
CO2		3.70	2.59	16.75	11.77
N2		22.70	21.41	102.86	97.14
O2		1.01	0.52	4.56	2.35
Afterburner output	(kgmol/h)				
H2O		43.74	46.47	60.61	72.82
CO2		19.53	18.43	32.59	27.61
N2		119.95	118.66	200.11	194.39
O2		5.31	4.83	8.87	6.66
total	(kgmol/h)	188.5	188.4	302.2	301.5
	(scm/h)	4610	4607	7390	7372
	(scfh)	162818	162694	260960	260339
	(scm/min.)	76.8	76.8	123.2	122.9
	(scfm)	2713.6	2711.6	4349.3	4339.0
Composition	H2O	23.2%	24.7%	20.1%	24.2%
	CO2	10.4%	9.8%	10.8%	9.2%
	N2	63.6%	63.0%	66.2%	64.5%
	O2	2.8%	2.6%	2.9%	2.2%

Appendix X - Table 3: Heat and Mass Balance for a Natural Gas Afterburner

Basis: soil treatment capacity determined for a plasma afterburner (Table 1)

Assumptions: natural gas, air fraction of 1.1

		Thermal desorption		Conventional incineration	
		fuel oil	nat. gas	fuel oil	nat. gas
Heat balance and gas requirement					
Capacity	(kg soil/h)	1919	1941	2334	2417
Enthalpy rise	(kJ/h)	2455303	2455303	2455303	2455303
Heat available	(Btu/scf)	265	265	265	265
at 2500°F	(kJ/scf)	280	280	280	280
Gas required	(scf/h)	8781.64	8781.64	8781.64	8781.64
Mass balance and output composition					
Secondary combustion gas	(lbmol/scf)	(lbmol/h)			
H2O	0.006	50.22	50.22	50.22	50.22
CO2	0.003	22.75	22.75	22.75	22.75
N2	0.021	187.83	187.83	187.83	187.83
O2	0.001	4.54	4.54	4.54	4.54
		(kgmol/h)			
H2O		22.78	22.78	22.78	22.78
CO2		10.32	10.32	10.32	10.32
N2		85.20	85.20	85.20	85.20
O2		2.06	2.06	2.06	2.06
Kiln gas	(kgmol/kg soil)	0.030	0.029	0.073	0.070
H2O		0.016	0.017	0.020	0.024
CO2		0.002	0.001	0.007	0.005
N2		0.012	0.011	0.044	0.040
O2		0.001	0.000	0.002	0.001
		(kgmol/h)			
H2O		57.17	57.02	170.81	170.09
CO2		29.77	32.50	46.64	58.84
N2		3.70	2.59	16.75	11.77
O2		22.70	21.41	102.86	97.14
		1.01	0.52	4.56	2.35
Afterburner output	(kgmol/h)				
H2O		52.55	55.28	69.42	81.62
CO2		14.02	12.92	27.07	22.09
N2		107.90	106.61	188.05	182.34
O2		3.06	2.58	6.62	4.41
total	(kgmol/h)	177.5	177.4	291.2	290.5
		(scm/h)			
		4341	4338	7120	7103
		(scfh)			
		153310	153185	251452	250831
		(scm/min.)			
		72.4	72.3	118.7	118.4
		(scfm)			
		2555.2	2553.1	4190.9	4180.5
Composition	H2O	29.6%	31.2%	23.8%	28.1%
	CO2	7.9%	7.3%	9.3%	7.6%
	N2	60.8%	60.1%	64.6%	62.8%
	O2	1.7%	1.5%	2.3%	1.5%

Appendix XI - Table 1: Heat and Mass Balance for Fuel Oil #2 Combustion

Basis: 1 gal. fuel oil

Total air fraction	1.1	1.2	1.3	
Air moisture (lb H ₂ O/lb dry air)	0.013	0.013	0.013	Assumed
Total air (lb/gal)	114.640	125.062	135.483	Reported (1)
Dry air (lb/gal)	113.169	123.457	133.744	
Air moisture (lb/gal)	1.471	1.605	1.739	
Dry gas (lb/gal)	115.115	125.537	135.958	Reported (1)
Water (lb/gal)	8.615	8.751	8.886	Reported (1)

Note: mass figures in subsequent rows are expressed in lbmol/gal

Dry air	3.9240	4.2808	4.6375
Air moisture	0.0817	0.0891	0.0965
Stoichiometric air	3.5673	3.5673	3.5673
O ₂	0.7491	0.7491	0.7491
N ₂	2.8182	2.8182	2.8181
Excess air	0.3567	0.7135	1.0702
O ₂	0.0749	0.1498	0.2247
N ₂	0.2818	0.5636	0.8454

Assumptions: hydrocarbon fuel, complete combustion

An oxygen balance determines the dry gas composition and the average molecular weight.

Total water	0.478	0.486	0.493
Water from combustion	0.397	0.397	0.397
Stoichiometric dry gas			
CO ₂	0.551	0.551	0.551
N ₂	2.818	2.818	2.818
Excess dry gas			
O ₂	0.075	0.150	0.225
N ₂	0.282	0.564	0.845
Total dry gas	3.726	4.082	4.439
CO ₂	14.8%	13.5%	12.4%
O ₂	2.0%	3.7%	5.1%
N ₂	83.2%	82.8%	82.5%
MW	30.45	30.31	30.19
(lb/gal)	113.432	123.717	134.003
Error relative to figures reported by Brunner	-1.5%	-1.4%	-1.4%
O ₂ fraction reported in Perry's (Fig. 9-30)	2.0%	3.7%	5.2%

(1) Brunner 1996 (Table 9.4)

Appendix XI - Table 2: Heat and Mass Balance for Natural Gas Combustion

Basis: 1 scf natural gas

Total air fraction	1.05	1.10	1.15	
Air moisture (lb H ₂ O/lb dry air)	0.013	0.013	0.013	Assumed
Total air (lb/scf)	0.755	0.791	0.827	Reported (1)
Dry air (lb/scf)	0.745	0.781	0.816	
Air moisture (lb/scf)	0.010	0.010	0.011	
Dry gas (lb/scf)	0.712	0.748	0.784	Reported (1)
Water (lb/scf)	0.103	0.103	0.104	Reported (1)

Note: mass figures in subsequent rows are expressed in lbmol/scf

Dry air	0.02584	0.02708	0.02831
Air moisture	0.00054	0.00056	0.00059
Stoichiometric air	0.02461	0.02461	0.02462
O ₂	0.00517	0.00517	0.00517
N ₂	0.01944	0.01944	0.01945
Excess air	0.00123	0.00246	0.00369
O ₂	0.00026	0.00052	0.00078
N ₂	0.00097	0.00194	0.00292

Assumptions: hydrocarbon fuel, complete combustion

An oxygen balance determines the dry gas composition and the average molecular weight.

Total water	0.006	0.006	0.006
Water from combustion	0.005	0.005	0.005
Stoichiometric dry gas			
CO ₂	0.003	0.003	0.003
N ₂	0.019	0.019	0.019
Excess dry gas			
O ₂	0.000	0.001	0.001
N ₂	0.001	0.002	0.003
Total dry gas	0.023	0.024	0.026
CO ₂	11.1%	10.6%	10.0%
O ₂	1.1%	2.1%	3.0%
N ₂	87.8%	87.3%	87.0%
MW	29.82	29.78	29.72
(lb/scf)	0.693	0.729	0.764
Error relative to figures reported by Brunner	-2.6%	-2.5%	-2.5%
O ₂ fraction reported in Perry's (Fig. 9-30)	1.1%	2.1%	3.1%

(1) Brunner 1996 (Table 9.4)

Appendix XI - Table 3: Heat and Mass Balance for Primary Soil Incineration

Basis: 1 kg wet soil

Neglected: heat of vaporization and fuel value of combustible soil components

Mass of wet soil (kg)	1			
Moisture content (%)	25			
Kiln temperature (°C)	1010	(1850°F)		
Initial temperature (°C)	10	(50°F)		
Mass of dry soil (kg)	0.75			
Dry soil Cp (kJ/kg.K)	1		average over 100-1000°C	
Mass of water (kg)	0.25			
Mass of water (kgmol)	0.01387347			
Heat of evap. (kJ/kgmol)	40669		@ 1 atm	
Water Cp (kJ/kgmol.K)	75.7		average over 10-100°C	
Steam Cp (kJ/kgmol.K)	39.17		average over 100-1010°C	
Heat balance				
		(kJ)		
Dry soil heating		750		
Water heating		95		
Water vapourization		564		
Steam heating		495		
Heat requirement	1903.256		1803.944 Btu	
Losses (%)	0%			
Fuel requirement (gal.)	0.0283		63718 Btu/gal.	Heat available at the kiln temperature (Brunner 1996, Tables 9.4 & 9.5)
Gas requirement (scf)	4.040		447 Btu/scf	

Heat supply

Assumption: 0.013 lb moisture/lb dry air

		fuel oil #2	natural gas
Air fraction		1.2	1.1
Mass air (lb)		3.541	3.20
Comb. T° (°F)		1850	1850
Heat available (Btu)		1804	1804

Gas volumes and composition

Assumptions: hydrocarbon fuel, complete combustion

Neglected: vaporization and combustion products of soil components

Dry gas	(lb)		3.554		3.022
	MW	30.31		29.78	
	(lbmol)		0.117		0.101
	(kgmol)		0.053		0.046
	CO2	13.5%	0.007	10.6%	0.005
	N2	82.8%	0.044	87.3%	0.040
	O2	3.7%	0.002	2.1%	0.001
Water					
	combustion	(lb)	0.243		0.416
		(lbmol)	0.013		0.023
		(kgmol)	0.006		0.010
	soil moisture	(kgmol)	0.014		0.014
Total gas output (kgmol)					
	CO2	9.8%	0.007	6.9%	0.005
	N2	60.2%	0.044	57.1%	0.040
	O2	2.7%	0.002	1.4%	0.001
	H2O	27.3%	0.020	34.6%	0.024
	Total		0.073		0.070
	(scm)		1.789		1.721
	(scf)		63.195		60.782

Appendix XI - Table 4: Heat and Mass Balance for Primary Soil Desorption

Basis: 1 kg wet soil

Neglected: heat of vapourization and fuel value of combustible soil components

Mass of wet soil (kg)	1			
Moisture content (%)	25			
Kiln temperature (°C)	260	(500°F)		
Initial temperature (°C)	10	(50°F)		
Mass of dry soil (kg)	0.75			
Dry soil Cp (kJ/kg.K)	1		average over 100-1000°C	
Mass of water (kg)	0.25			
Mass of water (kgmol)	0.01387347			
Heat of evap. (kJ/kgmol)	40669		@ 1 atm	
Water Cp (kJ/kgmol.K)	75.7		average over 10-100°C	
Steam Cp (kJ/kgmol.K)	35.2		average over 100-260°C	
Heat balance		(kJ)		
Dry soil heating	187.500			
Water heating	94.520			
Water vapourization	564.220			
Steam heating	78.135			
Heat requirement	924.376	876.142	Btu	
Losses (%)	0%			
Fuel requirement (gal.)	0.008	115277	Btu/gal.	Heat available at
Gas requirement (scf)	1.109	790	Btu/scf	the kiln temperature
				(Brunner 1996,
				Tables 9.4 & 9.5)

Heat supply

Assumption: 0.013 lb moisture/lb dry air

		fuel oil #2	natural gas
Air fraction		1.200	1.100
Mass air (lb)		0.951	0.877
Combustion T (°F)		500	500
Heat available (Btu)		876.142	876.142

Gas volumes and composition

Assumptions: hydrocarbon fuel, complete combustion

Neglected: vapourization and combustion products of soil components

Dry gas	(lb)	0.954		0.830
	MW	30.31	29.78	
	(lbmol)	0.031		0.028
	(kgmol)	0.014		0.013
	CO2	13.5%	10.6%	0.001
	N2	82.8%	87.3%	0.011
	O2	3.7%	2.1%	0.000
Water				
combustion	(lb)	0.065		0.114
	(lbmol)	0.004		0.006
	(kgmol)	0.002		0.003
soil moisture	(kgmol)	0.014		0.014
Total gas output (kgmol)				
	CO2	6.5%	4.5%	0.001
	N2	39.7%	37.5%	0.011
	O2	1.8%	0.9%	0.000
	H2O	52.1%	57.0%	0.017
	Total	0.030		0.029
	(scm)	0.729		0.719
	(scf)	25.729		25.377

Appendix XII Fuel Value Estimation for a PCB Dielectric Fluid

Du Long's approximation is a standard method for estimating the heating value of hydrocarbon fuels (Brunner 1996). Its applicability to non-conventional fuels such as chlorinated compounds is questionable. Accordingly, the following calculation is treated as an order-of-magnitude approximation.

Du Long's correlation for the high fuel value in Btu/lb is expressed as:

$$Q = 14544C + 62028(H_2 - 0.125O_2) + 4050S \quad (\text{equation XII-1})$$

where C, H₂, O₂, and S are the weight fractions of these components. If an inert is present, these fractions add up to (1 - inert fraction). For chlorinated aromatic hydrocarbons, two calculation methods were used: (1) treating chlorine as an inert, and (2) treating chlorine as an inert and subtracting the hydrogen released as HCl (unavailable for combustion). Table XII-1 summarizes the results for tetrachlorobiphenyl (C₁₂H₆Cl₄), trichlorobenzene (C₆H₃Cl₃), and a typical dielectric fluid blend of 60 wt% tetrachlorobiphenyl and 40 wt% trichlorobenzene.

Table XII-1: Fuel Value Approximations (Q) Using DuLong's Formula

Compound	MW	C wt frac.	H ₂ wt frac.	Cl wt frac.	Q (1) (MJ/kgmol)	Q (2) (MJ/kgmol)
C ₁₂ H ₆ Cl ₄	291.991	0.494	0.021	0.486	5 750	5 170
C ₆ H ₃ Cl ₃	181.449	0.397	0.017	0.586	2 880	2 440
Blend	234.730				4 260	3 750

Comparison with the assumed combustion heat

The heat balance assumes a contribution of 1500 kW from liquid waste combustion. This assumption assigns the waste a fuel value that depends on treatment capacity. Assigned values were calculated for pure tetrachlorobiphenyl and for the dielectric blend, based on the treatment capacity obtained with these wastes.

Table XII-2: Comparison of Estimated and Assumed Fuel Values

Compound	Capacity (kg/h)	Q (2) (kJ/kg)	Assigned Q (kJ/kg)	Difference
C ₁₂ H ₆ Cl ₄	589.7	17690	9315	-47%
Blend	633.4	13440	8525	-37%

If DuLong's approximation applies, more heat is available from liquid waste combustion than was assumed in the heat balance. In the case of the dielectric fluid, the heat balance underestimates the contribution of the waste by nearly 40%. Due to uncertainty regarding the applicability of DuLong's approximation, the assumption is deemed reasonable. It prevents overestimation of the waste treatment capacity, and helps balance heat losses unaccounted for in the process model.

**Appendix XIII - Table 1: Operating Costs Common to All Options, in 1997 US\$
(Douglas 1988)**

Manufacturing costs

Operating labour (one technician, 24 hrs/day)	230000	(Soucy 1999)
Direct supervision & clerical labour (5% operating labour)	11500	
Maintenance (common base)	80000	
Labour, supervision & maintenance	321500	
Plant overhead (40% of labour, supervision & maintenance)	128600	

General expenses

Administrative expenses, executive salaries, legal costs, communications (5% of labour, supervision & maintenance)	16075	
--	-------	--

Common operating costs **386,175**

**Appendix XIII - Table 2: Case I - Plasma Afterburner Option
Investment Summary, in 1997 US\$
(Douglas 1988)**

Equipment cost based on correlations

	Unit only	Unit with instrumentation, controls and equipment	Installed cost	
primary kiln (1)		263840	369376	
afterburner (2)		39233	54926	2.8%
plasma system (3)			1500000	77.4%
quench tank (2)	13832		30015	1.5%
quench pump (4)		2263	3169	0.2%
venturi, cooler & pump (1)		144908	202871	10.5%
venturi fan (4)		47704	66786	3.4%
absorber (1)	28351		61544	3.2%
absorber pump (4)		2263	3169	0.2%
absorber fan (4)		10620	14858	0.8%
Total (afterburner and gas cleaning)			1,937,347	100%
Total (gas cleaning only)			382,421	19.7%

Total capital investment	actual value	adjusted value * (basis for some factored estimates)	
Onsite direct costs	1937347	737347	
Offsite direct costs	331806		45% (onsite costs)
Indirect costs	267288		25% (onsite + offsite costs)
Fixed capital investment (FCI)	2536442	1336442	direct + indirect costs
Total capital investment (TCI)	2,536,442	1,336,442	<u>Assumptions</u> Additional working capital and start-up costs are equivalent for all alternatives.

- (1) Vatajuk and Neveril 1984
- (2) Douglas 1998
- (3) Mustoe 1999, Nelson 1999
- (4) ASPEN

**Appendix XIII - Table 3: Case I - Plasma Afterburner Option
Operating Cost Summary, in 1997 US\$
(Douglas 1988)**

Cost of utilities	fuel oil #2	170 \$/m3	0.64352 \$/gal.			
in 1996 US \$	electricity	0.08 \$/kWh				
(Turton et al. 1998)	water	0.0067 \$/scm	0.000121 \$/kgmol			
	air	0.023 \$/scm				
	oxygen	0.01552 \$/scft	0.548084 \$/scm			
Utility consumption			hourly use			
(ASPEN)		electricity	water	fuel oil	oxygen	air
		(kWh)	(kgmol)	(gal.)	(scm)	(scm)
	afterburner					
	plasma gas				42.75	135
	plasma power	1000				
	fan power	5.03				
	quench					
	water		167.49			
	pump power	1.31				
	venturi					
	water		493.01			
	pump power	1.31				
	fan power	5.53				
	absorber					
	water		677.02			
	pump power	1.31				
	fan power	5.53				
Total (afterburner & gas cleaning)		1020.01	1337.51	0.00	42.75	135.00
Hourly costs (1996 US\$)		61.20	0.16	0.00	23.43	3.11
Hourly costs (1997 US\$)		61.92	0.16	0.00	23.71	3.14
Total (gas cleaning only)		14.98	1337.51	0.00	0.00	0.00
Hourly costs (1996 US\$)		0.90	0.16	0.00	0.00	0.00
Hourly costs (1997 US\$)		0.91	0.16	0.00	0.00	0.00
Hourly utility costs	total	electricity	water	fuel oil	oxygen	air
afterburner & gas cleaning	88.93	69.6%	0.2%	0.0%	26.7%	3.5%
gas cleaning only	1.07	1.21% of total				
without oxygen	65.23	73.3% of total				
Total operating costs						
Annual utility costs	with oxygen in the plasma gas	without oxygen in the plasma gas				
(8400 h/yr)	747038	547902	63.9%	56.5%		
Maintenance (6% FCI*)	80186	80186	6.9%	8.3%		
Supplies (0.9% FCI*)	12028	12028	1.0%	1.2%		
Fixed charges (3% FCI)	76093	76093	6.5%	7.8%		
Depreciation (10% TCI)	253644	253644	21.7%	26.2%		
Total operating costs	1,168,990	969,854	100%	100%		

**Appendix XIII - Table 4: Case I - Fuel Afterburner Option
Investment Summary, in 1997 US\$
(Douglas 1988)**

Equipment cost based on correlations

	Unit only	Unit with instrumentation, controls and equipment	Installed cost	
primary kiln (1)		263840	369376	
afterburner (1)		201760	282464	37.9%
quench tank (2)	18753		40694	5.5%
quench pump (3)		2437	3412	0.5%
venturi, cooler & pump (1)		173431	242804	32.6%
venturi fan (3)		55364	77510	10.4%
absorber (1)	35978		78072	10.5%
absorber pump (3)		2612	3656	0.5%
absorber fan (3)		12361	17306	2.3%
Total (afterburner and gas cleaning)			745,918	100%
Total (gas cleaning only)			463,454	62.1%

Total capital investment

Onsite direct costs	745918	
Offsite direct costs	335663	45% (onsite costs)
Indirect costs	270395	25% (onsite + offsite costs)
Fixed capital investment (FCI)	1351977	direct + indirect costs

Total capital investment (TCI)	1,351,977	Assumptions
		Additional working capital and start-up costs are equivalent for all alternatives.

- (1) Vatajuk and Neveril 1984
- (2) Douglas 1988
- (3) ASPEN

**Appendix XIII - Table 5: Case I - Fuel Afterburner Option
Operating Cost Summary, in 1997 US\$
(Douglas 1988)**

Cost of utilities	fuel oil #2	170 \$/m3	0.64352 \$/gal.			
in 1996 US \$	electricity	0.06 \$/kWh				
(Turton et al. 1998)	water	0.0067 \$/scm	0.000121 \$/kgmol			
	air	0.023 \$/scm				
	oxygen	0.01552 \$/scft	0.548084 \$/scm			
Utility consumption			hourly use			
(ASPEN)		electricity	water	fuel oil	oxygen	air
		(kWh)	(kgmol)	(gal.)	(scm)	(scm)
	afterburner					
	fuel oil			63.40		
	fan power	8.62				
	quench tank					
	water		281.27			
	pump power	1.31				
	venturi, cooler & pump					
	water		835.57			
	pump power	1.75				
	fan power	10.12				
	absorber					
	water		1260.00			
	pump power	2.62				
	fan power	10.12				
	Total (afterburner & gas cleaning)	34.53	2376.85	63.40	0.00	0.00
	Hourly costs (1996 US\$)	2.07	0.29	40.80	0.00	0.00
	Hourly costs (1997 US\$)	2.10	0.29	41.28	0.00	0.00
	Total (gas cleaning only)	25.91	2376.85	0.00	0.00	0.00
	Hourly costs (1996 US\$)	1.55	0.29	0.00	0.00	0.00
	Hourly costs (1997 US\$)	1.57	0.29	0.00	0.00	0.00
Hourly utility costs		total	electricity	water	fuel oil	oxygen
afterburner & gas cleaning	43.67	4.8%	0.7%	94.5%	0.0%	0.0%
gas cleaning only	1.86	4.27%	of total			
Total operating costs						
Annual utility costs	366799	57.7%				
(8400 h/yr)						
Maintenance (6% FCI)	81119	12.8%				
Supplies (0.9% FCI)	12168	1.9%				
Fixed charges (3% FCI)	40559	6.4%				
Depreciation (10% TC)	135198	21.3%				
Total operating costs	635,842	100%				

**Appendix XIII - Table 6: Case I - Primary Chamber Unit
Investment Summary, in 1997 US\$
(Douglas 1988)**

Equipment cost based on correlations

	Unit only	Unit with instrumentation, controls and equipment	Installed cost
incineration kiln at 1010°C (1)		263840	369376

Total capital investment

Onsite direct costs	369376	
Offsite direct costs	166219	45% (onsite costs)
Indirect costs	133899	25% (onsite + offsite costs)
Fixed capital investment	669495	direct + indirect costs

Total capital investment	669,495	<u>Assumptions</u> Working capital and start-up costs are equivalent for all alternatives.
---------------------------------	----------------	---

(1) Vatauvuk and Neveril 1984

**Appendix XIII - Table 7: Case I - Primary Chamber Unit
Operating Cost Summary, in 1997 US\$
(Douglas 1988)**

Cost of utilities in 1996 US \$ (Turton et al. 1998)	fuel oil #2	170 \$/m3	0.64352 \$/gal.
	electricity	0.06 \$/kWh	
	water	0.0067 \$/scm	0.000121 \$/kgmol
	air	0.023 \$/scm	
	oxygen	0.01552 \$/scft	0.548084 \$/scm

Utility consumption

	electricity (kWh)	water (kgmol)	<u>hourly use</u> fuel oil (gal.)	oxygen (scm)	air (scm)
incineration kiln (1010°C)			69.72		
Total	0.00	0.00	69.72	0.00	0.00
Hourly costs (1996 US\$)	0.00	0.00	44.87	0.00	0.00
Hourly costs (1997 US\$)	0.00	0.00	45.39	0.00	0.00

Hourly utility costs
total 45.39

Fixed Capital Investment (FCI)	669495
Total Capital Investment (TCI)	669495

Total operating costs

Annual utility costs (8400 h/yr)	381316	74.1%
Maintenance (6% FCI)	40170	7.8%
Supplies (0.9% FCI)	6025	1.2%
Fixed charges (3% FCI)	20085	3.9%
Depreciation (10% TCI)	66949	13.0%
Total operating costs	514,545	100%

**Appendix XIII - Table 8: Case II - Plasma Afterburner Option
Investment Summary, in 1997 US\$
(Douglas 1988)**

Equipment cost based on correlations

	Unit only	Unit with instrumentation, controls and equipment	Installed cost	
primary kiln (1)		237974	333163	
afterburner (2)		39233	54926	3.0%
plasma system (3)			1500000	81.0%
quench tank (2)	7725		16762	0.9%
quench pump (4)		2263	3169	0.2%
venturi, cooler & pump (1)		118149	165408	8.9%
venturi fan (4)		41785	58498	3.2%
absorber (1)	16977		36840	2.0%
absorber pump (4)		2263	3169	0.2%
absorber fan (4)		9227	12918	0.7%
Total (afterburner and gas cleaning)			1,851,691	100%
Total (gas cleaning only)			296,765	16.0%

Total capital investment	actual value	adjusted value * (basis for some factored estimates)	
Onsite direct costs	1851691	651691	
Offsite direct costs	293261		45% (onsite costs)
Indirect costs	236238		25% (onsite + offsite costs)
Fixed capital investment (FCI)	2381190	1181190	direct + indirect costs
Total capital investment (TCI)	2,381,190	1,181,190	Assumptions Additional working capital and start-up costs are equivalent for all alternatives.

- (1) Vatavuk and Neveril 1984
- (2) Douglas 1998
- (3) Mustoe 1999, Nelson 1999
- (4) ASPEN

**Appendix XIII - Table 9: Case II - Plasma Afterburner Option
Operating Cost Summary, in 1997 US\$
(Douglas 1988)**

Cost of utilities in 1996 US \$ (Turton et al. 1998)	fuel oil #2	170 \$/m ³	0.64352 \$/gal.			
	electricity	0.06 \$/kWh				
	water	0.0067 \$/scm	0.000121 \$/kgmol			
	air	0.023 \$/scm				
	oxygen	0.01552 \$/scf	0.548084 \$/scm			
Utility consumption (ASPEN)				hourly use		
		electricity (kWh)	water (kgmol)	fuel oil (gal.)	oxygen (scm)	air (scm)
	afterburner					
	torch gas				42.75	135
	power	1000				
	fan power	1.83				
	quench tank					
	water		61.38			
	pump power	1.31				
	venturi, cooler & pump					
	water		177.97			
	pump power	1.31				
	fan power	1.47				
	absorber					
	water		172.15			
	pump power	1.31				
	fan power	1.47				
	Total (afterburner & gas cleaning)	1008.70	411.50	0.00	42.75	135.00
	Hourly costs (1996 US\$)	60.52	0.05	0.00	23.43	3.11
	Hourly costs (1997 US\$)	61.23	0.05	0.00	23.71	3.14
	Total (gas cleaning only)	6.87	411.50	0.00	0.00	0.00
	Hourly costs (1996 US\$)	0.41	0.05	0.00	0.00	0.00
	Hourly costs (1997 US\$)	0.42	0.05	0.00	0.00	0.00
Hourly utility costs		total	electricity	water	fuel oil	oxygen
	afterburner & gas cleaning	88.13	69.5%	0.1%	0.0%	26.9%
	gas cleaning only	0.47	0.5% of total			
	without oxygen	63.68	73.1% of total			
Total operating costs						
		with oxygen in the plasma gas		without oxygen in the plasma gas		
Annual utility costs (8400 h/yr)		740321	65.4%	541185	58.1%	
Maintenance (6% FCI)		70871	6.3%	70871	7.6%	
Supplies (0.9% FCI)		10631	0.9%	10631	1.1%	
Fixed charges (3% FCI)		71436	6.3%	71436	7.7%	
Depreciation (10% TCI)		238119	21.0%	238119	25.5%	
Total operating costs		1,131,378	100%	932,242	100%	

**Appendix XIII - Table 10: Case II - Fuel Afterburner Option
Investment Summary, in 1997 US\$
(Douglas 1988)**

Equipment cost based on correlations

	Unit only	Unit with instrumentation, controls and equipment	Installed cost	
primary kiln (1)		237974	333163	
afterburner (1)		189689	265565	40.5%
quench tank (2)	14321		31077	4.7%
quench pump (3)		2263	3169	0.5%
venturi, cooler & pump (1)		147329	206261	31.5%
venturi fan (3)		47704	66786	10.2%
absorber (1)	29608		64248	9.8%
absorber pump (3)		2263	3169	0.5%
absorber fan (3)		10620	14868	2.3%
Total (afterburner and gas cleaning)			655,143	100%
			389,578	59.5%

Total capital investment

Onsite direct costs	655143	
Offsite direct costs	294814	45% (onsite costs)
Indirect costs	237489	25% (onsite + offsite costs)
Fixed capital investment (FCI)	1187446	direct + indirect costs

Total capital investment (TCI)	1,187,446	<u>Assumptions</u> Additional working capital and start-up costs are equivalent for all alternatives.
---------------------------------------	------------------	--

- (1) Vataavuk and Neveril 1984
- (2) Douglas 1998
- (3) ASPEN

**Appendix XIII - Table 11: Case II - Fuel Afterburner Option
Operating Cost Summary, in 1997 US\$
(Douglas 1988)**

Cost of utilities	fuel oil #2	170 \$/m3	0.64352 \$/gal.			
in 1996 US \$	electricity	0.06 \$/kWh				
(Turton et al. 1998)	water	0.0067 \$/scm	0.000121 \$/kgmol			
	air	0.023 \$/scm				
	oxygen	0.01552 \$/scft	0.548084 \$/scm			
Utility consumption				hourly use		
(ASPEN)		electricity	water	fuel oil	oxygen	air
		(kWh)	(kgmol)	(gal.)	(scm)	(scm)
	afterburner					
	fuel oil			63.40		
	fan power	5.43				
	quench tank					
	water		177.13			
	pump power	1.31				
	venturi, cooler & pump					
	water		523.32			
	pump power	1.31				
	fan power	6.15				
	absorber					
	water		756.13			
	pump power	1.31				
	fan power	6.15				
	Total (afterburner & gas cleaning)	21.67	1456.57	63.40	0.00	0.00
	Hourly costs (1996 US\$)	1.30	0.18	40.80	0.00	0.00
	Hourly costs (1997 US\$)	1.32	0.18	41.28	0.00	0.00
	Total (gas cleaning only)	16.23	1456.57	0.00	0.00	0.00
	Hourly costs (1996 US\$)	0.97	0.18	0.00	0.00	0.00
	Hourly costs (1997 US\$)	0.99	0.18	0.00	0.00	0.00
Hourly utility costs		total	electricity	water	fuel oil	oxygen
	afterburner & gas cleaning	42.77	3.1%	0.4%	96.5%	0.0%
	gas cleaning only	1.16	2.72% of total			
Total operating costs						
Annual utility costs		359294	60.3%			
(8400 h/yr)						
Maintenance (6% FCI)		71247	12.0%			
Supplies (0.9% FCI)		10687	1.8%			
Fixed charges (3% FCI)		35623	6.0%			
Depreciation (10% TCI)		118745	19.9%			
Total operating costs		595,595	100%			

**Appendix XIII - Table 12: Case II - Primary Chamber Unit
Investment Summary, in 1997 US\$
(Douglas 1988)**

Equipment cost based on correlations

	Unit only	Unit with instrumentation, controls and equipment	Installed cost
desorption kiln at 260°C (1)		237974	333163

Total capital investment

Onsite direct costs	333163	
Offsite direct costs	149923	45% (onsite costs)
Indirect costs	120772	25% (onsite + offsite costs)
Fixed capital investment	603858	direct + indirect costs

Total capital investment	603,858	<u>Assumptions</u> Working capital and start-up costs are equivalent for all alternatives.
---------------------------------	----------------	---

(1) Vatajuk and Neveril 1984

**Appendix XIII - Table 13: Case II - Primary Chamber Unit
Operating Cost Summary, in 1997 US\$
(Douglas 1988)**

Cost of utilities in 1996 US \$ (Turton et al. 1998)	fuel oil #2	170 \$/m3	0.64352 \$/gal.		
	electricity	0.06 \$/kWh			
	water	0.0067 \$/scm	0.000121 \$/kgmol		
	air	0.023 \$/scm			
	oxygen	0.01552 \$/scf	0.548084 \$/scm		
Utility consumption			<u>hourly use</u>		
		electricity (kWh)	water (kgmol)	fuel oil (gal.)	oxygen (scm) air (scm)
desorption kiln (260°C)				14.58	
Total		0.00	0.00	14.58	0.00 0.00
Hourly costs (1996 US\$)		0.00	0.00	9.38	0.00 0.00
Hourly costs (1997 US\$)		0.00	0.00	9.49	0.00 0.00
Hourly utility costs					
total					9.49
Fixed Capital Investment (FCI)		603858			
Total Capital Investment (TCI)		603858			
Total operating costs					
Annual utility costs (8400 h/yr)		79742	39.9%		
Maintenance (6% FCI)		36231	18.1%		
Supplies (0.9% FCI)		5435	2.7%		
Fixed charges (3% FCI)		18116	9.1%		
Depreciation (10% TCI)		60386	30.2%		
Total operating costs		199,909	100%		

**Appendix XIII - Table 14: Case III - Plasma Furnace Option
Investment Summary, in 1997 US\$
(Douglas 1988)**

Equipment cost based on correlations

	Unit only	Unit with instrumentation, controls and equipment	Installed cost	
furnace (2)		70717	99004	5.0%
plasma system (3)			1500000	75.5%
quench tank (2)	13389		29055	1.5%
quench pump (4)		2263	3169	0.2%
venturi, cooler & pump (1)		142034	198848	10.0%
venturi fan (4)		50316	70442	3.5%
absorber (1)	30444		66064	3.3%
absorber pump (4)		2437	3412	0.2%
absorber fan (4)		11143	15600	0.8%
Total (afterburner and gas cleaning)			1,985,593	100%
Total (gas cleaning only)			386,588	19.5%

Total capital investment	actual value	adjusted value * (basis for some factored estimates)	
Onsite direct costs	1985593	785593	
Offsite direct costs	353517		45% (onsite costs)
Indirect costs	284777		25% (onsite + offsite costs)
Fixed capital investment (FCI)	2623887	1423887	direct + indirect costs
Total capital investment (TCI)	2,623,887	1,423,887	<u>Assumptions</u> Additional working capital and start-up costs are equivalent for all alternatives.

- (1) Vatauvak and Nevenil 1984
- (2) Douglas 1998
- (3) Mustoe 1999, Nelson 1999
- (4) ASPEN

**Appendix XIII - Table 15: Case III - Plasma Furnace Option
Operating Cost Summary, in 1997 US\$
(Douglas 1988)**

Cost of utilities in 1996 US \$ (Turton et al. 1998)	nat. gas	0.085 \$/scm				
	electricity	0.06 \$/kWh				
	water	0.0067 \$/scm	0.000121 \$/kgmol			
	air	0.023 \$/scm				
	oxygen	0.01552 \$/scf	0.548084 \$/scm			
Utility consumption (ASPEN)				hourly use		
		electricity (kWh)	water (kgmol)	nat. gas (scm)	oxygen (scm)	air (scm)
plasma furnace						
torch gas					42.75	135
power		1000				
fan power		4.86				
quench tank						
water			154.60			
pump power		1.31				
venturi, cooler & pump						
water			466.15			
pump power		1.31				
fan power		6.71				
absorber						
water			826.68			
pump power		1.75				
fan power		6.71				
Total (furnace & gas cleaning)		1022.65	1447.43	0.00	42.75	135.00
Hourly costs (1996 US\$)		61.36	0.17	0.00	23.43	3.11
Hourly costs (1997 US\$)		62.08	0.18	0.00	23.71	3.14
Total (gas cleaning only)		17.78	1447.43	0.00	0.00	0.00
Hourly costs (1996 US\$)		1.07	0.17	0.00	0.00	0.00
Hourly costs (1997 US\$)		1.08	0.18	0.00	0.00	0.00
Hourly utility costs	total	electricity	water	fuel oil	oxygen	air
furnace & gas cleaning	89.11	69.7%	0.2%	0.0%	26.6%	3.5%
gas cleaning only	1.26	1.4%				
without oxygen	65.40	73.4%				
Total operating costs						
		with oxygen in the plasma gas	without oxygen in the plasma gas			
Annual utility costs (8400 h/yr)	748495	53.0%	549360	55.6%		
Maintenance (6% FCI*)	85433	7.2%	85433	8.6%		
Supplies (0.9% FCI*)	12815	1.1%	12815	1.3%		
Fixed charges (3% FCI)	78717	6.6%	78717	8.0%		
Depreciation (10% TCI)	262389	22.1%	262389	26.5%		
Total operating costs	1,187,849	100%	988,714	100%		

**Appendix XIII - Table 16: Case III - Natural Gas Furnace Option
Investment Summary, in 1997 US\$
(Douglas 1988)**

Equipment cost based on correlations

	Unit only	Unit with instrumentation, controls and equipment	Installed cost	
natural gas furnace (2)	99817		216603	32.3%
quench tank (2)	17831		38693	5.8%
quench pump (4)		2263	3169	0.5%
venturi, cooler & pump (1)		167361	234305	34.9%
venturi fan (4)		55364	77510	11.6%
absorber (1)	36708		79657	11.9%
absorber pump (4)		2612	3656	0.5%
absorber fan (4)		12361	17306	2.6%
Total (afterburner and gas cleaning)			670,899	100%
Total (gas cleaning only)			454,297	67.7%

Total capital investment

Onsite direct costs	670899	
Offsite direct costs	301905	45% (onsite costs)
Indirect costs	243201	25% (onsite + offsite costs)
Fixed capital investment (FCI)	1216005	direct + indirect costs

Total capital investment (TCI)	1,216,005	Assumptions Additional working capital and start-up costs are equivalent for all alternatives.
---------------------------------------	------------------	--

- (1) Vatauvuk and Nevenil 1984
- (2) Douglas 1998
- (3) ASPEN

**Appendix XIII - Table 17: Case III - Natural Gas Furnace Option
Operating Cost Summary, in 1997 US\$
(Douglas 1988)**

Cost of utilities in 1996 US \$ (Turton et al. 1998)	nat. gas	0.085 \$/scm				
	electricity	0.06 \$/kWh				
	water	0.0067 \$/scm	0.000121 \$/kgmol			
	air	0.023 \$/scm				
	oxygen	0.01552 \$/scf	0.548084 \$/scm			
Utility consumption (ASPEN)				hourly use		
			electricity (kWh)	water (kgmol)	nat. gas (scm)	oxygen (scm)
					air (scm)	
	gas furnace					
	nat. gas				229.04	
	fan power		8.02			
	quench tank					
	water			255.17		
	pump power		1.31			
	venturi, cooler & pump					
	water			767.37		
	pump power		1.31			
	fan power		10.34			
	absorber					
	water			1288.60		
	pump power		1.75			
	fan power		10.34			
	Total (furnace & gas cleaning)		33.05	2311.14	229.04	0.00
	Hourly costs (1996 US\$)		1.98	0.28	19.47	0.00
	Hourly costs (1997 US\$)		2.01	0.28	19.70	0.00
	Total (gas cleaning only)		25.03	2311.14	0.00	0.00
	Hourly costs (1996 US\$)		1.50	0.28	0.00	0.00
	Hourly costs (1997 US\$)		1.52	0.28	0.00	0.00
Hourly utility costs	total					
furnace & gas cleaning	21.99	9.1%	1.3%	89.6%	0.0%	0.0%
gas cleaning only	1.80	8.2% of total				
Total operating costs						
Annual utility costs (8400 h/yr)	184688	43.3%				
Maintenance (6% FCI)	72960	17.1%				
Supplies (0.9% FCI)	10944	2.6%				
Fixed charges (3% FCI)	36480	8.5%				
Depreciation (10% TCI)	121601	28.5%				
Total operating costs	426,673	100%				

Appendix XIV Incremental Cash Flow Model
(Park et al. 1995)

Operating activities	Cash revenues	0
	- Expenses	- (total annual operating costs)
	operating costs	
	depreciation allowance	
	Taxable income	- (total annual operating costs)
- Income taxes (40%)	+ 0.4(total annual operating costs)	
Net income	- 0.6(total annual operating costs)	
+ depreciation allowance	+ 0.1(total capital investment)	
Net operating cash flow		
year 0	0	
years 1-10	- 0.6(TOC) + 0.1(TCI)	
Investing activities		
- Capital investments (at year 0)	- (total capital investment)	
+ Salvage value (assumed negligible)	0	
- Disposal tax effect	0	
- Working capital (none additional)	0	
+ Working capital recovery	0	
Net investing cash flow		
year 0	- (TCI)	
years 1-10	0	
Financing activities		
+ Loan	0	
- Repayment of principal	0	
Net financing cash flow		
years 0-10	0	

Appendix XV Hifi23 Torch Simulation Contour Maps

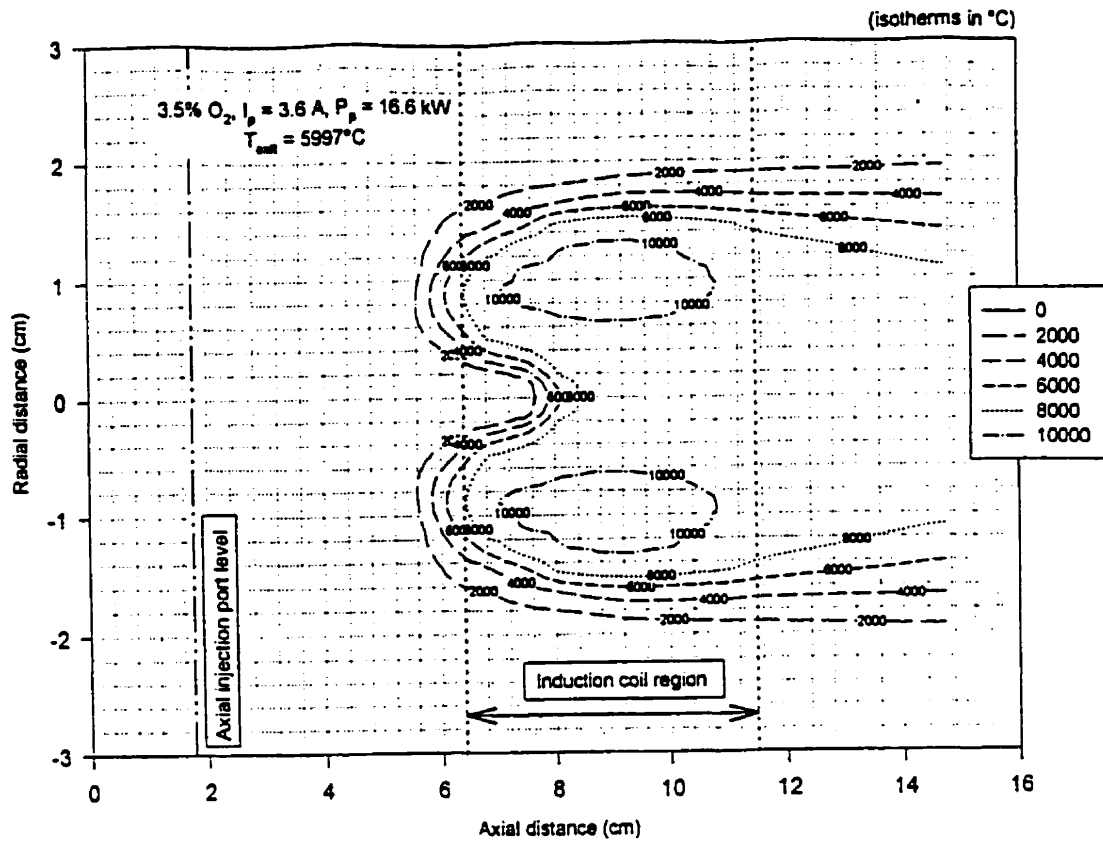


Figure XV-A: Temperature Map at Low Current and Low Oxygen Content

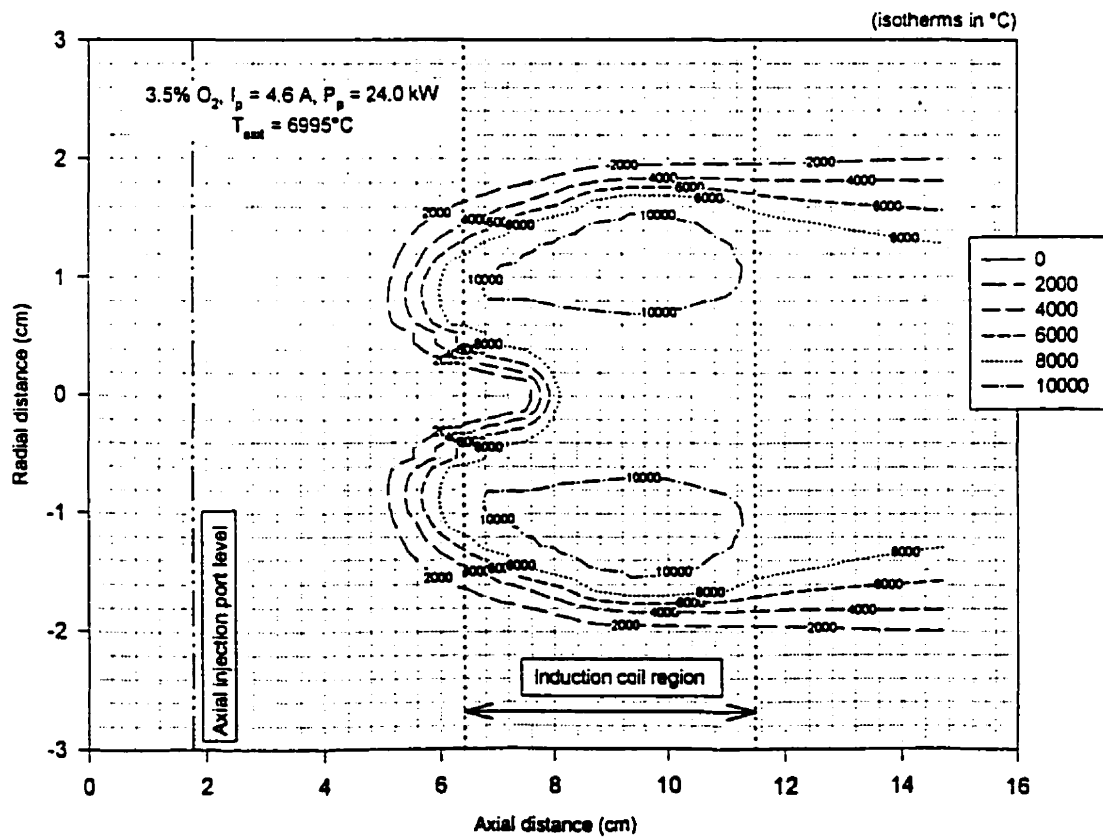


Figure XV-B: Temperature Map at High Current and Low Oxygen Content

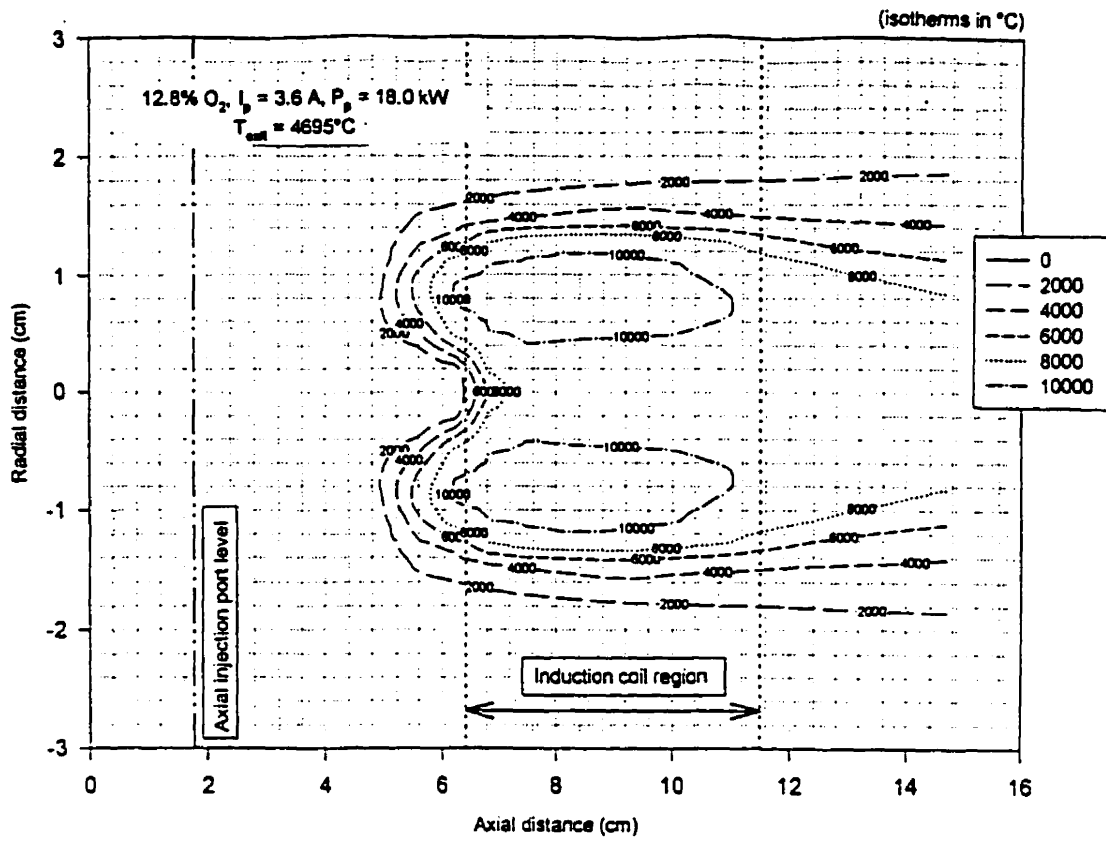


Figure XV-C: Temperature Map at Low Current and High Oxygen Content

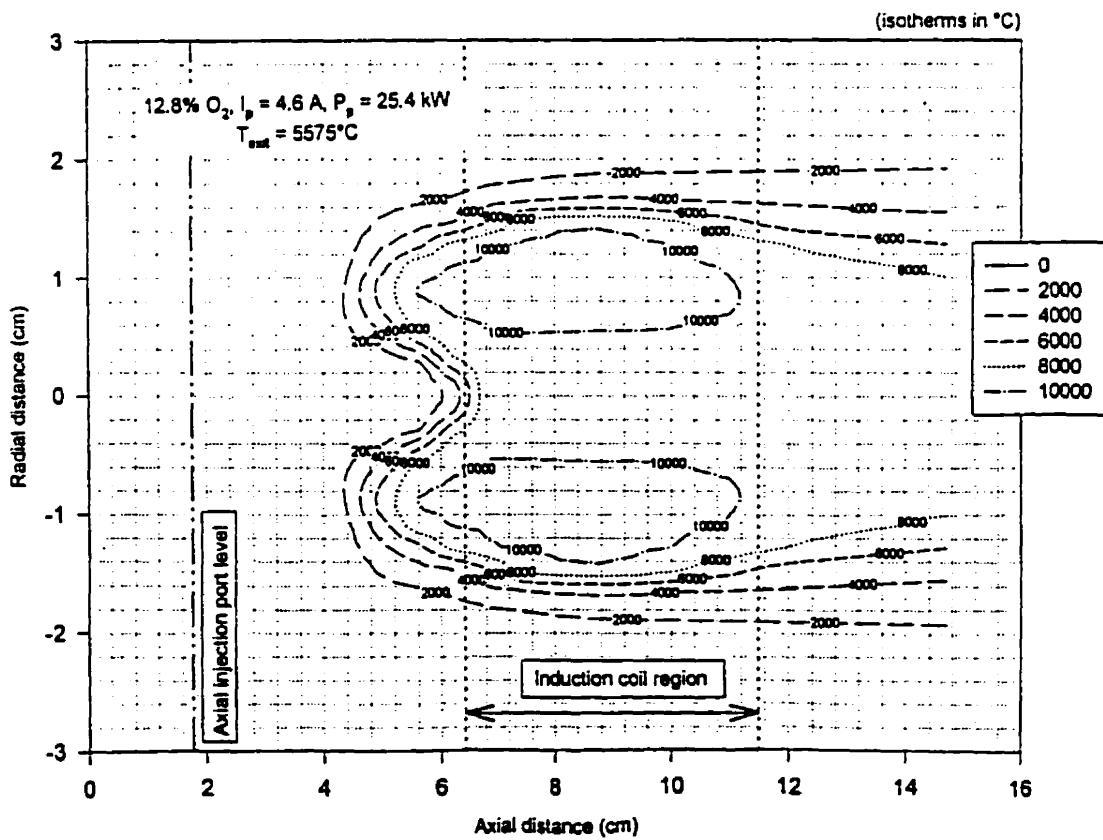


Figure XV-D: Temperature Map at High Current and High Oxygen Content

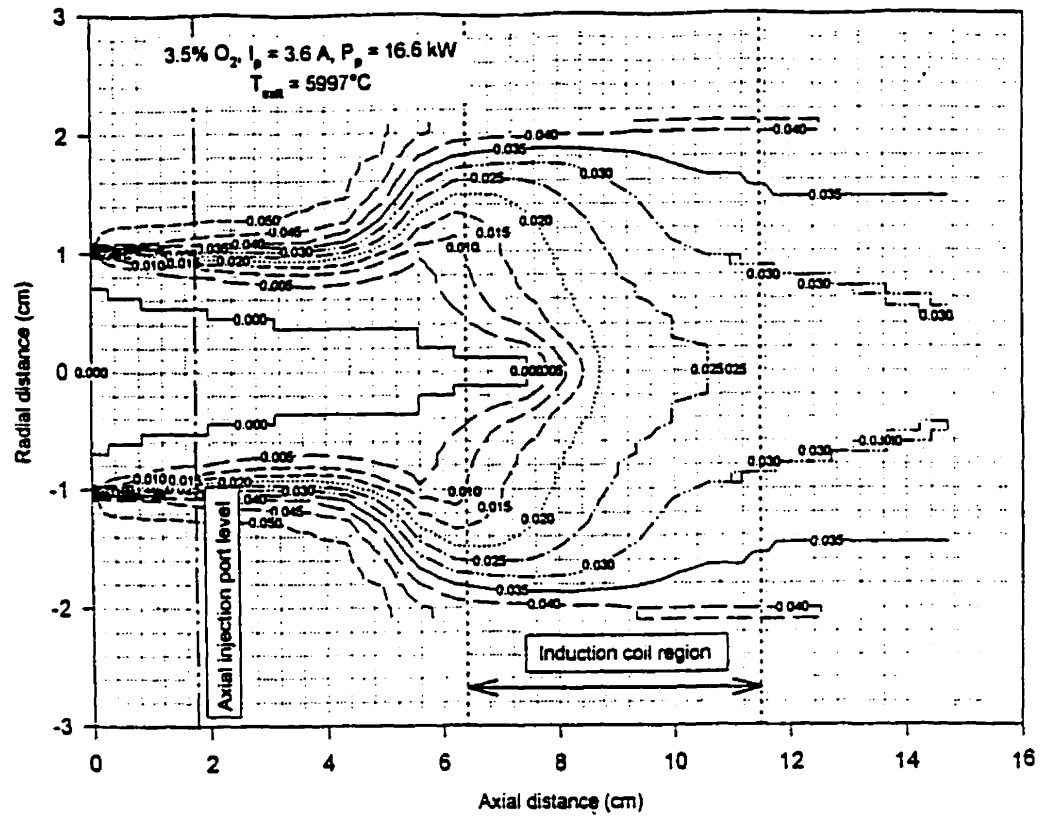


Figure XV-E: Concentration Map at Low Current and Low Oxygen Content

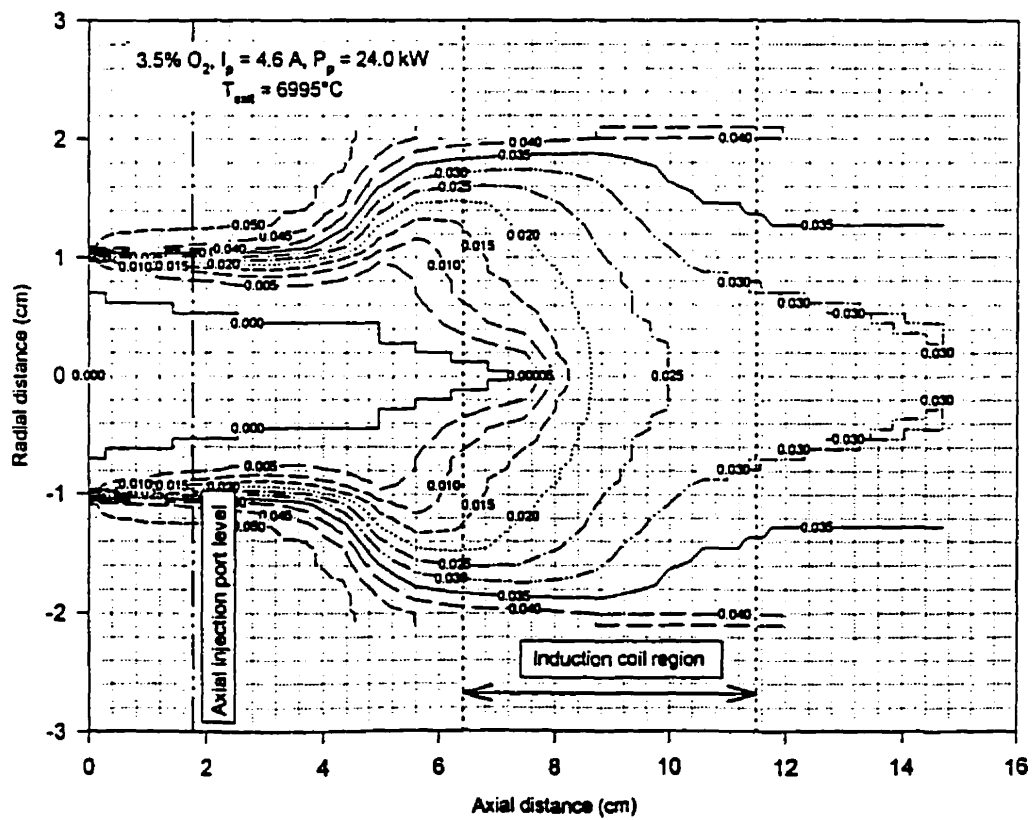


Figure XV-F: Concentration Map at High Current and Low Oxygen Content

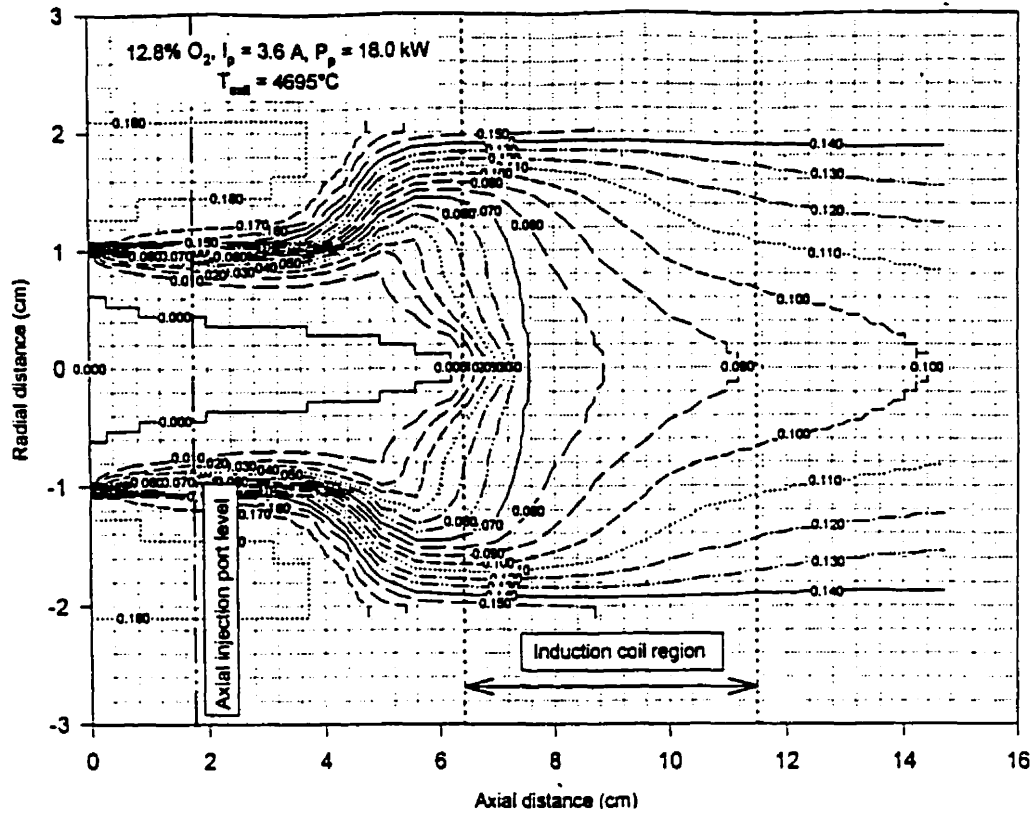


Figure XV-G: Concentration Map at Low Current and High Oxygen Content

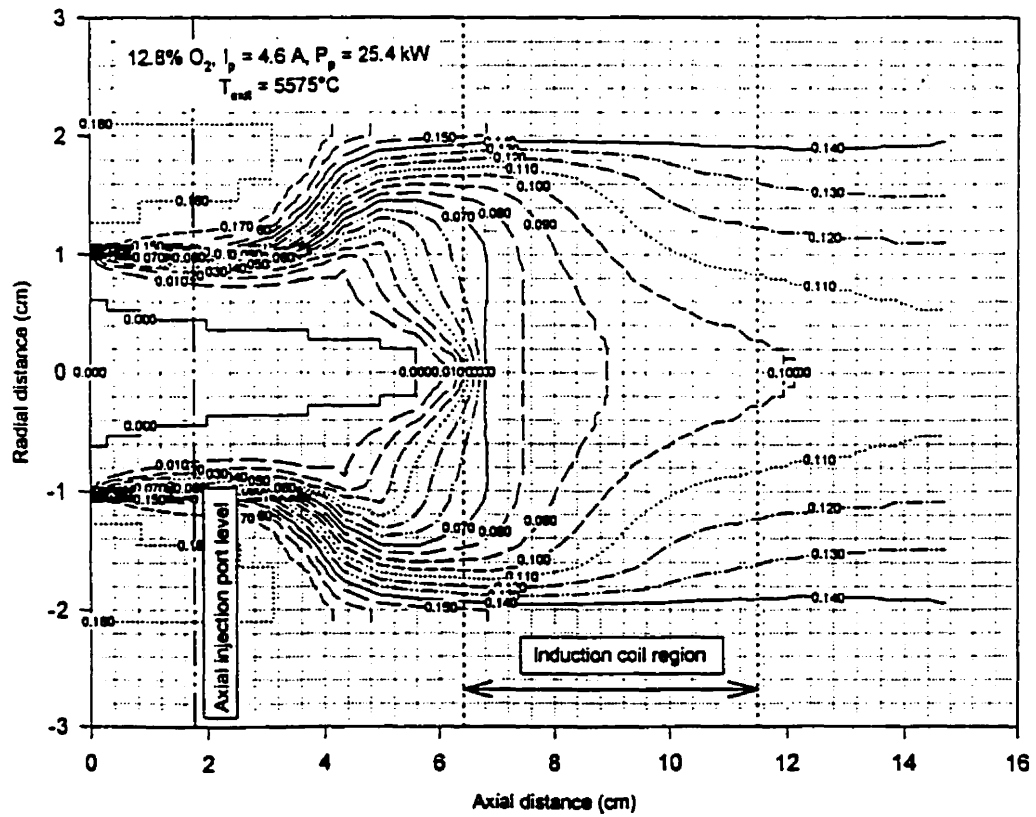


Figure XV-H: Concentration Map at High Current and High Oxygen Content

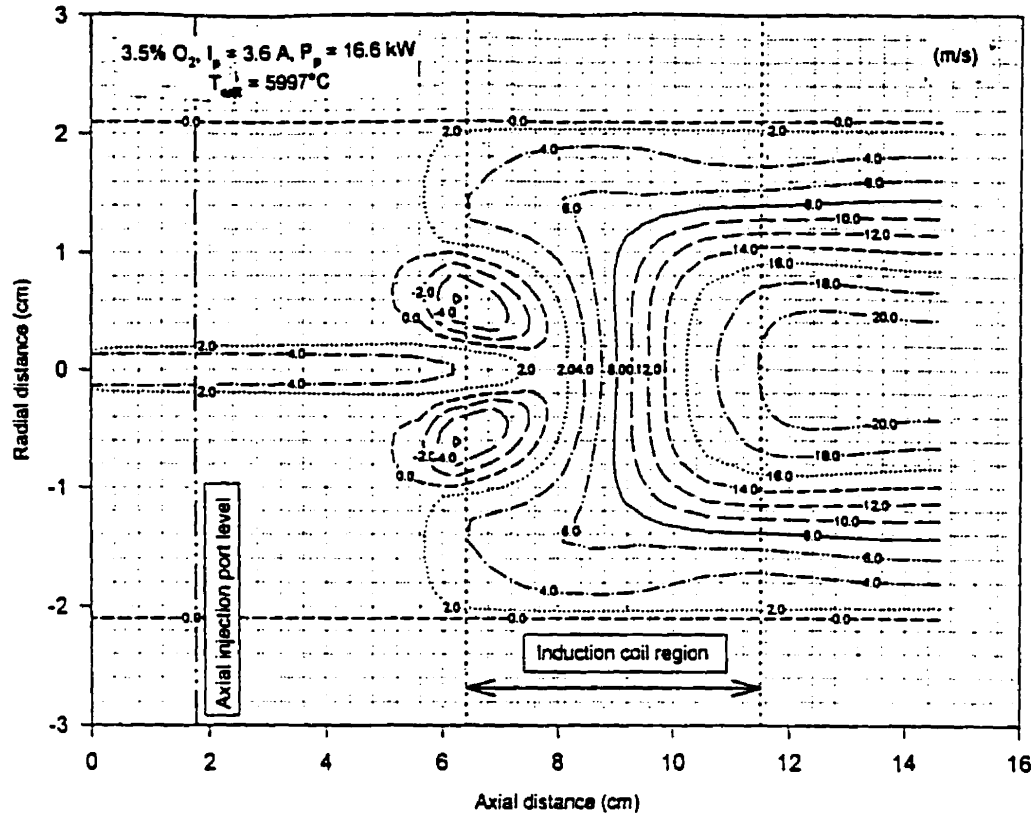


Figure XV-I: Axial Velocity Map at Low Current and Low Oxygen Content

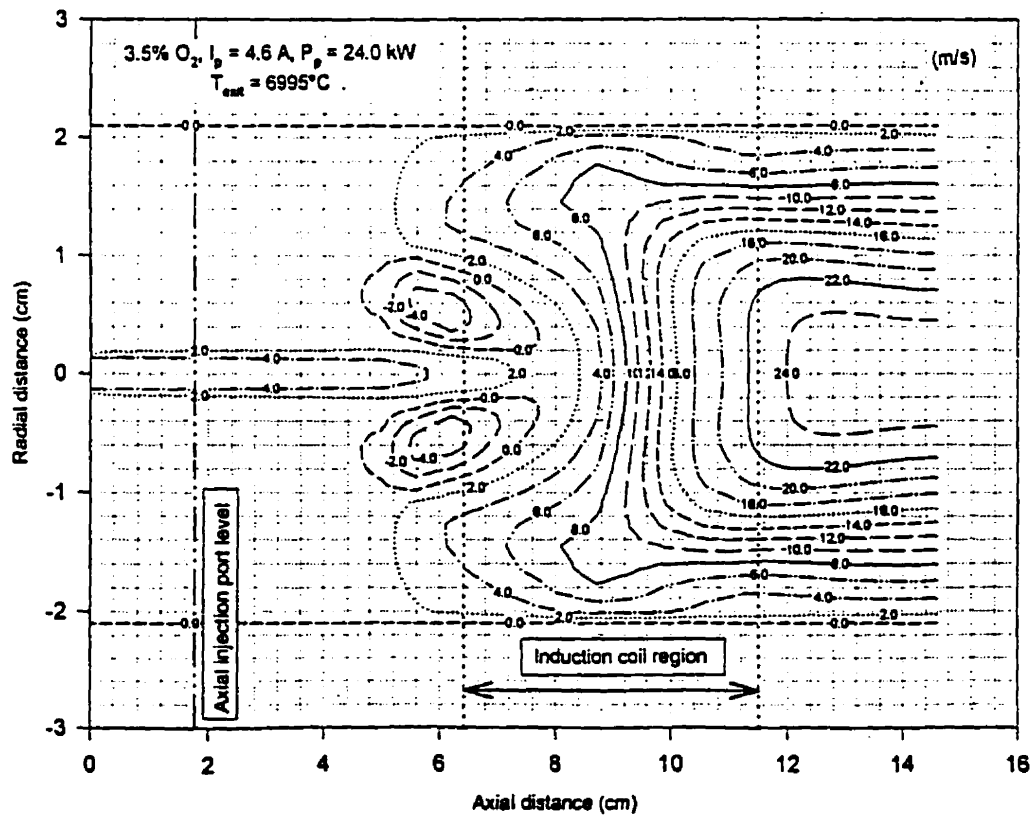


Figure XV-J: Axial Velocity Map at High Current and Low Oxygen Content

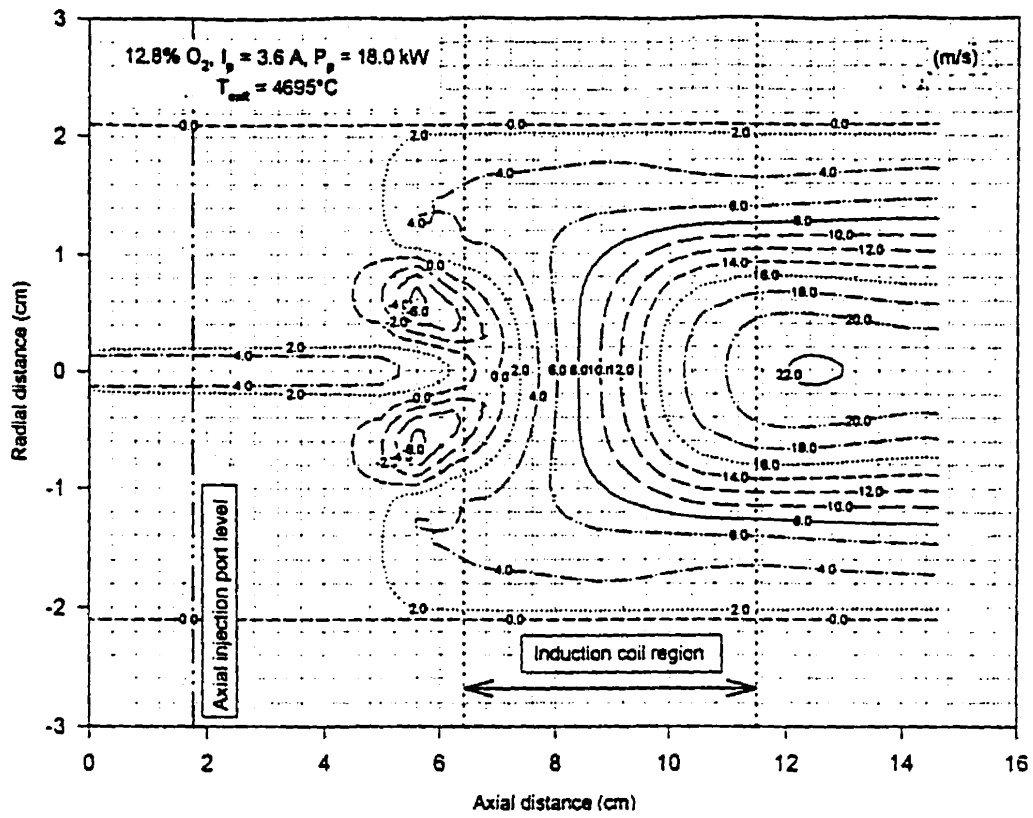


Figure XV-K: Axial Velocity Map at Low Current and High Oxygen Content

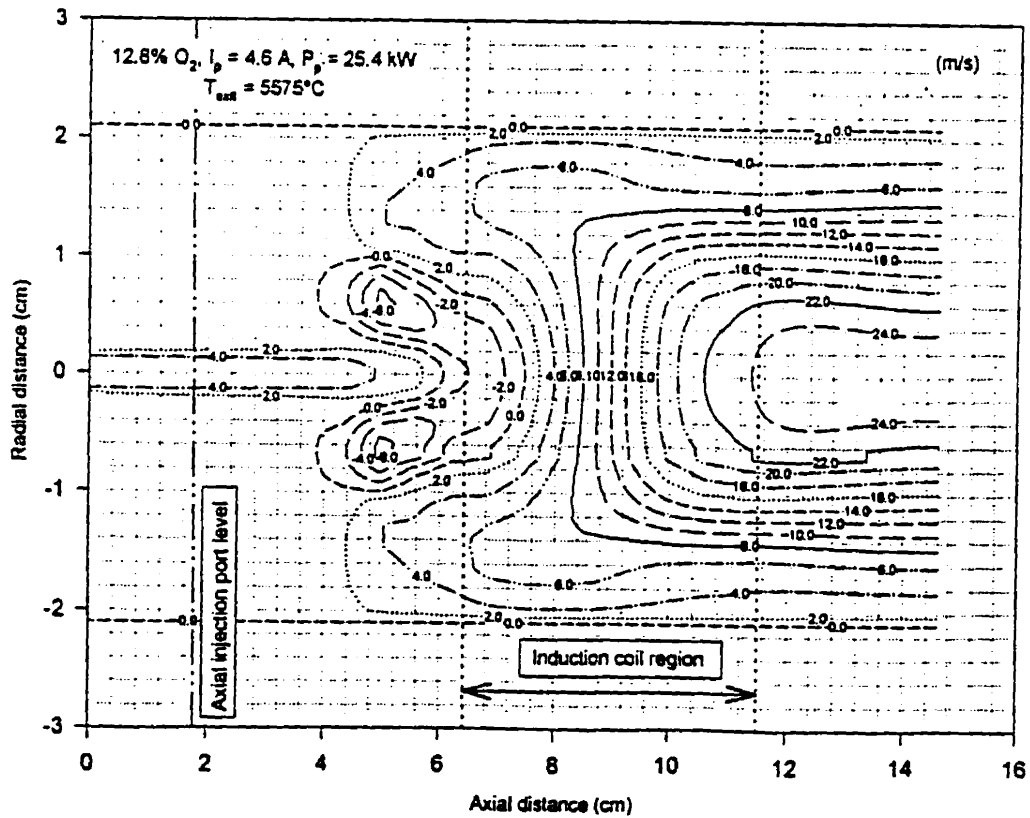


Figure XV-L: Axial Velocity Map at High Current and High Oxygen Content